STUDY OF VIBRATION CHARACTERISTICS OF SKEW LAMINATED COMPOSITE SANDWICH PLATES AND SHELLS OPERATING IN HYGRO AND THERMAL ENVIRONMENTS

Thesis

Submitted in partial fulfillment of the requirements for the degree of

DOCTOR OF PHILOSOPHY

By

VINAYAK BASAVANTH KALLANNAVAR

DEPARTMENT OF MECHANICAL ENGINEERING

NATIONAL INSTITUTE OF TECHNOLOGY KARNATAKA,

SURATHKAL, MANGALORE-575025

JULY, 2022

DECLARATION

I hereby declare that the Research Thesis entitled **"STUDY OF VIBRATION CHARACTERISTICS OF SKEW LAMINATED COMPOSITE SANDWICH PLATES AND SHELLS OPERATING IN HYGRO AND THERMAL ENVIRONMENTS"** which is being submitted to the **National Institute of Technology Karnataka, Surathkal,** in partial fulfillment of the requirements for the award of the Degree of **Doctor of Philosophy** in **Mechanical Engineering** is a *bonafide report of the research work carried out by me*. The material contained in this Research Thesis has not been submitted to any other Universities or Institutes for the award of any degree.

Register Number: **187504 187ME024**

Name of the Research Scholar: **VINAYAK BASAVANTH KALLANNAVAR**

Signature of the Research Scholar: *Bkallann*
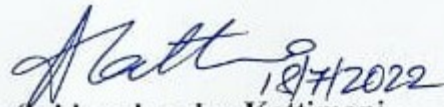
Department of Mechanical Engineering

Place: NITK, Surathkal

Date: 18.07.2022

CERTIFICATE

This is to certify that the Research Thesis entitled "STUDY OF VIBRATION CHARACTERISTICS OF SKEW LAMINATED COMPOSITE SANDWICH PLATES AND SHELLS OPERATING IN HYGRO AND THERMAL ENVIRONMENTS" submitted by **Mr. VINAYAK BASAVANTH KALLANNAVAR** **(Register Number: 187504 187ME024)** as the record of the research work carried out by him, *is accepted as the Research Thesis submission* in partial fulfillment of the requirements for the award of the degree of **Doctor of Philosophy.**

Research Guide

18/7/2022

Dr. Subhaschandra Kattimani

Associate Professor

Department of Mechanical Engineering

NITK, Surathkal

Chairman-DRPC 19 7 2022

Department of Mechanical Engineering

National Institute of Technology Karnataka, Surathkal

Dedicated to

My Parents
Prof. Basavanth Kallannavar and Smt. Vimala Kallannavar
And

INDIAN ARMED FORCES

ACKNOWLEDGEMENT

It provides immense pleasure to acknowledge all the people who have assisted, encouraged and supported me throughout my dissertation. It is my modest appreciation towards everyone who has sacrificed their comfort in some form or other on the successful completion of my doctoral studies.

First of all, I would like to express my sincere gratitude, regards, and thanks to my research supervisor Dr. Subhaschandra Kattimani, Associate Professor, Department of Mechanical Engineering, National Institute of Technology Karnataka (N.I.T.K), Surathkal, for considering me worthy of working under his esteemed guidance. I'm sure without his guidance, this work would not have taken this final shape. His interest and confidence in me were the reason for all the success I have made.

I take this opportunity to thank Dr. Ravikiran Kadoli, Professor and Head, Department of Mechanical Engineering, for his continuous and timely support. I also thank the former heads of the department, Prof. Narendranath S, Prof. Shrikantha S. Rao, and Prof. S M Kulkarni, for their constant support and guidance. I would like to express my deepest appreciation to the members of the research progress assessment committee, Dr. sharnappa Joladarashi and Dr. Pathipati Srihari, for their valuable remarks, suggestions, and technical advice during the length of my research.

I wish to express my sincere gratitude to all the faculty members of the Department of Mechanical Engineering, N.I.T.K Surathkal, for their unbiased appreciation and support all throughout this research work.

ABSTRACT

This dissertation presents an investigation of the influence of temperature and moisture on free vibration characteristics of laminated composite, hybrid composite, and sandwich panels. The composite sandwich panels (plates and shells) considered to be made of laminated composite material face sheets, and softcore materials as the core materials. A finite element (FE) formulation is developed for the whole model using a layerwise first-order shear deformation theory (FSDT) considering the uniform temperature and moisture concentration rise. The influence of temperature and moisture on the natural frequencies of various shell structures such as cylindrical, ellipsoid, hyperbolic, and spherical shells are investigated and compared with the frequencies of flat sandwich plates. Effects of length to width ratio, length to thickness ratio, radius to length ratio, the ratio of core thickness to the thickness of the face sheet, skew angle, boundary conditions on the vibration characteristics of the skew laminated composite sandwich panels are studied. Additionally, an attempt has been made to investigate the challenges in an experimental vibration study of the laminated composite sandwich plates with a 3D printed Polylactic acid (PLA) core.

Furthermore, an artificial neural network (ANN) based predictive model is established to understand the influence of temperature and moisture on the skew sandwich plates. Further study has been extended to investigate the performance of active constrained layer damping (ACLD) of a laminated composite sandwich plate operating in a thermal environment. Additionally, an experimental investigation is performed to understand the influence of temperature on the natural frequency of laminated composite sandwich plates operating in sub-ambient temperatures. Consequently, the present investigation is believed to be enormously helpful in the field of computational mechanics and structural health monitoring of composite sandwich structures operating in challenging environments suitable for various industrial applications.

KEYWORDS: Sandwich plates and shells; Free vibration; Shear deformation theory; Natural frequency, Influence of temperature and moisture; Active constrained layer damping, Artificial neural network.

CONTENTS

3 NEURAL NETWORK-BASED VIBRATION STUDY OF LAMINATED COMPOSITE SANDWICH PLATES OPERATING IN THERMAL AND MOISTURE ENVIRONMENTS

4 FREE VIBRATION STUDY OF DOUBLY-CURVED SANDWICH SHELLS OPERATING IN THERMAL AND MOISTURE CONDITIONS

5 FREE VIBRATION BEHAVIOR OF POROUS DOUBLY-CURVED SKEW LAMINATED COMPOSITE SANDWICH SHELLS WITH 3D PRINTED PLA CORE IN THERMAL ENVIRONMENT

LIST OF FIGURES

xiv

LIST OF TABLES

Chapter 1

INTRODUCTION

In this chapter, basic introduction and comprehensive literature survey related to laminated composite and composite sandwich materials are presented. The physics behind the vibration characteristics of the laminated composite sandwich (LCS) structures are unveiled. Significant discoveries of many engineers and researchers with respect to the LCS structures and their applications are presented. Particular emphasis is given to vibration characteristics and vibration attenuation characteristics of sandwich structures operating in various challenging environmental conditions. From the widespread literature review, the prominent research gaps have been identified and are taken into consideration for framing the research objectives of this dissertation. In the end, the organization of the thesis chapters has been outlined.

1.1 SANDWICH COMPOSITE MATERIALS

The ever-increasing demand for high-performing and efficient materials has led researchers to look for alternate materials. The catastrophic failure of the isotropic and homogeneous materials in high-end engineering applications in challenging working environments has accelerated the quest to find new materials. The immediate alternatives adopted were the alloys, which are easily obtained by mixing two or more metal elements to form the respective metal alloys. Primarily, the alloys are meant to exploit the superior characteristics of the constituent materials. However, the drawbacks of the constituent materials come along with it. For example, some metals are prone to corrosion, and such inherent properties of the materials will also exist in the resulting metal alloys. The laminated composite materials are slowly replacing the metals and their alloys in high-end engineering applications because the composite materials offer superior material properties such as high strength to weight ratio, high modulus, enhanced flexural rigidity, etc. Hence, laminated composite structures are extensively being used in prominent engineering fields such as acoustics, automotive, aviation, biomedical, civil engineering, marine structures, etc.

The composite materials are formed by combining two or more insoluble constituent materials at a macroscopic level. One component is called the matrix phase, and the one which is embedded is called the reinforcing phase. The matrix phase materials are usually continuous, and the reinforcing phase may be in the form of flake, particle, or fiber. In most cases, the fiber-reinforced composite materials are used due to their superior characteristics such as high ductility, high toughness, better transfer of loads from matrix to fiber, and retains excellent bending flexibility.

Modern engineering structures often experience transverse loads and undergo bending. The structures under bending loads experience maximum stresses at the top and bottom surfaces and exhibit minimum stress magnitudes at the center. Sandwich structures are most suitable for such applications, as they are made of thin and strong facings and soft and thick core (Altenbach *et al*., 2018). Materials used for core are usually thick and low-density materials such as viscoelastic materials, polymer foams, and aramid papers. The commonly used face sheet materials are fiber-reinforced polymer composites such as glass-epoxy, graphite-epoxy, carbon-epoxy, kevlar-epoxy, etc. The basic idea behind the sandwich structures is to enhance the flexural rigidity of a structure without a considerable increase in the system's mass. The importance of core geometry on bending characteristics can be demonstrated by considering a simply supported beam with a rectangular cross-section, as shown in Figure 1.1.
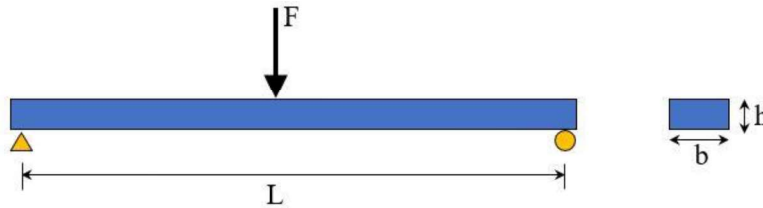
Figure 1.1: Schematic representation of a simply supported beam under central point load.

The bending moment of the rectangular beam can be given as,

$$M = \frac{\sigma}{y} I = \left(\frac{\sigma}{h/2} \right) \left(\frac{bh^3}{12} \right) = \frac{\sigma bh^2}{6} \tag{1.1}$$

From Eqn. 1.1, it is evident that the bending moment of the structure is largely dependent on the thickness of the structure. Considerable changes in bending moment can be observed for small variations in the magnitude of thickness of the structure.

Similarly, the central deflection for a simply supported rectangular beam with central load can be given as,

$$\delta = \frac{FL^3}{48EI} = \frac{FL^3}{48E\left(bh^3\big/12\right)} \qquad (1.2)$$

Where,

F= Applied point load; L= Span length of the beam; E= Young's modulus of the material; b= width of the beam; h= thickness of the beam; I= Area moment of inertia; M= bending moment; y= Distance from neutral axis to outer fibre, σ= Bending stress. From Eqn. 1.2, it can be seen that the central deflection of the structure is inversely proportional to the cube of the thickness of a structure. Hence, with an increase in the thickness of the structure, the central deflection of the system reduces drastically. The LCS structures enjoy superior flexural rigidity as the thin composite face sheets endure stresses present in the outer section and the thicker core ensures enhanced area moment of inertia of the structure.

1.2. APPLICATIONS OF SANDWICH STRUCTURES

The LCS structures have attracted many prominent fields of engineering due to their exceptional mechanical and thermal characteristics. The LCS structures are effectively and efficiently being used in automotive, aviation, biomedical, marine engineering fields. The aircraft components such as elevons, rudders, fins, wings, nose, landing gear doors, spoilers, pylons, fairings, floor panels, etc., are majorly made of LCS structures. The civil and the military aircrafts such as XB 70 valkyrie, F-14 tomcat, Dassault Mirage F1, Boeing B747, B787, ATR 72, Airbus A380, A350, Starship NC 51, etc., extensively use laminated composites and LCS structures in their components. The cone section of the Ariane-5 spacecraft is primarily made of aluminum foam sandwich structures. In marine applications, foam-based LCS structures are commonly used to construct the deck, hull, bow, stern, funnel, interiors, etc. The sandwich structures also find their applications in body panels of automotive and railway structures (Castanie et al., 2020: Palomba et al., 2021).

1.3. HYGROTHERMAL ENVIRONMENT

In high-end engineering applications, the materials are expected to work efficiently even in challenging and hazardous environments such as high operating temperature, presence of moisture, and chemical environments. Dynamically changing environmental and loading conditions may adversely affect the behavior of structures. On exposure to hazardous environments, composite structures may lose their structural integrity due to the contraction or expansion of layers. The unequal expansion or contraction between neighboring layers may introduce residual stresses in a structure. In elevated thermal conditions, the bond between the fibers and the matrix may weaken, resulting in the reduction of strength and stiffness of a composite structure (Garg *et al*., 2019). The phenomenon of weakening of bonds on exposure to an elevated hygrothermal environment was reasoned by many researchers using the scanning electron microscope (SEM) images (Putic *et al*., 2007: Islam *et al*., 2010: Rezaei *et al*., 2018: Shah *et al*., 2019: Gagani *et al*., 2019).

Similarly, in the presence of a moisture environment, water absorption and desorption characteristics of both fiber and matrix materials are different. In the case of resin (matrix), complete recovery of stiffness and bending strength is possible for the water uptake and desorption cycle. In contrast, for the composite materials, complete recovery is not possible. Additionally, resin degradation is supplemented by the differential swelling stress magnitudes for accelerated aging and hygrothermal aging, which causes fiber-resin interface damage (Guermazi *et al*., 2016: Rocha *et al*., 2017). The schematic representation of the fiber-matrix debonding phenomenon is presented in Figure 1.2
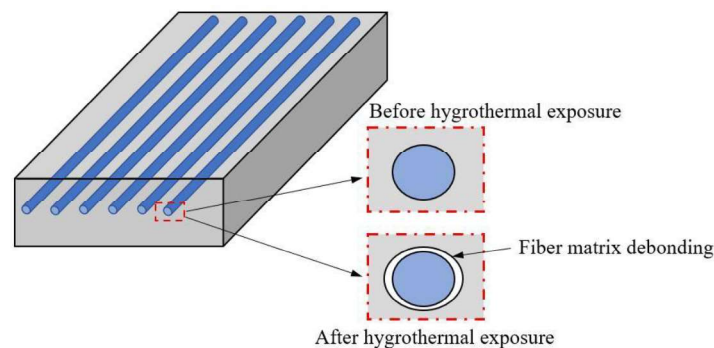
Figure 1.2: Pictorial representation of the influence of hygrothermal environment on the fiber-reinforced composites.

Further, the cracks formed in composite structures during fabrication, assemblage, or usage become prominent failure zones in elevated thermal settings. In high-temperature conditions, the fracture toughness of the structure reduces, i.e., with a rise in temperature, the load at the breakpoint of composite reduces considerably (Kaya *et al.*, 2020). Hence, the material's mechanical properties, such as modulus, strength, stiffness, etc., reduce substantially with increasing temperature and moisture values (Shokry *et al.*, 2014). The material constituent relationship for the structure operating in a hygrothermal environment can be written as:

$$\{\sigma\} = [C]\{\varepsilon_m - \varepsilon_t - \varepsilon_c\} \tag{1.3}$$

where. [C] is the material constant matrix or stiffness matrix.

1.4. STRUCTURAL HEALTH MONITORING

Constantly changing environmental conditions may unfavorably affect the performance of materials, which in turn may cause untimely damage to the structures. A systematic health monitoring mechanism should be devised to avoid premature failure of the structures. The constant health monitoring of structures enables engineers to detect anomalies in time and begin suitable repair and maintenance work. Additionally, a systematic scientific study may lead to detection of the source of structural errors, and subsequently, an appropriate action plan can be devised to avoid future occurrences. The process of employing a damage identification strategy for aerospace, civil, and mechanical engineering structures is generally referred to as structural health monitoring (SHM) (Farrar *et al.*, 2007). Vibration-based SHM techniques are the predominantly used non-destructive damage detection methods (Sharnappa *et al.*, 2007: Nguyen *et al.*, 2018: Bouazza *et al.*, 2020). High-precision sensors such as accelerometers, strain gauges, velocity transducers, laser displacement sensors, etc., are strategically placed on structures to obtain the structural responses, mode shapes, natural frequencies, damping parameters, etc. Meticulous engineering evaluation of measured responses can detect and/or predict the magnitude of damage. The accurate predictive models based on the pre-existing dataset are a more appropriate option for SHM applications. The artificial neural network (ANN) techniques are often used for developing predictive models based on the preliminary dataset (Salehi *et al.*, 2018). The ANN technique has been extensively and effectively employed in civil

engineering applications and is rapidly gaining importance in other prominent engineering areas also (Marques and Anderson 2001; Marques *et al*., 2005, 2017; Paula *et al*., 2019; Paula and Marques 2019).

In the recent past, ANNs have been used extensively by researchers for structural engineering applications such as failure prediction, crack detection, delamination identification, quantification of damage magnitude, predicting the size and position of cutouts (Elshafey *et al*., 2013: Atilla *et al*., 2020), determining mechanical characteristics (Sharma *et al*., 2020: Mouloodi *et al*., 2020), etc. Recently, Zenzen *et al.* (2020) adopted a transmissibility damage indicator and an ANN to predict damage location and size. The transmissibility function and mode shapes were used to estimate the damage location, and then the trained ANN model was used to predict the extent of the damage. The proposed model was intended for fast prediction with highly accurate results without the need to collect all modal analysis data. Gomes *et al*. (2019) used a combination of a genetic algorithm (GA) and an ANN for delamination identification of plate-like structures. Fisher information matrix criteria were used to optimize the sensor position, and a feed-forward ANN was used to detect the damage based on data obtained from finite element (FE) analysis. Rjoub and Alshatnawi (2020) established a mathematical model to investigate the vibration response of simply-supported porous functionally graded (FG) plates using Reddy's third-order plate theory. The results obtained were then used to train the ANN model to predict the natural frequency of a system. It was claimed that the developed ANN model could be easily modified to predict the frequency response for other boundary conditions. Using numerical methods, Atilla *et al*. (2020) investigated the influence of location, diameter, and the number of circular cutouts on composite plate's modal and buckling behavior. Further, the ANN model was developed using the Levenberg–Marquardt backpropagation algorithm to predict the natural frequency and buckling loads of composite plates.

Elshafey *et al.* (2013) developed an effective ANN model for crack width prediction of thick and thin concrete members using the feed-forward backpropagation method. It was reported that the predicted average crack width results were more accurate than the results obtained using the rules in existing building codes. Oliver *et al*. (2020) successfully developed an ANN-based damage detection module for

6

composite plates using frequency shifts. The developed damage detection module used the modal data obtained from the FE analysis for training. The severity and position of predicted damage were reported to have 95% accuracy. Jalal *et al.* (2020) developed an optimum ANN model to predict the strength of a rubberized cement composite based on experimentally obtained characteristics of composites. The predicted strength values were reported to have 98% accuracy. Jodaei *et al.* (2012) used a state-space-based differential quadrature technique to study the frequency response of FG annular plates. In addition, an optimal ANN model was proposed for the prediction of the natural frequency of the systems operating under different boundary conditions. It was reported that the ANN model predicts frequencies with high accuracy and agrees well with the trend of semi-analytical results.

1.5. ANALYSIS OF LCS STRUCTURES

In the past few decades, many researchers have explored the vibration characteristics of LCS structures using both experimental and numerical techniques. This section discusses the most significant contributions of free vibration analysis of laminated composite and sandwich structures. Additional attention is given to the literature dealing with the hygrothermal analysis of LCS structures and the vibration attenuation characteristics of the smart composite structures. A brief review of the literature is presented under the following sub-sections:

- Free vibration of composite and sandwich composite structures
- Hygrothermal behavior of composite and sandwich composite structures
- Active vibration control of composite and sandwich composite structures

1.5.1. Free vibration of composite and sandwich composite structures

The mechanical components tend to vibrate during their operations due to intended or inadvertent forces present in a system. The unaccounted oscillations in the mechanical component modules may lead to the resonance of the structure. Hence, it is essential to identify the resonant frequency of the component assemblage in order to avoid catastrophic failure. The free vibration analysis of the structures provides necessary information on the resonance frequency values of a system. Initially, Raville and Ueng (1967) experimentally inspected the vibration characteristics of a simply

supported rectangular sandwich plate. Later, Wang (1997) effectively utilized the FSDT to numerically investigate the free vibration response of fiber-reinforced laminated composite plates. Yuan and Dave (2002) developed the spline finite strip model to predict the natural frequencies and the corresponding mode shapes of a rectangular sandwich plate. Chakrabarti and Sheikh (2004) introduced a new refined plate model to establish the vibrational behavior of a sandwich plate discretized with six noded triangular elements. The vibration characteristics of a layered sandwich plate were analyzed using the two higher-order shear deformable facet shell element mode by Khare *et al*. (2005). The differential quadrature method (DQM) was adopted by Alibeigloo and Emtehani (2015) to study the vibration response of FG carbon nanotube-reinforced composite (CNTRC) plates.

The scale-dependent physical properties, remarkable thermo-mechanical properties, and enhanced elastic properties have made the carbon nanotube (CNT) based composites a prominent choice for high-end engineering applications (Kundalwal and Meguide, 2015). The atomic arrangement, diameter and length of the tube, and morphology of tubes influence the properties of the CNT material. The nanotubes are commercially available in both single-walled and multi-walled structures. The CNTs are primarily produced using laser ablation, arc discharge, chemical vapor deposition, and gas-phase catalytic growth methods (Eric et al., 2001). The CNT-based composite structures are prepared by distributing the CNT particles in a suitable matrix solution. Based on the distribution of the pattern of CNTs, the composites are further classified as uniformly distributed, X-type, V-type, O-type, etc.

Biswal and Ray (2017) performed experimental and numerical investigations of the modal behavior of glass-epoxy and graphite-epoxy hybrid laminate composite plates. The well-established models such as FSDT and third-order shear deformation theories (TSDT) were fed with the mechanical properties obtained from the non-destructive ultrasonic sound velocity measurement setup. Further, the results obtained from numerical models were compared with the experimental results. Similarly, the influence of cutout parameters on vibration characteristics of a laminated composite plate was investigated by Dewang *et al.* (2020) using numerical and experimental techniques. The cutout shape, orientation, and position were observed to have considerable influence on the modal behavior of composite plates. Later, the modified

coupled stress theory and FSDT were utilized by Emadadi *et al*. (2019) to understand the vibration behavior of an annular sandwich plate with CNTRC face sheets and FG porous core. Garg *et al.* (2006) developed a higher-order shear deformation theory (HSDT) based isoparametric FE model to study the free vibration characteristics of skew laminated composite sandwich (SLCS) structures. The model was capable of predicting the realistic non-linear variation of through-thickness displacements of sandwich structures without using a shear correction factor.

The DQM based semi-analytical method was used by Heshmati and Daneshmand (2018) to investigate the modal characteristics of weight-efficient FG non-uniform porous plates. Katariya *et al.* (2021, 2020) performed an experimental and numerical investigation of epoxy-filled soft core sandwich plates with glass-epoxy face sheets to understand the linear and non-linear vibrational behavior of sandwich structures. Kiran *et al.* (2018, 2018a) studied the vibrational characteristics of FG porous skew magneto-electro-elastic (MEE) plate to understand the influence of porosity on the natural frequency of a system. Pan *et al*. (2002, 2005, 2013) obtained the exact solution for multi-layered and functionally graded MEE plates under static loading. Mahi *et al.* (2015) proposed a shear correction factor for novel hyperbolic shear deformation theory to investigate the free vibration characteristics of sandwich plates. Similarly, the experimental and numerical investigation of the vibration response of a glass-epoxy composite plate was reported by Mishra and Sahu (2015). Later, the vibration analysis of hybrid composite plates made of aluminum and glass-epoxy layers was reported by Prasad and Sahu (2018). Singh and Sahoo (2020) utilized the inverse hyperbolic shear deformation theory to investigate the static and vibration characteristics of the FG-CNTRC sandwich plates. Karimiasl and Ebrahimi (2019) used Reddy's TSDT to articulate the large amplitude vibrations of smart viscoelastic doubly-curved sandwich shell structure with magnetorheological layers and a flexible core. Pouresmaeeli and Fazelzadeh (2016) performed the modal analysis of the thick doubly curved carbon nanotube reinforced FG composite shells using the FSDT. The unified Fourier series solution for FG-CNTRC shells and plates was obtained by Qin *et al.* (2020) for arbitrary boundary conditions.

In addition, Rouj and Alshatnawi (2020) developed an analytic model to investigate the free vibration characteristics of an FG plate with uniformly distributed

pores and side surface cracks. Further, the ANN model was also developed to predict the natural frequency of the system. The multilayer ANN architecture was designed by Behera *et al.* (2016) to develop a prediction model to estimate the surface roughness and delamination in drilling of a glass fiber reinforced composite structure. Haji Agha Mohammad Zarbaf *et al.* (2018) proposed a novel ANN-based bridge cable tension estimation model to aid the timely structural health monitoring of civil structures. Similarly, Karnik *et al.* (2008) established an ANN-based predictive model to investigate the delamination behavior of carbon fiber reinforced structures as a function of high-speed drilling process parameters. Subsequently, Khatir *et al.* (2020) developed an improved ANN algorithm to detect a crack in the plate based on experimental and extended isogeometric analysis. Further, the combination of FE and ANN methods was used by Luo *et al.* (2020) to accurately and rapidly predict the types of curved shapes of composite laminates. Similarly, Qian *et al.* (2020) developed the Lamb-wave-based damage detection model of a laminated composite plate integrated with a piezoelectric sensor patch.

1.5.2. Hygrothermal behavior of composite and sandwich composite structures

The material properties of laminated composite structures tend to degrade upon exposure to elevated thermal and moisture environments. Reduction in material properties causes a considerable reduction in stiffness of the structure and, in turn, causes a reduction in the natural frequency of the system. In the past few decades, many researchers have studied and reported the influence of temperature and moisture on the free vibration characteristics of LCS structures using analytical, numerical, and experimental methods. Few such articles are discussed in this sub-section.

Abdelmalek *et al.* (2019) investigated the influence of temperature and moisture on the vibration characteristics of isotropic and orthotropic composite plates using n^{th}-order shear deformation theory. The temperature-dependent and moisture-dependent material properties were considered for the analysis. Kulkarni and Kapuria (2008) developed a new improved third-order zigzag theory for the static and dynamic analysis of sandwich plates. Similarly, Belarbi *et al.* (2017) generated a new higher-order layer-wise FE model for the static and dynamic analysis of laminated composite and sandwich plates. For simulations, the first-order displacement field theory was considered for face

sheets, whereas a higher-order displacement field theory was used for the core. Padhi and Pandit (2017) investigated the influence of temperature and moisture concentrations on the static and vibration response of sandwich plates using improved zigzag theory. Kheirikhah and Khosravi (2018) numerically investigated the vibrational and buckling response of composite sandwich plates reinforced with the Ni-Ti-based shape memory alloy wires.

Daikh et al. (2020) used HSDT to investigate the thermo-mechanical bending behavior of sandwich plates made of FG face sheets and fully ceramic core. Zhao et al. (2017) developed a piecewise shear deformation theory for free and forced vibration analysis of composite and sandwich plates in thermal environments. It was reported that for all the values of length to thickness ratio of the sandwich plate, the fundamental frequency reduced with an increase in temperature. Similarly, Joseph and Mohanty (2017) used FSDT to investigate the buckling and free vibration characteristics of a sandwich plate under a high-temperature environment. Soft viscoelastic core and FG material face sheets were considered for the analysis. Suresh Kumar et al. (2013) achieved active constrained layer damping (ACLD) of smart FG sandwich plates subjected to thermal loading. Zenkour and Alghanmi (2019) performed the static and dynamic analysis of sandwich plate consisting of an FG core and piezoelectric face sheets, operating under hygro-thermal and electro-mechanical sinusoidal loadings. Ding et al. (2018, 2019) experimentally investigated the influence of aging of sandwich composites consisting of vinyl-ester-based composite face sheets and polyvinyl chloride foam core in various harsh environments such as high temperature, moisture, and various hygrothermal profiles.

Garg et al. (2006) used HSDT to study the free vibration characteristics of isotropic, orthotropic, and sandwich skew laminates. Similarly, Park et al. (2008) explored the dynamic behavior of the skew sandwich plate with laminated composite faces using the HSDT. Subsequently, Chalak et al. (2014) developed a C^0 FE model based on higher-order zigzag theory to investigate the bending and free the vibration behavior of laminated soft core skew sandwich plates. Wang et al. (2000) used the p-Ritz method for vibrational analysis of skew sandwich plates composed of an orthotropic core and laminated face sheets. Chakrabarti and Sheikh (2004) developed a six-node triangular element based on refined plate theory for the vibrational analysis of

sandwich plates consisting of stiff laminated face sheets. Katariya et al. (2018) numerically investigated the bending and the free vibration behavior of skew sandwich plates with different core materials using the HSDT. It was reported that with an increase in skew angle, the magnitude of natural frequency increased, whereas a dip in central deflection value was observed.

Recently, Sharma *et al*. (2019) utilized a higher-order finite boundary element method to investigate the vibroacoustic characteristics of sandwich shells under harmonic loading in a hygrothermal environment. The influence of the hygrothermal environment on the non-linear transient response of the doubly-curved thick shells was investigated by Swamy and Sinha (2006). They reported that the influence of radius of shell curvature in the presence of a hygrothermal environment is most substantial. Kundu and Han (2009) investigated the effect of temperature and moisture on the vibration response of doubly-curved shells in the pre and post-buckled states. Particular emphasis was given to the occurrence of the snap-through phenomenon in the presence of a hygrothermal environment. Biswal *et al.* (2015, 2016) performed a numerical and experimental investigation to understand the influence of the hygrothermal environment on the free vibration response of a composite shallow shell. It was reported that the natural frequency of shallow composite shells reduced with an increase in moisture and temperature magnitudes. Ebrahimi and Barati (2017) utilized a nonlocal strain gradient model to study the vibration characteristics of the hygrothermally affected viscoelastic FG nanobeams. Nguyen *et al.* (2020, 2021) performed coupled hygro-thermo-mechanical analysis on viscoelastic laminated composite plates using the higher-order zigzag theory and smoothed FE formulation. Mahapatra *et al.* (2016) used a micromechanical approach to develop the Green-Lagrange type geometric nonlinearity model to define the non-linear vibration performance of doubly-curved shells operating in a hygrothermal environment.

Pouresmaeeli and Fazelzadeh (2016) investigated the vibrational performance of moderately thick doubly-curved FG-CNTRC shells using Galerkin's method combined with FSDT. Similarly, Lai *et al.* (2021) studied the influence of the thickness stretching on the static response of CNTRC doubly-curved nanoshells functioning in an elevated thermal environment and found that the deflection of nanoshell varies nonlinearly with a linear increase in temperature. Mehar *et al.* (2015, 2017, 2018, 2020)

utilized experimental and numerical methods to investigate the influence of temperature on the static and dynamic response of single-walled CNTRC doubly-curved shells. Phuong *et al.* (2019, 2020, 2020a) performed a non-linear thermo-mechanical buckling analysis of FG graphene-reinforced composite laminated shells surrounded by the elastic foundation. Nam *et al.* (2020) investigated the non-linear torsional buckling characteristics of FG-CNTRC cylindrical shells. Dat *et al.* (2020) studied the non-linear vibration behavior of a smart MEE sandwich plate with a CNTRC core working in a hygrothermal environment. Coupled magneto-electro-hygro-thermo-elastic model was generated using Reddy's higher-order theory, HSDT, and the closed-form solution was obtained using Galerkin's method. Zhu *et al.* (2012) employed FSDT to investigate static and dynamic characteristics of single-walled CNTRC plates. The results obtained from the FE model developed were in good agreement with the results exploited from ANSYS commercial package.

1.5.3. Active vibration control of composite and sandwich composite structures

In modern engineering structures, the prime importance of design is to develop compact and effective structural components. In order to achieve this, many moving and static components are placed in close proximity. Moving elements of structures tend to vibrate, making the system noisier and unstable. Most of the damaging and unwanted vibrations in a structure can be attenuated by providing suitable damping. The vibration control mechanism is broadly classified as passive and active vibration control systems. In a passive control structure, the damping mechanism is independent of the measure of vibration. For example, the rubber pads provided for the lathe bed have fixed damping capacity. The rubber pads will dampen the vibrating lathe bed independent of the magnitude of vibration. In an active vibration control system, feedback signals will be generated based on the signals obtained from a sensing element, i.e., the damping force is generated based on the magnitude of vibration. In recent times, piezoelectric materials are extensively being used for active control of various structures. Piezoelectric materials are extensively used as distributed sensors and actuators for vibration control based on the phenomenon of direct and converse piezoelectric effects. The piezo-sensors and actuators can be directly mounted on the base structures to achieve the self-monitoring and self-controlling capabilities (Bailey *et al.*, 1985: Crawley *et al.*, 1987:

Song *et al.*, 2001: Li 2012: Zhao *et al.*, 2020a). For satisfactory vibration attenuation of base structures, the monolithic piezoelectric materials need high-control voltage. Research about the development of low-control-authority monolithic piezoelectric materials led to the discoveries of ACLD treatment (Padeep and Ganesan, 2006: Ray and Pradhan 2006, 2007, 2008). In ACLD treatment, the piezoelectric materials are used as the constraining/actuating layer, and the viscoelastic materials are used as a constrained layer.

Many scientific articles have been published pertaining to the investigation of vibration attenuation characteristics of smart composite beams, plates, and shells integrated with the ACLD patches. Arafa and Baz (2000) developed a FE model to investigate the dynamic characteristics of isotropic beams integrated with the piezoelectric patches. Optimal sizing and placement of the actuating patches involving piezoelectric rods that are embedded in a viscoelastic matrix were studied. Baz and Ro (1996) experimentally achieved the vibration control of the isotropic plate embedded with the ACLD patches prepared by sandwiching the viscoelastic layer (DYAD 606) between the two layers of polyvinylidene fluoride (PVDF) films. Similarly, Chantalakhana and Stanway (2001) performed a numerical and experimental investigation of vibration attenuation characteristics of a clamped-clamped aluminum plate for the frequency range from 0 to 600 Hz. Lim *et al.* (2002) developed a three-dimensional closed-loop model to predict the effects of active-passive damping of the vibrating cantilever beam. Subsequently, Datta and Ray (2016) numerically investigated the ACLD treatment of orthotropic laminated composite plates using a three-dimensional fractional derivative model of the constrained viscoelastic layer in the time domain. Kattimani and Ray (2014, 2015, 2017a, 2017b, 2018) developed a three-dimensional FE model to control the geometrically non-linear vibration of multiferroic fibrous composite plates using ACLD treatment. It was reported that the electro-elastic and the magneto-elastic coupling display fringe upsurge in the stiffening effect of the plates. In contrast, their contributions to controlling the non-linear transient vibrations were reported as insignificant. Zhao *et al.* (2019) proposed a novel, simplified single-layer equivalent method to model the plate structure integrated with ACLD patches. They reported that the propped technique could give guidance for vibration attenuation of real-life engineering applications such as wind turbines and aircraft structures.

Sahoo and Ray (2019) performed numerical FE simulations to understand the effect of the shape of constraining layers on the performance of ACLD of laminated composite plates. It was reported that the elliptical ACLD patches are more efficient in attenuating the vibration levels of composite plates in comparison with the square and circular patches. Kanasogi and Ray (2013) investigated the performance of ACLD treatment of smart skew laminated composite plate using 1-3 piezoelectric composites. Suresh Kumar *et al.* (2012, 2013, 2016)) developed a three-dimensional FE model to investigate the performance of ACLD of the smart sandwich plate using vertically reinforced 1–3 PZC material. The effect of process parameters such as boundary conditions, face sheet fiber orientation, fiber orientation of 1-3 piezo-layer, different core materials, the ratio of core thickness to the thickness of face sheet, etc., on the vibration characteristics of a sandwich plate was comprehensively investigated. Further, the studies on vibration attenuation of geometrically non-linear vibrations of sandwich plates were also reported. Bendine *et al.* (2019) studied the influence of patch position on the active vibration control of a laminated composite plate integrated with the discrete piezoelectric patches. The optimal placement of the piezoelectric patches was estimated using a linear-quadratic index and genetic algorithm.

Zippo *et al.* (2015) achieved active vibration control of a free edge rectangular sandwich plate using a macro fiber composite (MFC) sensor and actuators. The carbon fiber reinforced polymer face sheets and polymer paper core were used for the fabrication of an LCS plate. The positive position feedback technique was utilized to control the single-input, single-output, and multiple-input, multiple-output systems up to the frequency range of 100 Hz. Sharma *et al.* (2015, 2016a, 2016b, 2018) numerically and experimentally investigated the active vibration control behavior of isotropic beams over a wide temperature range using a fuzzy logic controller algorithm. Further, the numerical study was extended to understand the damping characteristics of FG-CNTRC plates sandwiched between the piezoelectric face sheets. Similarly, Gupta *et al.* (2011) used analytical and experimental methods to investigate the active vibration control of the isotropic plate integrated with the piezoelectric sensor-actuator pair operating at elevated temperatures. Results suggested that the vibration attenuation performance is not maintained at high temperatures using a control law, which ignores the temperature-dependent material properties of PZT crystal. Shankar *et al.* (2017) developed a FE

model to investigate the vibration control characteristics of delaminated composite plates integrated with the piezoelectric actuators operating in a hygrothermal environment. It was reported that the frequency of the delaminated plate increased when the control voltage was applied. Sfarra *et al.* (2016) developed a novel non-destructive technique to predict the effect of the hygrothermal aging of the impacted composite material. Studies indicate that the hygrothermally aged laminates will have pronounced internal defects. Further, Li *et al.* (2019) utilized a temperature feedback control strategy to achieve active control of vibrating sandwich plates operating in the thermal environment. Piezoelectric fiber-reinforced composite actuator face sheets and laminated core were considered for the numerical simulation.

1.6. SCOPE AND OBJECTIVE OF THE DISSERTATION

The detailed literature survey indicates the increasing interest of engineers and researchers in LCS structures. The literature investigating the behavior of LCS structures in the presence of thermal, hygroscopic, hygrothermal, electrical fields, and magnetic fields are limited. Developing the mathematical models to represent the behavior of the sandwich structures in the presence of harsh environments is a challenging task. In the conventional approach, the coupling effect between the existing loadings is often neglected, which in turn will introduce errors or imprecise results. Modern computational techniques such as FE methods allow the introduction of complex coupling terms in the mathematical model to estimate the multiphysics response of the structures (Nguyen-Thoi *et al*., 2009, 2010, 2012). Even though the FE methods provide approximate results, they are often utilized to solve complex structural problems due to their superior computational speed.

The literature investigating the influence of temperature and moisture on the vibration characteristics of LCS structures are available in abundance. However, the papers reporting the coupled thermo-elastic and hygro-elastic relations considering the temperature-dependent and moisture-dependent material properties are scarce. Similarly, in most of the research work, the influence of temperature and moisture is introduced into the mathematical model as the force terms. The literature investigating the effect of temperature and moisture on the vibration response of the structures considering the reduction in stiffness are very minimum. Additionally, the research

outputs describing the predictive models to monitor the condition of the system in the presence of harsh environments are very few.

In the past few decades, many research groups have reported the influence of porosity on the natural frequency of the sandwich structure. However, only a few articles have addressed the combined effect of temperature and porosity on the free vibration response of LCS structures. The porosity in the 3D printed structures is unavoidable. To this end, to the best of the author's knowledge, the research works addressing the influence of temperature and porosity on the 3D printed structures are not available in the open literature. Moreover, the articles reporting the influence of temperature and moisture on the active vibration control of LCS structures may be found in the open-source. The effect of temperature on the active constrained layer damping characteristics of a structure is also reported by researchers (Ray and Batra 2008: Suresh Kumar *et al*., 2013). However, papers addressing the influence of temperature on the physical behavior of all the constituent materials (host structure, viscoelastic layer, and piezoelectric layer) of ACLD arrangement are scarce. Additionally, articles considering the degradation of material properties of the constituent materials of the ACLD treatment on exposure to the elevated thermal environment are not available.

The extensive literature review and the research gaps discussed in this section are subsequently considered as the research objectives of the present dissertation and are listed as follows,

- To investigate the vibrational characteristics of laminated composite, hybrid composite, and sandwich plates in the presence of elevated temperature and moisture environments.

- To develop a predictive model to monitor the vibration response of SLCS plates in thermal and moisture situations.

- To perform a FE analysis to investigate the vibration characteristics of the LCS plates and shells with functionally graded (FG) cores in the presence of the thermal and moisture environment.

- To study the influence of temperature and porosity on the free vibration behavior of SLCS plates and shells.

- To investigate the performance of ACLD treated SLCS plates operating in an elevated thermal atmosphere.

- To experimentally investigate the influence of the thermal fields on free vibration characteristics of LCS plates and compare the experimental results (natural frequencies) with the in-house developed FE model/code.

1.7. CONTRIBUTION FROM THE DISSERTATION

Contributions made in the area of vibrational analysis of LCS structures in thermal and moisture environments through this dissertation are as follows:

- The coupled thermo-elastic and hygro-elastic FE formulation based on the FSDT is successfully developed to investigate the free vibration behavior of skew laminated composites, hybrid composites, and sandwich structures.
- Detailed analysis of SLCS panels is presented by considering various material and geometric parameters.
- The predictive model is developed to understand the influence of temperature and moisture on the vibration response of LCS plates.
- The vibration behavior of the SLCS panels with FG core is investigated.
- The influence of temperature and porosity on the free vibration characteristics of SLCS panels is established.
- The influence of temperature on the vibration attenuation characteristics of ACLD treated SLCS plates is investigated.

1.8. OVERVIEW OF THE DISSERTATION WITH CHAPTER

The present dissertation is devoted to investigating the influence of temperature and moisture on the free vibration characteristics of SLCS panels using FE formulations. Further, the effect of material functional gradation and porosity of the core material is thoroughly studied. Coupled thermo-elastic and hygro-elastic constituent equations are used to derive the governing equation of motion of LCS panels. Thorough investigations are performed to establish the influence of process parameters such as aspect ratios, thickness ratios, skew angle, porosity, boundary conditions, etc., on the vibration characteristics of LCS panels.

The thesis consists of eight chapters. The first chapter presents a brief introduction and widespread literature survey on LCS structures. The noteworthy contributions related to the laminated composites, hybrid composites, and sandwich

structures operating in thermal and moisture environments are studied. Further, the recent developments and challenges of active vibration control of laminated composite structures are briefly presented. Subsequently, the scope and objectives for the current research are outlined based on the research gaps identified during the literature review.

In chapter 2, the detailed FE formulation based on layer-wise FSDT is presented to study the free vibration characteristics of skew laminated composite, hybrid composite, and sandwich plates operating in elevated thermal and moisture conditions. The temperature-dependent and moisture-dependent material properties of the glass-epoxy composite, graphite-epoxy composite, viscoelastic core materials are considered for analysis. Further, the influence of geometric parameters such as aspect ratios, thickness ratios, skew angle, fiber orientation, etc., on the natural frequency of the system is investigated.

Chapter 3 is concerned with developing an ANN-based predictive model to understand the influence of temperature and moisture on SLCS plates. The outcomes of the FE model developed in the preceding chapter were utilized to generate the dataset to train the neural network model. The natural frequencies obtained from the ANN model were compared with FSDT results.

In chapter 4, the detailed investigation of the effect of temperature and moisture on SLCS shells is presented. The temperature-dependent and moisture-dependent material properties of the FG-CNTRC core and graphite-epoxy face sheet materials were considered for the analysis. Additionally, the results obtained from doubly-curved shells such as cylindrical, ellipsoidal, hyperbolic, and spherical shells are compared with the sandwich plate.

The influence of temperature and porosity on the natural frequency of LCS shells with 3D printed PLA core is investigated in chapter 5. The temperature-dependent material properties of the 3D-printed PLA core material are considered for the simulations. Various through the thickness porosity distribution patterns were considered for the analysis. Additionally, the experimental challenges involved in the vibration study of the sandwich structures in thermal environments are presented.

Chapter 6 encapsulates the comprehensive investigation of the influence of temperature on the vibration attenuation characteristics of ACLD treated LCS plates. A new robust control strategy is proposed in order to replicate the experimental vibration

damping performance of sandwich plates with ACLD patches. The negative velocity feedback control law was incorporated to control the first few modes of the vibrating sandwich plate. Further, the influence of geometric parameters on vibration attenuation behavior is also explored.

In chapter 7, the experimental investigations are performed to understand the influence of temperature on the natural frequency of the LCS plates. The sandwich plates with glass-epoxy face sheets and 3D printed PLA core materials are considered for the vibrational study. The temperature-dependent material properties of the constituent materials were obtained from the tensile test procedure. Further, the experimental outcomes were compared with the results obtained from the in-house developed mathematical model.

At last, chapter 8 records the significant findings of the current dissertation. The possible future scopes in the investigation of LCS panels operating in elevated thermal and moisture environments are also documented. The list of references is presented at the end of the dissertation.

Chapter 2

FREE VIBRATIONAL BEHAVIOR OF COMPOSITE, HYBRID COMPOSITE, AND SANDWICH PLATES IN THERMAL AND MOISTURE CONDITIONS

This chapter investigates the influence of variation in the temperature and moisture on the free vibration response of skew laminated composite, hybrid composite, and sandwich composite plates. The finite element (FE) formulations defining the constituent equations are developed using the layer-wise first-order shear deformation theory. Uniform temperature and moisture concentration rise are considered to develop the coupled thermo-elastic and hygro-elastic relations. The glass-epoxy and graphite-epoxy composite materials are considered as the face sheet materials, and the soft-core viscoelastic materials such as DYAD 606 and EC 2216 are considered as the core. Linear strain-displacement relations are used to develop a mechanical stiffness matrix, and the initial stress stiffness matrix is generated using non-linear strain-displacement relations to represent the non-mechanical stiffness matrix. A parametric study is carried out to understand the influence of skew angle, length to width ratio, length to thickness ratio, core to face sheet thickness ratio, stacking sequence, fiber orientation, and boundary conditions on the vibration response of the skew laminated composite, hybrid composite, and sandwich plates.

2.1 INTRODUCTION

Composite materials are being widely used in the prominent fields of structural engineering such as aerospace, automobile, bio-medical, civil structures, etc. The properties of composite and sandwich composite materials, such as high specific strength, high specific modulus, high flexural rigidity, etc., are much superior as compared to the traditional metals and ceramics. In high-end engineering applications, materials are expected to work efficiently even in challenging and hazardous environments such as higher operating temperature, presence of moisture, and chemical environments. Dynamically changing environmental and loading conditions may adversely affect the behavior of structures.

In this chapter, the coupled thermo-elastic and hygro-elastic FE model is formulated using the FSDT to assess the free vibration response of composites, hybrid composites, and sandwich plates operating in elevated thermal and moisture environments. The equations of motion are derived using the dynamic version of the principle of virtual work. The influence of temperature and moisture on the fundamental natural frequency of laminated composite (LC) structures is investigated. In addition, the effect of material and geometric process parameters on the free vibration response of the composite structures is studied in detail.

2.2. PROBLEM DESCRIPTION

The schematic illustration of the skew laminated hybrid composite (LHC) and laminated composite sandwich (LCS) plates are demonstrated in Figures 2.1 (a) and (b), respectively. The LHC plate is made of alternating layers of fiber-reinforced orthotropic composite layers such as glass-epoxy and graphite-epoxy materials. In the case of sandwich plates, the top and bottom face sheets contain 'N' number of orthotropic polymer composite layers, and the core is made of soft-core viscoelastic material. The length, breadth, and thickness of the plate are denoted as a, b, and H, respectively. The thickness of each composite layer is considered as h, and half of the core thickness is symbolized as h_c. For the ease of simplification, the core is assumed to be an equivalent homogeneous continuum (Burlayenko and Sadowski, 2009: Sadowski and Bec, 2011).

Figure 2.2 illustrates the kinematics of the deformation of a sandwich plate in XZ and YZ-planes. The angles θ_x, ϕ_x, and α_x represent the rotation of a portion of the normal lying in the core, the bottom face sheet, and the top face sheet, respectively, in XZ-plane, whereas the angles θ_y, ϕ_y, and α_y respectively denote the same in YZ-plane. The displacement fields relating to the kinematics of deformation can be articulated as follows (Kumar *et al*., 2013, 2016: Reddy, 2003: Kanasogi and Ray, 2013),
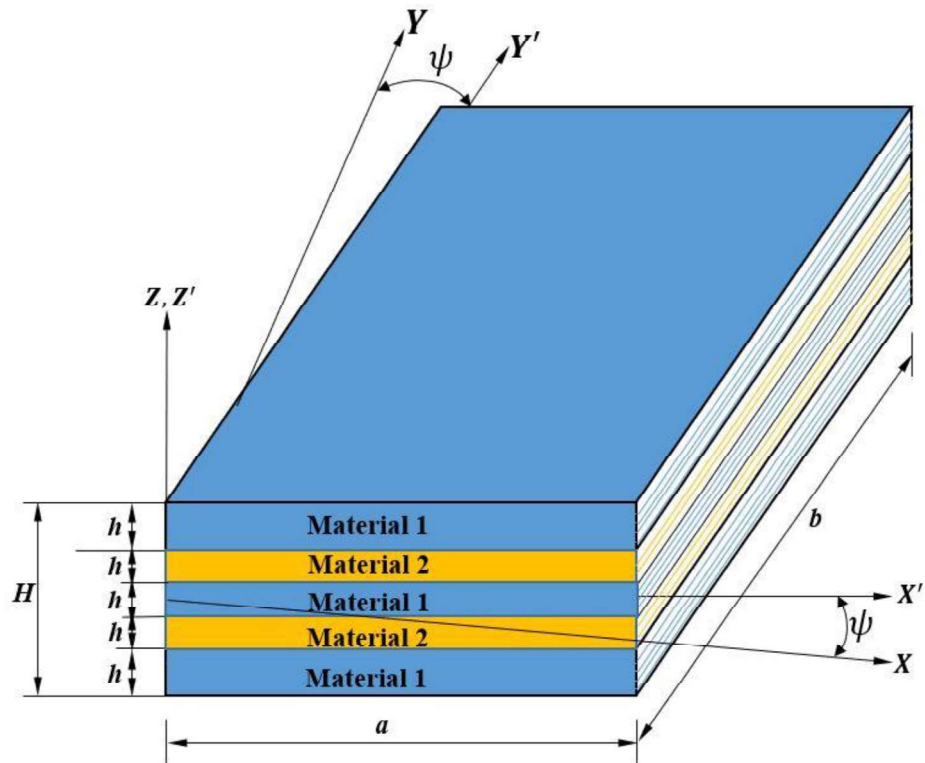
(a)
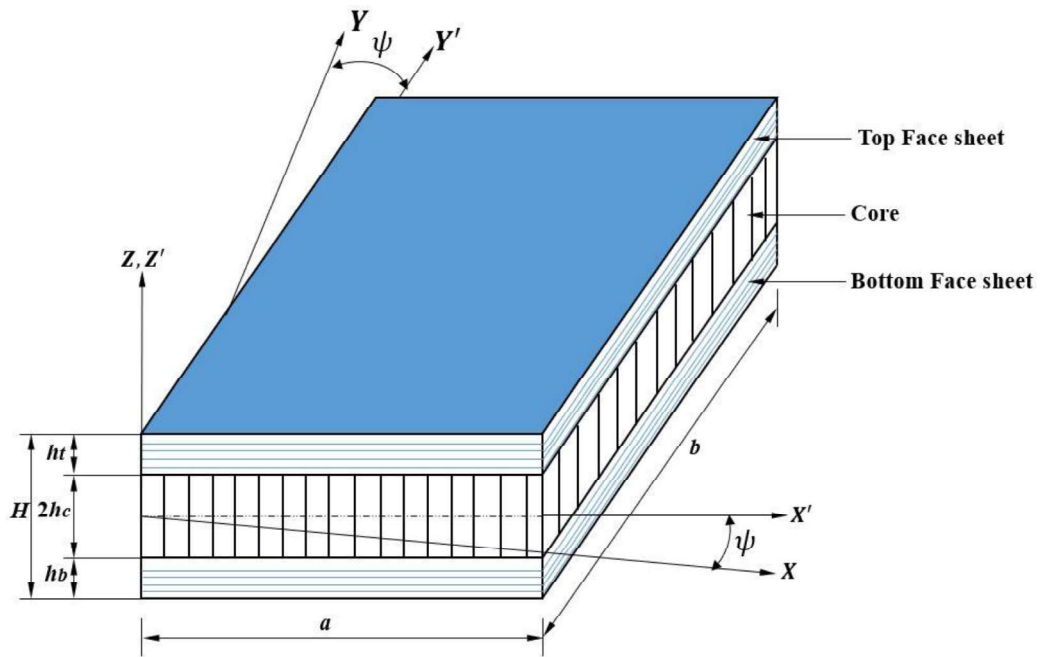
(b)

Figure 2.1: Schematic representation of the skew (a) LHC plate and (b) LCS plate.
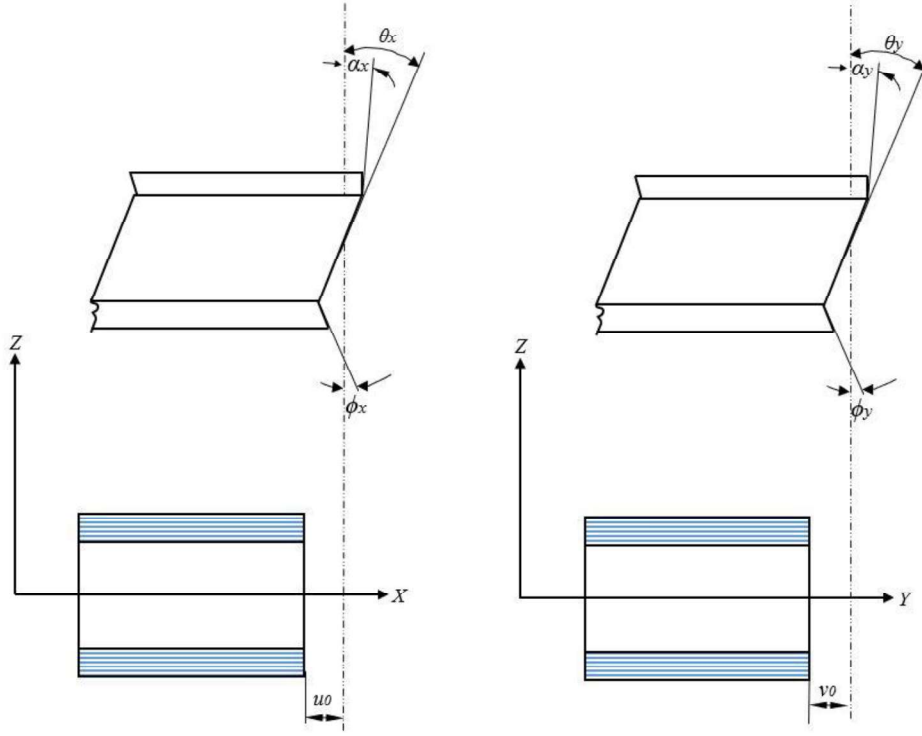
Figure 2.2: Schematic representation of kinematics of deformation of the LCS plate.

Axial displacements u_{to}, v_{to}, and w_{to} along X, Y, and Z directions, respectively, for the top face sheet:

$$
\begin{aligned}
u_{to}(x,y,z,t) &= u_0(x,y,t) + h_c\,\theta_x(x,y,t) + (z-h_c)\alpha_x(x,y,t) \\
v_{t0}(x,y,z,t) &= v_0(x,y,t) + h_c\,\theta_y(x,y,t) + (z-h_c)\alpha_y(x,y,t) \\
w_{to}(x,y,z,t) &= w_0(x,y,t)
\end{aligned}
\tag{2.1}
$$

Axial displacements u_{bo}, v_{bo}, and w_{bo} along X, Y, and Z directions, respectively, for the bottom face sheet:

$$
\begin{aligned}
u_{bo}(x,y,z,t) &= u_0(x,y,t) - h_c\,\theta_x(x,y,t) + (z+h_c)\phi_x(x,y,t) \\
v_{bo}(x,y,z,t) &= v_0(x,y,t) - h_c\,\theta_y(x,y,t) + (z+h_c)\phi_y(x,y,t) \\
w_{bo}(x,y,z,t) &= w_0(x,y,t)
\end{aligned}
\tag{2.2}
$$

Axial displacements u_{co}, v_{co}, and w_{co} along X, Y, and Z directions, respectively, for the core:

$$
\begin{aligned}
u_{co}(x,y,z,t) &= u_0(x,y,t) + z\,\theta_x(x,y,t) \\
v_{co}(x,y,z,t) &= v_0(x,y,t) + z\,\theta_y(x,y,t) \\
w_{co}(x,y,z,t) &= w_0(x,y,t)
\end{aligned}
\tag{2.3}
$$

in which "*t*" denotes time. u_0, v_0, and w_0 represent the displacement components along *X, Y,* and *Z* directions, respectively, of any arbitrary point on the mid-plane (i.e., *Z* = 0). For simplification, the translational displacements $\{d_{tr}\}$, are unglued from the rotational part $\{d_r\}$, as follows:

$$\{d_{tr}\} = \begin{bmatrix} u_0 & v_0 & w_0 \end{bmatrix}^T, \text{ and } \{d_r\} = \begin{bmatrix} \theta_x & \theta_y & \phi_x & \phi_y & \alpha_x & \alpha_y \end{bmatrix}^T \tag{2.4}$$

In order to implement the selective integration rule, the state of strain at any point in the overall plate is divided into the two strain vectors $\{\varepsilon_b\}$ and $\{\varepsilon_s\}$ can be written as:

$$\{\varepsilon_b\} = \{\varepsilon_x \quad \varepsilon_y \quad \varepsilon_{xy}\}^T, \text{ and } \{\varepsilon_s\} = \{\varepsilon_{xz} \quad \varepsilon_{yz}\}^T \tag{2.5}$$

where, ε_x and ε_y are the normal strains along *X* and *Y* directions, respectively. ε_{xy} is the in-plane shear strain, and ε_{xz}, ε_{yz} are the transverse shear strains. By using the displacement fields and linear strain-displacement relations, the strain vectors $\{\varepsilon_b\}_c$, $\{\varepsilon_b\}_b$, and $\{\varepsilon_b\}_t$ defining the state of in-plane and transverse normal strains at any point in the core, the bottom face sheet, and the top face sheets can be expressed as:

$$\{\varepsilon_b\}_b = \{\varepsilon_{bt}\} + [z_1]\{\varepsilon_{br}\}$$
$$\{\varepsilon_b\}_c = \{\varepsilon_{bt}\} + [z_2]\{\varepsilon_{br}\} \tag{2.6}$$
$$\{\varepsilon_b\}_t = \{\varepsilon_{bt}\} + [z_3]\{\varepsilon_{br}\}$$

Similarly, the strain vectors $\{\varepsilon_s\}_c$, $\{\varepsilon_s\}_b$, and $\{\varepsilon_s\}_t$ define the state of transverse shear strains at any point in the core, the bottom face sheet, and the top face sheets can be expressed as:

$$\{\varepsilon_s\}_b = \{\varepsilon_{st}\} + [z_4]\{\varepsilon_{sr}\}$$
$$\{\varepsilon_s\}_c = \{\varepsilon_{st}\} + [z_5]\{\varepsilon_{sr}\} \tag{2.7}$$
$$\{\varepsilon_s\}_t = \{\varepsilon_{st}\} + [z_6]\{\varepsilon_{sr}\}$$

The terms z_1 to z_6 are functions of the *Z*-coordinate of the point at evaluation. The various matrices presented in Eqns. 2.6 and 2.7 are defined in Appendix A. The complex modulus approach is adopted for modeling the viscoelastic materials. Hence, the shear modulus of the material is expressed as:

$$G = G'(1 + i\eta) \tag{2.8}$$

25

in which G' is storage modulus and η is the loss factor at any operating temperature and frequency. As the temperature 'T' changes, the values of storage modulus and loss factor change and can be denoted as:

$$G(T) = G'(T)[1 + i\eta(T)] \tag{2.9}$$

The constitutive relations for the structural behavior of the LC plate subjected to moisture and temperature are given by:

$$\{F\} = [D]\{\varepsilon\} - \{F^N\} \tag{2.10}$$

where,

$$\{F\} = \{N_x \quad N_y \quad N_{xy} \quad M_x \quad M_y \quad M_{xy} \quad Q_x \quad Q_y\}^T$$

$$\{F^N\} = \{N_x^N \quad N_y^N \quad N_{xy}^N \quad M_x^N \quad M_y^N \quad M_{xy}^N \quad 0 \quad 0\}^T$$

$$\{\varepsilon\} = \{\varepsilon_x^0 \quad \varepsilon_y^0 \quad \varepsilon_{xy}^0 \quad K_x \quad K_y \quad K_{xy} \quad \varphi_x \quad \varphi_y\}^T$$

$$[D] = \begin{bmatrix} A_{11} & A_{12} & A_{16} & B_{11} & B_{12} & B_{16} & 0 & 0 \\ A_{12} & A_{22} & A_{26} & B_{12} & B_{22} & B_{26} & 0 & 0 \\ A_{16} & A_{26} & A_{66} & B_{16} & B_{26} & B_{66} & 0 & 0 \\ B_{11} & B_{12} & B_{16} & D_{11} & D_{12} & D_{16} & 0 & 0 \\ B_{12} & B_{22} & B_{26} & D_{12} & D_{22} & D_{26} & 0 & 0 \\ B_{16} & B_{26} & B_{66} & D_{16} & D_{26} & D_{66} & 0 & 0 \\ 0 & 0 & 0 & 0 & 0 & 0 & S_{44} & S_{45} \\ 0 & 0 & 0 & 0 & 0 & 0 & S_{45} & S_{55} \end{bmatrix}$$

where, N_x, N_y, N_{xy} are the in-plane internal stress resultants, M_x, M_y, M_{xy} are the internal moment resultants, Q_x, Q_y are the transverse shear resultants, N_x^N, N_y^N, N_{xy}^N are the in-plane non-mechanical stress resultants due to moisture and temperature, M_x^N, M_y^N, M_{xy}^N are the non-mechanical moment resultants due to moisture and temperature, ε_x^0, ε_y^0, ε_{xy}^0 are the in-plane strains of the mid-plane, K_x, K_y, K_{xy} are the curvature of the plate and φ_x, φ_y are the shear rotations in the XZ and YZ- planes, respectively. The steady-state temperature and moisture variation are assumed throughout the analysis.

$$[A_{ij}, B_{ij}, D_{ij}] = \sum_{k=1}^{n} \int_{z_{k-1}}^{z_k} [\bar{Q}_{ij}^k]_k (1, z, z^2) dz \quad \text{for } i, j = 1, 2, 6. \tag{2.11}$$

26

$$[S_{ij}] = \sum_{k=1}^{n} \int_{z_{k-1}}^{z_k} \lambda [\overline{Q}_{ij}^k]_k \, dz \qquad for \ i,j = 4, 5. \tag{2.12}$$

λ is the shear correction factor and is assumed as 5/6 (Park *et al.*, 2008: Chakrabarti and Sheikh, 2004: Reddy, 2003). The non-mechanical force and moment resultants are expressed as follows:

$$\{N_x^N, \ N_y^N, \ N_{xy}^N\}^T = \sum_{k=1}^{n} [\overline{Q}_{ij}]_k \{e\}_k (z_k - z_{k-1}) \tag{2.13.a}$$

$$\{M_x^N, \ M_y^N, \ M_{xy}^N\}^T = \frac{1}{2} \sum_{k=1}^{n} [\overline{Q}_{ij}]_k \{e\}_k (z_k^2 - z_{k-1}^2) \quad for \ i,j = 1, 2, 6 \tag{2.13.b}$$

where,

$$[\overline{Q}_{ij}]_k = [T_1]^{-1}[Q_{ij}]_k[T_1] \qquad (i,j = 1, 2, 6)$$

$$[\overline{Q}_{ij}]_k = [T_2]^{-1}[Q_{ij}]_k[T_2] \qquad (i,j = 4, 5)$$

In which,

$$[T_1] = \begin{bmatrix} \cos^2\theta & \sin^2\theta & \sin\theta\cos\theta \\ \sin^2\theta & \cos^2\theta & -\sin\theta\cos\theta \\ -2\sin\theta\cos\theta & 2\sin\theta\cos\theta & \cos^2\theta - \sin^2\theta \end{bmatrix}; \ [T_2] = \begin{bmatrix} \cos\theta & \sin\theta \\ -\sin\theta & \cos\theta \end{bmatrix}$$

$$[Q_{ij}]_k = \begin{bmatrix} Q_{11} & Q_{12} & 0 \\ Q_{21} & Q_{22} & 0 \\ 0 & 0 & Q_{66} \end{bmatrix} \qquad (i,j = 1,2,6)$$

$$[Q_{ij}]_k = \begin{bmatrix} Q_{44} & 0 \\ 0 & Q_{55} \end{bmatrix} \qquad (i,j = 4,5)$$

where,

$$Q_{11} = \frac{E_1}{(1 - \upsilon_{12}\upsilon_{21})}; \ Q_{12} = \frac{\upsilon_{12}E_1}{(1 - \upsilon_{12}\upsilon_{21})}; \ Q_{22} = \frac{E_2}{(1 - \upsilon_{12}\upsilon_{21})}; \ Q_{66} = G_{12}; \ Q_{44} = G_{13}; \ Q_{55} = G_{23}$$

E_1, E_2 = Longitudinal and transverse elastic modulus of face sheets

G_{12}, G_{13}, G_{23} = in-plane and transverse shear modulus

$\upsilon_{12}, \upsilon_{21}$ = Major and minor Poisson's ratios

$$\{e\}_k = \{e_x, \ e_y, \ e_{xy}\}^T = [\overline{T}]\{\beta_1 \quad \beta_2\}_k^T(C - C_0) + [\overline{T}]\{\alpha_1 \quad \alpha_2\}_k^T(T - T_0) \tag{2.14}$$

$$\text{in which, } \overline{T} = \begin{bmatrix} \cos^2\theta & \sin^2\theta \\ \sin^2\theta & \cos^2\theta \\ \sin 2\theta & \cos 2\theta \end{bmatrix}$$

27

e_x, e_y, e_{xy} are the non-mechanical strains due to moisture and temperature, β_1 and β_2 are the moisture coefficients, α_1 and α_2 are the thermal coefficients, T and T_0 are elevated and reference temperature, respectively, C and C_0 are elevated and reference moisture profiles.

2.3. FINITE ELEMENT FORMULATION

The overall plate is discretized by the eight noded isoparametric quadrilateral elements. Three translational (u, v, w) and six rotational (θ_x, θ_y, ϕ_x, ϕ_y, α_x, α_y) degrees of freedom are considered at each node. Generalized displacement vectors associated with the i-th node ($i =1, 2, \ldots, 8$) of the element can be expressed as:

$$\{d_{tri}\} = \begin{bmatrix} u_{0i} & v_{0i} & w_{0i} \end{bmatrix}^T, \text{ and } \{d_{ri}\} = \begin{bmatrix} \theta_{xi} & \theta_{yi} & \phi_{xi} & \phi_{yi} & \alpha_{xi} & \alpha_{yi} \end{bmatrix}^T \qquad (2.15)$$

Thus the generalized displacement vector at any point within the element can be represented in terms of the nodal generalized displacement vectors.

$$\{d_{tr}\} = [N_{tr}]\{d_{tr}^e\}, \text{ and } \{d_r\} = [N_r]\{d_r^e\} \qquad (2.16)$$

in which, $[N_{tr}] = [N_{tr1} \ N_{tr2} \ \ldots \ N_{tr8}]^T$, and $[N_r] = [N_{r1} \ N_{r2} \ \ldots \ N_{r8}]^T$

$$N_{tri} = n_i I_{tr}, \ \ N_{ri} = n_i I_r \qquad (2.17)$$

$\{d_{tr}^e\} = [\{d_{tr1}^e\}^T \ \{d_{tr2}^e\}^T \ \ldots \ \{d_{tr8}^e\}^T]^T$, and $\{d_r^e\} = [\{d_{r1}^e\}^T \ \{d_{r2}^e\}^T \ \ldots \ \{d_{r8}^e\}^T]^T$

where, I_{tr} and I_r are (3 x 3) and (6 x 6) identity matrices, respectively, and n_i is the shape function of the natural coordinate associated with the i-th node.

2.3.1. Elemental stiffness matrix

The linear strain vector $\{\varepsilon\}$ can be expressed as,

$$\{\varepsilon\} = [B]\{\delta_e\} \qquad (2.18)$$

where,

$$\{\delta_e\} = \{u_1, v_1, w, \theta_{x1}, \theta_{y1}, \phi_{x1}, \phi_{y1}, \alpha_{x1}, \alpha_{x2}, \ldots, u_8, v_8, w, \theta_{x8}, \theta_{y8}, \phi_{x8}, \phi_{y8}, \alpha_{x8}, \alpha_{y8}\}^T$$

The strain vectors at any point within the element can be expressed as:

$$\{\varepsilon_b\}_b = [B_{tb}]\{d_{tr}^e\} + [z_1][B_{rb}]\{d_r^e\}$$

$$\{\varepsilon_b\}_c = [B_{tb}]\{d_{tr}^e\} + [z_2][B_{rb}]\{d_r^e\}$$

$$\{\varepsilon_b\}_t = [B_{tb}]\{d_{tr}^e\} + [z_3][B_{rb}]\{d_r^e\}, \qquad (2.19)$$

$$\{\varepsilon_s\}_b = [B_{ts}]\{d_{tr}^e\} + [z_4][B_{rs}]\{d_r^e\}$$

28

$$\{\varepsilon_s\}_c = [B_{ts}]\{d^e_{tr}\} + [z_5][B_{rs}]\{d^e_r\}$$

$$\{\varepsilon_s\}_t = [B_{ts}]\{d^e_{tr}\} + [z_6][B_{rs}]\{d^e_r\}$$

In which $[B_{tb}]$, $[B_{rb}]$, $[B_{ts}]$ and $[B_{rs}]$ are the nodal displacement matrices and are presented in Appendix B.

$$[K_e] = \int_{-1}^{+1}\int_{-1}^{+1}[B]^T[D][B]|J|d\xi d\eta \qquad (2.20)$$

2.3.2. Elemental initial stress stiffness matrix

Upon assuming that w does not vary with Z-axis, the non-linear strains of the plate can be expressed as,

$$\varepsilon_{xnl} = \frac{1}{2}[u^2_{,x} + v^2_{,x} + w^2_{,x} + 2z(u_{,x}\theta_{y,x} - v_{,x}\theta_{x,x}) + z^2(\theta^2_{y,x} + \theta^2_{x,x})]$$

$$\varepsilon_{ynl} = \frac{1}{2}[u^2_{,y} + v^2_{,y} + w^2_{,y} + 2z(u_{,y}\theta_{y,y} - v_{,y}\theta_{x,y}) + z^2(\theta^2_{y,y} + \theta^2_{x,y})]$$

$$\varepsilon_{xynl} = [u_{,x}u_{,y} + v_{,x}v_{,y} + w_{,x}w_{,y} + z(u_{,x}\theta_{y,y} + u_{,y}\theta_{y,x} - v_{,x}\theta_{x,y} - v_{,y}\theta_{x,x}) + z^2(\theta_{y,x}\theta_{y,y} + \theta_{x,x}\theta_{x,y})] \quad (2.21)$$

$$\varepsilon_{xznl} = [u_{,x}\theta_y - v_{,x}\theta_x + z(\theta_y\theta_{y,x} + \theta_x\theta_{x,x})]$$

$$\varepsilon_{yznl} = [u_{,y}\theta_y - v_{,y}\theta_x + z(\theta_y\theta_{y,y} + \theta_x\theta_{x,y})]$$

The non-linear strains can be expressed as:

$$\{\varepsilon_{nl}\} = \{\varepsilon_{xnl}, \varepsilon_{ynl}, \varepsilon_{xynl}\} = [R]\{d\}/2$$

where,

$$\{d\} = \{u_{,x}, u_{,y}, v_{,x}, v_{,y}, w_{,x}, w_{,y}, \theta_{x,x}, \theta_{x,y}, \theta_{y,x}, \theta_{y,y}, \phi_{x,x}, \phi_{x,y}, \phi_{y,x}, \phi_{y,y}, \alpha_{x,x}, \alpha_{x,y}, \alpha_{y,x},$$
$$\alpha_{y,y}, \theta_x, \theta_y, \phi_x, \phi_y, \alpha_x, \alpha_y\}^T \qquad (2.22)$$

Equation $\{d\}$ can be expressed as:

$$\{d\} = [G]\{\partial_e\} \qquad (2.23)$$

where,

$$[G] = \sum_{i=1}^{8}\begin{bmatrix} \hat{N} & \bar{O} & \bar{O} \\ \bar{O} & \hat{N} & \bar{O} \\ \bar{O} & \bar{O} & \hat{N} \\ \tilde{O} & \hat{I} & \tilde{O} \\ \tilde{O} & \tilde{O} & \hat{I} \end{bmatrix} \text{ in which, } \hat{N} = \begin{bmatrix} N_{i,x} & 0 & 0 \\ N_{i,y} & 0 & 0 \\ 0 & N_{i,x} & 0 \\ 0 & N_{i,y} & 0 \\ 0 & 0 & N_{i,x} \\ 0 & 0 & N_{i,y} \end{bmatrix}$$

$\bar{O}$ and $\tilde{O}$ are (6 x 3) and (3 x 3) null matrices, respectively. Similarly, the identity matrix $\hat{I}$ is of size (3 x 3). In general U_m can be given by,

$$U_m = \int_{A_e} \left(\frac{1}{2} N_x w_{,x}^2 + \frac{1}{2} N_y w_{,y}^2 + N_{xy} w_{,x} w_{,y} \right) dA$$

$$U_m = \frac{1}{2} \iint \begin{Bmatrix} w_{,x} \\ w_{,y} \end{Bmatrix}^T \begin{bmatrix} N_x & N_{xy} \\ N_{xy} & N_y \end{bmatrix} \begin{Bmatrix} w_{,x} \\ w_{,y} \end{Bmatrix} dxdy$$

$$U_m = \frac{1}{2} \{d\}^T [K_\sigma] \{d\}$$

Let, $\{w_{,x} \quad w_{,y}\}^T = [G]\{d\}$

$$[K_\sigma] = \iint [G]^T \begin{bmatrix} N_x & N_{xy} \\ N_{xy} & N_y \end{bmatrix} [G] dxdy$$

Similarly,

$$U_m = \int_{A_e} \begin{bmatrix} \frac{N_x}{2} \left(u_{,x}^2 + v_{,x}^2 + w_{,x}^2 + \frac{h^2}{12} \theta_{x,x}^2 + \frac{h^2}{12} \theta_{y,x}^2 \right) + \frac{N_y}{2} \left(u_{,y}^2 + v_{,y}^2 + w_{,y}^2 + \frac{h^2}{12} \theta_{x,y}^2 + \frac{h^2}{12} \theta_{y,y}^2 \right) \\ + \frac{N_{xy}}{2} \left(u_{,x} u_{,y} + v_{,x} v_{,y} + w_{,x} w_{,y} + \frac{h^2}{12} \theta_{x,x} \theta_{x,y} + \frac{h^2}{12} \theta_{y,x} \theta_{y,y} \right) + M_x \left(u_{,x} \theta_{y,x} - v_{,x} \theta_{x,x} \right) \\ + M_y \left(u_{,y} \theta_{y,y} - v_{,y} \theta_{x,y} \right) + M_{xy} \left(u_{,x} \theta_{y,y} + u_{,y} \theta_{y,x} - v_{,x} \theta_{x,y} - v_{,y} \theta_{x,x} \right) \\ + Q_x \left(u_{,x} \theta_y - v_{,x} \theta_x \right) + Q_y \left(u_{,y} \theta_y - v_{,y} \theta_x \right) \end{bmatrix} dA$$

As matrix $[G]$ is known the matrix $[S]$ can be computed subsequently. The initial stress stiffness matrix due to hygrothermal loads is given by:

$$[K_\sigma^e] = \int_{-1}^{+1} \int_{-1}^{+1} [G]^T [S][G] |J| d\xi d\eta \qquad (2.24)$$

The matrices denoted in the above equation are presented in Appendix C.

2.4. GOVERNING EQUATION

The dynamic version of the principle of virtual work is incorporated to obtain the equations of motion. The potential energy and kinetic energy of the structure can be expressed as

$$T_p^e = \frac{1}{2}\left[\{d_{tr}^e\}^T\left[K_{11}^e\right]\{d_{tr}^e\} + \{d_{tr}^e\}^T\left[K_{12}^e\right]\{d_r^e\} + \{d_r^e\}^T\left[K_{12}^e\right]^T\{d_{tr}^e\} + \{d_r^e\}^T\left[K_{22}^e\right]\{d_r^e\} - 2\{d_{tr}^e\}^T\{F^e\}\right] \quad (2.25)$$

$$T_k^e = \frac{1}{2}\int_0^{a_e}\int_0^{b_e}\overline{m}\{\dot{d}_{tra}^e\}^T[N]^T[N]\{\dot{d}_{tra}^e\}dxdy \quad (2.26)$$

The elemental stiffness matrix, the mass matrix, and the force vectors appearing in Eqns. 2.25 and 2.26 can be expressed as

$$\left[K_{11}^e\right] = \left[K_{11b}^e\right] + \left[K_{11s}^e\right] \quad (2.27)$$

$$\left[K_{12}^e\right] = \left[K_{12b}^e\right] + \left[K_{12s}^e\right] \quad (2.28)$$

$$\left[K_{22}^e\right] = \left[K_{22b}^e\right] + \left[K_{22s}^e\right] \quad (2.29)$$

$$\{F^e\} = \int_0^{a_e}\int_0^{b_e}[N_{tr}]^T\{f\}dxdy \quad (2.30)$$

$$\overline{m} = \sum_{k=1}^N \rho_{bot}(h_{k+1} - h_k) + 2\rho_{core}h_c + \sum_{k=1}^N \rho_{top}(h_{k+1} - h_k) \quad (2.31)$$

$$\left[M^e\right] = \int_0^{a_e}\int_0^{b_e}\overline{m}[N_t]^T[N_t]dxdy \quad (2.32)$$

in which,

$$\left[K_{11b}^e\right] = \int_{A_e}[B_{tb}]^T\left(\left[D_{11b}^{bot}\right] + \left[D_{11b}^{core}\right] + \left[D_{11b}^{top}\right]\right)[B_{tb}]dA^e$$

$$\left[K_{12b}^e\right] = \int_{A_e}[B_{tb}]^T\left(\left[D_{12b}^{bot}\right][B_{rb}] + \left[D_{12b}^{core}\right][B_{rb}] + \left[D_{12b}^{top}\right][B_{rb}]\right)dA^e$$

$$\left[K_{22b}^e\right] = \int_{A_e}\left([B_{rb}]^T\left[D_{22b}^{bot}\right][B_{rb}] + [B_{rb}]^T\left[D_{22b}^{core}\right][B_{rb}] + [B_{rb}]^T\left[D_{22b}^{top}\right][B_{rb}]\right)dA^e$$

$$\left[K_{11s}^e\right] = \int_{A_e}[B_{ts}]^T\left(\left[D_{11s}^{bot}\right] + \left[D_{11s}^{core}\right] + \left[D_{11s}^{top}\right]\right)[B_{ts}]dA^e$$

$$\left[K_{12s}^e\right] = \int_{A_e}[B_{ts}]^T\left(\left[D_{12s}^{bot}\right][B_{rs}] + \left[D_{12s}^{core}\right][B_{rs}] + \left[D_{12s}^{top}\right][B_{rs}]\right)dA^e$$

$$\left[K_{22s}^e\right] = \int_{A_e}\left([B_{rs}]^T\left[D_{22s}^{bot}\right][B_{rs}] + [B_{rs}]^T\left[D_{22s}^{core}\right][B_{rs}] + [B_{rs}]^T\left[D_{22s}^{top}\right][B_{rs}]\right)dA^e$$

in which,

$$\left[D_{11b}^{bot}\right] = \left[C_b^{bot}\right]h_b \;;\; \left[D_{11b}^{core}\right] = 2\left[C_b^{core}\right]h_c \;;\; \left[D_{11b}^{top}\right] = \left[C_b^{top}\right]h_t$$

$$\left[D_{11s}^{bot}\right] = \left[C_s^{bot}\right]h_b \;;\; \left[D_{11s}^{core}\right] = 2\left[C_s^{core}\right]h_c \;;\; \left[D_{ts}^{top}\right] = \left[C_s^{top}\right]h_t$$

31

$$\left[D_{12b}^{bot} \right] = \int_{h_1}^{h_2} \left[C_b^{bot} \right] [z_1] dz \; ; \; \left[D_{12b}^{core} \right] = \int_{h_2}^{h_3} \left[C_b^{core} \right] [z_2] dz \; ; \; \left[D_{12b}^{top} \right] = \int_{h_2}^{h_3} \left[C_b^{top} \right] [z_3] dz$$

$$\left[D_{12s}^{bot} \right] = \int_{h_1}^{h_2} \left[C_s^{bot} \right] [z_4] dz \; ; \; \left[D_{12s}^{core} \right] = \int_{h_2}^{h_3} \left[C_s^{core} \right] [z_5] dz \; ; \; \left[D_{12s}^{top} \right] = \int_{h_2}^{h_3} \left[C_s^{top} \right] [z_6] dz$$

$$\left[D_{22b}^{bot} \right] = \int_{h_1}^{h_2} [z_1]^T \left[C_b^{bot} \right] [z_1] dz \; ; \; \left[D_{22b}^{core} \right] = \int_{h_2}^{h_3} [z_2]^T \left[C_b^{core} \right] [z_2] dz$$

$$\left[D_{22b}^{top} \right] = \int_{h_2}^{h_3} [z_3]^T \left[C_b^{top} \right] [z_3] dz \; ; \; \left[D_{22s}^{bot} \right] = \int_{h_1}^{h_2} [z_4]^T \left[C_s^{bot} \right] [z_4] dz$$

$$\left[D_{22s}^{core} \right] = \int_{h_2}^{h_3} [z_5]^T \left[C_s^{core} \right] [z_5] dz \; ; \; \left[D_{22s}^{top} \right] = \int_{h_2}^{h_3} [z_6]^T \left[C_s^{top} \right] [z_6] dz$$

On solving and simplification, the equation of motion can be expressed as

$$\left[M^e \right] \{ \ddot{d}_{tr}^e \} + \left[K_{11}^e \right] \{ d_{tr}^e \} + \left[K_{12}^e \right] \{ d_r^e \} = \{ F^e \} \tag{2.33}$$

$$\left[K_{12}^e \right]^T \{ d_t^e \} + \left[K_{22}^e \right] \{ d_r^e \} = 0 \tag{2.34}$$

From the above equations,

$$\left[K_e \right] = \left[K_{11} \right] - \left[K_{12} \right] \left[K_{22} \right]^{-1} \left[K_{12} \right]^T \tag{2.35}$$

To obtain the elemental matrices corresponding to the bending and the transverse shear deformation, the three-point and two-point Gaussian integration rule is considered, respectively. The elemental matrices include the stiffness matrix $[K_e]$, the initial stress stiffness matrix $[K_\sigma^e]$, and the mass matrix $[M^e]$. The computed element matrices are then assembled to obtain the global stiffness matrices $[K]$, $[K_\sigma]$, and $[M]$. The global matrices are then used to compute the natural frequency of the system under free vibration as:

$$\left| [[K] + [K_\sigma]] - \omega^2 [M] \right| = 0 \tag{2.36}$$

where, ω is the natural frequency of the system. While dealing with skew plates, the skew coordinates (X', Y', Z') are considered in place of rectangular coordinates X, Y, Z. The generalized displacement vectors of an arbitrary point lying on the skew edge are transformed as follows:

$$\{d_{tr}\} = [\mathrm{L}_{tr}]\{d'_{tr}\}, \qquad \{d_r\} = [\mathrm{L}_r]\{d'_r\} \tag{2.37}$$

where, $\{d'_{tr}\}$ and $\{d'_r\}$ are generalized displacement vectors of the point concerning the new (X', Y', Z') coordinate system.

$$\{d'_{tr}\} = \begin{bmatrix} u'_0 & v'_0 & w'_0 \end{bmatrix}^T \text{ and } \{d'_r\} = \begin{bmatrix} \theta'_x & \theta'_y & \phi'_x & \phi'_y & \alpha'_x & \alpha'_y \end{bmatrix}^T \qquad (2.38)$$

The transformation matrices are given as:

$$[L_{tr}] = \begin{bmatrix} \cos\Psi & \sin\Psi & 0 \\ -\sin\Psi & \cos\Psi & 0 \\ 0 & 0 & 1 \end{bmatrix}; [L_r] = \begin{bmatrix} \cos\Psi & \sin\Psi & 0 & 0 & 0 & 0 \\ -\sin\Psi & \cos\Psi & 0 & 0 & 0 & 0 \\ 0 & 0 & \cos\Psi & \sin\Psi & 0 & 0 \\ 0 & 0 & -\sin\Psi & \cos\Psi & 0 & 0 \\ 0 & 0 & 0 & 0 & \cos\Psi & \sin\Psi \\ 0 & 0 & 0 & 0 & -\sin\Psi & \cos\Psi \end{bmatrix} (2.39)$$

The transformation matrices are multiplied with the global matrices, and the transformed global matrices are substituted in Eq. 2.36.

2.5. RESULTS AND DISCUSSIONS

In this section, the effect of temperature and moisture on free vibration characteristics of laminated composites, hybrid composites, and sandwich plates is investigated using numerical methods. Temperature-dependent material properties of the graphite-epoxy, glass-epoxy composite materials and DYAD 606, EC 2216 viscoelastic material properties considered for the analysis are presented in Tables 2.1 to 2.3, and Figure 2.3. All sides simply supported (SS) and clamped (CC) boundary conditions are adopted for the analysis. The corresponding constraining conditions can be given as,

Simply supported edge (SS):

$u_0 \neq 0; \theta_x \neq 0; \phi_x \neq 0; \alpha_x \neq 0; v_0 = w_0 = \theta_y = \phi_y = \alpha_y = 0$ at $X = 0, a$

$u_0 = w_0 = \theta_x = \phi_x = \alpha_x = 0; v_0 \neq 0; \theta_y \neq 0; \phi_y \neq 0; \alpha_y \neq 0$ at $Y = 0, b$

Clamped edge (CC):

$u_0 = v_0 = w_0 = \theta_x = \phi_x = \alpha_x = \theta_y = \phi_y = \alpha_y = 0$ at $X = 0, a$ and $Y = 0, b$

33

Table 2.1: Mechanical, thermal, and hygroscopic properties of the materials used for analysis (Ram and Sinha, 1992: Biswal *et al*., 2015: Nashif *et al*., 1975: Sharnappa et al., 2007).

Properties	Units	Material-1	Material-2 Graphite-Epoxy	Material-3 Glass-Epoxy	Material-4 Visco-elastic core
Elastic Moduli	GPa	$E_1 = 130$, $E_2 = 9.5$, $G_{12} = 6.0$, $G_{13} = G_{12}$, $G_{23} = 0.5G_{12}$	Table 2.2 & 2.3	Table 2.2 & 2.3	Figure 2.3
Poisson's Ratio	m/m	$\upsilon_{12} = 0.3$	$\upsilon_{12} = 0.3$	$\upsilon_{12} = 0.41$	$\upsilon_{12} = 0.49$
Density	kg/m^3	1600	1600	1690	1200
Coefficient of thermal expansion	/^{0}K	$\alpha_1 = -0.3e\text{-}6$ $\alpha_2 = 28.1e\text{-}6$	$\alpha_1 = -0.3e\text{-}6$ $\alpha_2 = 28.1e\text{-}6$	$\alpha_1 = -0.3e\text{-}6$ $\alpha_2 = 28.1e\text{-}6$	--
Coefficient of moisture expansion		$\beta_1 = 0$ $\beta_2 = 0.44$	$\beta_1 = 0$ $\beta_2 = 0.44$	$\beta_1 = 0$ $\beta_2 = 0.44$	--

Table 2.2: Material properties of graphite-epoxy and glass-epoxy lamina at different moisture concentrations $G_{13} = G_{12}$, $G_{23} = 0.5G_{12}$ (Ram and Sinha, 1992: Biswal *et al*., 2015).

Materials	Elastic Moduli (GPa)	0.00	0.25	0.50	0.75	1.00	1.25
Graphite-epoxy	E_1	130	130	130	130	130	130
	E_2	9.50	9.25	9.00	8.75	8.50	8.50
	G_{12}	6.0	6.0	6.0	6.0	6.0	6.0
Glass-epoxy	$E_1 = E_2$	15.94	15.72	15.32	14.8	--	--
	G_{12}	3.57	3.51	3.46	3.39	--	--

Table 2.3: Material properties of graphite-epoxy and glass-epoxy lamina at different temperatures $G_{13} = G_{12}$, $G_{23} = 0.5G_{12}$ (Ram and Sinha, 1992: Biswal *et al*., 2015).

Materials	Elastic Moduli (GPa)	300	325	350	375	400	425
Graphite-epoxy	E_1	130	130	130	130	130	130
	E_2	9.50	8.50	8.00	7.50	7.00	6.75
	G_{12}	6.0	6.0	5.5	5.0	4.75	4.5
Glass-epoxy	$E_1 = E_2$	15.94	15.74	15.48	14.12	--	--
	G_{12}	3.57	3.55	3.52	3.49	--	--
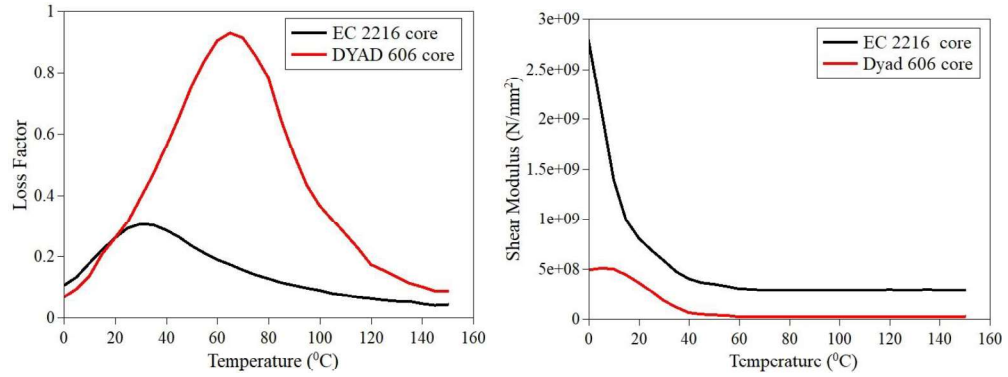
Figure 2.3: Viscoelastic core material properties of EC 2216 and DYAD 606 (Nashif *et al.*, 1975: Sharnappa *et al.*, 2007)

2.5.1. Convergence and validation study

The convergence study is carried out to obtain the non-dimensional frequencies of simply supported four-layer symmetric cross-ply laminated square composite plates at temperatures 300 K, 325 K, and 0.1 % moisture concentration for different mesh divisions. The length to thickness (*a/H*) ratio is considered as 100, and properties of material-1 are considered for the analysis. The obtained natural frequency is converted to non-dimensional form as:

$$\bar{\omega} = \frac{\omega a^2}{\pi^2 H} \sqrt{\frac{\rho}{E_t}} \tag{2.40}$$

where, $\bar{\omega}$ and ω are non-dimensional fundamental frequency and frequency of the system in rad/sec. The terms ρ and E_t indicate the density and the modulus of the composite laminate. The results obtained are listed in Table 2.4. As observed, the mesh size of 12×12 shows excellent convergence of the numerical solution for the free vibration of composite plates in the hygrothermal environment. Consequently, a mesh size of 12×12 is employed throughout the simulations.

The current formulation is validated for free vibration analysis of simply supported composite plates under elevated temperature and moisture conditions, as shown in Tables 2.5 and 2.6, respectively. An *a/H* ratio of 40 is considered for the analysis of graphite-epoxy four-layered symmetric cross-ply square composite plate (material-1). The non-dimensional fundamental natural frequencies obtained for varying the length to width (*a/b*) ratio, temperature, and moisture concentration values

are compared with the available literature. The present FE results show good agreement with the previous results reported in the literature (Ram and Sinha, 1992).

Non-dimensional fundamental frequencies of simply supported and clamped symmetric cross-ply 90°/0°/90°/0°/90° skew LC plates are extracted considering the a/H ratio as 10. The following material properties are considered for the analysis:

$E_1/E_2 = 40$, $E_2 = E_3$, $G_{12} = 0.6E_2$, $G_{13} = G_{23} = 0.5E_2$, $\upsilon_{12} = \upsilon_{13} = \upsilon_{23} = 0.25$.

From Table 2.7, it is evident that the results obtained from the current analysis are in good agreement with the published results (Garg *et al.*, 2006: Kanasogi and Ray, 2013: Wang, 1997). Further, results are also extracted for simply supported honeycomb skew sandwich plates with the following material and geometrical parameters:

$a/b = 1.5$, $E_f = 68.948$ GPa, $G_f = 25.924$ GPa, $\upsilon_f = 0.33$, $\rho_f = 2768$ kg/m^3,

$G_{23c} = 0.05171$ GPa, $G_{13c} = 0.13445$ GPa, $\rho_c = 121.83$ kg/m^3.

In addition, the analysis is carried out on simply supported cross-ply skew sandwich plate 0°/90°/C/0°/90° with the following geometrical and material parameters:

$a/b = 2$, $a/H = 40$, $t_c/t_f = 4$, $G_{23c} = 0.24132$ GPa, $G_{13c} = 0.11721$ GPa, $\rho_c = 2351.2$ kg/m^3.

$E_{1f} = 206.84$ GPa, $E_{3f} = 5.1711$ GPa, $G_{12f} = 5.1711$ GPa, $\upsilon_f = 0.25$, $\rho_f = 1603.1$ kg/m^3.

The results obtained for the skew honeycomb sandwich and cross-ply sandwich composite plates are presented in Table 2.8. The results indicate that the natural frequency (Hz) values acquired from the current formulation are in excellent conformity with the published results.

2.5.2. Skew LC plate

The influence of temperature and moisture on a skew LC plate with SS and CC boundary conditions are analyzed for various fiber orientation configurations. The effect of moisture on the free vibration characteristics of symmetric cross-ply skew LC plate (0°/90°/90°/0°) with SS boundary condition is presented in Figure 2.4. The properties of material-2 are considered for the analysis of composite plates having an a/H ratio of 50. It is evident from the results that the natural frequency reduces with an increase in moisture concentration due to a reduction in the stiffness of the system (Parhi *et al.*, 2001: Biswal *et al.*, 2016: Panda *et al.*, 2013: Amoushahi and

Goodarzian, 2018). The reduction in natural frequency is significant for smaller values of skew angle. As the skew angle increases, the effect of moisture concentration on the natural frequency of the system reduces. With an increase in a/b ratio, the value of the natural frequency of the LC plate increases due to an increase in stiffness of the system (Wang *et al*., 2000: Chakrabarti and Sheikh, 2004). The percentage increase of 475 % in natural frequency is observed from skew angle 0° to 60° (for $a/b = 2$), and 52.83 % reduction is noted for increasing moisture concentration values from 0.00 % to 0.75 % (for $a/b = 1$).

Figure 2.5 illustrates the effect of skew angle, a/b ratio, and a/H ratio on the fundamental frequency of skew LC plate in the presence of moisture (0.75 %) with SS edge constraints. It can be noted that for the lower values of a/b ratios (i.e., $a/b = 0.5$), the natural frequency decreases with an increase in a/H ratios. In contrast, the reverse trend is observed for the higher values of a/b ratios (i.e., $a/b > 0.5$). The increase in natural frequency is observed from an a/H ratio of 10 to 20, while the magnitude of frequency is reduced for all the higher values of a/H ratios due to localized shear deformation (Rath and Sahu, 2012). This scenario is more prominent for lower values of a/b ratios ($a/b < 1$). Similar observations were made by Patel *et al.* (2002). It can also be noted that the natural frequency consistently increases with an increase in skew angle (Park *et al*., 2008: Chalak *et al*., 2014: Katariya *et al*., 2018).

Similarly, Figure 2.6 encompasses the results for clamped symmetric cross-ply skew LC plate ($0°/90°/90°/0°$) in moisture environment using the properties of material-2. A constant a/H ratio of 50 is considered for the analysis. The results reveal that the natural frequency of an LC plate increases with an increase in skew angle and a/b ratio. The effect of the skew angle is more severe for higher values of a/b ratios. The maximum increment of 147 % in natural frequency is observed for increasing skew angle values from 0° to 60° (for $a/b = 2$) and maximum reduction of 8.86 % is noted for increasing moisture concentration values from 0.00 % to 0.75 % (for $a/b = 1$).

The effect of skew angle, a/b, and a/H ratios on the clamped LC plate in the elevated moisture setup (0.25 %) is presented in Figure 2.7. The results indicate that the natural frequency of the system increases with an increase in skew angle, a/b, and a/H ratios. To study the effect of material properties on the vibrational characteristics

of an LC plate, material-1 and material-2 are chosen for the analysis. Properties of material-2 vary with an increase in temperature, whereas properties of material-1 are independent of the temperature variations. The non-dimensional natural frequencies for varying temperature and a/b ratios are presented in Table 2.9 for the symmetric cross-ply skew LC plate (0°/90°/90°/0°) with SS boundary condition. For such investigation, the a/H ratio is adapted as 50.

It can be noticed from the results that the magnitude of natural frequency reduces with an increase in temperature. However, natural frequency increases with an increase in skew angle and a/b ratios. The increment of 181 % and 222 % in natural frequency is observed from skew angle 0º to 45º (for a/b = 2) for material-2 and material-1, respectively. The maximum reduction of 53.42 % and 25.52 % in frequency is noted for increasing temperature values from 325 K to 425 K (a/b = 1) for material-1 and material-2.

Consequently, it is evident from the results that the material properties play a very critical role in the modal analysis of composite plates. The significant variation in percentage changes in fundamental frequencies with respect to the geometrical parameters and temperature values are observed for both material-1 and material-2. It is also noticed that material-1 slightly under-predicts the natural frequency values. The material properties of composites generally degrade when they are exposed to elevated temperature and moisture environments. This, in turn, reduces the stiffness of a composite structure, i.e., with an increase in temperature and moisture, the stiffness of the composite structure reduces. The stiffness of any system is directly proportional to the natural frequency. Hence, with a reduction in stiffness of composite structures, the natural frequency of the system reduces (Ram and Sinha, 1992: Rath and Sahu, 2012: Prasad and Sahu, 2018: Biswal *et al.*, 2015, 2016a, 2016b, 2017).

Table 2.4: Convergence study of the $\bar{\omega}$ of 0°/90°/90°/0° LC plate with SS boundary condition.

Mesh Size	C=0.1%			T=300 K			T=325 K		
	Modes			Modes			Modes		
	1	2	3	1	2	3	1	2	3
4×4	9.0923	20.3942	39.4368	12.2375	24.0687	41.4426	7.2972	18.5509	38.5235
8×8	9.0576	19.8282	39.2614	12.2192	23.6879	41.3434	7.2492	17.8752	38.3130
10×10	9.0574	19.8265	39.2630	12.2194	23.6894	41.3474	7.2488	17.8717	38.3136
12×12	9.0573	19.8263	39.2642	12.2194	23.6903	41.3495	7.2486	17.8709	38.3144

Table 2.5: The $\bar{\omega}$ of 0°/90°/90°/0° LC plate with SS boundary condition for different temperature values.

Temperature (K)	a/b = 0.5		a/b = 1.0		a/b = 2.0	
	Ram and Sinha (1992)	Present	Ram and Sinha (1992)	Present	Ram and Sinha (1992)	Present
300	10.1714	10.2953	11.8934	12.1095	23.0044	23.4569
325	9.9067	10.4077	11.3951	12.1041	22.1934	23.6263
350	9.6410	10.2584	10.8916	11.7558	21.3008	23.2190
375	9.2964	10.1553	10.5476	11.4469	20.4877	22.8721
400	8.9498	10.1337	9.8887	11.2521	19.7508	22.7194
425	8.7633	9.9080	9.3896	10.8171	19.0919	22.2143

Table 2.6: The $\bar{\omega}$ of 0°/90°/90°/0° LC plate with SS boundary condition for different moisture conditions.

Moisture (%)	a/b = 0.5		a/b = 1.0		a/b = 2.0	
	Ram and Sinha (1992)	Present	Ram and Sinha (1992)	Present	Ram and Sinha (1992)	Present
0.00	10.2654	10.2953	11.8169	12.1095	22.8951	23.4569
0.25	9.6505	9.5870	10.9820	11.1004	21.6891	22.2170
0.50	8.8126	8.8313	9.9216	10.0005	20.3351	20.9189
0.75	8.2725	8.0156	8.8612	8.7768	18.9823	19.5524
1.00	7.3613	7.1202	7.6567	7.3689	17.7763	18.1034
1.25	6.5249	5.2376	6.5258	5.2374	16.4238	16.1422

Table 2.7: The $\bar{\omega}$ of symmetric cross-ply 90°/0°/90°/0°/90° skew LC plate.

Skew Angle	SS				CC			
	Garg et al., (2006)	Kanasogi and Ray (2013)	Wang (1997)	Present	Garg et al., (2006)	Kanasogi and Ray (2013)	Wang (1997)	Present
0º	1.5699	1.5635	1.5699	1.5368	2.3687	2.3201	2.3820	2.2403
15º	1.6874	1.6571	--	1.6245	2.4663	2.3699	--	2.2878
30º	2.0840	1.9596	2.0844	1.9012	2.7921	2.5366	2.7921	2.4434
45º	2.8925	2.4811	2.8825	2.3673	3.4739	2.8665	3.4738	2.7452

Table 2.8: Fundamental frequency (Hz) of LCS plate with SS boundary condition.

Skew Angle	Honeycomb				0°/90°/C/0°/90°			
	Garg et al. (2006) FSDT	Garg et al. (2006) HSDT	Raville and Ueng (1967)	Present	Garg et al. (2006) FSDT	Garg et al. (2006) HSDT	Yuan and Dawe (2002)	Present
0°	23.5279	23.4514	23.0000	23.5220	166.3086	152.2992	152.5800	152.5263
15°	24.9315	24.8438	--	24.2699	177.6942	161.7182	--	158.4616
30°	30.0623	29.9153	--	26.8034	217.7630	194.3770	--	178.4418

Table 2.9: Effect of temperature on the $\bar{\omega}$ of skew LCS plate with SS boundary conditions for varying a/b ratios.

a/b	Temperature (K)	Skew Angle (material-1)				Skew Angle (material-2)			
		0°	15°	30°	45°	0°	15°	30°	45°
0.5	325	9.5787	9.6997	10.1627	11.6766	10.1942	10.3164	10.7808	12.3215
	350	8.7540	8.8579	9.2760	10.7710	9.7826	9.8768	10.2779	11.7914
	375	7.8431	7.9263	8.2929	9.7803	9.4125	9.4745	9.8038	11.2894
	400	6.8115	6.8678	7.1736	8.6753	9.1245	9.1583	9.4213	10.8903
	425	5.1785	5.6098	5.8391	7.4046	8.5904	8.5903	8.7756	10.2226
1.0	325	11.1168	12.1077	14.7771	19.8308	11.7969	12.8238	15.5667	20.7686
	350	9.9695	11.0340	13.8286	19.0165	11.0709	12.1296	14.9712	20.3585
	375	8.6718	9.8434	12.8087	18.1645	10.3592	11.4512	14.4004	19.9898
	400	7.1420	8.4867	11.6985	17.2691	9.7459	10.9024	13.9964	19.8133
	425	5.1783	6.8660	10.4693	16.3231	8.7987	10.0304	13.2800	19.3030
2.0	325	22.2359	26.0434	36.1417	54.3490	23.2747	27.2859	37.8070	56.6782
	350	20.8319	24.8218	35.1834	53.5873	22.4052	26.4935	37.2089	56.3790
	375	19.3261	23.5367	34.1979	52.8143	21.5844	25.7423	36.6425	56.1076
	400	17.6925	22.1772	33.1829	52.0294	20.9575	25.2958	36.5436	56.4713
	425	15.8919	20.7285	32.1355	51.2321	19.9166	24.3924	35.8736	56.0540

(a)

(b)

(c)
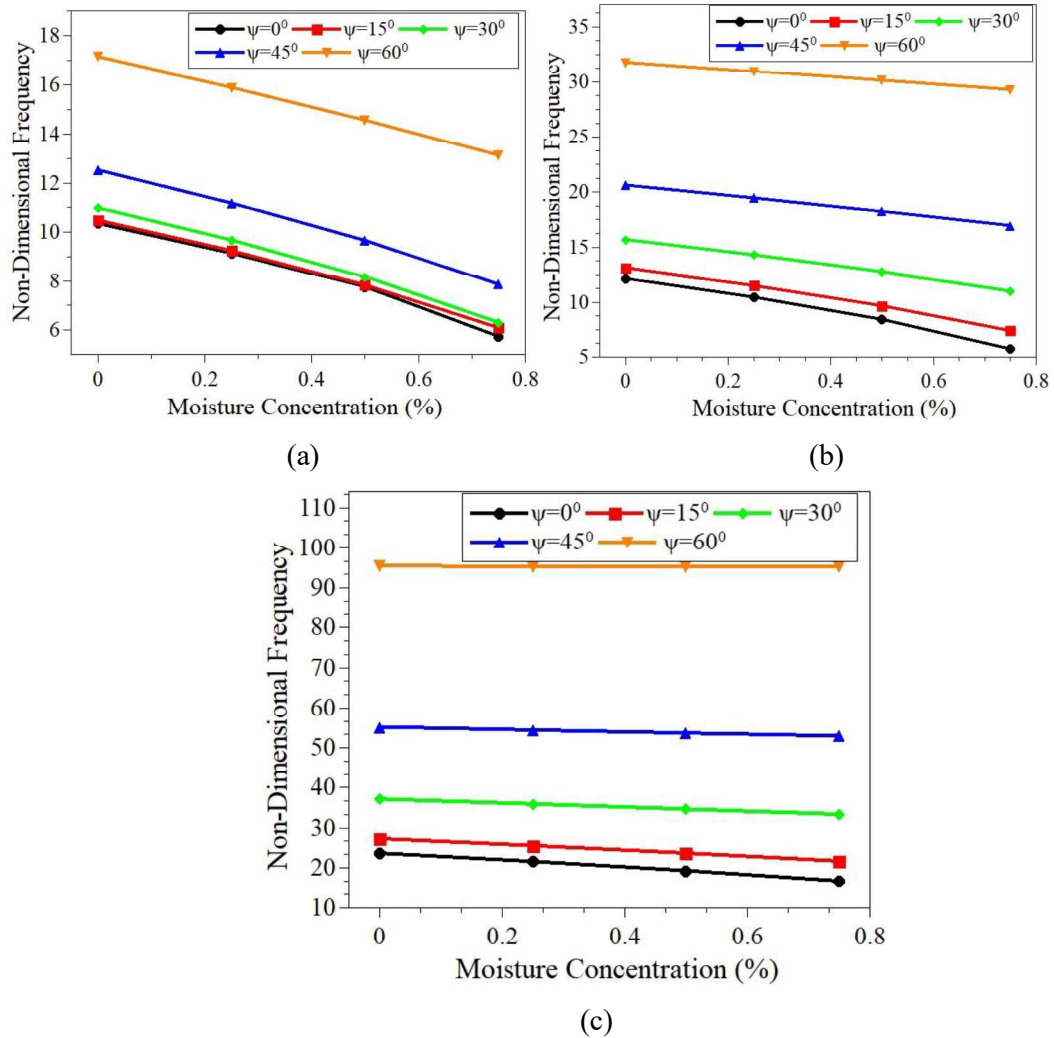
Figure 2.4: Effect of moisture concentration on the $\overline{\omega}$ of skew LC plate with SS boundary conditions for varying a/b ratios (a) $a/b = 0.5$ (b) $a/b = 1.0$ (c) $a/b = 2.0$.

(a)

(b)

(c)   (d)
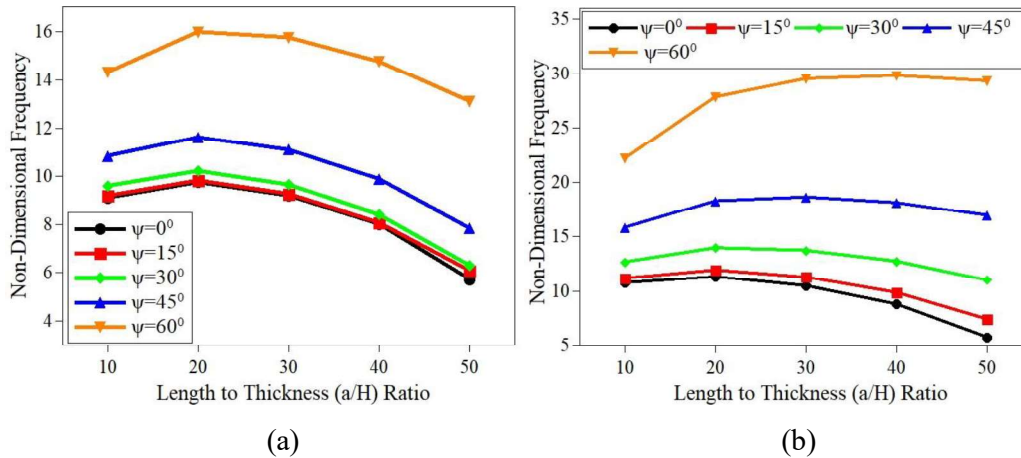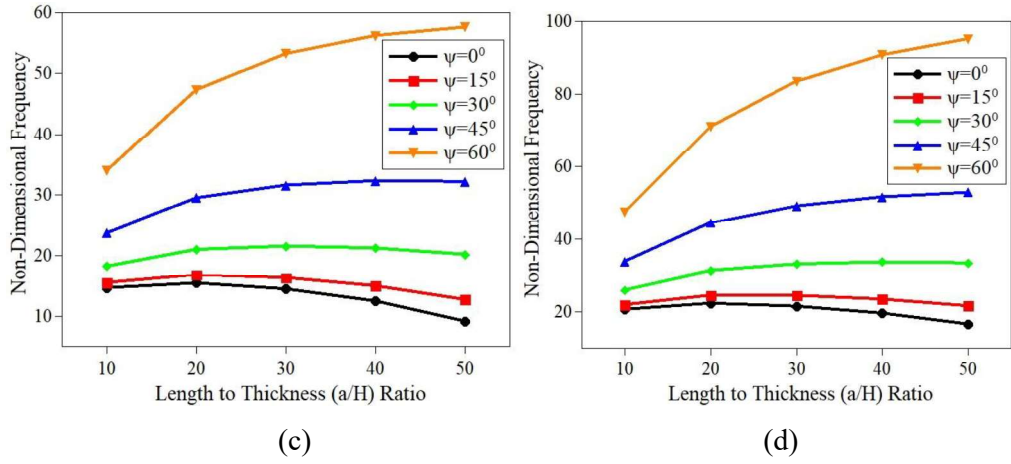
Figure 2.5: Effect of skew angle on the $\overline{\omega}$ of skew LC plate in presence of moisture (0.75 %) with SS boundary consition for varying a/b and a/H ratios (a) a/b = 0.5 (b) a/b = 1.0 (c) a/b = 1.5 (d) a/b = 2.0.

(a)   (b)

(c)
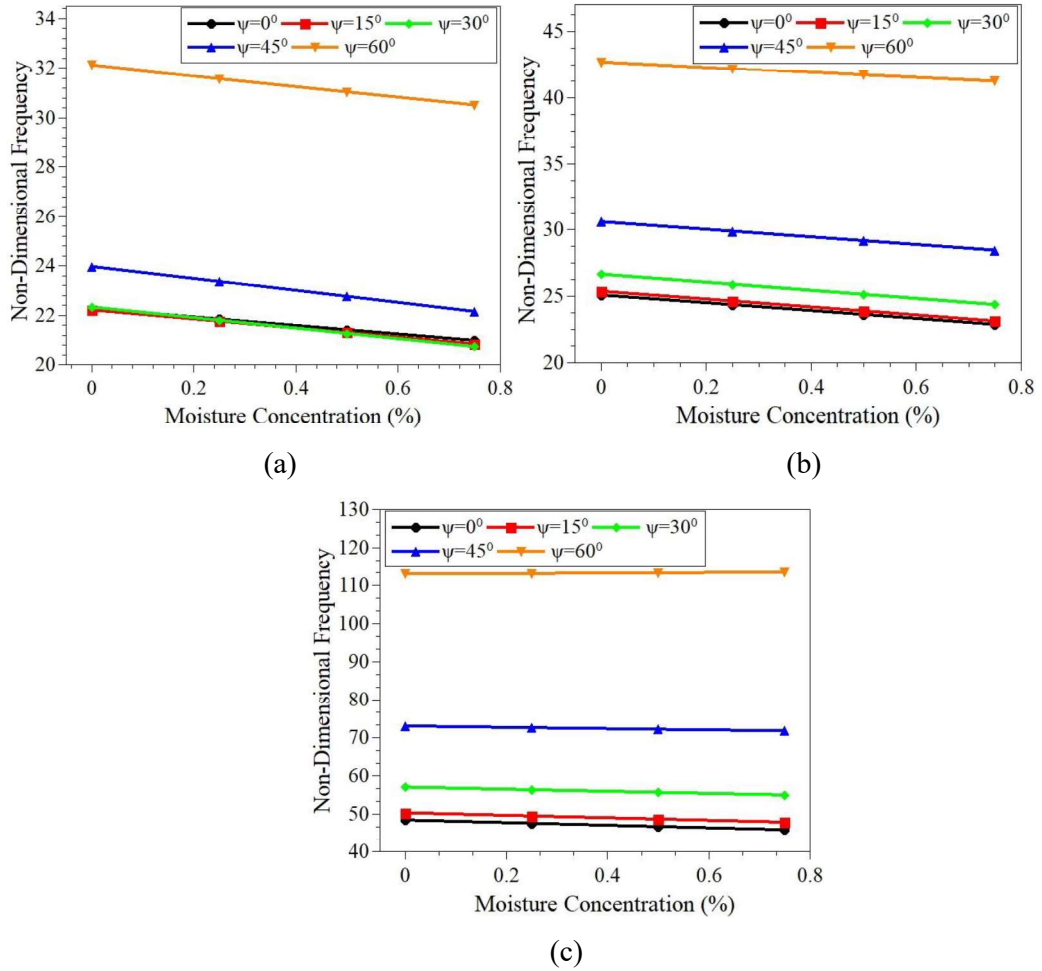
Figure 2.6: Effect of moisture concentration on the $\overline{\omega}$ of skew LC plate with CC boundary condition for varying a/b ratios (a) a/b = 0.5 (b) a/b = 1.0 (c) a/b = 2.0.

43

Therefore, it can be noted that the change in material properties due to variation in temperature and moisture concentration values are to be considered for the accurate prediction of the vibration response of a system (Padhi and Padit, 2017).

Figure 2.8 illustrates the effect of skew angle, a/b, and a/H ratios on the frequency response of a skew LC plate at elevated temperature (425 K) for SS boundary conditions. The results suggest that for the lower values of a/b ratios (i.e., $a/b < 1$), the natural frequency decreases with an increase in a/H ratios. In contrast, a reverse trend is observed for higher values of a/b ratios (i.e., $a/b > 1$). As the a/H ratio varies from 10 to 100, the plate transforms from thick plate to thin plate condition. With an increase in the a/H ratio, the ratio of the magnitude of the stiffness matrix to the mass matrix tends to have a constant value. In turn, the minimal variation in the natural frequency of the structure can be observed for higher values of a/H ratios ($a/H > 30$). Many researchers made similar observations for composite structures (Ebrahimi and Dabbagh, 2019: Chakrabarti and Sheikh, 2004: Reddy 2003). It can also be noted that the natural frequency of the system increases with an increase in skew angle.

2.5.3. Skew LHC plate

The study is extended to understand the effect of temperature and moisture on the vibration response of skew LHC plates. Temperature-dependent and moisture-dependent properties of the graphite-epoxy and glass-epoxy composites are considered for the analysis. The a/H ratio of the plate is considered as 50. The analysis is carried out to investigate the effect of moisture on the clamped graphite/glass/graphite skew LHC plate, and the results are presented in Table 2.10. Further, the effect of skew angle and aspect ratios on the natural frequency of clamped graphite/glass/graphite skew laminated hybrid composite plate is investigated. The results obtained in the presence of moisture (0.25%) are presented in Figure 2.9. It is observed that the fundamental frequency of the hybrid composite plate increases with increasing skew angle and aspect ratios. The effect of skew angle and a/H ratios are more predominant for higher values of a/b ratios.
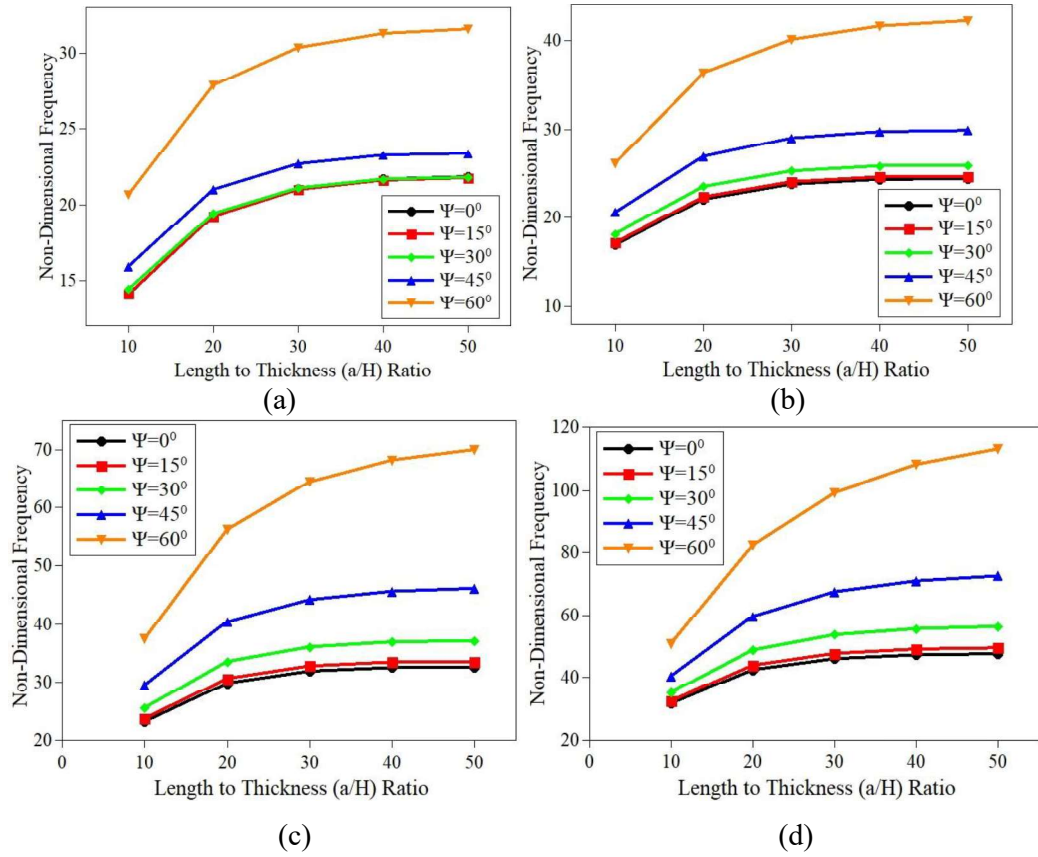
Figure 2.7: Effect of skew angle on the $\overline{\omega}$ of skew LC plate with CC boundary consition in presence of moisture (0.25 %) for varying a/b and a/H ratios (a) $a/b = 0.5$ (b) $a/b = 1.0$ (c) $a/b = 1.5$ (d) $a/b = 2.0$.

(c)   (d)
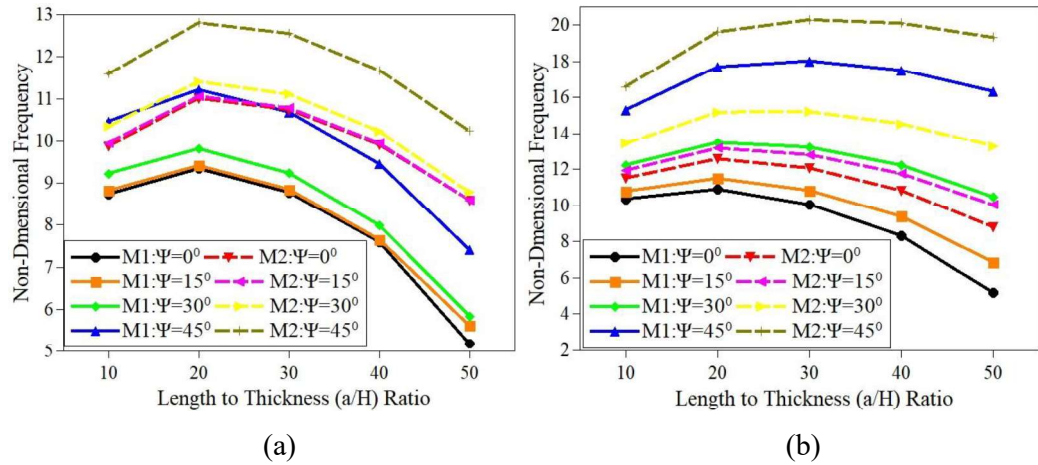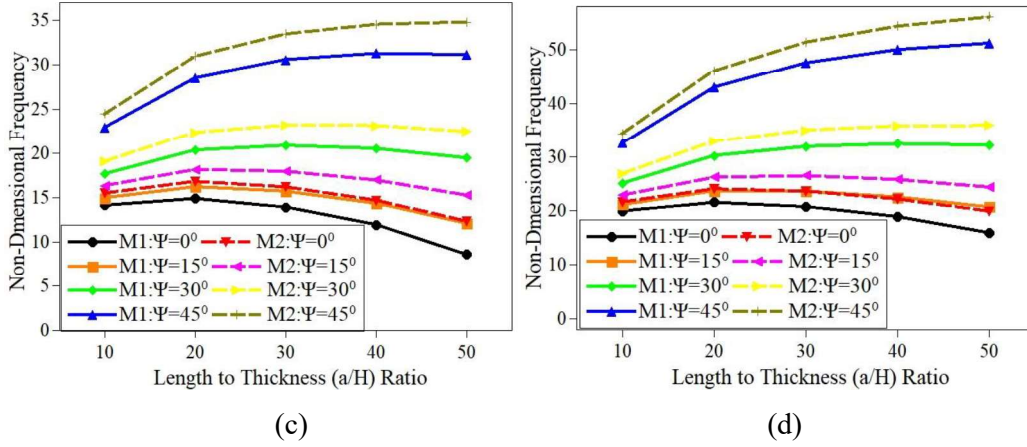
Figure 2.8: Effect of a skew angle the $\overline{\omega}$ of skew LC plate with SS boundary condition in presence of temperature (425 K) for varying a/b and a/H ratios (a) $a/b =$ 0.5 (b) $a/b = 1.0$ (c) $a/b = 1.5$ (d) $a/b = 2.0$ [M1: *material-1,* M2: *material-2*].

The effect of temperature on the fundamental frequency of the simply supported graphite/glass/graphite skew LHC plate is analyzed for varying skew angle and a/b ratios. The results obtained are enlisted in Table 2.11. From the results, it can be concluded that with an increase in skew angle and a/b ratios, the magnitude of natural frequency increases. However, the results also indicate that the natural frequency reduces with the increase in temperature. The maximum rise of 829 % in natural frequency is observed from skew angle 0° to 60° (for $a/b = 2$). A reduction of 61 % is noted for increasing temperature values from 300 K to 350 K. A similar trend in variation of the fundamental frequency is observed for clamped graphite/glass/graphite skew LHC plate with increasing temperature values. Figure 2.10 demonstrates the effect of skew angle, a/b, and a/H ratios on the natural frequency of simply supported graphite/glass/graphite skew LHC plate in the presence of temperature (350 K). The results suggest that for the lower values of a/b ratios (i.e., $a/b < 1$), the natural frequency decreases with an increase in a/H ratios. In contrast, the opposite trend is observed for the higher values of a/b ratios (i.e., $a/b > 1$).

The structural behavior of LHC is dependent on the stacking sequence of the constituting layers (Ma *et al*., 2020). In order to understand the impact of layer stacking sequence on the modal behavior of LHC plates, the analysis is carried out on glass/graphite/glass skew LHC plate for different a/b and a/H ratios. The results obtained for varying moisture concentration and temperature are presented in Tables 2.12 and 2.13. It can be seen from the tables that the natural frequency increases with

46

an increase in skew angle, *a*/*b,* and *a*/*H* ratios, and the fundamental frequency reduces with an increase in temperature and moisture concentration values. It can also be noted that the change in stacking sequence from graphite/glass/graphite to glass/graphite/glass considerably reduced the natural frequency, which in turn restricts the operating frequency of the system.

Table 2.10: Effect of moisture on the $\bar{\omega}$ of graphite/glass/graphite skew LHC plate with CC boundary conditions for varying *a*/*b* ratios.

a/*b*	Moisture Concentration (%)	Skew Angle				
		0⁰	15⁰	30⁰	45⁰	60⁰
	0.00	22.9179	22.7827	22.5394	22.9630	27.2015
	0.25	22.9105	22.6790	22.1111	21.9515	25.5257
0.5	0.50	18.4746	18.5528	18.9887	19.0840	22.2148
	0.75	7.4978	8.8840	12.1147	15.7031	19.1748
	0.00	24.5087	24.5520	24.9420	26.7956	34.0175
	0.25	23.4573	23.3885	23.4561	24.8778	31.8954
1.0	0.50	20.1751	20.0329	19.8730	21.0308	28.1470
	0.75	13.0846	13.9471	16.3612	17.2426	24.6087
	0.00	37.9109	39.0050	43.0542	53.3061	81.1168
	0.25	34.5362	35.6074	39.6437	50.0620	78.5519
2.0	0.50	29.1073	30.2186	34.4253	45.2343	74.2603
	0.75	23.3542	24.5474	29.0726	40.5407	70.5286

(a)

(b)

(c)   (d)
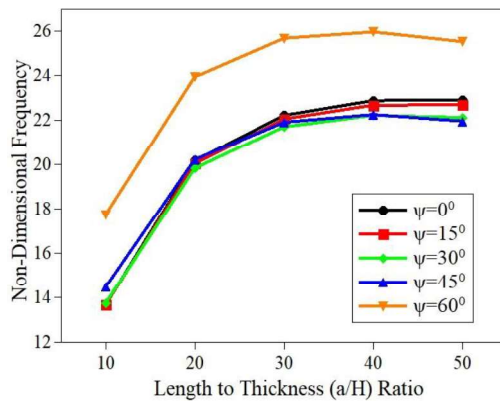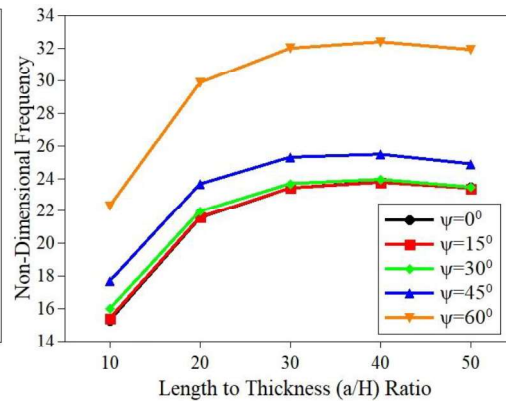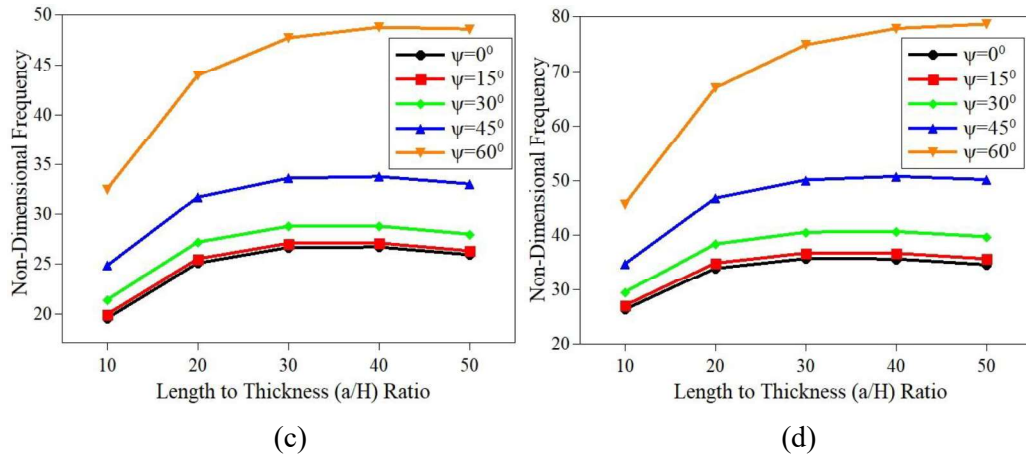
Figure 2.9: Effect of skew angle on the $\overline{\omega}$ of graphite/glass/graphite skew LHC plate with CC boundary condition in presence of moisture (0.25 %) for varying a/b and a/H ratios (a) $a/b = 0.5$ (b) $a/b = 1.0$ (c) $a/b = 1.5$ (d) $a/b = 2.0$.

Table 2.11: Effect of temperature on the $\overline{\omega}$ of /glass/graphite skew LHC plate with SS boundary conditions for varying a/b ratios.

a/b	Temperature (K)	Skew Angle				
		0°	15°	30°	45°	60°
	300	10.6719	10.7141	10.8481	11.5104	14.2239
0.5	325	9.8901	9.8110	9.5690	9.6545	11.8629
	350	5.5384	6.8662	7.3825	6.5567	8.0882
	300	11.9849	12.6369	14.1544	17.1370	24.5394
1.0	325	10.0948	10.7586	12.1102	14.9646	22.5490
	350	6.9783	7.6248	8.7387	11.6198	19.7308
	300	19.2370	22.6305	30.4766	43.7007	73.3314
2.0	325	15.0657	19.3529	28.0302	41.7670	72.1553
	350	7.5067	14.0096	24.0898	38.5970	69.7625

(a)   (b)

(c)   (d)
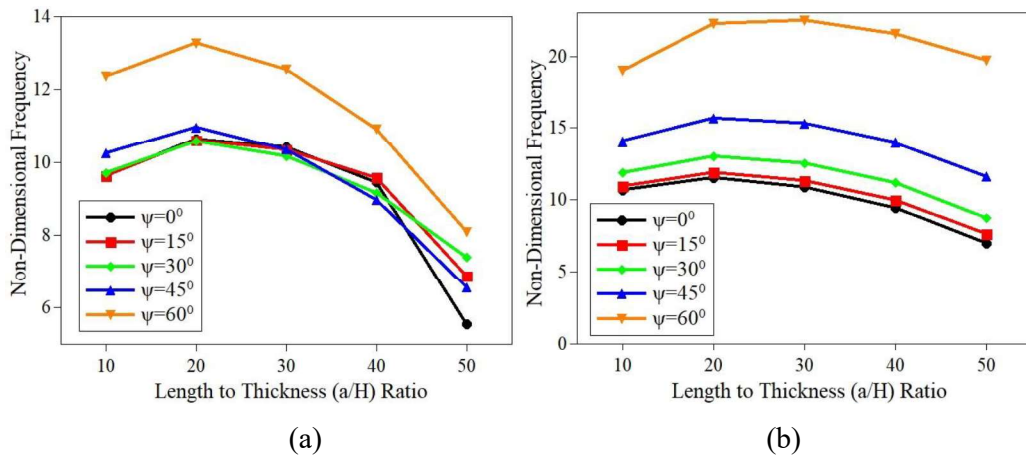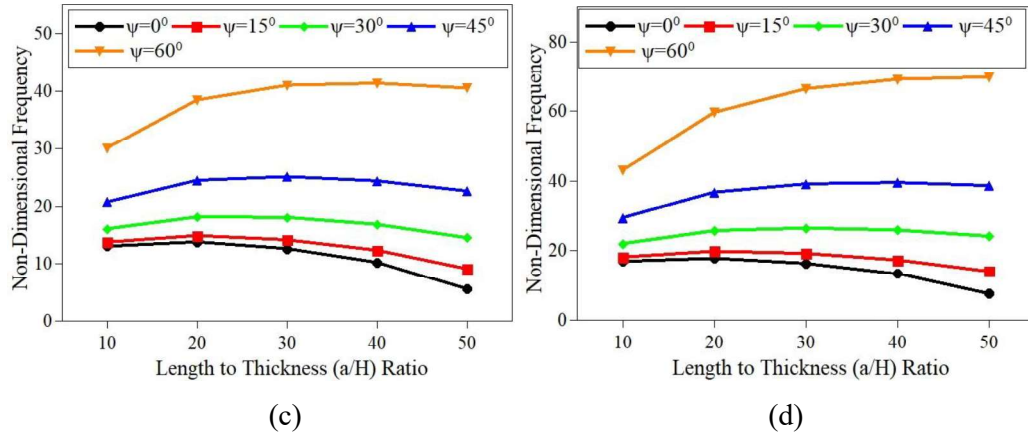
Figure 2.10: Effect of skew angle on the $\overline{\omega}$ of graphite/glass/graphite skew LHC plate (350 K) with SS boundary condition for varying a/b and a/H ratios (a) $a/b = 0.5$ (b) $a/b = 1.0$ (c) $a/b = 1.5$ (d) $a/b = 2.0$.

The analysis is also carried out for the clamped glass/graphite/glass skew LHC plates for varying temperature and moisture profiles. A similar trend in the fundamental frequency variation is observed for the clamped skew LHC plate. The investigations are further carried out for five-layered skew LHC plates for varying temperature and moisture concentration values. The parameters like skew angle, stacking sequence, a/b, and a/H ratios are also considered for the analysis.

The results obtained for the five-layered hybrid composite plate operating in thermal and moisture conditions indicate that the glass/graphite/glass/graphite/glass (GL/GR/GL/GR/GL: combination-1) combination has a higher fundamental natural frequency value compared to the graphite/glass/graphite/glass/graphite (GR/GL/GR/GL/GR: combination-2) combination. The maximum percentage increase of 117 % and 113 % in natural frequency is observed for the skew angle from 0° to 45° (for $a/b = 2$) for combination-1 and combination-2, respectively. Harmoniously, reduction of 25.67 % and 18.78 % in natural frequency is noted for increasing moisture concentration from 0.00 % to 0.75 % (for $a/b = 1$) for combination-1 and combination-2, respectively.

Additionally, an increment of 105 % in natural frequency is observed for an increase in skew angle from 0° to 45° (for $a/b = 2$ and $a/H = 50$) for combination-1, and an upsurge of 102 % is witnessed for combination-2. The reduction of 8.86 % and 10.04 % in frequency is noted for increasing temperature values from 300 K to 375 K (for $a/b = 1$) for combinations-1 and combination-2.

Effect of skew angle, a/b, and a/H ratios on the natural frequency of five-layered skew LHC plate in the presence of moisture (0.25 %) and temperature (325 K) are plotted in Figures 2.11 and 2.12, respectively. The results denote that for lower values of a/b ratios (i.e., $a/b < 1$), the natural frequency decreases with an increase in a/H ratios. In contrast, the reverse trend in variation is observed for the higher values of a/b ratios (i.e., $a/b > 1$). Natural frequencies obtained for material combination-1 are comparatively higher than the frequencies obtained from combination-2. It can also be observed that the fundamental frequency increases continuously with an increase in skew angle.

Table 2.12: Effect of moisture on the $\bar{\omega}$ of glass/graphite/glass skew LHC plate with SS boundary conditions for varying a/b and a/H ratios.

a/b	a/H	Moisture Concentration (%)	0⁰	15⁰	30⁰	45⁰	60⁰
					Skew Angle		
0.5	10	0.00	5.1304	5.3455	6.0839	7.7206	11.4585
		0.25	4.9600	5.1745	5.9126	7.5520	11.2990
		0.50	4.7927	5.0074	5.7477	7.3952	11.1650
		0.75	4.6238	4.8392	5.5831	7.2416	11.0408
	20	0.00	5.4207	5.6741	6.5391	8.4670	13.1030
		0.25	4.7256	4.9814	5.8569	7.8105	12.4996
		0.50	3.9177	4.1848	5.0943	7.1057	11.8831
		0.75	2.8961	3.1989	4.1984	6.3261	11.2382
1.0	10	0.00	7.7877	8.1524	9.3758	11.9526	17.2116
		0.25	7.5826	7.9514	9.1869	11.7832	17.0690
		0.50	7.3871	7.7620	9.0162	11.6457	16.9892
		0.75	7.1925	7.5748	8.8512	11.5205	16.9359
	20	0.00	8.3419	8.8492	10.5465	14.1967	22.3870
		0.25	7.5284	8.0635	9.8328	13.5793	21.8805
		0.50	6.6288	7.2079	9.0849	12.9647	21.4180
		0.75	5.5897	6.2406	8.2763	12.3302	20.9658
2.0	10	0.00	16.5683	18.0104	21.3118	26.7964	33.8994
		0.25	16.5690	18.0159	21.0937	26.6056	33.9909
		0.50	16.6818	18.1359	20.9418	26.5255	34.2310
		0.75	16.8442	17.9920	20.8164	26.4911	34.5781
	20	0.00	20.2274	21.5982	26.2409	36.2824	57.6272
		0.25	19.3136	20.7211	25.4599	35.6296	57.1172
		0.50	18.3796	19.8395	24.7167	35.0844	56.8525
		0.75	17.4025	18.9274	23.9720	34.5744	56.6848

Table 2.13: Effect of temperature on the $\bar{\omega}$ of glass/graphite/glass skew LHC plate with SS boundary conditions for varying a/b and a/H ratios.

a/b	a/H	Temperature (K)	Skew Angle 0º	15º	30º	45º	60º
0.5	10	300	5.1304	5.3455	6.0839	7.7206	11.4585
		325	5.0298	5.2445	5.9829	7.6220	11.3698
		350	4.9068	5.1199	5.8535	7.4832	11.2040
		375	4.8316	5.0458	5.7840	7.4262	11.1838
	20	300	5.4207	5.6741	6.5391	8.4670	13.1030
		325	5.0075	5.2613	6.1296	8.0690	12.7339
		350	4.5540	4.8091	5.6834	7.6372	12.3247
		375	4.0972	4.3595	5.2547	7.2438	11.9924
1.0	10	300	7.7877	8.1524	9.3758	11.9526	17.2116
		325	7.6668	8.0346	9.2675	11.8615	17.1510
		350	7.5102	7.8770	9.1053	11.6823	16.9132
		375	7.4330	7.8072	9.0592	11.6837	17.0133
	20	300	8.3419	8.8492	10.5465	14.1967	22.3870
		325	7.8507	8.3748	10.1162	13.8272	22.0937
		350	7.3196	7.8596	9.6395	13.3921	21.6694
		375	6.8132	7.3872	9.2511	13.1121	21.5337
2.0	10	300	16.5683	18.0104	21.3118	26.7964	33.8994
		325	16.6243	18.0622	21.2048	26.7285	33.9221
		350	16.3755	17.8282	20.9165	26.3647	34.0096
		375	16.7362	18.1999	20.9897	26.5941	35.0307
	20	300	20.2274	21.5982	26.2409	36.2824	57.6272
		325	19.6661	21.0636	25.7786	35.9271	57.4248
		350	19.0502	20.4588	25.1920	35.3166	56.6140
		375	8.5207	9.2980	11.6369	16.2120	26.5108

(a)

(b)

(c)

(d)
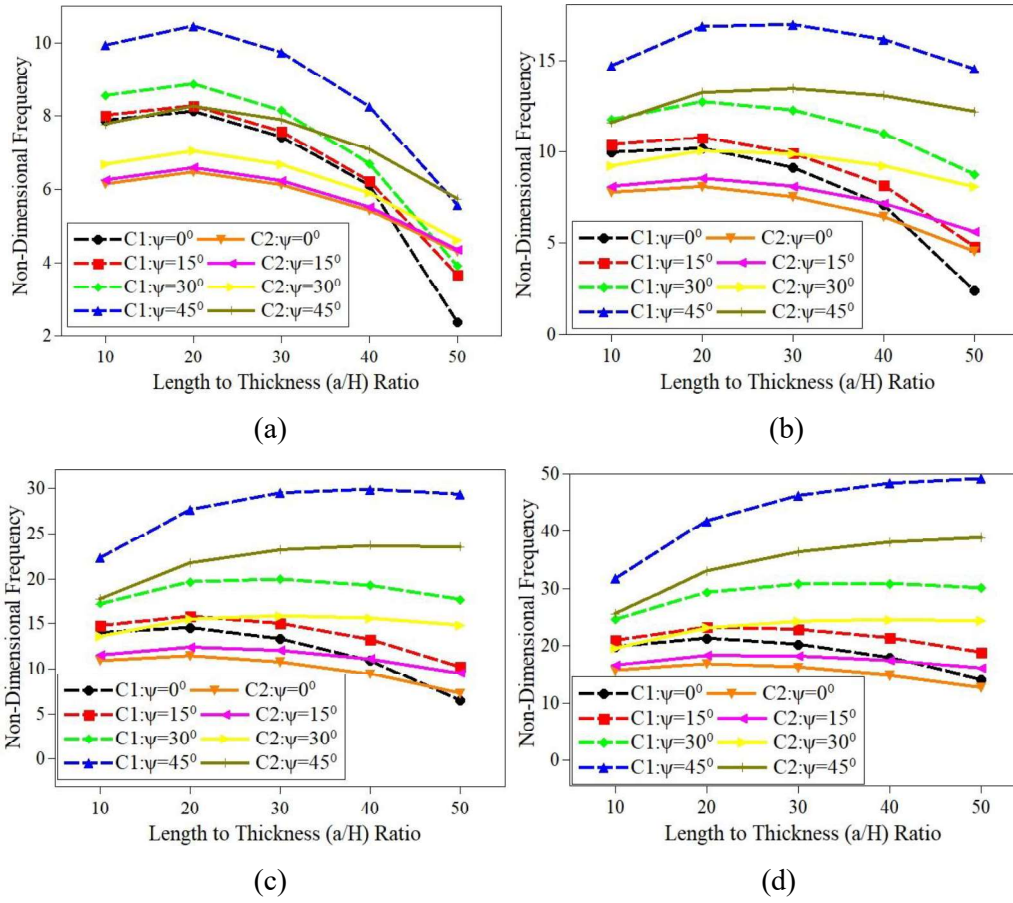
Figure 2.11: Effect of skew angle on the $\overline{\omega}$ of five-layered skew LHC plate in presence of moisture (0.25 %) with SS boundary condition for varying a/b and a/H ratios (a) $a/b = 0.5$ (b) $a/b = 1.0$ (c) $a/b = 1.5$ (d) $a/b = 2.0$.

(a)

(b)
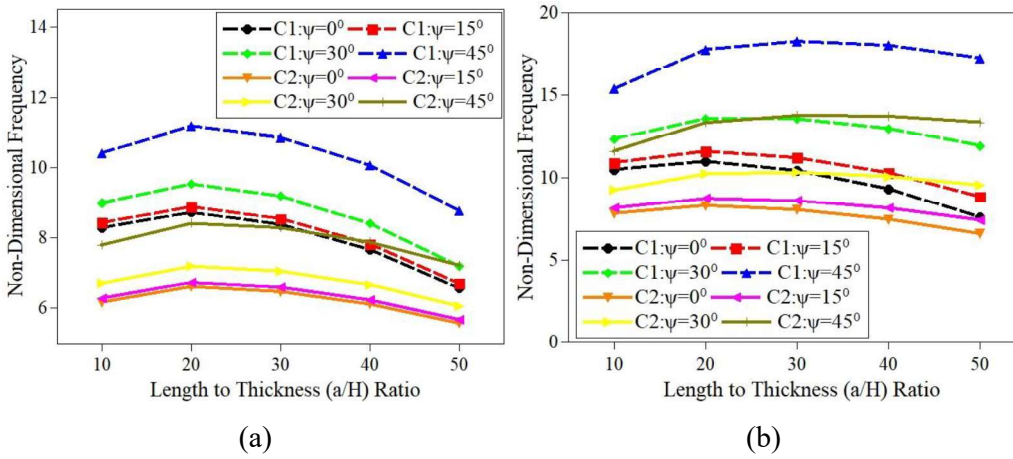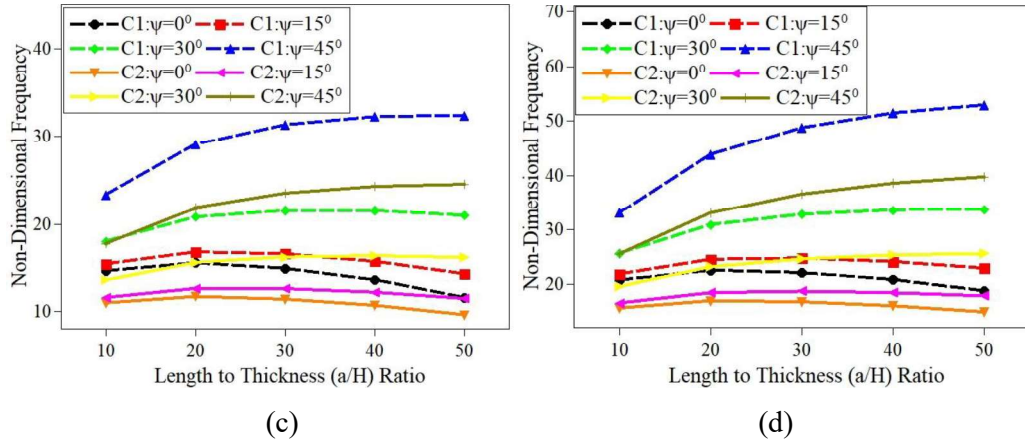
Figure 2.12: Effect of skew angle on the $\overline{\omega}$ of five-layered SS skew LHC plate with SS boundary condition in presence of temperature (325 K) for varying a/b and a/H ratios (a) $a/b = 0.5$ (b) $a/b = 1.0$ (c) $a/b = 1.5$ (d) $a/b = 2.0$.

In order to appreciate the influence of hybridization on the vibration characteristics of skew LC plates, the comparative results are extracted from the conventional composite plate and hybrid composite plates for varying temperature and moisture values. The plates considered are of zero skew angle, whereas the ratios a/b and a/H are considered as 2 and 50, respectively. material-2 and material-3 are considered for the analysis, and the results obtained are plotted in Figure 2.13. The hybrid composite plates with the graphite-epoxy lamina as middle layers exhibit higher frequencies at higher temperature and moisture concentration values. In contrast, the hybrid composite with glass fiber lamina as the central layer tends to showcase lower frequencies. From Figure 2.13, it is evident that the frequency plots of laminates cross each other with the increase in temperature and moisture, which indicates the variation in the slope of the fundamental frequency of the system with an increase in temperature and moisture. This suggests that the number of layers, stacking sequence, temperature, and moisture concentration have considerable influence on the modal behavior of hybrid composite plates and are to be chosen with at most care for particular applications.
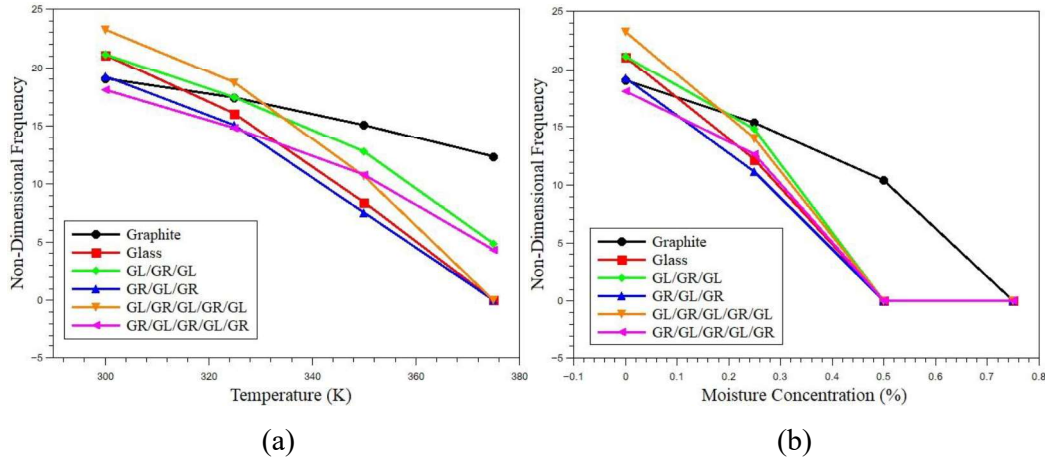
Figure 2.13: Variation in the $\overline{\omega}$ of conventional composite and hybrid composite plates for varying (a) temperature and (b) moisture profiles.

2.5.4. Skew LCS plate

The effect of temperature on free vibration characteristics of SS and CC skew LCS plates are presented in Table 2.14 for varying a/b and a/H ratios. The properties of graphite-epoxy face sheets and DYAD 606 core are considered for the analysis. The results indicate that the natural frequency reduces with an increase in temperature values. The percentage reduction of fundamental frequencies in the case of the SS plate is marginally higher than the CC plates. The maximum percentage increment of 35.53 % in natural frequency is observed for the skew angle from 0° to 45° (for $a/b =$ 2 and $a/H = 10$) for the SS plate. Further, a 22.64 % increase in natural frequency is noted for the CC plate. The natural frequency reduced up to 76.71 % and 67 % for increasing temperature values from 300 K to 375 K (for $a/b = 0.5$ and $a/H = 100$) for the SS and CC plate (for $a/b = 2$ and $a/H = 10$).

Analogously, the investigations are performed for the skew LCS plate considering graphite-epoxy face sheets and EC 2216 core with SS and CC boundary conditions. The results obtained are presented in Table 2.15. A percentage increase of 76.12 % and 24.21 % in natural frequency is observed for the skew angle from 0° to 45° (for $a/b = 2$ and $a/H = 100$) for the SS and CC plates, respectively. The maximum percentage reduction of 70.69 % is noted for increasing temperature values from 300 K to 375 K (for $a/b = 1$ and $a/H = 100$) for SS case, and for clamped plate, the reduction of 56.47 % is observed.

Table 2.14: Effect of temperature on the $\bar{\omega}$ of skew LCS plate with Dyad 606 core for varying a/b and a/H ratios.

a/b	a/H	Temperature (K)	Skew Angle (SS)			Skew Angle (CC)		
			0º	15º	30º	0º	15º	30º
0.5	10	300	4.3020	4.4226	4.7812	5.4474	5.4644	5.5649
		325	2.3147	2.3406	2.4330	2.5534	2.5748	2.6592
		350	1.7477	1.7699	1.8450	1.9264	1.9436	2.0087
		375	1.7054	1.7294	1.8052	1.8890	1.9053	1.9669
	50	300	21.5193	22.1243	23.9235	19.1207	19.3113	19.9656
		325	9.7994	9.9406	10.4091	10.5986	10.7275	11.1569
		350	7.3262	7.4356	7.7947	8.1201	8.2065	8.4971
		375	5.8881	5.9323	6.1048	7.5600	7.5582	7.6114
	100	300	43.0392	44.2494	47.8487	35.8753	36.2630	37.5810
		325	20.0887	20.3339	21.1833	20.8614	21.0909	21.8915
		350	15.1549	15.3374	15.9797	15.6426	15.8205	16.4342
		375	10.5938	10.7115	11.1445	12.7079	12.7867	13.0848
1.0	10	300	5.2130	5.3120	5.6528	6.4276	6.4894	6.7257
		325	2.7916	2.8453	3.0194	3.1369	3.1721	3.2931
		350	2.1131	2.1578	2.2912	2.3693	2.3944	2.4800
		375	2.0482	2.0977	2.2347	2.3173	2.3409	2.4214
	50	300	21.0898	21.3488	22.2307	23.4859	23.7027	24.4527
		325	12.4751	12.6105	13.0852	13.2707	13.4053	13.8563
		350	9.3303	9.4307	9.7822	10.0561	10.1523	10.4714
		375	7.0038	7.1115	7.4696	8.7084	8.7624	8.9750
	100	300	41.9201	42.3827	43.9481	44.6034	45.0224	46.4422
		325	25.4434	25.6859	26.5513	26.2357	26.4757	27.3024
		350	19.1961	19.3688	20.0061	19.6862	19.8661	20.4851
		375	13.0510	13.2171	13.8052	15.1044	15.2387	15.7008
2.0	10	300	8.5868	8.6251	9.6567	10.6458	10.8526	11.5424
		325	4.4921	4.6273	5.0275	5.0942	5.1719	5.4294
		350	3.4054	3.5052	3.7870	3.7912	3.8463	4.0302
		375	3.3096	3.4090	3.6812	3.6817	3.7342	3.9099
	50	300	43.0072	33.9276	35.9338	37.3976	37.9448	39.8110
		325	19.6977	19.9491	20.8332	21.0114	21.2806	22.1812
		350	14.6351	14.8185	15.4565	15.6647	15.8592	16.5268
		375	10.7217	11.0426	12.1065	13.5412	13.7851	14.6462
	100	300	86.0245	67.3101	70.6998	70.7178	71.6885	74.9682
		325	40.2257	40.7057	42.3923	41.5795	42.1066	43.8751
		350	30.2514	30.5880	31.7711	31.0987	31.4790	32.7508
		375	20.2094	20.5964	21.9163	23.6193	23.9603	25.1192

Table 2.15: Effect of temperature on the $\bar{\omega}$ of skew LCS plate with EC 2216 core for varying a/b and a/H ratios.

a/b	a/H	Temperature (K)	Skew Angle (SS)			Skew Angle (CC)		
			0º	15º	30º	0º	15º	30º
0.5	10	300	4.3020	4.4226	4.7812	7.7665	7.7846	7.9000
		325	4.5456	4.6555	4.9798	6.2615	6.2702	6.3525
		350	4.4860	4.6012	4.7630	5.8957	5.8992	5.9681
		375	4.4179	4.5386	4.8453	6.0555	6.0530	6.1067
	50	300	21.5193	22.1243	23.9235	28.1709	28.4626	29.4607
		325	22.7376	23.2894	18.2440	20.1950	20.3894	21.0520
		350	12.8294	13.0030	13.5753	16.4914	16.5995	17.0006
		375	10.9857	11.1250	11.5863	15.4958	15.5209	15.6904
	100	300	43.0392	44.2494	47.8487	53.3186	53.9337	55.9996
		325	45.4758	46.5796	49.8361	37.2236	37.6221	38.9699
		350	24.6428	24.9585	26.0190	28.3167	28.5933	29.5337
		375	20.4338	20.6968	21.5706	24.4787	24.6938	25.4294
1.0	10	300	7.1740	7.2982	7.7198	9.0763	9.1485	9.4267
		325	5.7104	5.8229	6.2082	7.2562	7.3198	7.5715
		350	5.2936	5.4097	5.8068	6.7955	6.8595	7.1136
		375	5.3400	5.4577	5.8639	6.9272	6.9897	7.2440
	50	300	42.9243	44.2044	33.6266	34.8440	35.1656	36.2640
		325	21.6947	21.9761	22.9318	24.5829	24.8094	25.5886
		350	15.9701	16.2222	17.0645	19.4555	19.6304	20.2344
		375	13.4862	13.7326	14.5322	17.6851	17.8086	18.2656
	100	300	85.8586	88.4152	66.8430	66.6574	67.3053	69.4769
		325	42.9391	43.4281	45.0772	46.0786	46.5108	47.9702
		350	30.9808	31.3754	32.6952	34.5357	34.8501	35.9211
		375	25.5508	25.9131	27.1043	29.4146	29.6770	30.5745
2.0	10	300	8.5868	9.4334	11.7369	14.6209	14.9129	15.9261
		325	9.0760	9.9512	10.6570	11.9724	12.2185	13.0456
		350	8.3503	8.7698	10.0728	11.3479	11.5820	12.3617
		375	8.3520	8.8013	10.1830	11.5705	11.8131	12.6217
	50	300	43.0072	47.2558	58.8203	55.3005	56.0776	58.7148
		325	45.4571	34.9186	37.1935	38.9586	39.5407	41.5342
		350	25.1173	25.7657	28.0001	30.5044	31.0050	32.7449
		375	21.0557	21.7574	24.1011	27.1173	27.5873	29.2601
	100	300	86.0245	94.5251	117.6662	105.6141	107.0357	111.8131
		325	90.9249	68.9524	72.6400	72.8602	73.8682	77.2768
		350	48.8569	49.7944	53.0157	54.3674	55.1539	57.8382
		375	40.1325	41.0582	44.1750	45.9767	46.6636	49.0261

Table 2.16: Effect of temperature on the $\bar{\omega}$ of clamped skew LCS plate with Dyad 606 core for varying t_c/t_f ratio.

t_c/t_f	a/H	Temperature (K)	0⁰	15⁰	30⁰	45⁰	60⁰
25	10	300	5.0513	5.0684	5.1583	5.4663	6.4383
		325	2.4593	2.4779	2.5500	2.7398	3.2272
		350	1.8445	1.8597	1.9188	2.0708	2.4349
		375	1.7845	1.7999	1.8611	2.0171	2.3763
	50	300	18.9555	19.1520	19.8262	21.3324	24.7788
		325	10.7406	10.8677	11.3044	12.2492	14.2291
		350	8.0758	8.1797	8.5262	9.2461	10.7047
		375	7.0312	7.0666	7.2160	7.6381	8.7969
	100	300	36.1590	36.5756	37.9774	40.9890	47.5404
		325	21.4825	21.7273	22.5728	24.4179	28.3299
		350	16.2664	16.4515	17.0945	18.4990	21.4464
		375	12.4815	12.5963	12.9913	13.8984	16.0642
50	10	300	4.8944	4.9995	4.8047	5.1110	5.9663
		325	2.3993	2.4185	2.4889	2.6613	3.1042
		350	1.8125	1.8267	1.8798	2.0155	2.3640
		375	1.7380	1.7495	1.7998	1.9431	2.3060
	50	300	24.4842	18.9093	19.6042	21.1259	24.5165
		325	10.8720	10.9961	11.4268	12.3700	14.3646
		350	8.1827	8.2814	8.6211	9.3509	10.8534
		375	6.6417	6.6996	6.9034	7.3817	8.5424
	100	300	48.9692	36.4600	37.9035	40.9709	47.5203
		325	21.6810	21.9357	22.8071	24.6856	28.6357
		350	16.5181	16.7109	17.3752	18.8118	21.8143
		375	12.3385	12.4560	12.8642	13.7963	15.9669
100	10	300	3.5563	3.6267	3.8522	4.2906	5.1165
		325	2.3218	2.3445	2.4232	2.5985	2.9996
		350	1.7743	1.7898	1.8444	1.9713	2.2850
		375	1.6884	1.6964	1.7341	1.8541	2.1990
	50	300	17.7838	18.1360	19.2647	21.4588	25.5966
		325	10.9320	11.0583	11.4934	12.4393	14.4362
		350	8.2852	8.3825	8.7189	9.4476	10.9647
		375	6.4056	6.4688	6.6852	7.1751	8.3207
	100	300	35.5677	36.2721	38.5296	42.9180	51.1942
		325	21.7391	22.0011	22.8914	24.7919	28.7594
		350	16.6375	16.8369	17.5179	18.9753	22.0060
		375	12.1487	12.2728	12.6991	13.6503	15.8028

Table 2.17: Effect of temperature on the $\bar{\omega}$ of skew LCS plate with Dyad 606 core for CC boundary conditions for varying fiber orientation.

Fiber Orientation	Temperature (K)	Skew Angle 0⁰	15⁰	30⁰	45⁰	60⁰
30⁰	300	37.6500	40.1176	43.5892	48.5901	57.5226
	325	21.6582	21.8934	22.8208	24.7719	28.7662
	350	16.5893	16.7894	17.5156	19.0132	22.0498
	375	11.9320	11.8987	12.2835	13.3096	15.6028
60⁰	300	42.1986	44.6780	47.4590	50.4854	55.5930
	325	21.6280	21.9078	22.8543	24.8087	28.7993
	350	16.5990	16.8237	17.5478	19.0309	22.0217
	375	11.6278	11.7162	12.2335	13.3698	15.8906
90⁰	300	44.9064	44.7543	44.7264	45.7568	49.5259
	325	21.6513	21.9393	22.8923	24.8675	28.9293
	350	16.6281	16.8446	17.5555	19.0131	21.9692
	375	11.5741	11.7516	12.3782	13.7746	16.8174

Further, to appreciate the effect of the ratio of core thickness to the thickness of the face sheet (t_c/t_f) on the free vibration characteristics of the skew LCS plate, the analysis is performed on the sandwich plate considering graphite-epoxy as face sheets and DYAD 606 as core material. Non-dimensional fundamental frequencies obtained for the skew sandwich plate with varying t_c/t_f ratios are presented in Table 2.16.

From the outcomes tabulated in Table 2.16, it is apparent that the fundamental frequency of the sandwich plate reduces with the increase in t_c/t_f ratio. For the increment in skew angle from 0⁰ to 60⁰, the natural frequency increases up to 44 % (for t_c/t_f = 100 and a/H = 100). Further, for the rise of temperature values from 300 K to 375 K, the frequency reduces up to 74.80 % (for t_c/t_f = 50 and a/H = 100).

Investigations are further carried out to understand the effect of fiber orientation of composite face sheets on vibrational characteristics of skew sandwich plates. The clamped skew LCS plate with Dyad 606 core and graphite face sheets are considered for the analysis with t_c/t_f, a/b, and a/H ratios as 100, 0.5, and 100, respectively. The results obtained from the simulation are presented in Table 2.17. It may be noted that in the ambient temperature, the magnitude of the fundamental frequency of the sandwich plate increases with an increase in fiber orientation.

Table 2.18: Effect of temperature and moisture on the $\overline{\omega}$ of skew LCS plate with CC boundary conditions for varying a/b and a/H ratios.

a/H	Skew Angle	Temperature (K)				Moisture Concentration (%)			
		300	325	350	375	0.00	0.25	0.50	0.75
	0°	5.4474	5.4434	5.4394	5.4355	5.4474	5.4395	5.4316	5.4236
	15°	5.4644	5.4600	5.4556	5.4512	5.4644	5.4559	5.4474	5.4389
10	30°	5.5649	5.5592	5.5536	5.5479	5.5649	5.5546	5.5442	5.5339
	45°	5.9348	5.9270	5.9192	5.9114	5.9348	5.9214	5.9080	5.8946
	60°	7.0850	7.0742	7.0633	7.0525	7.0850	7.0672	7.0494	7.0315
	0°	9.2693	9.2606	9.2519	9.2431	9.2693	9.2519	9.2345	9.2171
	15°	9.3085	9.2990	9.2895	9.2801	9.3085	9.2901	9.2717	9.2533
20	30°	9.4904	9.4787	9.4670	9.4553	9.4904	9.4690	9.4475	9.4260
	45°	10.0567	10.0411	10.0254	10.0098	10.0567	10.0297	10.0028	9.9758
	60°	11.7532	11.7305	11.7078	11.6851	11.7532	11.7159	11.6786	11.6412
	0°	19.1207	19.1019	19.0832	19.0645	19.1207	19.0838	19.0471	19.0104
	15°	19.3113	19.2912	19.2712	19.2511	19.3113	19.2726	19.2340	19.1954
50	30°	19.9656	19.9413	19.9169	19.8926	19.9656	19.9209	19.8763	19.8318
	45°	21.4492	21.4168	21.3845	21.3522	21.4492	21.3931	21.3372	21.2815
	60°	24.9547	24.9087	24.8629	24.8171	24.9547	24.8790	24.8035	24.7283
	0°	35.8753	35.8404	35.8054	35.7705	35.8753	35.8066	35.7381	35.6696
	15°	36.2630	36.2253	36.1875	36.1498	36.2630	36.1904	36.1179	36.0455
100	30°	37.5810	37.5345	37.4880	37.4415	37.5810	37.4960	37.4111	37.3265
	45°	40.4746	40.4122	40.3498	40.2875	40.4746	40.3669	40.2594	40.1523
	60°	46.9691	46.8804	46.7920	46.7037	46.9691	46.8233	46.6781	46.5335

59

However, in the case of elevated temperatures and smaller skew angles, the magnitude of the sandwich plate's frequency reduces with an increase in fiber orientation. As the skew angle increases from 0° to 60°, the natural frequency increases up to 52.75 % for 30° fiber angle. Additionally, the reduction in natural frequency up to 74.23 % is noted for increasing temperature values from 300 K to 375 K (for 375 K and 90° fiber orientation).

Furthermore, the effect of temperature and moisture on a skew sandwich plate is investigated by considering the graphite-epoxy face sheet and Dyad 606 flexible core. The material properties considered are assumed to be independent of temperature and moisture. The ratios t_c/t_f and a/b are considered as 10 and 0.5, respectively. The results obtained for varying skew angles, a/H ratios, temperature, and moisture profiles are listed in Table 2.18. The increase in skew angle and a/H ratio cause the upsurge of frequency values, whereas the natural frequency reduces with an increase in temperature and moisture values. The natural frequency reduces up to 0.58 % and 0.95 % for the increment in temperature from 300 K to 375 K and moisture values from 0.00 % to 0.75 %.

2.6 CONCLUSION

This chapter investigates the effect of variation of temperature and moisture concentration on the free vibration characteristics of laminated composite, hybrid composite, and sandwich plates using the FE method. An eight-node isoparametric element with nine degrees of freedom per node is considered in the FE formulation. The results suggest that the change in material properties due to variations in temperature and moisture should be considered to obtain an accurate response of the system. The effect of geometrical parameters such as boundary conditions, stacking sequences, a/b, and a/H ratios on the free vibration characteristics have been studied. The results reveal that the plates with all sides clamped have a higher magnitude of non-dimensional fundamental frequencies in comparison with the simply supported plates. Whereas, in the presence of elevated temperature and moisture concentration values, the simply supported plates are found to have more variations in the fundamental frequencies in comparison with the clamped plates.

Further, the non-dimensional frequency of the LC, LHC, and LCS plate increases with an increase in skew angle, *a*/*b,* and *a*/*H* ratios. The reduction in natural frequency under the temperature and moisture is significant for smaller values of skew angles. Hence, the plates with higher skew angles are more resistant to temperature and moisture environments. In the case of hybrid composite plates, the stacking sequence and number of layers exhibit a significant effect on the vibration response of the system. Moreover, for the LCS sandwich plate, the ratio of core thickness to the thickness of the face sheet significantly dictates the vibrational behavior of the system. The fundamental frequency of the plate considerably reduces with an increase in t_c/t_f ratio. Further, with the increase in fiber orientation of the face sheet of sandwich plates, the natural frequency of the system noticeably reduces.

Chapter 3

NEURAL NETWORK-BASED VIBRATION STUDY OF LAMINATED COMPOSITE SANDWICH PLATES OPERATING IN THERMAL AND MOISTURE ENVIRONMENTS

In this chapter, a predictive model is developed to investigate the influence of temperature and moisture on the vibration response of a skew laminated composite sandwich (SLCS) plate using the artificial neural network technique. The FE model developed in the previous chapter is used to extract about 11,520 natural frequency data points of the laminated composite sandwich (LCS) plate operating in the elevated thermal and moisture environment. The Levenberg-Marquardt-algorithm is used to train the neural network. The temperature-dependent material properties of the graphite-epoxy composite face sheets and DYAD 606 viscoelastic core are used for the analysis. The competency of the developed model is verified by performing various simulations to understand the influence of process parameters on the natural frequency of the system. Further, the results obtained from the predictive model are compared with the results of the developed numerical model.

3.1 INTRODUCTION

Polymer composite materials have gained substantial importance in high-end structural engineering streams such as aerospace, automobile, biomedical, construction, naval industries, etc. These structures are often subjected to transverse or bending loads in real-time applications imparting maximum stresses at the surface of the structure, whereas the center of the structure experiences minimum stresses. The lightweight sandwich structures are highly suited for such applications (Khare *et al*., 2005). The constituent materials of the sandwich structures are expected to operate in challenging working atmospheres such as high operating temperature, presence of moisture, electric and magnetic fields to get inducted into prominent fields of structural engineering components.

Constantly changing environmental conditions may cause untimely damage to the structures. In order to avoid this, systematic health monitoring mechanisms are to be devised. Hence, the systematic and periodic health monitoring of the structures is one of the prominent requirements in high-end engineering applications. The timely detection of damages in the structural components requires systematic scientific study. In order to identify the root cause of the defect, proper engineering analysis of the damage is essential. Based on the analysis data, a suitable corrective action and/or mechanism can be devised to avoid future occurrences of the defect. The vibration-based structural health monitoring (SHM) techniques are slowly finding their way in the aerospace, civil, and mechanical engineering domains.

3.2. PROBLEM DESCRIPTION

In order to appreciate the influence of thermal and moisture environment on the free vibration behavior of SLCS plate (as shown in Figure 2.1), the simulations are performed considering graphite-epoxy composite face sheets and DYAD 606 viscoelastic core. The moisture-dependent and temperature-dependent material properties of graphite-epoxy and DYAD 606 core materials are considered for the investigation. The temperature-dependent and moisture-dependent material properties of the graphite-epoxy composite materials with the step size of 25 K and 0.25 %, respectively, are presented by Ram and Sinha (1992). Hence, the interpolation models are developed to obtain the modulus values for smaller intervals of temperature and moisture using the curve fitting technique, as follows:

Moisture dependent material properties:

$$E_1[GPa] = 130$$
$$E_2[GPa] = \left(\left(3.588 \times 10^{-15} \times M^2 \right) + M \right) + 9.5 \qquad (3.1)$$
$$G_{12}[GPa] = 6$$

Temperature-dependent material properties

$$E_1[GPa] = 130$$
$$E_2[GPa] = \left(5.3333 \times 10^{-8} \times \Delta T^4 \right) - \left(1.3333 \times 10^{-5} \times \Delta T^3 \right) + \left(0.001167 \times \Delta T^2 \right) - \left(0.06167 \times \Delta T \right) + 9.5 \quad (3.2)$$
$$G_{12}[GPa] = 2.168 \times e^{-\left(\frac{\Delta T - 23.24}{33.34} \right)^2} + 4.844 \times e^{-\left(\frac{\Delta T + 84.4}{105.2} \right)^2} + 3.007 \times e^{-\left(\frac{\Delta T + 16.19}{27.43} \right)^2}$$

3.2.1. Artificial neural network

The artificial neural network (ANN) is an information processing computational model made of an interconnected group of artificial neurons (Behera *et al.*, 2016). The ANN is capable of learning and processing like a typical human brain hence the name. These are often used for data fitting and pattern recognition. The trained ANN can then be used to predict or estimate the new independent data set. The ANN consists of three main parts, namely; the input layer, hidden layer, and output layer. All three layers are interconnected through the synapse to transfer the signals or information among each other. Each connection has its weights which change in line with the learning procedure until the expected outcomes are achieved. The hidden layer is composed of a summation unit and an activation block. The summation unit adds the product of input and its weight to the biases. The bias provides flexibility to the activation function to efficiently map the input and outputs. The activation function introduces the nonlinear properties to the network, which enables the network to generate the relationship for complex nonlinear models. The sigmoidal mathematical function and hyperbolic tangent mathematical functions are commonly used activation functions to solve engineering problems. The training process is repeated to adjust the weights till the expected results are obtained (Cascardi *et al.*, 2017).

In the present study, 11,520 non-dimensional natural frequency data points are collected from the numerical model developed in chapter 2. The MATLAB simulation tool is used to incorporate the feed-forward backpropagation network. A sigmoid transfer function is used for the input and hidden layer, while the linear transfer function is used for the output layer. The parameters considered to generate the data set are listed in Table 3.1, and the architecture employed is schematically represented in Figure 3.1.

The data was divided into 70 % for training, 15 % for validation, and 15 % for testing. The Levenberg-Marquardt algorithm was used to train the network. A trial-and-error method was used to find the optimum number of neurons to model the network architecture with eight inputs and one output. From Figure 3.2, it is evident that the ANN architecture with a single layer with eight neurons is an optimal option

as it has the minimum mean square error (MSE) and maximum correction coefficient (R) value, i.e., 1.2667 and 0.9929, respectively.

Table 3.1: Parameters considered for the simulations.

Parameters	Range
Temperature	300 K, 325 K, 350 K, 375 K, 400 K
Moisture	0 % 0.25 %, 0.5 %, 0.75 %, 1 %
Boundary conditions	SS, CC
Length to breadth (a/b) ratio	0.5, 1, 2
Length to thickness (a/H) ratio	10, 20, 50
The ratio of core thickness to the thick of face sheets (t_c/t_f)	2, 5, 10, 50
Fiber orientation of composite face sheets	0°, 30°, 45°, 60°
Skew angle	0°, 15°, 30°, 45°
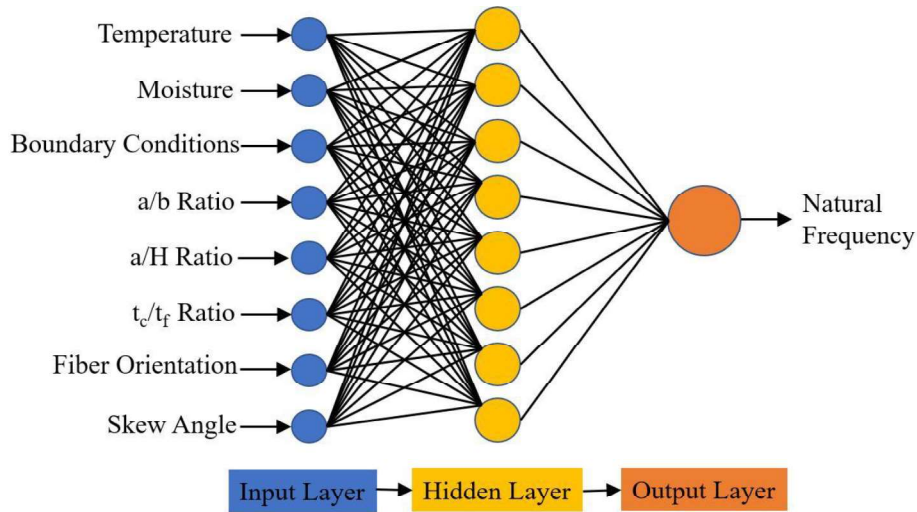
Figure 3.1: The architecture of the proposed ANN prediction model.

The developed ANN architecture was trained using a data set obtained from the numerical method. The results presented in Figure 3.3 indicate that the proposed ANN model gives a good estimate of the numerical model results. The training, validation, and testing show coefficient correlation values as 0.9929, 0.9931, and 0.9929, respectively. The overall coefficient relation value of 0.9929 was observed. The global training results (performance) and the histogram of error of the proposed architecture are presented in Figure 3.4. To comprehensively evaluate the developed ANN model, the ANN results and the numerical results are plotted in Figure 3.5. The results reveal that the ANN model predicted values are of good accuracy. The

developed ANN model is then can be used to predict the influence of thermal and moisture environments on the vibration response of LCS plates.
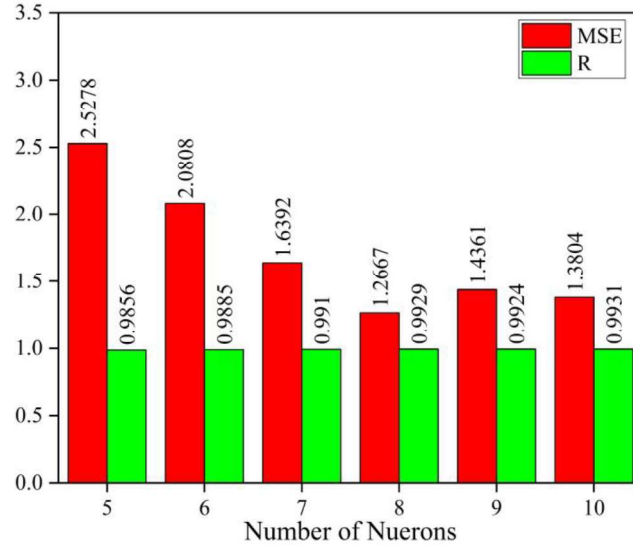
Figure 3.2: Comparison of MSE and R values for optimal selection of the number of neurons.

The weight and bias values of the developed ANN model are as follows,

$$w_1 = \begin{bmatrix} 3.7524 & 0.4466 & 5.0637 & 1.7067 & -0.3174 & -2.2000 & 0.0471 & -0.0981 \\ 2.0649 & -0.1999 & 2.7643 & -0.2413 & -1.7082 & -0.0936 & -0.0751 & -0.0703 \\ 3.6450 & 0.4307 & 4.9177 & 1.6818 & -0.3057 & -4.0082 & 0.0472 & -0.0959 \\ -3.4439 & -0.0825 & -4.6190 & 0.2096 & 0.4477 & -0.9254 & 0.0578 & 0.0729 \\ 0.4032 & 0.0318 & 0.5317 & 0.3477 & 0.1834 & -0.3018 & 0.2158 & 0.1567 \\ 1.6700 & -0.1419 & 2.2369 & -0.1925 & -0.7835 & -0.1024 & -0.0429 & -0.0466 \\ -0.8854 & 0.0038 & -1.2460 & 0.2094 & 0.1925 & -0.5381 & 0.6624 & 0.3592 \\ -3.3518 & -0.1604 & -4.5060 & 0.1849 & 0.6400 & -1.7129 & 0.0502 & 0.0615 \end{bmatrix} \tag{3.3}$$

$$b_1 = \begin{bmatrix} 4.8158 & 2.8938 & 6.6011 & -3.3592 & -2.2787 & 2.2545 & -0.7854 & -4.1450 \end{bmatrix}^T \tag{3.4}$$

$$w_2 = \begin{bmatrix} -6.4103 & 3.2353 & 6.5786 & 4.1011 & 2.8221 & -8.2553 & -0.0988 & -2.1999 \end{bmatrix} \tag{3.5}$$

$$b_2 = 8.4861 \tag{3.6}$$

where, w_1 and b_1 are the weight and bias of the hidden layer, and w_2 and b_2 are the weight and bias of the output layer.

3.3. RESULTS AND DISCUSSIONS

The influence of temperature on the frequency response of an SLCS plate is investigated considering all sides simply supported (SS) and clamped (CC) boundary

conditions. The length to thickness (a/H) ratio of 50, length to breadth (a/b) ratio of 2, and the t_c/t_f ratio of 2 is considered for the analysis. The non-dimensional frequency values for varying temperature and skew angle are presented in Figure 3.6. For both SS and CC boundary conditions, the natural frequency follows the decreasing trend with increasing temperature values. It can also be noted that the frequency value increases with an increase in skew angle for all the temperature values considered. From Figure 3.6, it is also evident that the results predicted by the ANN model are of good accuracy and show a similar trend to the results obtained from the numerical model.
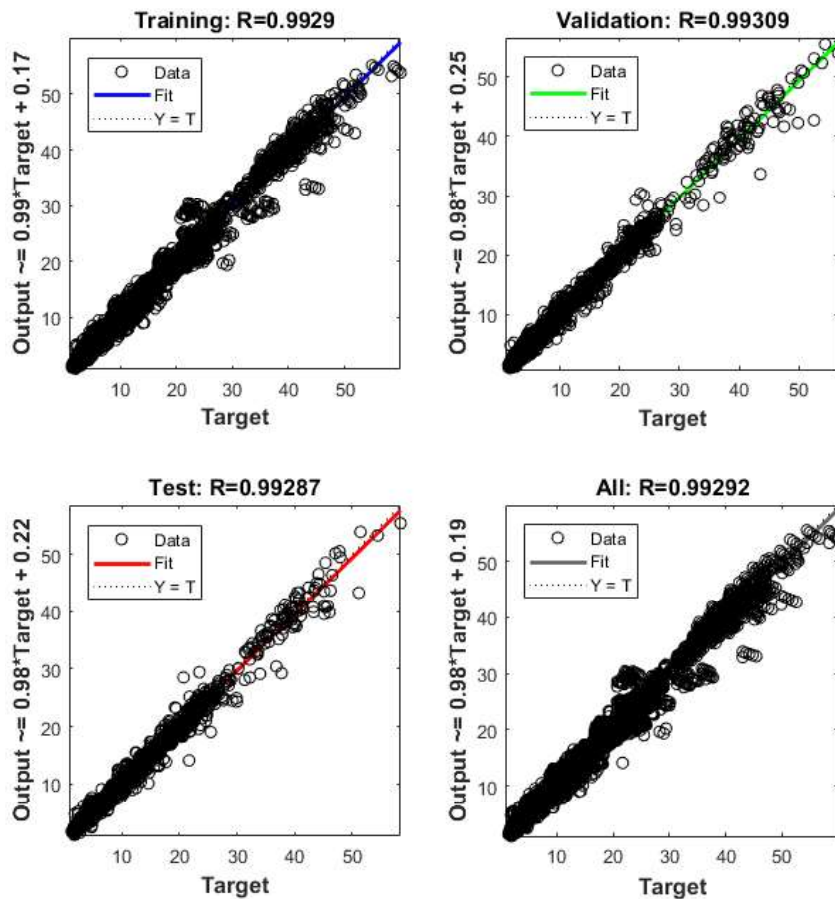
Figure 3.3: Regression results of training, validation, and test results of neural network.

Simulations are also carried out to understand the effect of moisture on the natural frequency of the LCS plates operating under SS and CC boundary constraints. The ANN prediction results and the numerical simulation results are presented in

Figure 3.7. The results show that the frequency of the structure reduces with an upsurge in moisture concentration values for both the boundary conditions considered. For all the moisture concentration values considered, the natural frequency values witnessed an increasing trend with the increase in the skew angle. It can also be observed that the results predicted by the ANN model are of decent accuracy. From Figures 3.6 and 3.7, it is evident that the variation in natural frequency predicted by the ANN model is in line with the trend followed by the numerical model in the presence of thermal and moisture environments.
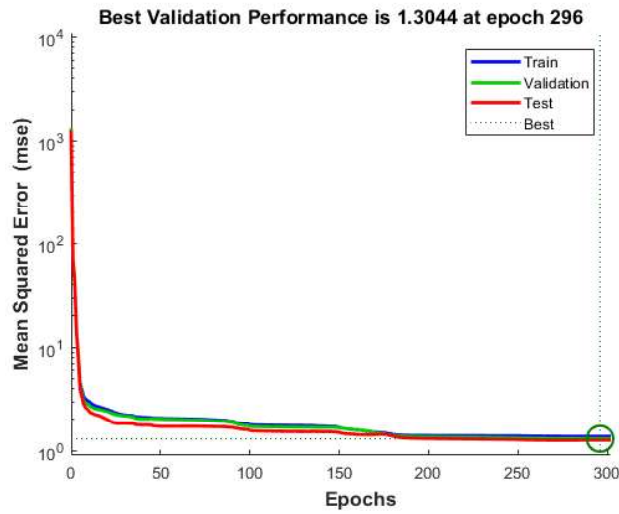
(a)
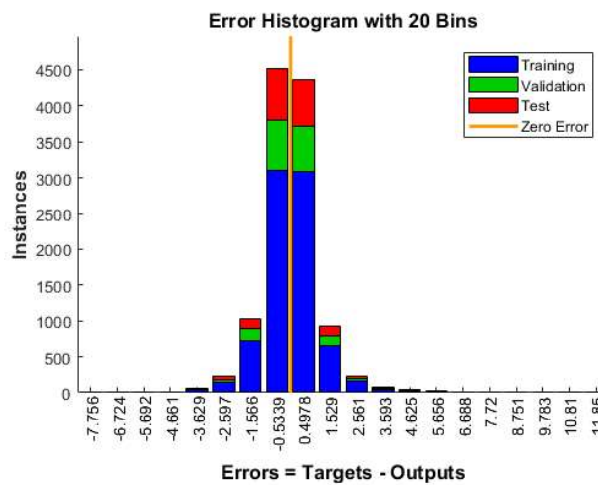
(b)

Figure 3.4: Schematic representation of (a) ANN training performance (b) histograms of error values of the developed predictive model.

69
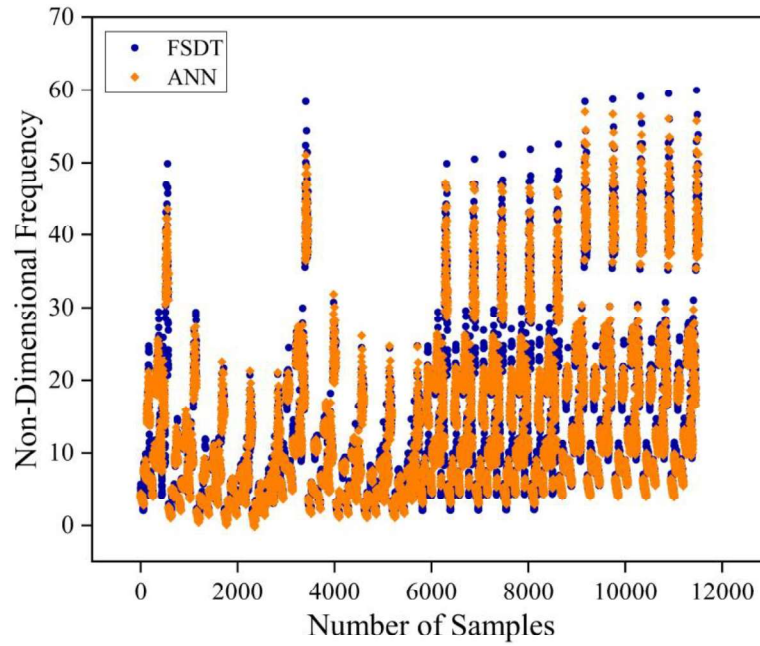
Figure 3.5: Scatter plot to compare the target results and the ANN predicted fundamental natural frequency values.

| (a) | (b) |
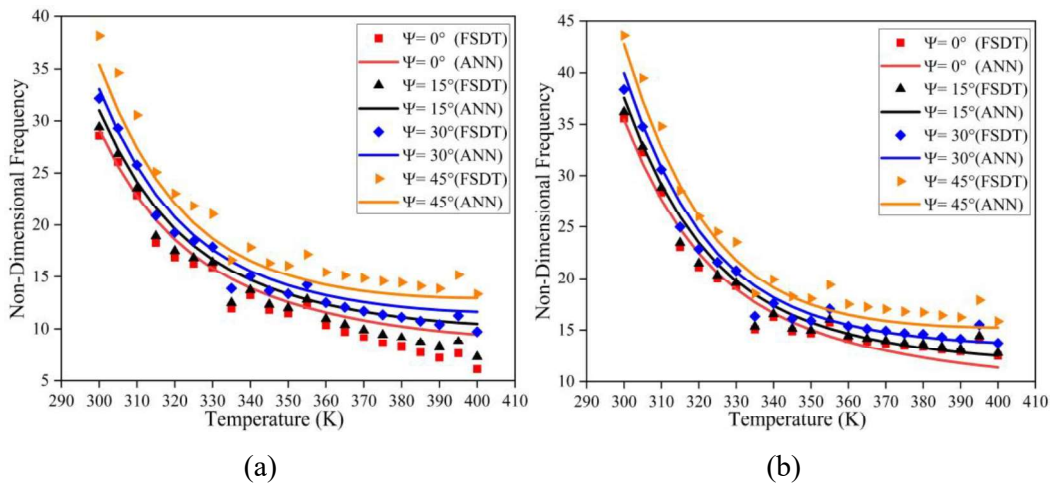
Figure 3.6: Influence of thermal environment on the fundamental frequency of SLCS plate under (a) SS and (b) CC boundary conditions.

The material properties of composite materials generally degrade when exposed to elevated temperature and moisture environments. This, in turn, reduces the stiffness of the composite structure, i.e., with an increase in temperature and moisture, the stiffness of the composite structure reduces. Hence, the natural frequency of the structure reduces with an increase in temperature and moisture concentration values (Chandra et al., 2019: Rath and Sahu, 2012: Ram and Sinha 1992).
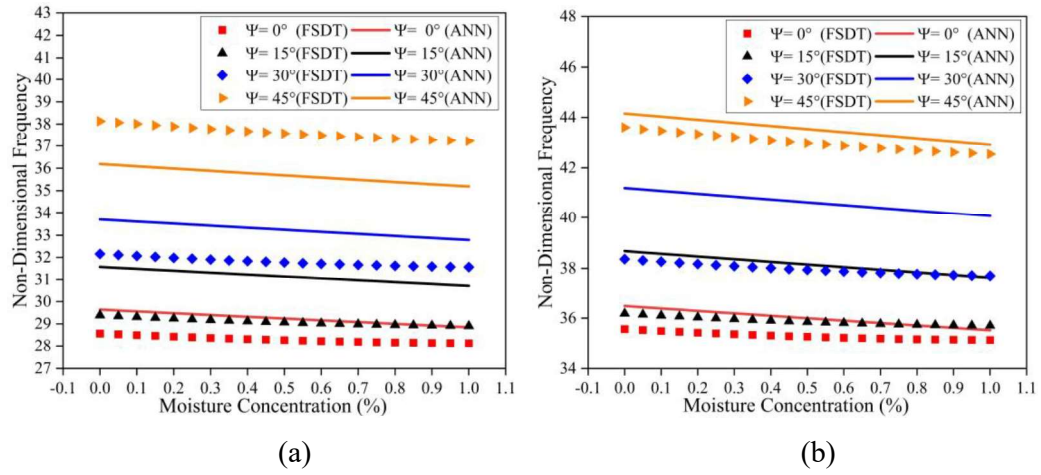
Figure 3.7: Influence of moisture environment on the fundamental frequency of SLCS plate under (a) SS and (b) CC boundary conditions.

Figure 3.8 illustrates the effect of skew angle, a/b ratio, and a/H ratio on the modal behavior of the SLCS plate (with $t_c/t_f = 2$) in the elevated thermal environment (325 K) with SS boundary condition. Results indicate the upsurge in the frequency value with the increase in a/b and a/H ratios. As the a/H ratio varies from 10 to 50, the plate transforms from thick plate to thin plate condition. As the a/b and a/H ratio increases, the ratio of the magnitude of the stiffness matrix to the mass matrix tends to increase continuously. Many researchers have reported similar observations for various composite structures (Garg et al., 2019: Rath and Sahu, 2012: Sit and Ray, 2019). The same trend in variation of natural frequency values for clamped boundary conditions can be observed, as presented in Figure 3.9.

Simulations are performed to understand the effect of skew angle and the aspect (a/b and a/H) ratios on the fundamental frequency of the SLCS plate in the presence of moisture (0.25 %) for both SS and CC boundary conditions. From the results presented in Figures 3.10 and 3.11, it can be observed that the non-dimensional frequency of the system increases with an increase in a/b ratio, a/H ratio, and skew angle in the presence of a moisture environment. From Figures 3.8-3.11, it is apparent that the results predicted by the ANN model to understand the effect of geometrical parameters of the LCS plate such as a/b ratio, a/H ratio, and skew angle operating in the hygrothermal environment are of good accuracy and are in line with the numerical results.

Further investigations are performed to comprehend the influence of t_c/t_f ratio on the modal behavior of SLCS plates operating in elevated thermal and moisture environments. The a/H ratio and skew angles were considered as 10 and 45º, respectively, for the analysis.

(a)

(b)

(c)
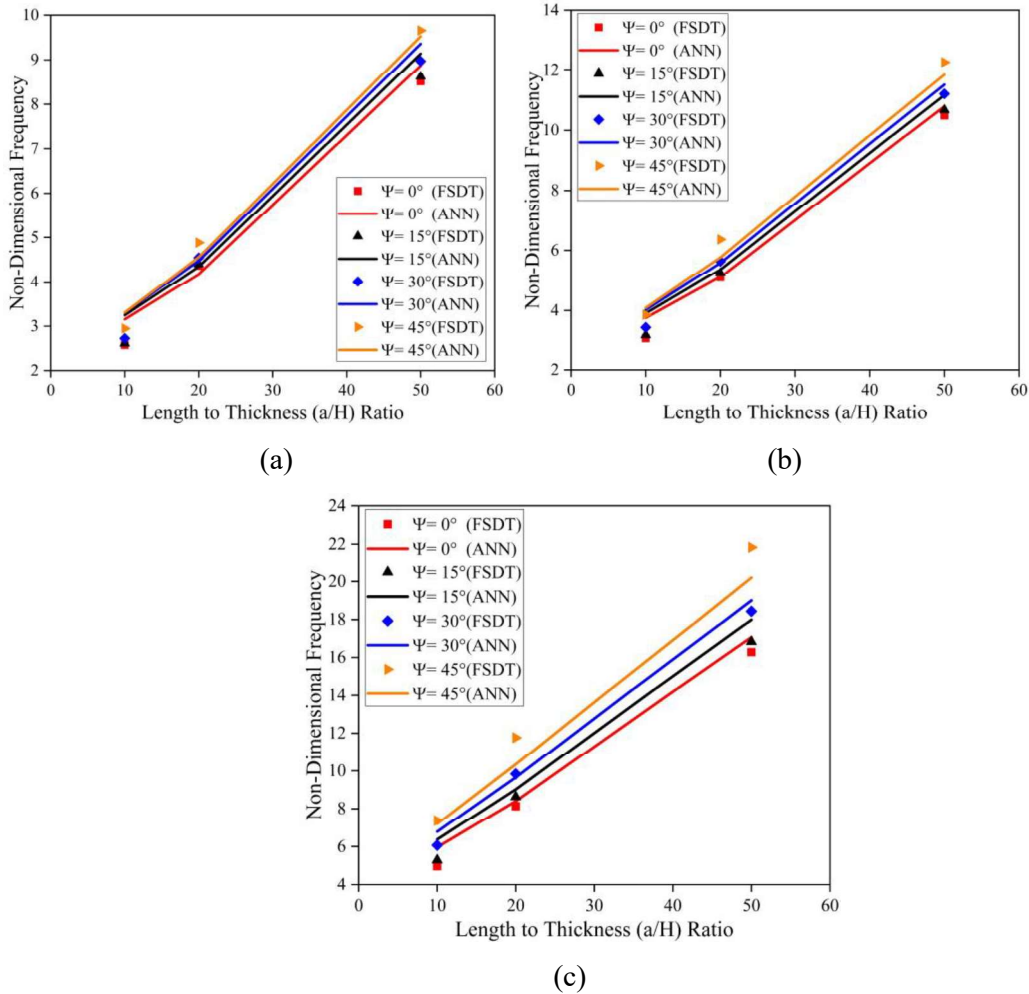
Figure 3.8: Influence of skew angle on SLCS plate operating at elevated thermal environment (325 K) with SS boundary condition for varying a/b and a/H ratios (a) $a/b = 0.5$ (b) $a/b = 1.0$ (c) $a/b = 2.0$.

The non-dimensional fundamental frequency values obtained for clamped sandwich plate operating at 400 K for various a/b ratios and t_c/t_f ratios are presented in Figure 3.12a. The results show that the natural frequency considerably reduces with an increase in t_c/t_f ratio at an elevated thermal environment. Similar observations were reported by many researchers at ambient and elevated thermal environments (Yuan and Dawe, 2002: Dat *et al*., 2020). The clamped LCS plates are also investigated in

moisture environments to understand the impact of t_c/t_f ratio on the natural frequency of the system. The results obtained for the LCS plate operating in a 1 % moisture concentration environment are plotted in Figure 3.12b. The frequency of the system reduced continuously with an increase in moisture concentration value. It can also be observed that the influence of t_c/t_f ratio is more prominent for higher values of a/b ratios for both thermal and moisture cases.

(a)   (b)

(c)
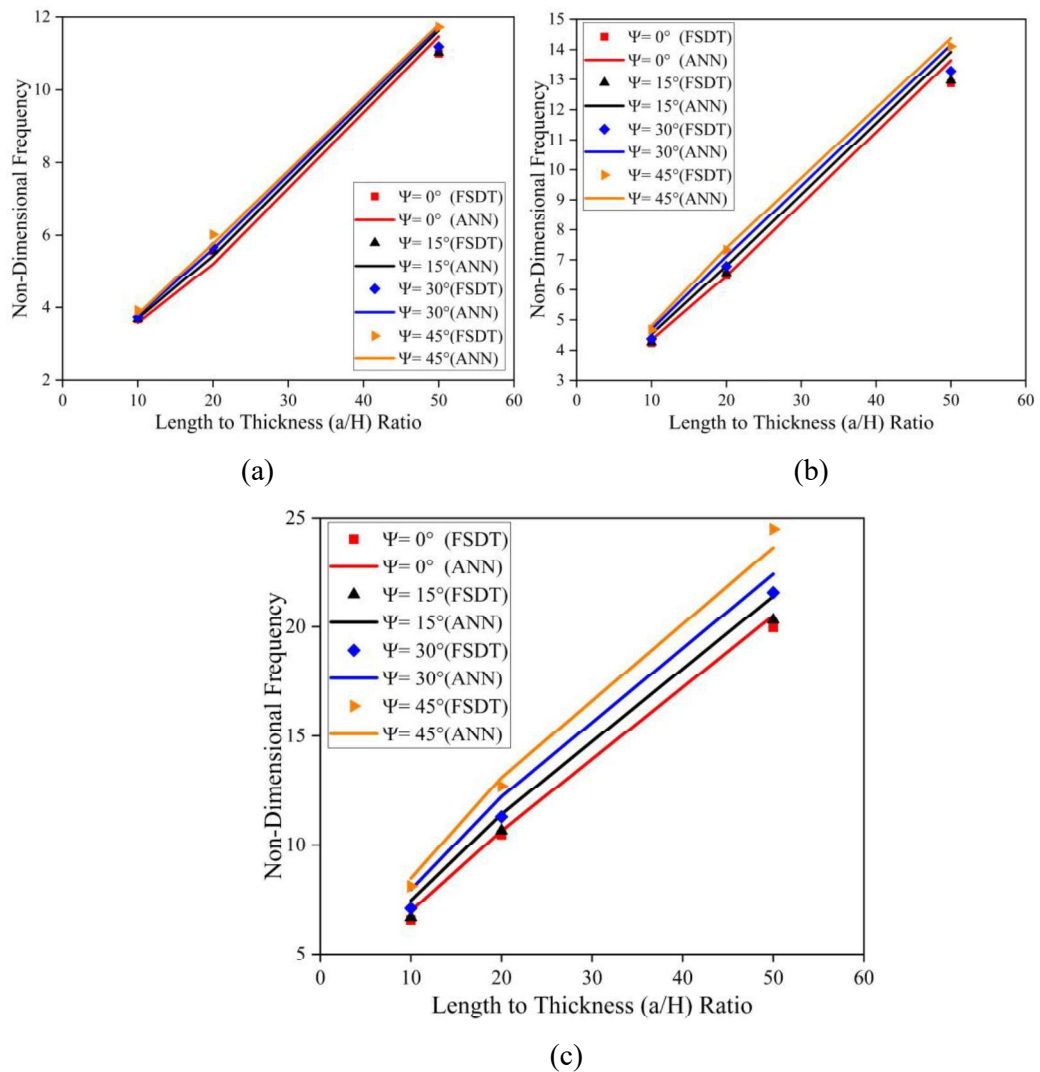
Figure 3.9: Influence of skew angle on the SLCS plate operating at elevated thermal environment (325 K) with CC boundary condition for varying a/b and a/H ratios (a) $a/b = 0.5$ (b) $a/b = 1.0$ (c) $a/b = 2$.

The investigation is further extended to understand the effect of fiber orientation of the face sheet of an LCS plate on the modal behavior of the system

operating in an elevated thermal and moisture environment. The a/b ratio, t_c/t_f ratio, and skew angles were considered as 0.5, 2, and 0⁰, respectively, for the analysis. The results obtained for sandwich plates operating at 375 K temperature for various a/H ratios are presented in Figure 3.13. It can be noted from the results that for both SS and CC conditions, the non-dimensional fundamental frequency considerably reduces with the increase in fiber orientation angle. In contrast, the frequency increases with an increase in the a/H ratio.

(a)

(b)

(c)
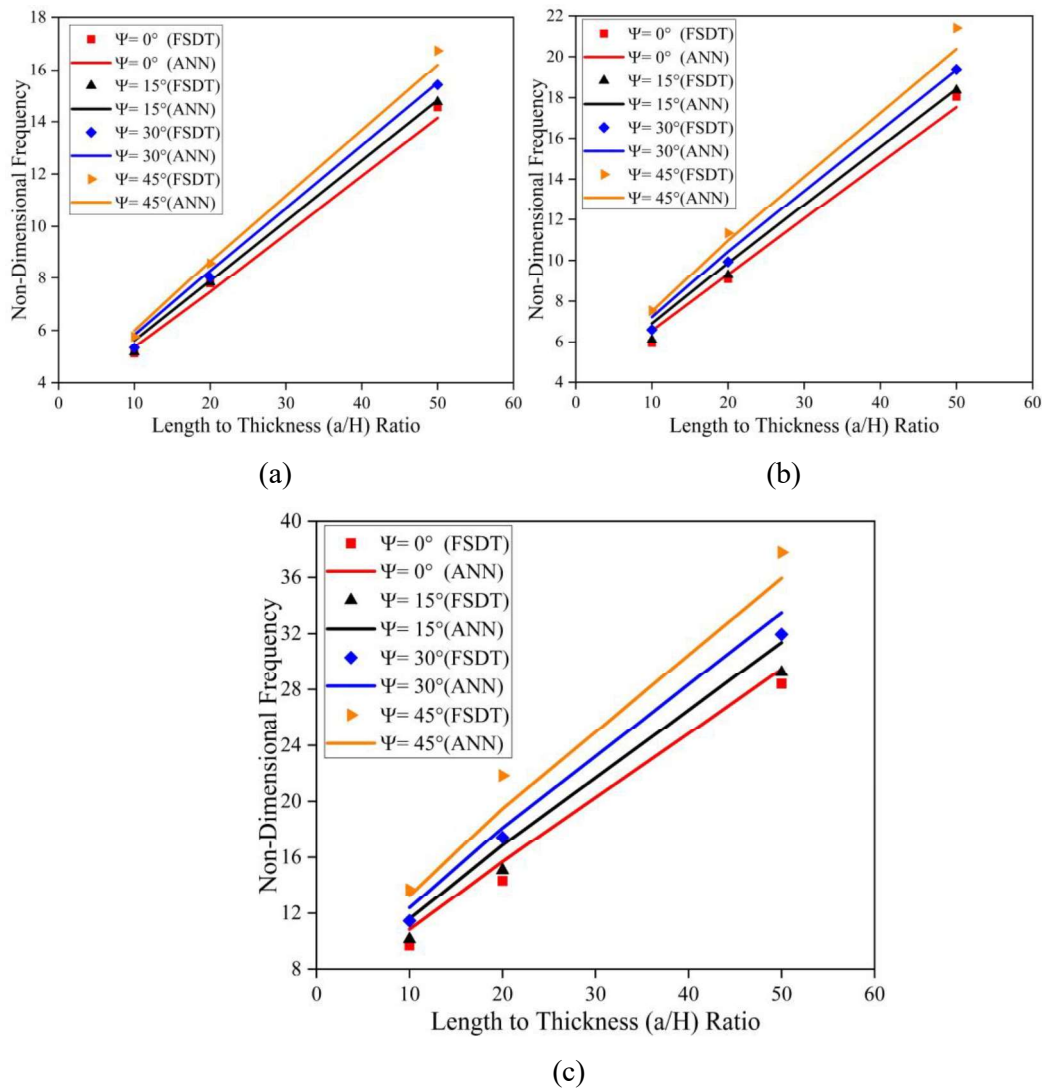
Figure 3.10: Influence of skew angle on SLCS plate in presence of moisture (0.25 %) with SS boundary condition for varying a/b and a/H ratios (a) $a/b = 0.5$ (b) $a/b = 1.0$ (c) $a/b = 2.0$.

(a)   (b)

(c)
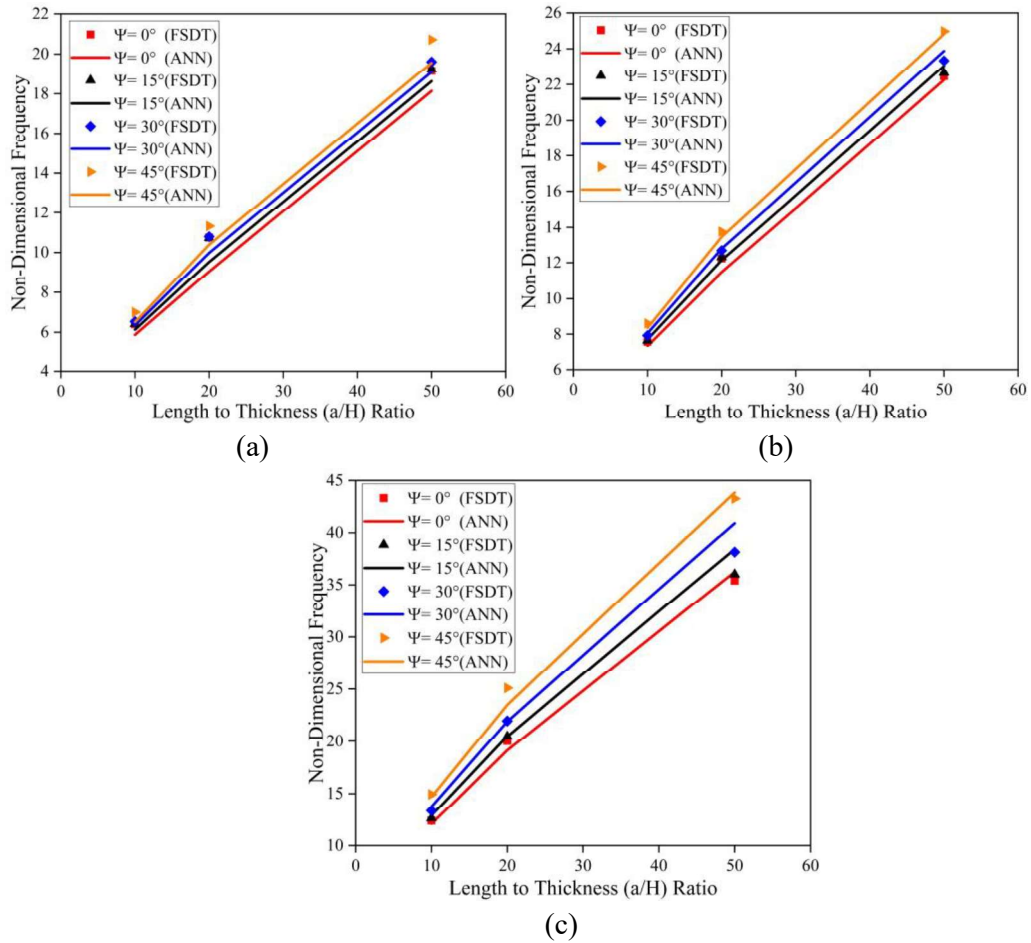
Figure 3.11: Influence of skew angle on SLCS plate in presence of moisture (0.25 %) with CC boundary condition for varying a/b and a/H ratios (a) $a/b = 0.5$ (b) $a/b = 1.0$ (c) $a/b = 2.0$.

(a)   (b)
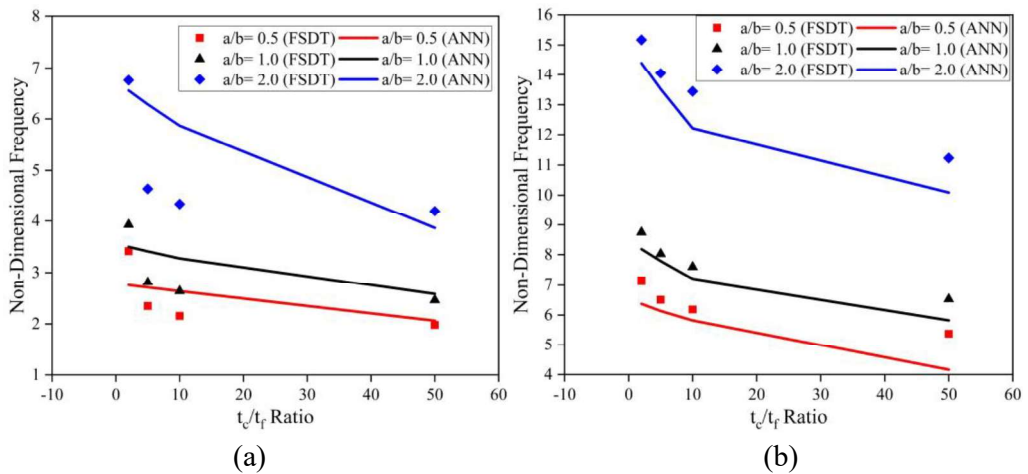
Figure 3.12: Influence of t_c/t_f ratio on a SLCS plate with CC boundary condition in the presence of (a) temperature (400 K) and (b) moisture (1.0 %) for varying a/b ratios.

The investigations are also performed to understand the effect of fiber orientation on the vibration characteristics of SLCS plates operating in a moisture (0.75 %) environment. The results plotted in Figure 3.14 reveal that the fundamental frequency reduces with an increase in fiber orientation angle from 0° to 60°. Additionally, it is also noted that the results predicted by the ANN model follow the same trend as that of the results obtained from the numerical model with decent accuracy.

(a)   (b)
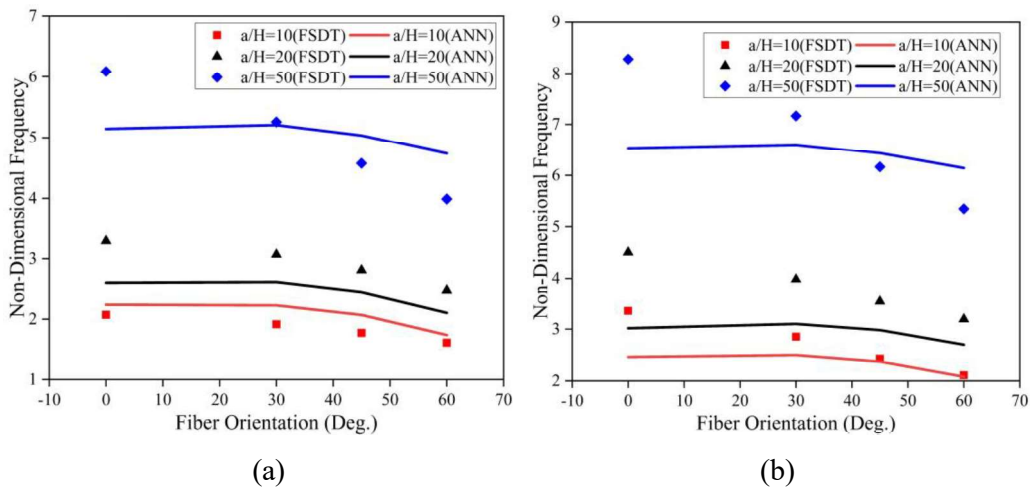
Figure 3.13: Influence of face sheet fiber orientation angle on the SLCS plate in the presence of elevated thermal environment (375 K) for varying a/H ratios operating under (a) SS and (b) CC boundary conditions.

(a)   (b)
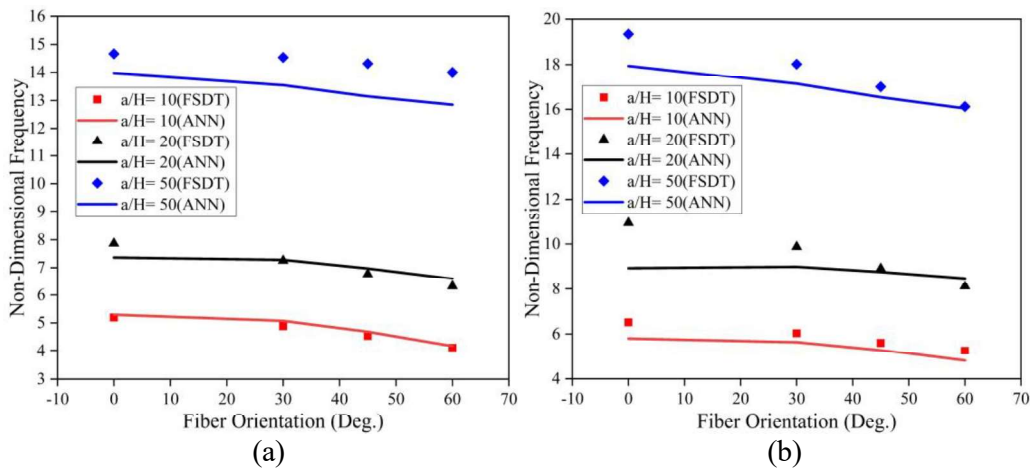
Figure 3.14: Influence of face sheet fiber orientation angle on an SLCS plate in the presence of moisture environment (0.75 %) for varying a/H ratios operating under (a) SS and (b) CC boundary conditions.

3.4. CONCLUSIONS

In this chapter, a methodology was suggested to appreciate the effect of thermal and moisture environments on the vibration characteristics of SLCS plates using numerical (FE) and predictive ANN models. The results obtained from the established FE model are used to train and develop an efficient ANN predictive model to estimate the fundamental frequencies of LCS plates operating in elevated thermal and moisture environments. The ANN predicted results are found to be of good accuracy. The effective utilization of the current model may significantly improve the SHM techniques of the engineering structures as this helps in the early detection of damage and suggestion of subsequent corrective measures. The effect of geometrical parameters such as boundary conditions, stacking sequences, skew angle, a/b, and a/H ratios on the free vibration characteristics have been studied. From simulation results, it is noted that the simply supported plates are more susceptible to changing thermal and moisture environments. Further, the non-dimensional frequency increases with an increase in aspect ratios and skew angles of the sandwich plate. Results indicate that the plates with lesser skew angles are the least resilient to hygrothermal environments. The natural frequency of the LCS plate noticeably reduces with an increase in fiber orientation of the face sheet and t_c/t_f ratio.

Chapter 4

FREE VIBRATION STUDY OF DOUBLY-CURVED SANDWICH SHELLS OPERATING IN THERMAL AND MOISTURE CONDITIONS

This chapter presents the influence of temperature and moisture on the free vibration characteristics of doubly-curved skew laminated composite sandwich (SLCS) panels. The coupled hygro-elastic and thermo-elastic relations for a laminated composite sandwich (LCS) shells/panels are formulated using first-order shear deformation theory. The non-mechanical stiffness matrices are represented by the initial stress stiffness matrix developed using nonlinear strain-displacement relations. The temperature-dependent and moisture-dependent material properties are considered to analyze the LCS cylindrical, ellipsoid, hyperbolic, spherical shells, and flat plates. The face sheets of the panels are considered to be made of graphite-epoxy composite, and the core is of carbon nanotube-reinforced composite (CNTRC) material. Several numerical examples are comprehensively studied to establish the influence of temperature, moisture, the volume fraction of carbon nanotubes in the core material, functional gradation types, skew angle, length to width ratio, length to thickness ratio, radius to length ratio, the core thickness to face sheet thickness ratios, and edge constraints on the vibration responses of SLCS shells.

4.1 INTRODUCTION

In modern engineering applications, the structures made of metals and ceramics are gradually being replaced by the LCS structures due to their superior mechanical, thermal, and vibroacoustic properties. The sandwich structures of different shapes (i.e., not necessarily flat) are being used in prominent engineering fields. The contemporary engineering materials are expected to work in hazardous environmental conditions such as high temperature, moisture, chemical, electric and magnetic fields. Hence, it is very much essential to critically analyze the behavior of the structures operating in harmful environments.

In this chapter, the influence of temperature and moisture on the free vibration characteristics of doubly-curved SLCS shells with CNTRC core is presented. The temperature-dependent and moisture-dependent material properties of the graphite-epoxy face sheet and CNTRC core materials are considered for the study. In order to incorporate the skewness of the structure in the FE model, the local skew coordinates are transformed onto the global coordinates. The influence of various geometric and material parameters on the natural frequency of doubly-curved SLCS shells is comprehensively investigated.

4.2. PROBLEM DESCRIPTION

A schematic representation of doubly-curved SLCS shells/panels of length a, width b, and thickness H is presented in Figure 4.1. The two curvatures in XZ and YZ planes measured from the neutral axis ($Z = 0$) are named R_1 and R_2. The doubly-curved shell/panel structures such as spherical ($R_1 = R_2 = R$), ellipsoidal ($R_1 = R$; $R_2 = 2R$), hyperbolic ($R_1 = R$; $R_2 = -R$), and cylindrical shells ($R_1 = R$; $R_2 = \infty$) are considered for the investigation. The results obtained for the mentioned shell structures are compared to the flat plate results considering $R_1 = \infty$; $R_2 = \infty$ with identical mechanical properties. The various shapes of the doubly-curved shells/panels used for the analysis are schematically presented in Figure 4.2. The sandwich structure's top and bottom face sheets consist of graphite-epoxy composite material, whereas the CNTRC material is considered for the core. The face sheet's thickness is considered as h ($h = h_t = h_b$), and the half core thickness as h_c. The rotation components of the normal lying on the top face sheet, bottom face sheet, and core are represented as α_x, ϕ_x, and θ_x, respectively, in the XZ plane. Similarly, α_y, ϕ_y, and θ_y are denoted for the YZ plane. The most commonly used boundary conditions are considered for the analysis and are illustrated in Figure 4.3.

The displacement fields relating to the kinematics of deformation of doubly-curved SLCS shells are articulated using the FSDT. The translational and rotational displacement components are expressed as,

$$\{d_m\} = \begin{bmatrix} u_0 & v_0 & w_0 \end{bmatrix}^T, \text{ and } \{d_n\} = \begin{bmatrix} \theta_x & \theta_y & \phi_x & \phi_y & \alpha_x & \alpha_y \end{bmatrix}^T \quad (4.1)$$
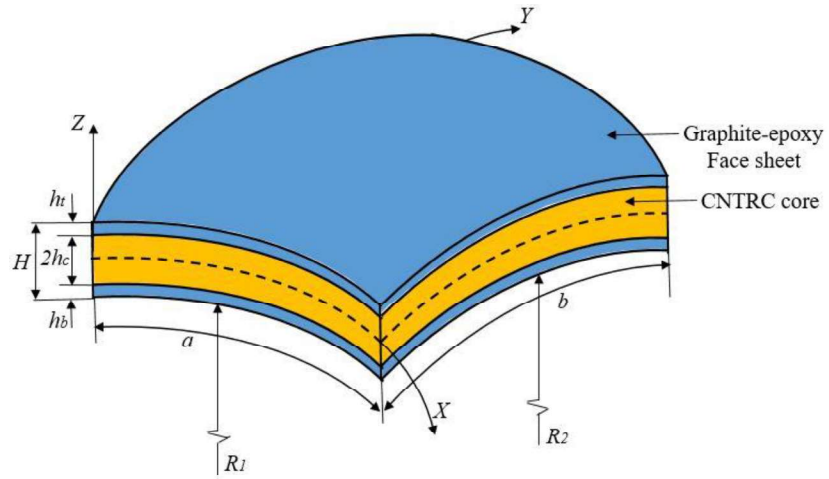
Figure 4.1: Schematic representation of the doubly-curved LCS shell.
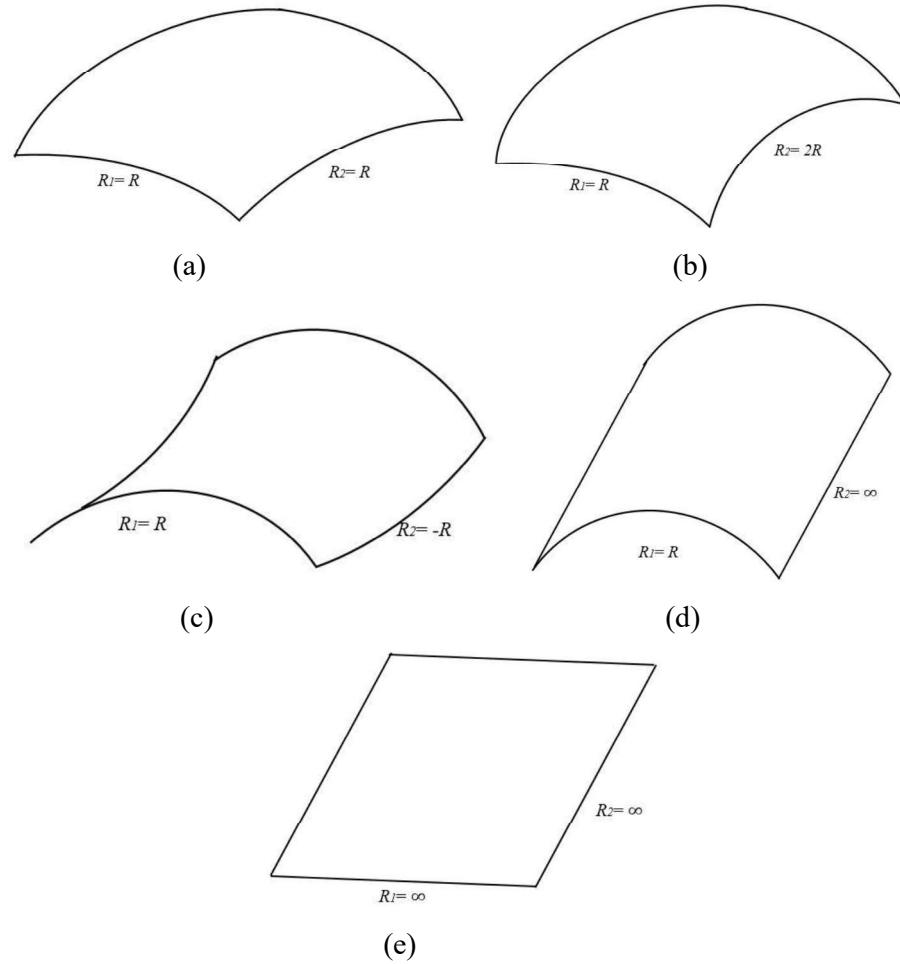
Figure 4.2: Schematic illustrations of (a) spherical, (b) ellipsoidal, (c) hyperbolic, (d) cylindrical shells, and (e) flat plate.

(a) SS (b) CC (c) SC (d) CS
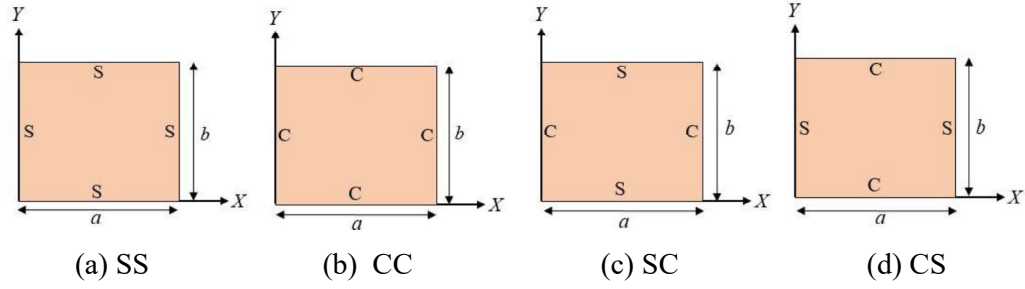
Figure 4.3: Schematic representation of various boundary conditions incorporated (a) all sides simply supported, (b) all sides clamped, (c) opposite sides simply supported (at *X*=0 & *a*) and other two sides are clamped, and (d) opposite sides clamped (at *Y*=0 & *b*) and other two sides are simply supported.

The corresponding strains are divided into the two strain vectors $\{\varepsilon_b\}$ and $\{\varepsilon_s\}$ in order to implement the selective integration rule.

$$\{\varepsilon_b\}_{bo} = \{\varepsilon_{bt}\} + [z_1]\{\varepsilon_{br}\}; \quad \{\varepsilon_b\}_{co} = \{\varepsilon_{bt}\} + [z_2]\{\varepsilon_{br}\}; \quad \{\varepsilon_b\}_{to} = \{\varepsilon_{bt}\} + [z_3]\{\varepsilon_{br}\} \tag{4.2}$$

$$\{\varepsilon_s\}_{bo} = \{\varepsilon_{st}\} + [z_4]\{\varepsilon_{sr}\}; \quad \{\varepsilon_s\}_{co} = \{\varepsilon_{st}\} + [z_5]\{\varepsilon_{sr}\}; \quad \{\varepsilon_s\}_{to} = \{\varepsilon_{st}\} + [z_6]\{\varepsilon_{sr}\} \tag{4.3}$$

in which,

$$\{\varepsilon_{bt}\} = \left[\frac{\partial u_0}{\partial x} \quad \frac{\partial v_0}{\partial y} \quad \frac{\partial u_0}{\partial y} + \frac{\partial v_0}{\partial x}\right]^T ; \quad \{\varepsilon_{st}\} = \left[\frac{\partial w_0}{\partial x} \quad \frac{\partial w_0}{\partial y}\right]^T$$

$$\{\varepsilon_{br}\} = \left[\frac{\partial \theta_x}{\partial x} \quad \frac{\partial \theta_y}{\partial y} \quad \frac{\partial \theta_y}{\partial x} + \frac{\partial \theta_x}{\partial y} \quad \frac{\partial \phi_x}{\partial x} \quad \frac{\partial \phi_y}{\partial y} \quad \frac{\partial \phi_y}{\partial x} + \frac{\partial \phi_x}{\partial y} \quad \frac{\partial \alpha_x}{\partial x} \quad \frac{\partial \alpha_y}{\partial y} \quad \frac{\partial \alpha_y}{\partial x} + \frac{\partial \alpha_x}{\partial y}\right]^T$$

$$\{\varepsilon_{sr}\} = \left[\theta_x \quad \theta_y \quad \phi_x \quad \phi_y \quad \alpha_x \quad \alpha_y\right]^T$$

$$[z_1] = \begin{bmatrix} -h_c & 0 & 0 & z+h_c & 0 & 0 & 0 & 0 & 0 \\ 0 & -h_c & 0 & 0 & z+h_c & 0 & 0 & 0 & 0 \\ 0 & 0 & -h_c & 0 & 0 & z+h_c & 0 & 0 & 0 \end{bmatrix}$$

$$[z_2] = \begin{bmatrix} z & 0 & 0 & 0 & 0 & 0 & 0 & 0 & 0 \\ 0 & z & 0 & 0 & 0 & 0 & 0 & 0 & 0 \\ 0 & 0 & z & 0 & 0 & 0 & 0 & 0 & 0 \end{bmatrix}; \quad [z_3] = \begin{bmatrix} h_c & 0 & 0 & 0 & 0 & 0 & z-h_c & 0 & 0 \\ 0 & h_c & 0 & 0 & 0 & 0 & 0 & z-h_c & 0 \\ 0 & 0 & h_c & 0 & 0 & 0 & 0 & 0 & z-h_c \end{bmatrix}$$

$$[z_4] = \begin{bmatrix} h_c/R_1 & 0 & 1-\left(z+h_c/R_1\right) & 0 & 0 & 0 \\ 0 & h_c/R_2 & 0 & 1-\left(z+h_c/R_2\right) & 0 & 0 \end{bmatrix}; \quad [z_5] = \begin{bmatrix} 1-z/R_1 & 0 & 0 & 0 & 0 & 0 \\ 0 & 1-z/R_2 & 0 & 0 & 0 & 0 \end{bmatrix}$$

$$[z_6] = \begin{bmatrix} -h_c/R_1 & 0 & 0 & 0 & 1-\left(z-h_c/R_1\right) & 0 \\ 0 & -h_c/R_2 & 0 & 0 & 0 & 1-\left(z-h_c/R_2\right) \end{bmatrix}$$

82

where, $\{\varepsilon_b\}_{bo}$, $\{\varepsilon_b\}_{co}$, and $\{\varepsilon_b\}_{to}$ corresponding to the state of in-plane and transverse strains at any point in the bottom face sheet, core, and the top face sheets, respectively. Similarly, the strain vectors $\{\varepsilon_s\}_{co}$, $\{\varepsilon_s\}_{bo}$, and $\{\varepsilon_s\}_{to}$ represent the out-of-plane transverse shear strains. The terms z_1 to z_6 are functions of the Z-coordinate of the point at evaluation. The constitutive relations for the LCS structure exposed to moisture and thermal environment are given by:

$$\{F\} = [D]\{\varepsilon\} - \{F^N\} \tag{4.4}$$

where,

$$\{F\} = \{N_x \quad N_y \quad N_{xy} \quad M_x \quad M_y \quad M_{xy} \quad Q_x \quad Q_y\}^T$$

$$\{F^N\} = \{N_x^N \quad N_y^N \quad N_{xy}^N \quad M_x^N \quad M_y^N \quad M_{xy}^N \quad 0 \quad 0\}^T$$

$$\{\varepsilon\} = \{\varepsilon_x^0 \quad \varepsilon_y^0 \quad \varepsilon_{xy}^0 \quad K_x \quad K_y \quad K_{xy} \quad \varphi_x \quad \varphi_y\}^T$$

In which, [D]: Load-strain relationship matrix; N_x, N_y, N_{xy}: In-plane internal stress resultants; M_x, M_y, M_{xy}: Internal moment resultants; Q_x, Q_y: Transverse shear resultants; N_x^N, N_y^N, N_{xy}^N: In-plane hygrothermal force resultants; M_x^N, M_y^N, M_{xy}^N: hygrothermal moment resultants; ε_x^0, ε_y^0, ε_{xy}^0: In-plane strains of the mid-plane; K_x, K_y, K_{xy}: Curvature of the plate; φ_x, φ_y: Shear rotations in the *XZ* and *YZ*-planes, respectively. The terms used in the force vector $\{F^N\}$ are instrumental in developing the initial stress stiffness matrix $[K_\sigma]$.

4.3. FINITE ELEMENT FORMULATION

The FE model of the doubly-curved SLCS shell structures is discretized using the eight noded isoparametric quadrilateral elements. Each node of the element is assumed to have nine degrees of freedom, i.e., six rotation (θ_x, θ_y, ϕ_x, ϕ_y, α_x, α_y) and three translational (u, v, w). The displacement vectors connected with the *i*-th node (i = 1, 2, …, 8) of the element can be pronounced as:

$$\{d_{mi}\} = \begin{bmatrix} u_{0i} & v_{0i} & w_{0i} \end{bmatrix}^T \text{ and } \{d_{ni}\} = \begin{bmatrix} \theta_{xi} & \theta_{yi} & \phi_{xi} & \phi_{yi} & \alpha_{xi} & \alpha_{yi} \end{bmatrix}^T \tag{4.5}$$

Thus, the elemental displacement vector at any point on the element can be used to represent generalized displacement vectors as;

$\{d_m\} = [N_m]\{\mathrm{d}_m^e\}$ and $\{d_n\} = [N_n]\{\mathrm{d}_n^e\}$

where, $\{\mathrm{d}_m^e\} = [\{\mathrm{d}_{m1}^e\}^T \quad \{\mathrm{d}_{m2}^e\}^T \quad ... \quad \{\mathrm{d}_{m8}^e\}^T]^T$ and $\{\mathrm{d}_n^e\} = [\{\mathrm{d}_{n1}^e\}^T \quad \{\mathrm{d}_{n2}^e\}^T \quad ... \quad \{\mathrm{d}_{n8}^e\}^T]^T$

And $[N_m]$ & $[N_n]$ are the shape function matrices related to translational and rotational components.

4.3.1. Elemental stiffness matrix

The strain vectors at any point within the element can be expressed as:

$$\{\varepsilon_b\}_{bo} = [\mathrm{B}_{tb}]\{\mathrm{d}_m^e\} + [z_1][\mathrm{B}_{rb}]\{\mathrm{d}_n^e\}$$
$$\{\varepsilon_b\}_{co} = [\mathrm{B}_{tb}]\{\mathrm{d}_m^e\} + [z_2][\mathrm{B}_{rb}]\{\mathrm{d}_n^e\}$$
$$\{\varepsilon_b\}_{to} = [\mathrm{B}_{tb}]\{\mathrm{d}_m^e\} + [z_3][\mathrm{B}_{rb}]\{\mathrm{d}_n^e\}$$
$$\{\varepsilon_s\}_{bo} = [\mathrm{B}_{ts}]\{\mathrm{d}_m^e\} + [z_4][\mathrm{B}_{rs}]\{\mathrm{d}_n^e\}$$
$$\{\varepsilon_s\}_{co} = [\mathrm{B}_{ts}]\{\mathrm{d}_m^e\} + [z_5][\mathrm{B}_{rs}]\{\mathrm{d}_n^e\}$$
$$\{\varepsilon_s\}_{to} = [\mathrm{B}_{ts}]\{\mathrm{d}_m^e\} + [z_6][\mathrm{B}_{rs}]\{\mathrm{d}_n^e\}$$

(4.6)

In which $[\mathrm{B}_{tb}]$, $[\mathrm{B}_{rb}]$, $[\mathrm{B}_{ts}]$ and $[\mathrm{B}_{rs}]$ are the nodal displacement matrices and are presented as follows,

$$[B_{tbi}] = \begin{bmatrix} \dfrac{\partial n_i}{\partial x} & 0 & \dfrac{1}{R_1} \\ 0 & \dfrac{\partial n_i}{\partial y} & \dfrac{1}{R_2} \\ \dfrac{\partial n_i}{\partial y} & \dfrac{\partial n_i}{\partial x} & 0 \end{bmatrix}; \quad [B_{tsi}] = \begin{bmatrix} -\dfrac{1}{R_1} & 0 & \dfrac{\partial n_i}{\partial x} \\ 0 & -\dfrac{1}{R_2} & \dfrac{\partial n_i}{\partial y} \end{bmatrix};$$

$$[B_{rsi}] = \begin{bmatrix} 1 & 0 & 0 & 0 & 0 & 0 \\ 0 & 1 & 0 & 0 & 0 & 0 \\ 0 & 0 & 1 & 0 & 0 & 0 \\ 0 & 0 & 0 & 1 & 0 & 0 \\ 0 & 0 & 0 & 0 & 1 & 0 \\ 0 & 0 & 0 & 0 & 0 & 1 \end{bmatrix};$$

$$[B_{rbi}] = \begin{bmatrix} \dfrac{\partial n_i}{\partial x} & 0 & \dfrac{\partial n_i}{\partial y} & 0 & 0 & 0 & 0 & 0 & 0 \\ 0 & \dfrac{\partial n_i}{\partial y} & \dfrac{\partial n_i}{\partial x} & 0 & 0 & 0 & 0 & 0 & 0 \\ 0 & 0 & 0 & \dfrac{\partial n_i}{\partial x} & 0 & \dfrac{\partial n_i}{\partial y} & 0 & 0 & 0 \\ 0 & 0 & 0 & 0 & \dfrac{\partial n_i}{\partial y} & \dfrac{\partial n_i}{\partial x} & 0 & 0 & 0 \\ 0 & 0 & 0 & 0 & 0 & 0 & \dfrac{\partial n_i}{\partial x} & 0 & \dfrac{\partial n_i}{\partial y} \\ 0 & 0 & 0 & 0 & 0 & 0 & 0 & \dfrac{\partial n_i}{\partial y} & \dfrac{\partial n_i}{\partial x} \end{bmatrix}^T$$

In general, the element stiffness matrix is given by,

$$[K_e] = \int\limits_{-1}^{+1}\int\limits_{-1}^{+1} [B]^T[D][\mathrm{B}]|J|d\xi d\eta \tag{4.7}$$

84

4.3.2. Elemental initial stress stiffness matrix

The nonlinear strains can be expressed as:

$$\{\varepsilon_{nl}\} = \{\varepsilon_{xnl}, \varepsilon_{ynl}, \varepsilon_{xynl}\} = [R]\{d\}/2$$

where,

$$\{d\} = \{u_{,x}, u_{,y}, v_{,x}, v_{,y}, w_{,x}, w_{,y}, \theta_{x,x}, \theta_{x,y}, \theta_{y,x}, \theta_{y,y}, \phi_{x,x}, \phi_{x,y}, \phi_{y,x}, \phi_{y,y}, \alpha_{x,x}, \alpha_{x,y}, \alpha_{y,x},$$
$$\alpha_{y,y}, \theta_x, \theta_y, \phi_x, \phi_y, \alpha_x, \alpha_y\}^T \tag{4.8}$$

Equation $\{d\}$ can be expressed as:

$$\{d\} = [G]\{\partial_e\} \tag{4.9}$$

where, $[G]$ is the shape function operating matrix. The initial stress stiffness matrix due to hygrothermal loads is given by:

$$[K_\sigma^e] = \int_{-1}^{+1}\int_{-1}^{+1} [G]^T[S][G]|J|d\xi d\eta \tag{4.10}$$

The matrix $[S]$ contains the in-plane initial internal force, moment resultants, and transverse shear resultant terms.

4.4. EQUATION OF MOTION

The governing equations of a doubly-curved sandwich shell in a hygrothermal environment are derived using the dynamic version of the principle of virtual work (Suresh Kumar and Ray, 2012). The potential energy and kinetic energy of the overall sandwich structure can be written as:

$$T_p = \frac{1}{2}\left\{ \left(\sum_{k=1}^{N}\int_{\Omega}\left(\{\varepsilon_b^k\}_{bo}^T\{\sigma_b^k\}_{bo} + \{\varepsilon_s^k\}_{bo}^T\{\sigma_s^k\}_{bo}\right)d\Omega\right) + \left(\int_{\Omega}\left(\{\varepsilon_b\}_{co}^T\{\sigma_b\}_{co} + \{\varepsilon_s\}_{co}^T\{\sigma_s\}_{co}\right)d\Omega\right) \right.$$
$$\left. + \left(\sum_{k=1}^{N}\int_{\Omega}\left(\{\varepsilon_b^k\}_{to}^T\{\sigma_b^k\}_{to} + \{\varepsilon_s^k\}_{to}^T\{\sigma_s^k\}_{to}\right)d\Omega\right) - \int_A\{d\}^T\left(\{f\}\right)dA \right\} \tag{4.11}$$

$$T_k = \frac{1}{2}\left\{ \left(\sum_{k=1}^{N}\int_{\Omega}\rho_{bo}^k\left(\dot{u}_{bo}^2 + \dot{v}_{bo}^2 + \dot{w}_{bo}^2\right)d\Omega\right) + \left(\rho_{co}\int_{\Omega}\left(\dot{u}_{co}^2 + \dot{v}_{co}^2 + \dot{w}_{co}^2\right)d\Omega\right) + \left(\sum_{k=1}^{N}\int_{\Omega}\rho_{to}^k\left(\dot{u}_{to}^2 + \dot{v}_{to}^2 + \dot{w}_{to}^2\right)d\Omega\right) \right\} \tag{4.12}$$

In which, 'N' indicates the number of orthotropic composite layers in the top and bottom face sheets. Substituting the respective terms in Eqns. 4.11 & 4.12, and on solving we get,

$$T_p^e = \frac{1}{2}\Big[\{d_m^e\}^T\big[K_{mm}^e\big]\{d_m^e\} + \{d_m^e\}^T\big[K_{mn}^e\big]\{d_n^e\} + \{d_n^e\}^T\big[K_{mn}^e\big]^T\{d_m^e\} + \{d_n^e\}^T\big[K_{nn}^e\big]\{d_n^e\} - 2\{d_m^e\}^T\{F^e\}\Big] \quad (4.13)$$

$$T_k^e = \frac{1}{2}\int_0^{a_e}\int_0^{b_e}\overline{m}\{\dot{d}_m^e\}^T[N]^T[N]\{\dot{d}_m^e\}\,dxdy \qquad (4.14)$$

where,

$$\big[K_{mm}^e\big] = \big[K_{mmb}^e\big] + \big[K_{mms}^e\big]; \quad \big[K_{mn}^e\big] = \big[K_{mnb}^e\big] + \big[K_{mns}^e\big]; \quad \{F^e\} = \int_0^{a_e}\int_0^{b_e}[N_m]^T\{f\}\,dxdy;$$

$$\overline{m} = \sum_{k=1}^{N}\rho_{bo}(h_{k+1}-h_k) + 2\rho_{co}h_c + \sum_{k=1}^{N}\rho_{to}(h_{k+1}-h_k); \quad [M^e] = \int_0^{a_e}\int_0^{b_e}\overline{m}[N_m]^T[N_m]\,dxdy;$$

in which,

$$\big[K_{mmb}^e\big] = \int_{A_e}[B_{tb}]^T\big(\big[D_{mmb}^{bo}\big] + \big[D_{mmb}^{co}\big] + \big[D_{mmb}^{to}\big]\big)[B_{tb}]\,dA^e$$

$$\big[K_{mnb}^e\big] = \int_{A_e}[B_{tb}]^T\big(\big[D_{mnb}^{bo}\big][B_{rb}] + \big[D_{mnb}^{co}\big][B_{rb}] + \big[D_{mnb}^{to}\big][B_{rb}]\big)\,dA^e$$

$$\big[K_{nnb}^e\big] = \int_{A_e}\big([B_{rb}]^T\big[D_{nnb}^{bo}\big][B_{rb}] + [B_{rb}]^T\big[D_{nnb}^{co}\big][B_{rb}] + [B_{rb}]^T\big[D_{nnb}^{to}\big][B_{rb}]\big)\,dA^e$$

$$\big[K_{mms}^e\big] = \int_{A_e}[B_{ts}]^T\big(\big[D_{mms}^{bo}\big] + \big[D_{mms}^{co}\big] + \big[D_{mms}^{to}\big]\big)[B_{ts}]\,dA^e$$

$$\big[K_{mns}^e\big] = \int_{A_e}[B_{ts}]^T\big(\big[D_{mns}^{bo}\big][B_{rs}] + \big[D_{mns}^{co}\big][B_{rs}] + \big[D_{mns}^{to}\big][B_{rs}]\big)\,dA^e$$

$$\big[K_{nns}^e\big] = \int_{A_e}\big([B_{rs}]^T\big[D_{nns}^{bo}\big][B_{rs}] + [B_{rs}]^T\big[D_{nns}^{co}\big][B_{rs}] + [B_{rs}]^T\big[D_{nns}^{to}\big][B_{rs}]\big)\,dA^e$$

where,

$$\big[D_{mmb}^{bo}\big] = \big[C_b^{bo}\big]h_b; \quad \big[D_{mmb}^{co}\big] = 2\big[C_b^{co}\big]h_c; \quad \big[D_{mmb}^{to}\big] = \big[C_b^{to}\big]h_t$$

$$\big[D_{mms}^{bo}\big] = \big[C_s^{bo}\big]h_b; \quad \big[D_{mms}^{co}\big] = 2\big[C_s^{co}\big]h_c; \quad \big[D_{ts}^{to}\big] = \big[C_s^{to}\big]h_t$$

$$\big[D_{mnb}^{bo}\big] = \int_{h_1}^{h_2}\big[C_b^{bo}\big][z_1]\,dz; \quad \big[D_{mnb}^{co}\big] = \int_{h_2}^{h_3}\big[C_b^{co}\big][z_2]\,dz; \quad \big[D_{mnb}^{to}\big] = \int_{h_2}^{h_3}\big[C_b^{to}\big][z_3]\,dz$$

$$\big[D_{mns}^{bo}\big] = \int_{h_1}^{h_2}\big[C_s^{bo}\big][z_4]\,dz; \quad \big[D_{mns}^{co}\big] = \int_{h_2}^{h_3}\big[C_s^{co}\big][z_5]\,dz; \quad \big[D_{mns}^{to}\big] = \int_{h_2}^{h_3}\big[C_s^{to}\big][z_6]\,dz$$

$$\big[D_{nnb}^{bo}\big] = \int_{h_1}^{h_2}[z_1]^T\big[C_b^{bo}\big][z_1]\,dz; \quad \big[D_{nnb}^{co}\big] = \int_{h_2}^{h_3}[z_2]^T\big[C_b^{co}\big][z_2]\,dz;$$

$$\big[D_{nnb}^{to}\big] = \int_{h_2}^{h_3}[z_3]^T\big[C_b^{to}\big][z_3]\,dz; \quad \big[D_{nns}^{bo}\big] = \int_{h_1}^{h_2}[z_4]^T\big[C_s^{bo}\big][z_4]\,dz;$$

$$\big[D_{nns}^{co}\big] = \int_{h_2}^{h_3}[z_5]^T\big[C_s^{co}\big][z_5]\,dz; \quad \big[D_{nns}^{to}\big] = \int_{h_2}^{h_3}[z_6]^T\big[C_s^{to}\big][z_6]\,dz$$

Applying the dynamic version of the virtual work principle we get,

$$\left[M^e \right]\left\{ \ddot{d}_m^e \right\} + \left[K_{mm}^e \right]\left\{ d_m^e \right\} + \left[K_{mn}^e \right]\left\{ d_n^e \right\} = \left\{ F^e \right\} \tag{4.15}$$

$$\left[K_{mn}^e \right]^T \left\{ d_m^e \right\} + \left[K_{nn}^e \right]\left\{ d_n^e \right\} = 0 \tag{4.16}$$

Finally, the elemental matrices are combined together to form the global equation of motion as,

$$\left[M \right]\left\{ \ddot{X} \right\} + \left[K_{mm} \right]\left\{ X \right\} + \left[K_{mn} \right]\left\{ X_r \right\} = \left\{ F \right\} \tag{4.17}$$

$$\left[K_{nm} \right]\left\{ X \right\} + \left[K_{nn} \right]\left\{ X_n \right\} = 0 \tag{4.18}$$

where, $\left[M \right]$ is the global mass matrix, $\left[K_{mm} \right]$, $\left[K_{mn} \right]$, and $\left[K_{nn} \right]$ are the global stiffness matrices. The natural frequency of the sandwich structure can be obtained as follows:

$$\left\| \left[[K] + [\mathrm{K}_\sigma] \right] - \omega_n^2 [M] \right\| = 0 \tag{4.19}$$

On solving, we get the entire set of natural frequencies of the structure, i.e., ω_n. where, $n = 1, 2, \ldots, p$ (p is the number of degrees of freedom of the system).

4.5. RESULTS AND DISCUSSIONS

In this section, the temperature-dependent and moisture-dependent material properties are invoked into the analysis to investigate the influence of the temperature and moisture on the vibration response of doubly-curved SLCS shells. The moisture-dependent and temperature-dependent material properties of the graphite-epoxy composite face sheet listed in Tables 2.2 and 2.3 are considered for the analysis. In case of the core material, the volume fraction of the CNT and the epoxy are considered to change linearly along the thickness of the shell to obtain the functionally graded CNTRC core. The commonly used four types of gradations, namely FG-UD (volume fraction of CNT is maintained uniformly), FG-V (CNT volume fractions varies linearly high to low from top to bottom surface), FG-O (CNT volume fractions are higher at the mid-plane and less in the top and bottom surfaces), and FG-X (CNT volume fractions are higher at the top and bottom surface of the panel and minimum at the mid-plane) are considered for the analysis. The gradation scheme is pictorially demonstrated in Figure 4.4.

(a)   (b)   (c)   (d)
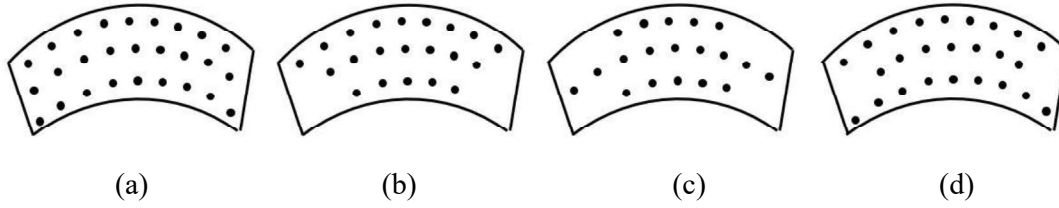
Figure 4.4: Pictorial representation CNT gradation types (a) FG-UD, (b) FG-V, (c) FG-O, and (d) FG-X.

The volume fraction of the CNT distribution types are represented as (Alibeigloo and Emtehani, 2015: Dat *et al.*, 2020),

$$V_{CNT}(z) = V_{CNT}^* \qquad \text{(FG-UD CNTRC)} \qquad (4.20.a)$$

$$V_{CNT}(z) = \left(1 + \frac{2z}{h_c}\right) V_{CNT}^* \qquad \text{(FG-V CNTRC)} \qquad (4.20.b)$$

$$V_{CNT}(z) = 2\left(1 - \frac{2|z|}{h_c}\right) V_{CNT}^* \qquad \text{(FG-O CNTRC)} \qquad (4.20.c)$$

$$V_{CNT}(z) = 2\left(\frac{2|z|}{h_c}\right) V_{CNT}^* \qquad \text{(FG-X CNTRC)} \qquad (4.20.d)$$

$$V_m(z) = 1 - V_{CNT}^*(z) \qquad (4.21)$$

In which V_{CNT}^* is the CNT volume fraction. The volume fractions considered for the analysis and the corresponding efficiency parameters are presented in Table 4.1.

Table 4.1: Values of the CNT efficiency parameters corresponding to CNT volume fraction values (Dat et al., 2020).

V_{CNT}^*	η_1	η_2	η_3
0.12	0.137	1.022	0.715
0.17	0.141	1.626	1.138
0.24	0.141	1.585	1.109

The material properties of the matrix in the presence of temperature and moisture are presented as (Alibeigloo and Emtehani, 2015: Dat *et al.*, 2020),

$v_m = 0.34$, $\rho_m = 1200$ kg/m^3, $\beta_m = 2.68e\text{-}3$ / wt % of H_2O,

$$\alpha_m = 45\left(1 + 0.0001\Delta T\right) \times 10^{-6} \ / K ; \ E_m = \left(3.51 - 0.003T - 0.142M\right) \quad GPa \qquad (4.22)$$

where, $T = T_0 + \Delta T$, M $= M_0 + \Delta M$. In which ΔT & ΔM are temperature and moisture increments, and $T_0 = 300$ K, $M = 0$ wt % of H_2O. Similarly, the temperature and

moisture dependent material properties of CNT material are given as (Alibeigloo and Emtehani, 2015: Dat *et al.*, 2020),

$\nu_{12}{}^{CNT} = 0.175$, $\rho^{CNT} = 1400$ kg/m^3,

$$E_{11}^{CNT}\left[TPa\right] = 6.3998 - 4.33817 \times 10^{-3}T + 7.43 \times 10^{-6}T^2 - 4.45833 \times 10^{-9}T^3 \qquad (4.23.a)$$

$$E_{22}^{CNT}\left[TPa\right] = 8.02155 - 5.420375 \times 10^{-3}T + 9.725 \times 10^{-6}T^2 - 5.5625 \times 10^{-9}T^3 \qquad (4.23.b)$$

$$G_{12}^{CNT}\left[TPa\right] = 1.40755 - 3.476208 \times 10^{-3}T - 6.965 \times 10^{-6}T^2 + 4.479167 \times 10^{-9}T^3 \qquad (4.23.c)$$

$$\alpha_{11}^{CNT}\left[10^{-6}/K\right] = -1.12515 + 0.02291688T - 2.887 \times 10^{-5}T^2 + 1.13625 \times 10^{-8}T^3 \qquad (4.23.d)$$

$$\alpha_{22}^{CNT}\left[10^{-6}/K\right] = 5.43715 - 0.984625 \times 10^{-4}T - 2.9 \times 10^{-7}T^2 - 1.25 \times 10^{-11}T^3 \qquad (4.23.e)$$

The effective properties of the CNTRC core material can be computed as (Alibeigloo and Emtehani, 2015: Dat *et al.*, 2020),

$$E_{11}^{c} = V_m E_m + \eta_1 V_{CNT} E_{11}^{CNT} \;;\; \frac{\eta_2}{E_{22}^{c}} = \frac{V_m}{E_m} + \frac{V_{CNT}}{E_{22}^{CNT}} \;;\; \frac{\eta_3}{G_{12}^{c}} = \frac{V_m}{E_m} + \frac{V_{CNT}}{G_{12}^{CNT}} \qquad (4.24)$$

$$\nu_{12}^{c} = V_{CNT}^{*}\nu_{12}^{CNT} + V_m \nu_m \qquad (4.25)$$

The thermal expansion and moisture expansion coefficients of the CNTRC core are conveyed as (Alibeigloo and Emtehani, 2015: Dat *et al.*, 2020),

$$\alpha_{11}^{c} = \frac{V_{CNT}E_{11}^{CNT}\alpha_{11}^{CNT} + V_m E_m \alpha_m}{V_{CNT}E_{11}^{CNT} + V_m E_m} \;;\; \alpha_{22}^{c} = (1+\nu_m)E_m\alpha_m + (1+\nu_{12}^{CNT})V_{CNT}\alpha_{22}^{CNT} - \nu_{12}\alpha_{11} \qquad (4.26.a)$$

$$\beta_{11}^{c} = \frac{V_{CNT}E_{11}^{CNT} + V_m E_m \beta_m}{V_{CNT}E_{11}^{CNT} + V_m E_m} \;;\; \beta_{22}^{c} = (1+\nu_m)E_m\beta_m - \nu_{12}\beta_{11} \qquad (4.26.b)$$

4.5.1. Convergence and validation study

The convergence and validation study of the FE model developed in the previous section is performed to authenticate the natural frequency results extracted from the formulation. The simply supported graphite-epoxy laminated composite plate operating in 0.1 % moisture concentration and 325 K temperature environment is considered for the study. The outcomes enlisted in Table 4.2 show that the results

obtained from the mesh size of 12×12 are apparently coinciding with the results of 16×16 mesh size up to the third decimal position. Consequently, a mesh size of 12×12 was adopted throughout the simulation to save computational time. The simulations are performed on the simply supported skew honeycomb and cross-ply sandwich plates to understand the influence of skew angle on the natural frequency of the system. The results tabulated in Table 4.3 implies that the frequency values determined from the current model are in excellent agreement with the results presented in the pieces of literature.

Table 4.2: Convergence and validation study of the cross-ply (0°/90°/90°/0°) composite plate with SS boundary condition.

Mesh Size	$T = 325$ K			$C = 0.1$ %		
	Mode Numbers			Mode Numbers		
	1	2	3	1	2	3
4×4	7.2972	18.5509	38.5235	9.0923	20.3942	39.4368
8×8	7.2492	17.8752	38.3130	9.0576	19.8282	39.2614
12×12	7.2486	17.8709	38.3144	9.0573	19.8263	39.2642
16×16	7.2485	17.8706	38.3141	9.0571	19.8261	39.2639

Table 4.3: Fundamental natural frequency (Hz) of the skew sandwich plate with SS boundary condition.

Structure	Source	Skew Angle		
		0°	15°	30°
0°/90°/C/0°/90°	Raville and Ueng (1967)	152.5800	--	--
	Garg *et al.* (2006) FSDT	166.3086	177.6942	217.7630
	Garg *et al.* (2006) HSDT	152.2992	161.7182	194.3770
	Present	152.5263	158.4616	178.4418
Honeycomb	Raville and Ueng (1967)	23.0000	--	--
	Garg *et al.* (2006) FSDT	23.5279	24.9315	30.0623
	Garg *et al.* (2006) HSDT	23.4514	24.8438	29.9153
	Present	23.5220	24.2699	26.8034

Table 4.4 compares the natural frequency results obtained from the current formulation and the published literature for a simply supported spherical shell. It can be witnessed that the extent of the influence of the radius to length (R/a) ratio on fundamental frequency predicted by the present formulation is in good agreement with the existing literature (Reddy, 2003). Further simulations were performed to understand the effect of gradation and volume fraction of CNTRC material on the system's fundamental frequency. The results obtained for the CNTRC plate considering the geometrical parameters as $b = 50×H$ and $H = 2$ mm are tabulated in

Table 4.5. From Table 4.5, it is apparent that the obtained results are in a good match with existing literature.

4.5.2. Doubly-curved LCS shell

The influence of temperature on the natural frequency of doubly-curved SLCS shells for different boundary conditions is investigated. The sandwich structures of length to thickness (a/H) ratio of 40, length to width (a/b) ratio of 2, and the ratio of core to the face sheet thickness (t_c/t_f) ratio of 1 are considered for the analysis. The first two natural frequencies of the uniformly distributed FG-CNTRC core with a 0.28 volume fraction are presented in Figure 4.5. In Figure 4.5, the numbers 1 and 2 indicate the first and second natural frequency of doubly-curved sandwich shell, respectively (e.g., SS1 and SS2 indicate the first and second natural frequencies of simply supported doubly-curved sandwich panels). The results presented in Figure 4.5 infer that the natural frequency of the structure substantially reduces with an increase in temperature. It may be due to a reduction in stiffness of the structure on exposure to an elevated thermal environment (Garg *et al.*, 2019). It can also be noted that the CC boundary condition has a higher natural frequency, and the lowest is observed for the SS boundary condition. The deviation between the natural frequencies for the CC and CS boundary constraints is very minimal. For CC and CS conditions, the edges along the length (i.e., $X= 0$ & a) have clamped boundary conditions, and for SS and SC conditions, the simply supported edge constraint is employed along the length. The stiffness of the structure (plate/shell) reduces as the boundary condition changes from CC to other constraints such as SS, SC, and CS conditions (Vinyas and Kattimani, 2017). For the current analysis, an a/b ratio of 2 is employed, i.e., the edges along the length (i.e., $X= 0$ & a) are longer than the edges along the width of the plate (i.e., $Y= 0$ & b). Hence, the structure with CC and CS boundary conditions will have a minimal deviation in the stiffness values and, in turn, will have apparently identical natural frequencies. From Figure 4.5, it can also be noted that even though the longest edges have the same edge constraints, the natural frequency of the SC condition is much higher than the structure with the SS boundary condition. This indicates that the clamped edge condition is more dominant in dictating the variations in natural frequency values than the simply supported edge condition.

Table 4.4: Influence of radius to length (R/a) ratio on the $\bar{\omega}$ of cross-ply laminated spherical shells with SS boundary condition.

Fiber Orientation	R/a Ratio	a/H= 100		a/H= 10	
		Reddy (2003)	Present	Reddy (2003)	Present
0°/90°/0°	1	125.990	125.8942	16.1150	15.5874
	5	30.9930	31.0361	12.3720	11.4820
	10	20.3470	20.3997	12.2150	11.3047
	10^{30}	15.1830	15.2483	12.1620	11.2453
0°/90°/0°/90°	1	126.330	126.2253	16.1720	15.6731
	5	31.0790	31.1205	12.4370	11.5715
	10	20.3800	20.4329	12.2800	11.3945
	10^{30}	15.1840	15.2493	12.2260	11.3355

Table 4.5: Comparison of the $\bar{\omega}$ of CNTRC plate.

V^*_{CNT}	Mode	FG- UD			FG- O		
		Alibeigloo Emtehani, (2015)	Zhu et al. (2012)	Present	Alibeigloo Emtehani, (2015)	Zhu et al. (2012)	Present
0.11	1	19.1680	19.2230	19.0314	14.2800	14.3020	14.0368
	2	23.2840	23.4080	22.6967	19.3060	19.3730	18.4783
	3	34.0540	34.6690	33.2554	31.0920	31.6150	29.9640
0.14	1	21.3280	21.3540	21.2779	15.7990	15.8010	15.6337
	2	25.1990	25.2950	24.7418	20.5170	20.5630	19.8066
	3	35.6790	36.2670	35.0520	32.0060	32.5090	31.0241
0.17	1	23.6220	23.6970	23.6556	17.5310	17.5440	17.3381
	2	28.8250	28.9870	28.3397	23.7300	23.7830	22.8468
	3	42.3860	43.1650	41.7581	38.2570	38.8550	37.0788

It is important to note that for all the shell types and boundary constraints considered, the influence of the temperature is prominent in the first mode. For the first mode, the maximum percentage reduction in frequency value is observed for SS (SS1) boundary condition (41.25 %), and a minimum reduction is noticed for CS (CS1) boundary condition (5.34 %). Whereas, the second mode exhibits an 8.16 % reduction in frequency for SS (SS2) edge constraint and a minimum of 2.52 % for CS (CS2) boundary constraint. Further, it is witnessed that the spherical sandwich shells possess higher natural frequency, and the flat sandwich plate exhibits the lowest magnitude of frequency. In the presence of temperature, the flat sandwich plate is the most affected structure with the highest percentage reduction in natural frequency value. However, the spherical sandwich shell is the most thermal resistant arrangement.

The effect of moisture on the first two natural frequencies of the doubly-curved sandwich shells for different boundary conditions is presented in Figure 4.6. The doubly-curved sandwich structure (with a/b =2, a/H =40, t_c/t_f = 2, and R/a = 10) with uniformly distributed FG-CNTRC core (with V^*_{CNT} = 0.28) is considered for the analysis. It is evident from the results that the natural frequencies of the structure reduce with an increase in moisture concentration values. Composite material's properties generally degrade when exposed to elevated temperature and moisture environments (Ray, 2006). This, in turn, reduces the stiffness of the composite structure, i.e., with an increase in temperature and moisture, the stiffness of the composite structure reduces. The stiffness of any system is directly proportional to the natural frequency. Hence, with the reduction in stiffness of composite structures, the natural frequency of the system reduces (Parhi *et al*., 2001: Biswal *et al*., 2017). It is evident from the results that the spherical sandwich plate exhibits the higher natural frequency and the flat sandwich plate has the least frequency magnitude. The doubly-curved shell structures with CC boundary conditions exhibit higher natural frequency values, whereas the SS edge conditions show the lowest frequency magnitude. The maximum percentage reduction in frequency magnitude of 38.85 % is observed for the flat sandwich plate with SS (SS1) boundary constraints, while the spherical sandwich shell with CC (CC1) condition experiences the lowest of 7.83 % reduction.

Similarly, a minimum of 0.10 % and a maximum of 4.58 % reduction of the second natural frequency is seen for CC (CC2) and SS (SS2) edge constraints, respectively. The results show that the effect of temperature and moisture is prominent for the first vibratory mode of the sandwich shells. It can also be noted that the natural frequency of the flat sandwich plates is more affected by environmental exposure and the spherical sandwich shell structures are least affected.

The effect of CNT volume fraction and temperature on the vibration response of doubly-curved sandwich shells has been studied. The uniformly distributed CNTRC core with the CNT volume fractions of 0.12, 0.17, and 0.28 with their respective efficiency parameters are used for the analysis. The first two natural frequency magnitudes obtained for doubly-curved sandwich shells (with $a/b = 1$, $a/H = 40$, $t_c/t_f = 1$, and $R/a = 10$) with SS boundary condition are shown in Figure 4.7. From the results, it is clear that the natural frequency of the structure upsurges with a rise in the volume fraction of CNT. The variation may be due to an increase in the stiffness of the sandwich shells upon the increase in the volume fraction of CNT (Dat et al., 2020). It is notable that for all the temperatures and volume fractions considered, the spherical sandwich panels have the highest natural frequency values (S1 and S2). The lowest natural frequency is observed for the hyperbolic shell (H1) and flat sandwich plate (P2) for the first and second natural frequencies. The results show that the spherical shells are least affected by the thermal exposure for all the volume fractions considered. The frequency percentage reduction of 28.56 % and 30.56 % are remarked for the first two modes of vibrations of the spherical shells (for $V_{CNT}^* = 0.12$). The maximum percentage reduction in frequency is noticed for the hyperbolic sandwich shell with 59.08 % and 39.39 % reduction for the first two natural frequencies (for $V_{CNT}^* = 0.28$). For the flat sandwich plates, 58.54 % and 41.23 % reduction is noted (for $V_{CNT}^* = 0.28$) for the first and second modes of vibrations, respectively.

Further investigation is extended to understand the influence of CNT volume fraction and moisture concentration on the vibration characteristics of doubly-curved sandwich shells. From the results presented in Figure 4.8, it is evident that the natural frequency of the doubly-curved sandwich structure diminishes with a rise in moisture concentration values for all the CNT volume fractions considered. It can also be

witnessed that the system's natural frequency increases with the increase in V^*_{CNT} values in elevated moisture environments. The results indicate that the spherical sandwich shells are considerably resistant to high moisture environments with frequency reduction of 24.41 % and 40.75 %, respectively, for the first two natural frequency values (for V^*_{CNT} = 0.28). Meanwhile, the maximum percentage reduction of 50.71 % is observed for the second mode of the flat sandwich plate (for V^*_{CNT} = 0.12).

Furthermore, the study is extended to understand the influence of functional gradation type on the natural frequency of doubly-curved sandwich shells operating in elevated thermal environments. The most commonly used four types of gradation are considered for the investigation, namely, FG-X, FG-O, FG-V, and FG-UD. The doubly-curved sandwich shells with an a/b ratio of 2, a/H ratio of 40, a R/a ratio of 10, and the core with the CNT volume fraction of 0.17 under SS boundary conditions are considered for the investigation and the outcomes found are presented in Figure 4.9. For all the temperature values considered, it is observed that the FG-X and FG-V gradation types showed the highest natural frequency values, and the FG-O type gradations exhibit the lowest value. The results show that the spherical shell structure is more resistant to temperature variation, with the lowest percentage reduction in the fundamental frequency of 25.85 % (for FG-O). The sandwich plates are observed to be more vulnerable to thermal environments with the maximum percentage reduction of 31.13 % (for FG-X). It can also be noted that the deviation in percentage reduction in the natural frequency of the shell structures for various gradations is very minimal. Similar variation in the fundamental frequency of the doubly-curved shell structures observed in the presence of moisture environment and the obtained results are documented in Figure 4.10. The influence of moisture is more prominent on the sandwich flat plates with a 65.42 % reduction in fundamental frequency, whereas the spherical sandwich shell is observed to have the slightest variation in frequency (52.57 %) value upon exposure to the moisture environment.
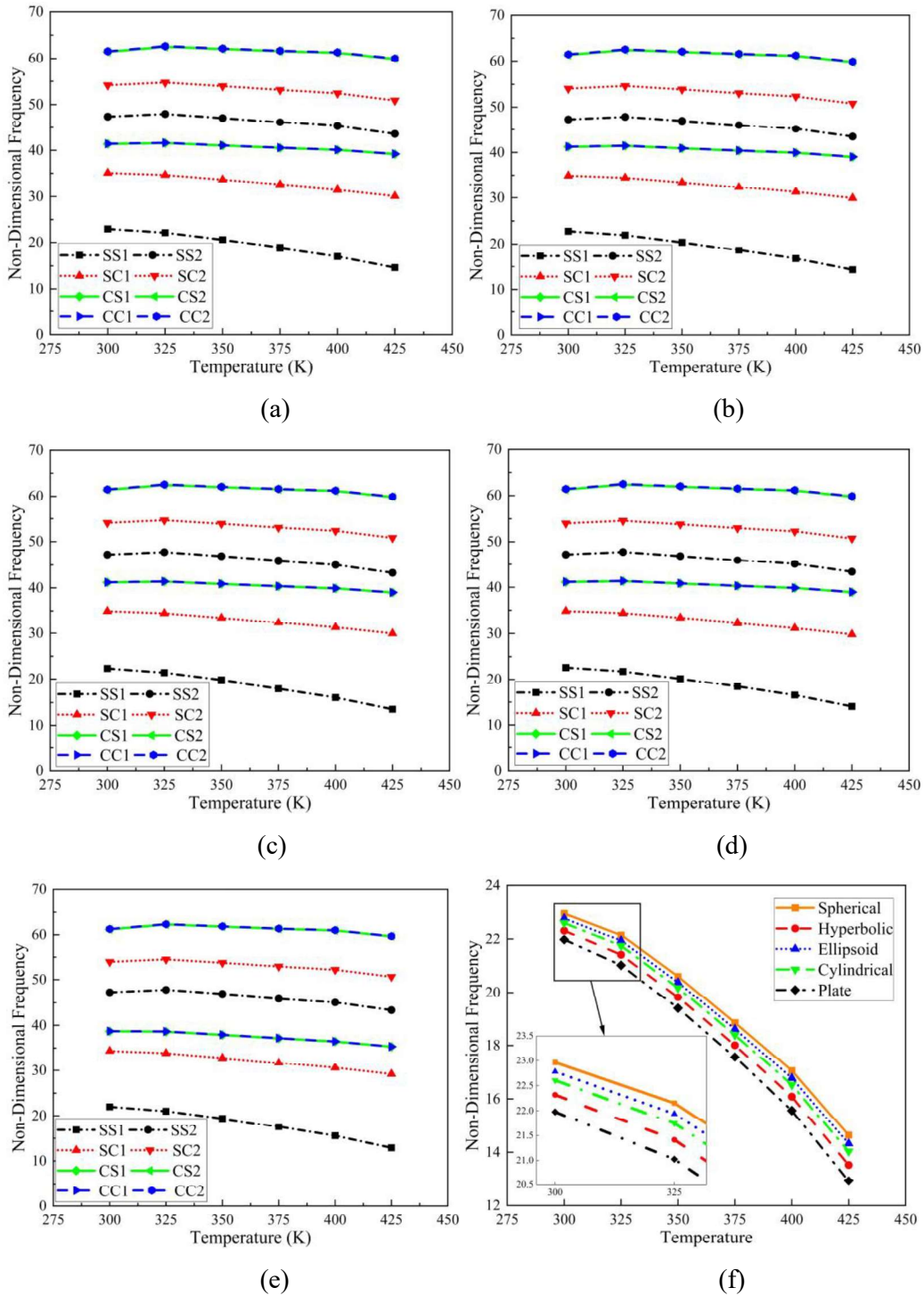
Figure 4.5: Effect of temperature on the first two natural frequencies of doubly-curved sandwich (a) spherical, (b) elliptical, (c) hyperbolic, (d) cylindrical shells, (e) sandwich plate, and (f) influence of temperature on the fundamental natural frequency of the sandwich shells with SS boundary conditions.
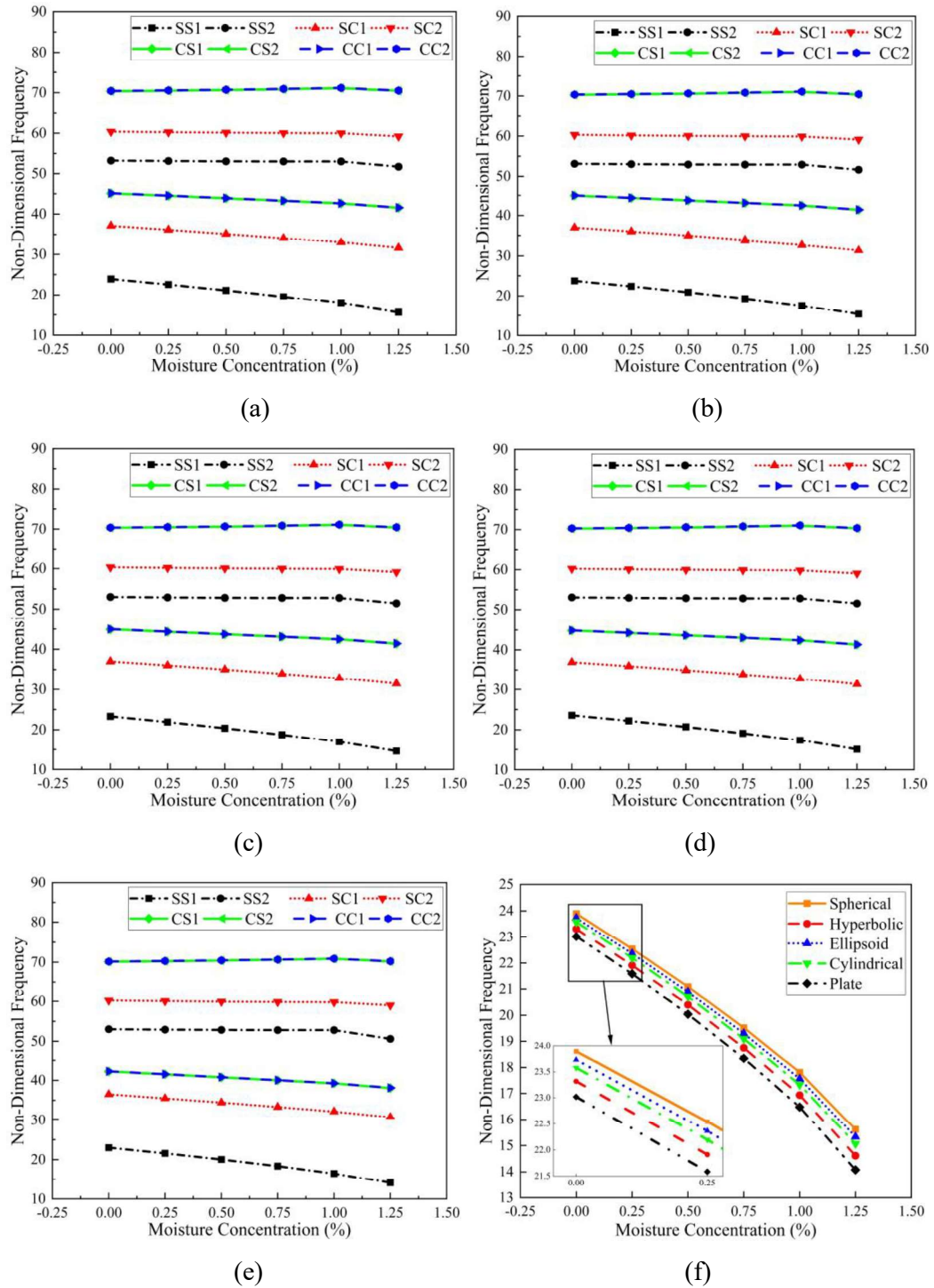
Figure 4.6: Effect of moisture on the first two natural frequencies of the doubly-curved sandwich (a) spherical, (b) elliptical, (c) hyperbolic, (d) cylindrical shells, (e) sandwich plate, and (f) influence of moisture on the fundamental natural frequency of the sandwich shells with SS boundary conditions.
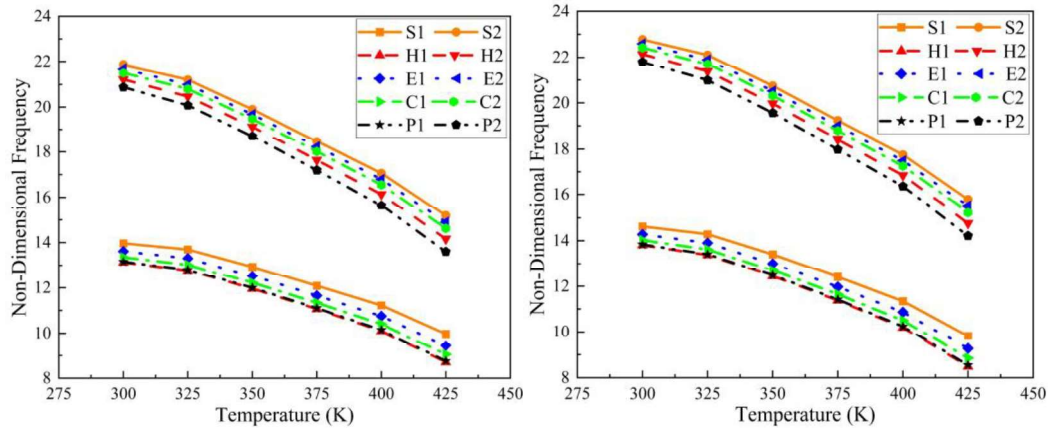
(a) (b)
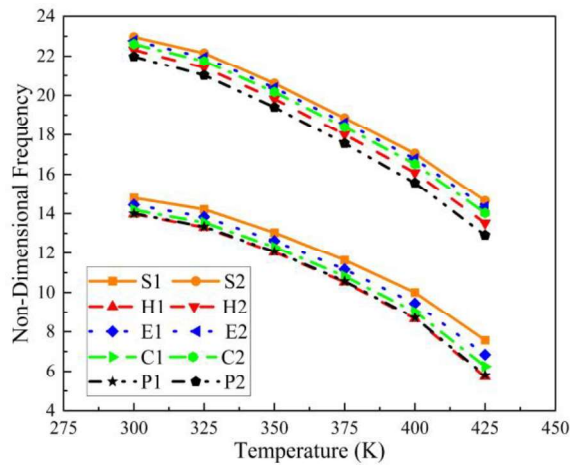
(c)

Figure 4.7: Effect of temperature on the natural frequency of doubly-curved LCS shells for CNT volume fractions of (a) 0.12, (b) 0.17, and (c) 0.28.

(a) (b)

(c)
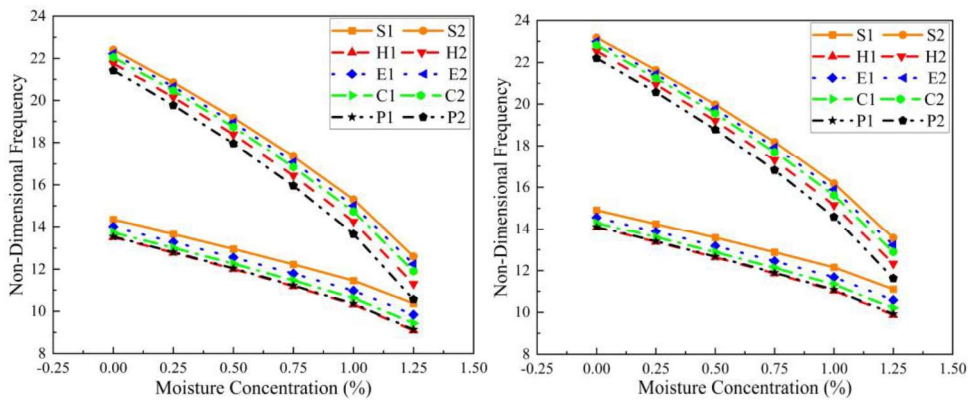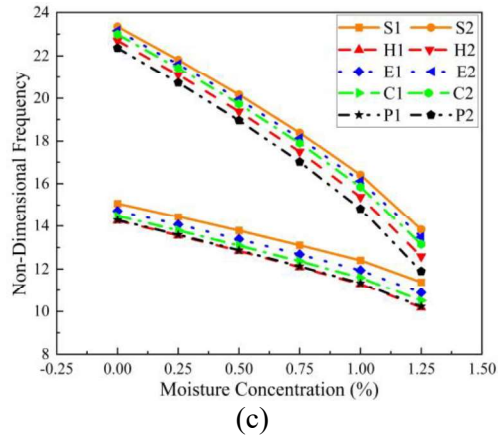
Figure 4.8: Effect of moisture on the natural frequency of doubly-curved LCS shells for CNT volume fractions of (a) 0.12, (b) 0.17, and (c) 0.28

(a)

(b)

(c)

(d)
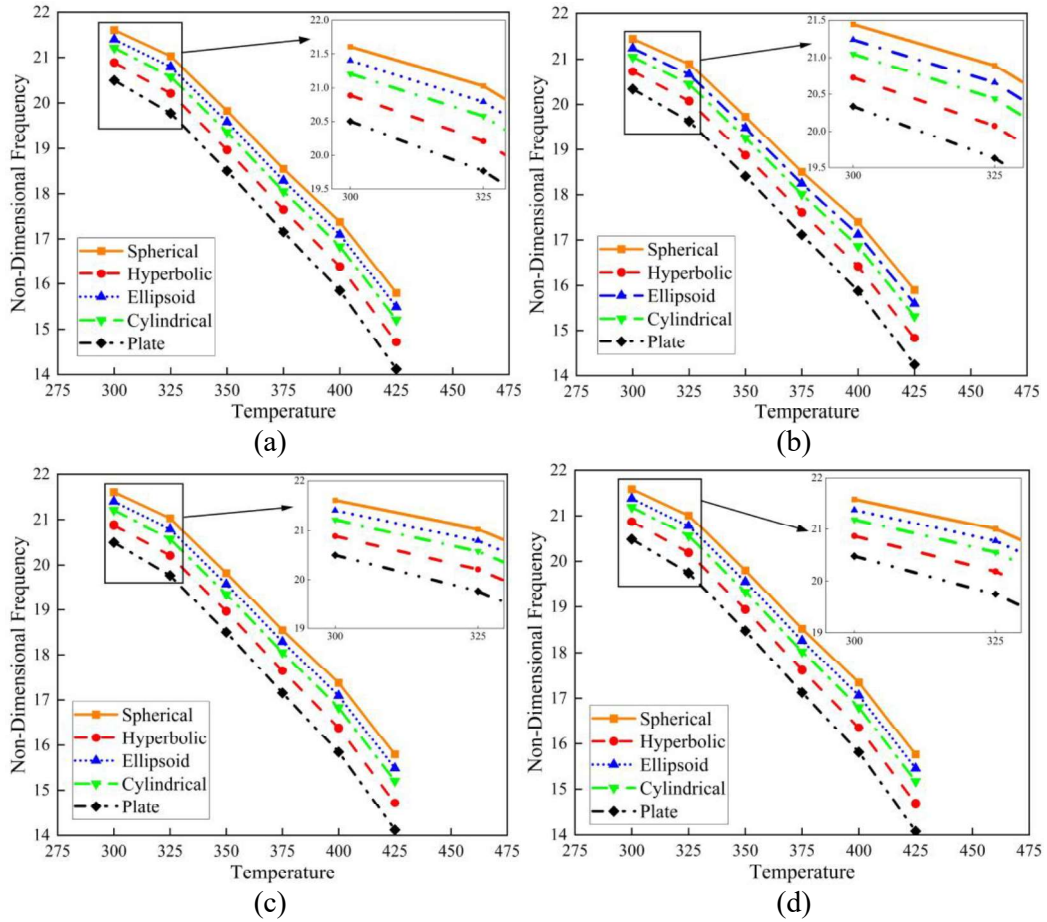
Figure 4.9: Effect of temperature on the natural frequency of the doubly-curved LCS shells for gradation pattern of (a) FG-X, (b) FG-O, (c) FG-V, and (d) FG-UD type.

(a)

(b)

(c)

(d)
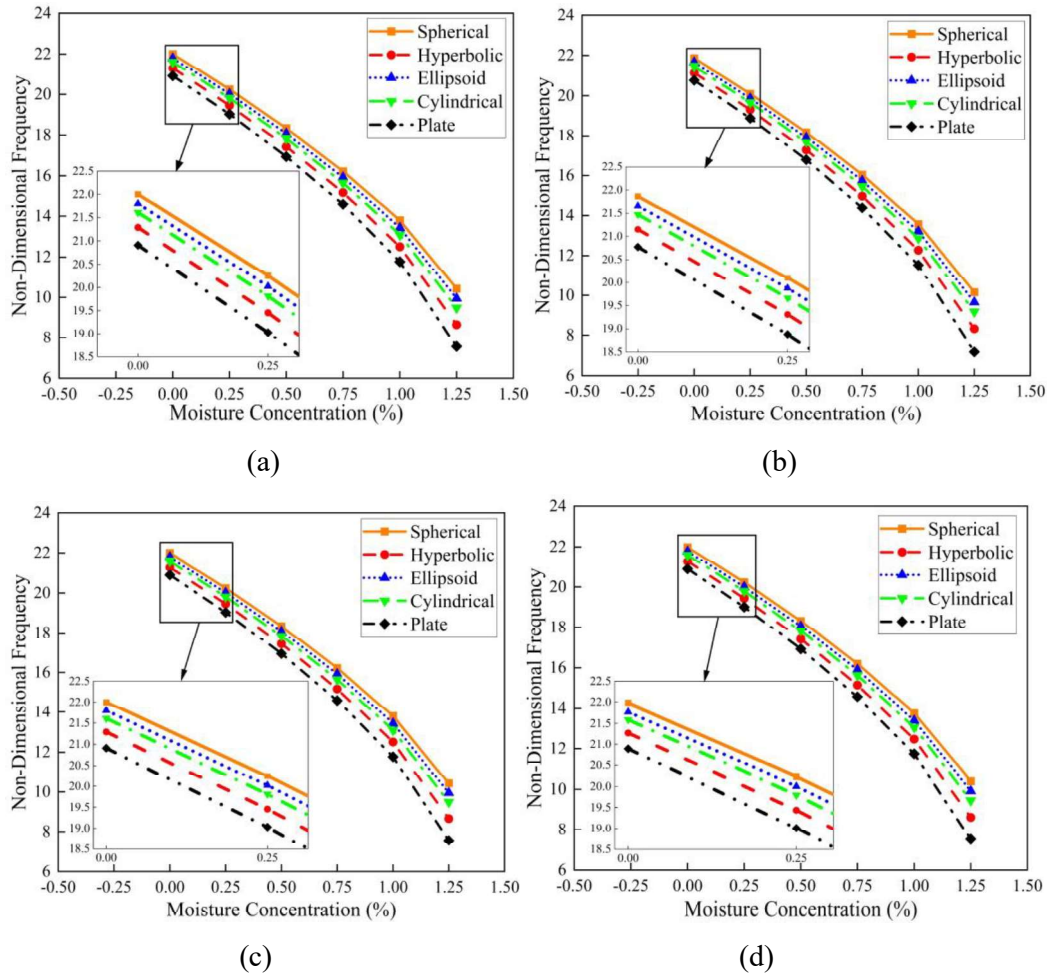
Figure 4.10: Effect of moisture on the natural frequency of the doubly-curved LCS shells for gradation pattern of (a) FG-X, (b) FG-O, (c) FG-V, and (d) FG-UD type.

The influence of radius to length (R/a) ratio on the vibration characteristics of doubly-curved sandwich shells operating at 425 K temperature for different boundary conditions is studied. The CNTRC core with FG-X gradation and 0.17 volume fraction is considered. The aspect ratios considered are $a/b = 2$ and $a/H = 10$. It is obvious from Figure 4.11 that the system's natural frequency reduces considerably with an increase in R/a ratios for all the boundary constraints considered. As the R/a ratio reached 10^{30} (large value), the fundamental frequency of all the considered doubly-curved sandwich shell structures coincides with the frequency of flat sandwich plates. This is mainly due to the transformation of shell structures into the flat plates with a drastic increase in radius value, i.e., the curved plates with higher radius will enact as the plate structures (Reddy, 2003). As the R/a ratio increases from 1 to 10^{30},

the highest percentage reduction in the fundamental frequency of 42.38 % is observed for all spherical shells with CC boundary conditions. The least reduction of 14.58 % is seen for hyperbolic sandwich shell structure with SS edge constraints. Similar variations in natural frequencies are also noticed for the doubly-curved sandwich structures operating at a 1.25 % moisture concentration environment, as revealed in Figure 4.12. The maximum reduction in the fundamental frequency of 40.92 % is noticed for a spherical sandwich shell with CC boundary conditions, whereas the hyperbolic sandwich shell produced the lowest reduction of 14.01 %.
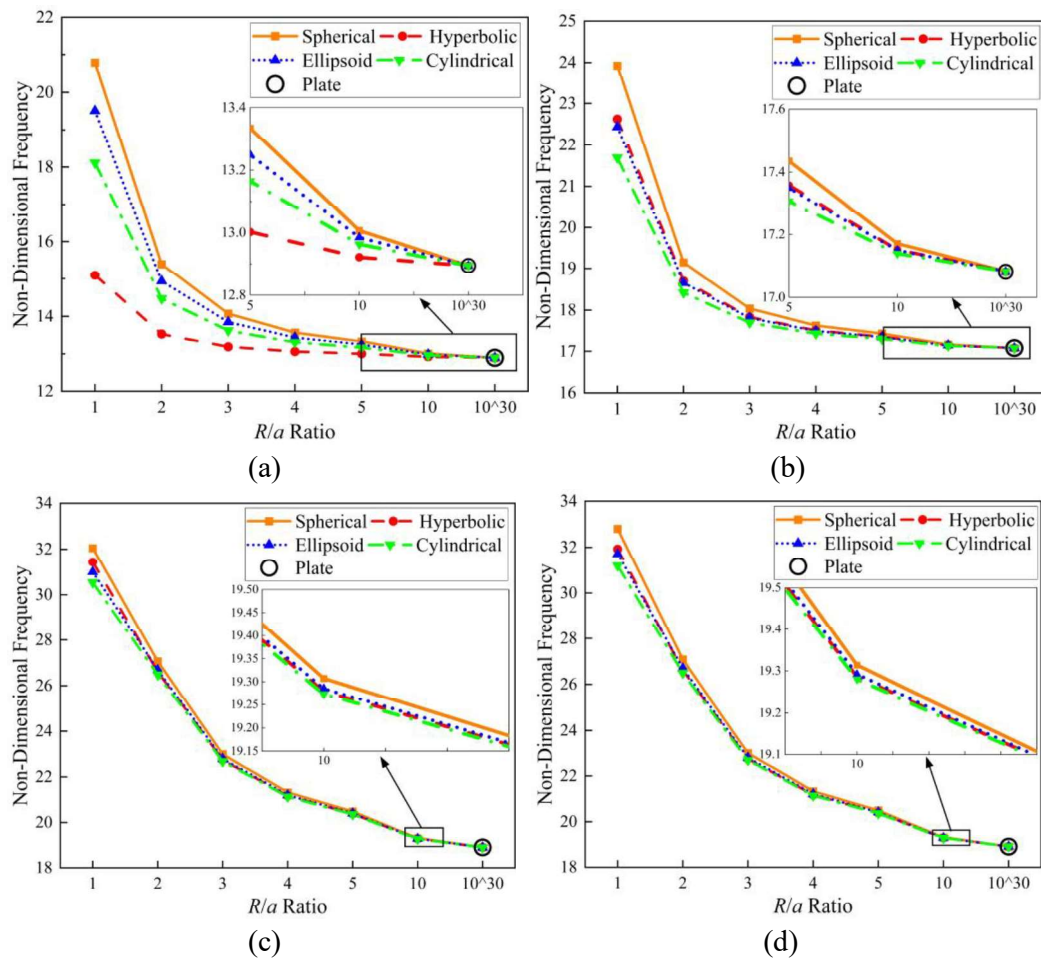
Figure 4.11: Effect of temperature and *R/a* ratios on the natural frequency of doubly-curved LCS shells for (a) SS, (b) SC, (c) CS, and (c) CC boundary conditions.
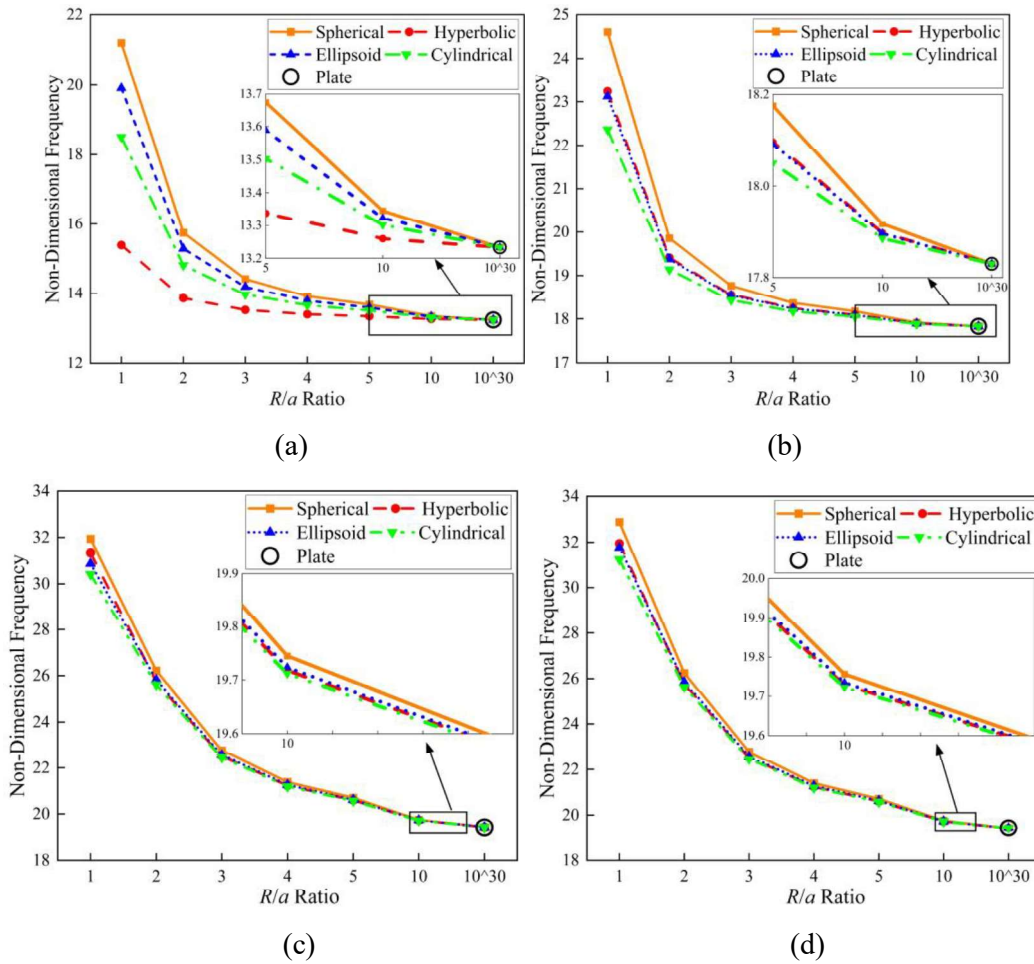
Figure 4.12: Effect of moisture and R/a ratios on the natural frequency of doubly-curved LCS shells for (a) SS, (b) SC, (c) CS, and (c) CC boundary conditions.

In this section, the combined effect of the radius to length (R_1/a) and radius to width (R_2/b) ratio of the doubly-curved sandwich shells operating in elevated thermal (400 K) and moisture (1 %) environments has been discussed. The first three natural frequencies obtained for the sandwich shell (with $a/b = 1$, $a/H = 10$, $t_c/t_f = 1$) with uniformly distributed CNTRC core under CS edge constraints are tabularized in Tables 4.6 and 4.7. The results show that the natural frequency of the system considerably reduces with an increase in R_1/a and R_2/b ratios for all the CNT volume fractions considered. Figures 4.13 (a) and (b) encompass the influence of skew angle on the doubly-curved sandwich shells operating at 400 K temperature and 1 % moisture concentration, respectively. The CNT volume fraction of 0.12 is considered to obtain the FG-X graded CNTRC core. The SC boundary constraint is used to

analyze doubly-curved sandwich shells with an a/b ratio of 1, a/H ratio of 50, R/a ratio of 10, and t_c/t_f ratio of 1. The results indicate that with an increase in skew angle, the structure's natural frequency increases considerably for thermal and moisture environmental conditions. It is mainly due to a rise in the structure's stiffness with an increase in the skew angles (Garg *et al.*, 2006). It is worth noting that for higher values of skew angles (skew angles > 45º), the natural frequency of all the doubly-curved sandwich shells tends to converge (except for flat plate structure). In the presence of the thermal environment, as the skew angle increases from 0º to 60º, the cylindrical sandwich shell shows the highest percentage increment in the frequency of 122 % and the lowest of 102 % for the spherical panel. Similarly, in the presence of a moisture environment, the spherical sandwich shell shows the lowest increase in the frequency of 90.33 % and the highest variation of 110 % for the cylindrical sandwich shell.

(a)   (b)
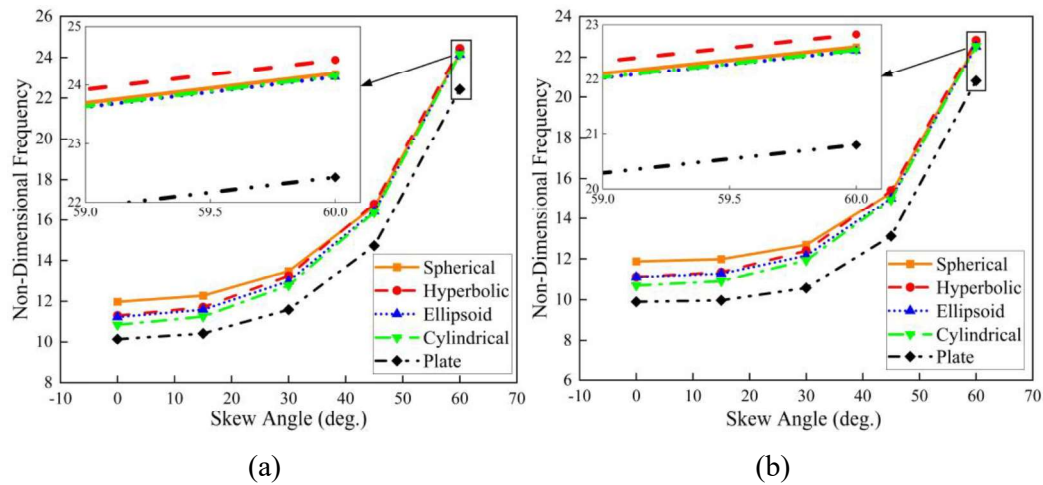
Figure 4.13: Effect of skew angle on the natural frequency of doubly-curved LCS shells for SC boundary condition operating at (a) 400 K temperature and (b) 1 % moisture concentration.

Figures 4.14 (a) and (b) elaborate the influence of t_c/t_f ratio on the doubly-curved sandwich shells operating at 325 K temperature and 0.25 % moisture concentration, respectively. The sandwich shells with a/b Ratio of 1, a/H Ratio of 50, R/a ratio of 10, the skew angle of 15º under CC boundary conditions were considered for the analysis. The CNT volume fraction of 0.17 is imposed for the FG-O type CNTRC core. It is apparent from the outcomes that the fundamental frequency of the shell structures reduces with an increase in t_c/t_f ratio. The trend in the variation of

natural frequencies is may be due to the reduction in stiffness of the sandwich shell (Dat *et al*., 2020). For the sandwich shell operating at 325 K, the minimum reduction of 38.10 % was observed in the frequency value for the spherical shell structure. In contrast, for the flat sandwich plate, the maximum reduction of 67.12 % is noted. Similarly, for structures operating at a 0.25 % moisture environment, the minimum reduction of 19.07 % is sighted for spherical shells, and the maximum of 21.90 % is perceived for the flat plate structure.

(a)   (b)
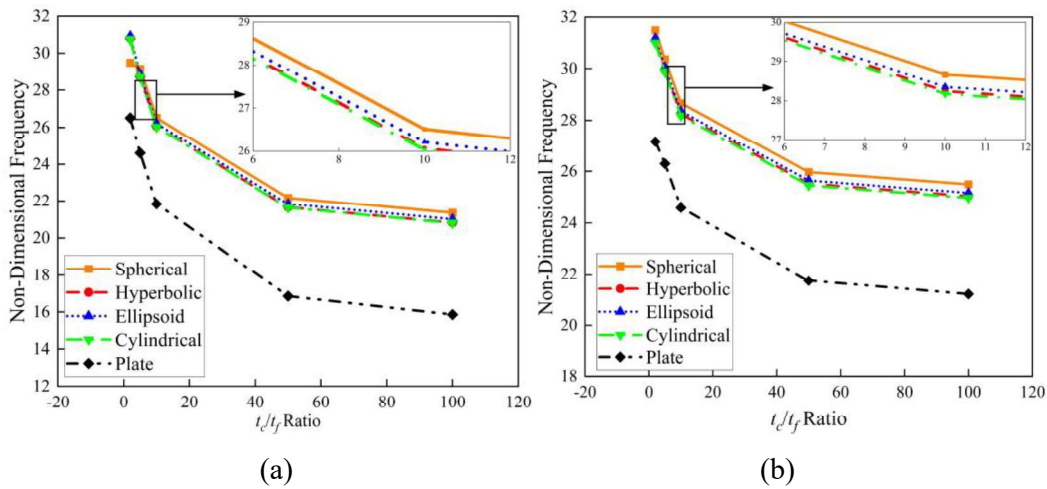
Figure 4.14: Effect of t_c/t_f ratio on the natural frequency of clamped doubly-curved LCS shells operating at (a) 325 K temperature and (b) 0.25 % moisture concentration.

Additionally, the study is also extended to understand the influence of *a/b* and *a/H* ratios on the vibration response of sandwich shells operating in high thermal and moisture environments. The doubly-curved sandwich shells with uniformly distributed CNTRC core having a skew angle of 30⁰ under SS edge constraints were considered for the analysis. Tables 4.8 and 4.9 presents the influence of *a/b* and *a/H* ratios on the natural frequency of the sandwich shells operating in 325 K and 0.25 % moisture concentration environments.

From the results, it is observed that the natural frequency increases with a rise in *a/b* and *a/H* ratios. This is due to an increase in stiffness of the sandwich shell structure with an increase in *a/b* and *a/H* ratios (Garg *et al*., 2006). However, it is also noticed that for *a/H* > 50, the natural frequency of the sandwich structures reduces with an increase in the *a/H* ratio. With the rise of the *a/H* ratio from 2 to 100, the structure transforms from thick to thin.

Table 4.6: Effect of R_1/a and R_2/b ratios on the natural frequency of doubly-curved LCS shells in the presence of thermal environment (400 K).

R_1/a	R_2/b	$V^*_{CNT}= 0.12$			$V^*_{CNT}= 0.17$			$V^*_{CNT}= 0.28$		
		1	2	3	1	2	3	1	2	3
2	2	21.1856	21.9504	23.3659	22.5933	24.2059	25.4457	23.6488	24.9136	26.5751
	5	20.6535	21.5037	23.2721	22.0793	23.7843	25.4004	23.1585	24.4991	26.5526
	10	20.5430	21.4278	23.2402	21.9732	23.7125	25.3783	23.0580	24.4284	26.5348
	100	20.4738	21.3913	23.2114	21.9070	23.6778	25.3554	22.9957	24.3941	26.5144
5	2	13.6619	16.8856	21.9594	15.0072	19.1162	24.2538	15.5294	19.7915	24.9728
	5	12.9560	16.7591	21.5448	14.3445	19.0314	23.8637	14.8857	19.7186	24.5900
	10	12.8275	16.7301	21.4801	14.2252	19.0101	23.8028	14.7705	19.6995	24.5302
	100	12.7612	16.7099	21.4540	14.1643	18.9942	23.7781	14.7120	19.6847	24.5059
10	2	12.0233	15.6266	21.9480	13.4142	17.9312	24.2488	13.8046	18.5079	24.9695
	5	11.2801	15.5084	21.5457	12.7264	17.8534	23.8704	13.1315	18.4401	24.5984
	10	11.1552	15.4855	21.4850	12.6121	17.8373	23.8134	13.0201	18.4256	24.5425
	100	11.0998	15.4721	21.4626	12.5620	17.8272	23.7923	12.9714	18.4162	24.5217
100	2	11.3581	15.1546	21.7106	12.7803	17.4943	24.2355	13.1222	18.0364	24.9568
	5	10.6341	15.0568	21.5411	12.1142	17.4337	23.8680	12.4678	17.9844	24.5966
	10	10.5241	15.0420	21.4842	12.0140	17.4244	23.8146	12.3694	17.9764	24.5442
	100	10.4861	15.0365	21.4652	11.9794	17.4209	23.7967	12.3355	17.9733	24.5267

Table 4.7: Effect of R_1/a and R_2/b ratios on the natural frequency of doubly-curved LCS shells in the presence of moisture environment (1 %).

R_1/a	R_2/b	$V^*_{CNT}= 0.12$			$V^*_{CNT}= 0.17$			$V^*_{CNT}= 0.28$		
		1	2	3	1	2	3	1	2	3
2	2	21.1856	21.9504	23.3659	22.5933	24.2059	25.4457	23.6488	24.9136	26.5751
	5	20.6535	21.5037	23.2721	22.0793	23.7843	25.4004	23.1585	24.4991	26.5526
	10	20.5430	21.4278	23.2402	21.9732	23.7125	25.3783	23.0580	24.4284	26.5348
	100	20.4738	21.3913	23.2114	21.9070	23.6778	25.3554	22.9957	24.3941	26.5144
5	2	13.6619	16.8856	21.9594	15.0072	19.1162	24.2538	15.5294	19.7915	24.9728
	5	12.9560	16.7591	21.5448	14.3445	19.0314	23.8637	14.8857	19.7186	24.5900
	10	12.8275	16.7301	21.4801	14.2252	19.0101	23.8028	14.7705	19.6995	24.5302
	100	12.7612	16.7099	21.4540	14.1643	18.9942	23.7781	14.7120	19.6847	24.5059
10	2	12.0233	15.6266	21.9480	13.4142	17.9312	24.2488	13.8046	18.5079	24.9695
	5	11.2801	15.5084	21.5457	12.7264	17.8534	23.8704	13.1315	18.4401	24.5984
	10	11.1552	15.4855	21.4850	12.6121	17.8373	23.8134	13.0201	18.4256	24.5425
	100	11.0998	15.4721	21.4626	12.5620	17.8272	23.7923	12.9714	18.4162	24.5217
100	2	11.3581	15.1546	21.7106	12.7803	17.4943	24.2355	13.1222	18.0364	24.9568
	5	10.6341	15.0568	21.5411	12.1142	17.4337	23.8680	12.4678	17.9844	24.5966
	10	10.5241	15.0420	21.4842	12.0140	17.4244	23.8146	12.3694	17.9764	24.5442
	100	10.4861	15.0365	21.4652	11.9794	17.4209	23.7967	12.3355	17.9733	24.5267

Table 4.8: Effect of *a/b* and *a/H* ratios on the natural frequency of doubly-curved LCS shells in the presence of thermal environment (325 K).

a/b Ratio	a/H Ratio	Shell Type				
		Spherical	Hyperbolic	Ellipsoid	Cylindrical	Plate
0.5	2	2.7977	2.7904	2.7967	2.7952	2.7977
	5	5.1564	5.1542	5.1437	5.1391	5.1304
	10	7.4445	7.4398	7.4085	7.3957	7.3621
	50	13.2520	13.1360	12.727	12.5300	11.8820
	100	15.1520	11.3230	13.216	12.3860	9.4306
1	2	3.9801	3.9749	3.9776	3.9758	3.9750
	5	6.4151	6.3991	6.4044	6.3982	6.3833
	10	9.3179	9.2767	9.2877	9.2708	9.2206
	50	16.4080	15.8310	15.9660	15.7180	14.8050
	100	18.5260	16.3170	16.9090	15.9400	11.7590
2	2	6.3067	6.3059	6.3064	6.3062	6.3070
	5	11.1300	11.1140	11.1250	11.1210	11.0950
	10	16.7500	16.7110	16.7350	16.7230	16.6470
	50	31.5990	31.1210	31.3910	31.2410	30.0760
	100	35.5520	33.8370	34.8080	34.2680	29.6910

Table 4.9: Effect of *a/b* and *a/H* ratios on the natural frequency of doubly-curved LCS shells in the presence of moisture environment (0.25 %).

a/b Ratio	a/H Ratio	Shell Type				
		Spherical	Hyperbolic	Ellipsoid	Cylindrical	Plate
0.5	2	2.7224	2.7159	2.7216	2.7202	2.7223
	5	5.2960	5.2940	5.2838	5.2794	5.2724
	10	7.7372	7.7332	7.7029	7.6908	7.6621
	50	12.7910	12.6695	12.2499	12.0467	11.4174
	100	14.0313	7.7439	11.9142	10.7344	6.0996
1	2	3.9462	3.9409	3.9437	3.9420	3.9414
	5	6.6044	6.5889	6.5944	6.5884	6.5757
	10	9.6622	9.6231	9.6338	9.6177	9.5740
	50	15.7337	15.1429	15.2817	15.0274	14.1301
	100	16.3169	13.7605	14.5001	13.3750	8.2480
2	2	6.1083	6.1076	6.1081	6.1079	6.1085
	5	11.4353	11.4203	11.4306	11.4265	11.4038
	10	17.4004	17.3641	17.3870	17.3764	17.3088
	50	30.8369	30.3670	30.6328	30.4859	29.3699
	100	32.0487	30.2156	31.2572	30.6804	25.8178

As the a/H ratio increases, the ratio of the stiffness matrix to the mass matrix tends to have a constant value. In turn, the minimal variation in the natural frequency of the system is observed for higher values of a/H ratios ($a/H > 50$). Whereas in some cases, the structure tends to become less stiff as it transforms from a thick plate to a thin plate, and hence a slight reduction in frequency values is observed. Many researchers made similar observations for composite structures (Reddy, 2003: Chakrabarti and Sheikh, 2004).

4.6. CONCLUSIONS

In this chapter, the influence of moisture and temperature on the free vibration response of doubly-curved SLCS shells/panels is presented. The temperature-dependent and moisture-dependent material properties of graphite-epoxy composite face sheets and CNTRC core materials are considered for the analysis. The vibration performance of the doubly-curved panel structures such as cylindrical, ellipsoidal, hyperbolic, and spherical shells is investigated along with the flat plate module. The study was also devoted to understanding the effect of functional gradation type and CNT volume fraction on the natural frequency of sandwich shells operating in elevated thermal and moisture environments. The sandwich plates with FG-X gradation were observed to be more vulnerable to thermal and moisture changes. For all the thermal and moisture conditions considered, the magnitude of natural frequency increases with an increase in a V^*_{CNT} value.

The simulation results suggest that the natural frequency of sandwich shell structures decreases with the rise in moisture and temperature values for all the shell geometry and functional gradation types considered. It was observed that the thermal and moisture environments predominantly influence the natural frequency of the flat sandwich plate structure, whereas the spherical sandwich shell emerges as a highly resistant structure for the changing environmental conditions. The effect of geometrical parameters such as skew angle, a/b Ratio, a/H Ratio, R/a ratios, and t_c/t_f ratio on the free vibration characteristics has been studied. Further, the influence of boundary conditions reveals that the shells with the CC boundary constraint exhibit a higher magnitude of non-dimensional fundamental frequencies. Meanwhile, the least magnitude is observed for the SS boundary constraints.

Chapter 5

FREE VIBRATION BEHAVIOR OF POROUS DOUBLY-CURVED SKEW LAMINATED COMPOSITE SANDWICH SHELLS WITH 3D PRINTED PLA CORE IN THERMAL ENVIRONMENT

This chapter deals with the investigation of the influence of temperature and porosity on the free vibration response of doubly-curved skew laminated composite sandwich (SLCS) shells. The temperature-dependent material properties of the graphite-epoxy face sheet and a 3D printed PLA core are considered for the analysis. Uniform temperature rise condition is considered to develop the coupled thermo-elastic relations using first-order shear deformation theory (FSDT). A comprehensive parametric study has been performed to appreciate the effect of temperature, geometric restraints, and material constraints of a laminated composite sandwich (LCS) cylindrical, ellipsoidal, hyperbolic, spherical shells, and flat plates. Further, the experimental challenges involved in studying the vibration characteristics of doubly-curved sandwich shells with 3D printed PLA core in the thermal environment are discussed.

5.1 INTRODUCTION

The quest to replace traditional materials to cope with modern engineering problems has led researchers to explore advanced materials. The materials such as carbon nano-tube reinforced composites, viscoelastic materials, functionally graded materials, etc., are being extensively investigated for application-oriented explicit problems (Joseph and Mohanty, 2017: Daikh *et al*., 2020). Fabrication of these materials to the required shape and dimension is a challenging task. Advanced manufacturing techniques such as additive manufacturing are widely being used to produce such complex structural components of prominent engineering applications. In additive manufacturing, fused deposition modeling (FDM) is a highly preferred technique to produce structures with good mechanical properties (Liu *et al*., 2019). The parts fabricated using the FDM techniques are extensively used in crewless aerial

vehicles, spacecraft structures, etc. (Galatas et al., 2018: Schubert and Dafnis, 2019). In the FDM, the thermoplastic filaments are melted through the nozzle and deposited on the printing bed. The molten filament is deposited line by line and layer by layer to obtain the desired three-dimensional (3D) product of the required dimension and shape. Hence, the FDM process is also famously known as 3D printing.

This chapter presents the influence of temperature and porosity on the free vibration characteristics of doubly-curved SLCS shells with 3D printed PLA core. The temperature-dependent material properties of the face sheet and the core materials are considered to analyze the cylindrical, ellipsoidal, hyperbolic, spherical doubly-curved sandwich shells and flat sandwich plates. The effect of the significant parameters such as a/b ratio, a/H ratio, t_c/t_f ratio, R/a ratio, skew angle, porosity distribution type, and boundary conditions on the vibrations response of the skew sandwich shells operating under different thermal environments is studied. Further, the challenges involved in the experimental investigation of the vibration study of the sandwich structures with 3D printed PLA core are explored.

5.2. PROBLEM DESCRIPTION

The mathematical formulation developed in the previous chapter is utilized to understand the vibration response of porous doubly-curved sandwich shells in the presence of elevated thermal environments. It is well established that in the presence of the thermal environment, mechanical properties of composite materials considerably reduce due to the weakening of the bond between the reinforcement and the matrix materials (Rezaei *et al*., 2018). Ram and Sinha (1991, 1992) comprehensively reported the diminishing moduli values of the graphite-epoxy composite materials in elevated thermal environments. The reported moduli values are considered as the material properties of graphite-epoxy face sheets in the current investigation. The temperature-dependent material properties of the 3D printed PLA materials obtained using a computerized universal testing machine are incorporated for the analysis.

Due to the design constraints of a nozzle and the difference in nozzle and printing bed temperatures, it is almost impossible to avoid the pores in the 3D printed products. Hence, three different types of porosity distribution patterns in the thickness

directions are considered to numerically investigate the influence of porosity on the free vibration characteristics of doubly-curved sandwich shells operating in elevated thermal environments. The effective material properties of the porous 3D printed core for all the porosity distribution patterns considered are computed as follows: (Xue *et al*., 2019)

Type-1: Porosity is maximum at the mid-plane and minimum at the top and bottom surface of the core.

$$
\begin{aligned}
E_e &= E_1\left(1 - e_0 \cos\left(\pi z / 2t_c\right)\right) \\
G_e &= G_1\left(1 - e_0 \cos\left(\pi z / 2t_c\right)\right) \\
\rho_e &= \rho_1\left(1 - e_m \cos\left(\pi z / 2t_c\right)\right)
\end{aligned}
\tag{5.1}
$$

Type-2: Porosity is maximum at the bottom surface and minimum at the top surface of the core.

$$
\begin{aligned}
E_e &= E_1\left(1 - e_0 \cos\left(\pi z / 2t_c + \pi/4\right)\right) \\
G_e &= G_1\left(1 - e_0 \cos\left(\pi z / 2t_c + \pi/4\right)\right) \\
\rho_e &= \rho_1\left(1 - e_m \cos\left(\pi z / 2t_c + \pi/4\right)\right)
\end{aligned}
\tag{5.2}
$$

Type-3: Porosity is uniformly distributed through the thickness of the core.

$$
\begin{aligned}
E_e &= E_1\left(1 - e_0 \eth\right) \\
G_e &= G_1\left(1 - e_0 \eth\right) \\
\rho_e &= \rho_1\sqrt{\left(1 - e_m \eth\right)} \\
\eth &= 1/e_0 - 1/e_0\left(2/\pi\sqrt{1/e_0} - 2\pi + 1\right)^2
\end{aligned}
\tag{5.3}
$$

where, e_0 and e_m are porosity coefficient and porosity coefficient for mass density, respectively. Pictorial representations of the porosity distribution types are presented in Figure 5.1.

The three-point and two-point Gaussian integration rules are used to resolve the matrices corresponding to the bending and shear deformations, respectively. The shear correction factor 5/6 is considered for the analysis. The simulations are

performed for doubly-curved sandwich shells considering all sides simply supported (SS) and clamped (CC) boundary conditions.

(a)   (b)   (c)
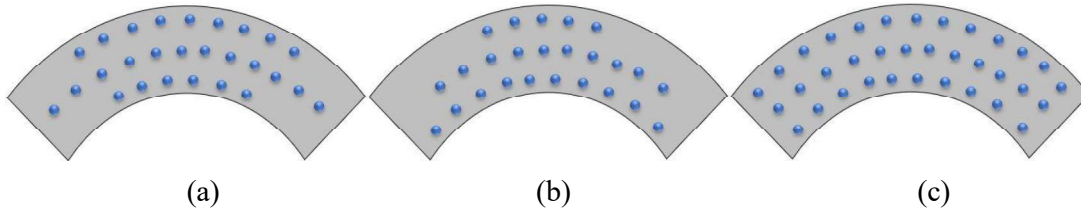
Figure 5.1: The porosity distribution types across the thickness of the 3D printed PLA core of the doubly-curved sandwich shell (a) type-1, type-2, and (c) type-3.

5.3. RESULTS AND DISCUSSIONS

In this study, the material properties of the graphite-epoxy composite material are chosen from the literature. The temperature-dependent material properties of the 3D printed PLA materials are obtained using a computerized universal testing machine (H75KS, Tinius Olsen, UK) in line with the ASTMD-638. Firstly, the dog bone-shaped tensile test samples (shown in Figure 5.2 (a)) printed using 'Pratham 5.0' 3D printer are thermally aged for 12 hours in a thermal chamber (Ultra Thermo Scientific, India). The thermal chamber is capable of preserving the desired temperature with an accuracy of ±1 K is used for the experimentation. The printing parameters considered to produce the tensile test samples are tabulated in Table 5.1. Four temperatures intervals like 300 K, 325 K, 350 K, and 375 K were selected for the investigation. Then the tensile tests are performed on the thermally aged samples (shown in Figures 5.2(b) and 5.2(c)). For accurate evaluation of modulus values of the PLA material, the tests are conducted on three samples for every desired temperature. The stress-strain curves obtained from the tensile tests are plotted in Figure 5.2(d). The average elastic modulus and standard deviation results computed from the stress-strain curves are presented in Table 5.2.

Table 5.1: Printing Parameters Considered.

Description	Unit	Value
Platform temperature	⁰C	60
Nozzle temperature	⁰C	220
Printing speed	mm/min	45
Infill Percentage	%	80
Layer Height	mm	0.2
Print Accuracy	mm	±1
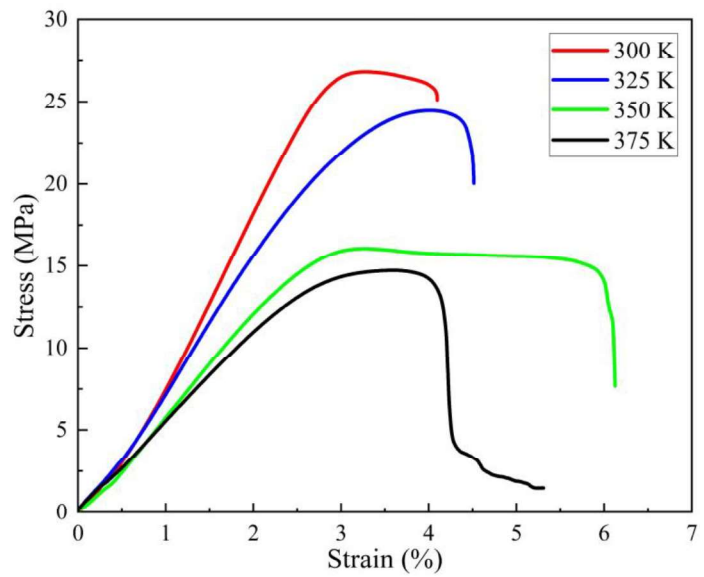
Figure 5.2: Pictorial representation of (a) 3D printed PLA tensile test specimen, (b) tensile test set up, (c) centrally broken specimen, and (d) stress v/s strain curves for thermally aged samples.

From the tensile test results, it is evident that the elastic modulus of the 3D printed PLA sample reduces considerably with an increase in temperature. The stress-strain curves demonstrate that the percentage strain at a breakpoint is the highest for the samples thermally aged at 350 K. Similarly, the standard deviation of elastic

modulus values of the samples thermally aged at 350 K is much higher compared to other temperatures. To reason the behavior of PLA samples thermally aged 350 K, the differential scanning calorimetry (DSC) tests are performed. The DSC tests were performed with a heating rate of 10 °C/min, and the obtained results are plotted in Figure 5.3. From the DSC test results, the glass transition temperature (T_g) of the PLA sample was found to be at 336.07 K. The polymer substrate changes from a rigid glassy material to a soft material near to its T_g value (Becker and Locascio, 2002). Due to the increased softness in the material, the PLA flows excessively near the T_g value. Hence, the percentage strain at 350 K is much higher compared to other temperatures. Similarly, due to induced plasticity near the T_g value, it is difficult to achieve the repeatability of the results of tensile tests at 350 K. Which in turn, causes the drastic increase in the standard deviation of the modulus values of the PLA sample at 350 K.

Table 5.2: Effect of Temperature on the elastic modulus of 3D printed PLA samples.

Temperature (K)	Young's Modulus (GPa)
300	0.7255 ± 0.0608
325	0.7225 ± 0.0107
350	0.6559 ± 0.1029
375	0.5115 ± 0.0665
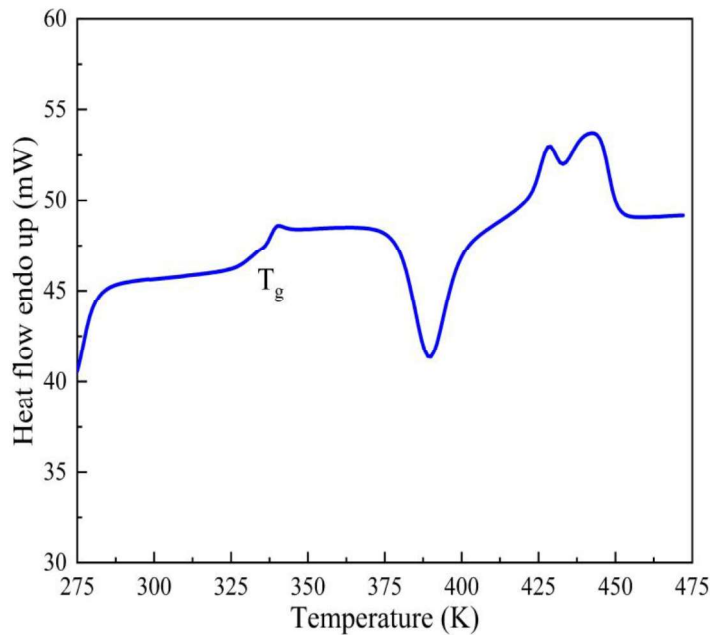
Figure 5.3: The DSC test results of the 3D printed PLA sample.

5.3.1. Convergence and validation study

The convergence and validation studies are performed with the well-established models available in the open literature in order to ensure the accuracy and legitimacy of the developed FE model. The isotropic square steel plate with porosity distribution along the thickness with material properties as E = 200 GPa, υ = 0.3, G = 76.923 GPa, ρ = 7850 kg/m^3 is considered for the study. The non-porous square steel plates with an a/H ratio of 10 and 100 under SS and CC boundary conditions are considered for convergence study. The obtained natural frequencies are non-dimensionalized as,

$$\omega_n = \omega \left(\frac{b}{\pi} \right)^2 \left(\frac{\rho H}{D} \right)^{\frac{1}{2}}$$

(5.4)

where, ω_n and ω are the non-dimensional frequency and frequency of the system in rad/sec, respectively. The results presented in Table 5.3 indicate that the non-dimensional natural frequency values converge at the mesh size of 16×16. Consequently, the 16×16 mesh size is adopted throughout the simulations. From the results, it is also evident that the first five natural frequency values obtained from the current formulations are in good agreement with the published results. Further, the validation study is performed on the square porous steel plate with various porosity distribution patterns and porosity coefficient values. The obtained results for SS and CC boundary conditions are tabulated in Tables 5.4 and 5.5, respectively. From the outcomes, it is apparent that the results obtained are in excellent conformity with the results reported in the literature (Xue *et al.*, 2019). The slight difference between the results is may be due to the utilization of different plate theories and computational schemes used to generate the results.

5.3.2. Numerical results

The effect of temperature and porosity on the free vibration characteristics of doubly-curved LCS shells are investigated for the SS and CC boundary conditions. The doubly-curved sandwich shell with a/b = 1, a/H = 40, t_c/t_f = 5, and 0°/C/0° orientation is considered for the analysis. The first two modes of vibration of porous spherical sandwich shells operating in elevated thermal environments with different porosity distribution patterns are presented in Figure 5.4.

Table 5.3: Convergence study of the ω_n of a non-porous square steel plate.

Boundary Conditions	a/H	Mode	Present (2 × 2)	Present (4 × 4)	Present (8 X 8)	Present (12 × 12)	Present (16 × 16)	Xue et al. (2019)	Mahi et al. (2015)
SS	100	1	2.7530	2.0120	1.9994	1.9994	1.9994	1.9993	1.9993
		2	22.2046	5.1779	4.9965	4.9963	4.9964	4.9958	4.9955
		3	25.3998	5.1779	4.9965	4.9963	4.9964	4.9958	4.9955
		4	36.3072	9.7385	8.0002	7.9906	7.9907	7.9888	7.9885
		5	36.3072	10.2578	9.9836	9.9848	9.9854	9.9871	9.9839
	10	1	1.9280	1.9409	1.9448	1.9454	1.9456	1.9317	1.9319
		2	6.1371	4.6030	4.6655	4.6743	4.6772	4.6084	4.6098
		3	6.1371	4.6030	4.6655	4.6743	4.6772	4.6084	4.6098
		4	6.9022	6.4331	6.5012	6.5136	6.5179	6.5234	6.5234
		5	6.9022	6.4331	6.5012	6.5136	6.5179	6.5234	6.5234
CC	100	1	2.9778	4.5156	3.6565	3.6429	3.6422	3.6419	3.6420
		2	72.2873	8.3222	7.4760	7.4253	7.4226	7.4222	7.4214
		3	72.28730	8.3222	7.476	7.4253	7.4225	7.4222	7.4214
		4	103.2230	11.2653	11.1873	10.9503	10.9368	10.9342	10.9336
		5	103.2230	11.9208	13.3694	13.2949	13.2915	13.3012	13.2911
	10	1	2.7468	3.2780	3.3125	3.3164	3.3176	3.2954	3.3092
		2	10.3223	6.0758	6.3311	6.3573	6.3653	6.2859	6.3317
		3	10.3223	6.0758	6.3311	6.3573	6.3653	6.2859	6.3317
		4	10.9888	8.1420	8.8537	8.9297	8.9525	8.8099	8.8957
		5	10.9888	9.0432	10.4017	10.5233	10.5603	10.3790	10.5036

Table 5.4: Validation study of a square steel plate with SS boundary condition for different types of porosity.

Porosity Type	Mode	Porosity Coefficient							
		0.1		0.2		0.3		0.4	
		Xue et al. (2019)	Present	Xue et al. (2019)	Present	Xue et al. (2019)	Present	Xue et al. (2019)	Present
Type-1	1	1.9956	1.9671	1.9937	1.9339	1.9941	1.8999	1.9978	1.8652
	2	4.9866	4.9157	4.9817	4.8327	4.9826	4.7476	4.9916	4.6609
	3	4.9866	4.9157	4.9817	4.8327	4.9826	4.7476	4.9916	4.6609
	4	7.9740	7.8617	7.9660	7.7289	7.9674	7.5929	7.9815	7.4542
	5	9.9684	9.8241	9.9582	9.6583	9.9596	9.4883	9.9770	9.3150
Type-2	1	1.9718	1.9769	1.9415	1.9543	1.9075	1.9319	1.8685	1.9100
	2	4.9271	4.9400	4.8513	4.8836	4.7663	4.8277	4.6690	4.7729
	3	4.9271	4.9400	4.8513	4.8836	4.7663	4.8277	4.6690	4.7729
	4	7.8790	7.9006	7.7578	7.8104	7.6218	7.7209	7.4662	7.6332
	5	9.8498	9.8728	9.6982	9.7600	9.5283	9.6482	9.3337	9.5387
Type-3	1	1.9663	1.9504	1.9309	1.8985	1.8925	1.8431	1.8503	1.7836
	2	4.9135	4.8739	4.8250	4.7441	4.7289	4.6058	4.6235	4.4571
	3	4.9135	4.8739	4.8250	4.7441	4.7289	4.6058	4.6235	4.4571
	4	7.8572	7.7947	7.7157	7.5872	7.5620	7.3660	7.3934	7.1281
	5	9.8226	9.7405	9.6457	9.4812	9.4536	9.2047	9.2428	8.9075

Table 5.5: Validation study of a square steel plate with CC boundary condition for different types of porosity.

Porosity Type	Mode	Porosity Coefficient							
		0.1		0.2		0.3		0.4	
		Xue et al. (2019)	Present	Xue et al. (2019)	Present	Xue et al. (2019)	Present	Xue et al. (2019)	Present
Type-1	1	3.6351	3.5833	3.6316	3.5228	3.6322	3.4608	3.6387	3.3976
	2	7.4083	7.3027	7.4007	7.1794	7.4017	7.0530	7.4146	6.9242
	3	7.4083	7.30269	7.4007	7.1794	7.4017	7.05301	7.4146	6.9242
	4	10.9134	10.7602	10.902	10.5785	10.9031	10.3923	10.9217	10.2025
	5	13.2754	13.0769	13.2609	12.8561	13.2617	12.6298	13.2836	12.3991
Type-2	1	3.5918	3.6011	3.5366	3.5600	3.4746	3.5192	3.4036	3.4792
	2	7.3202	7.3388	7.2076	7.2550	7.0813	7.1719	6.9367	7.0905
	3	7.3202	7.3388	7.2076	7.2550	7.0813	7.1719	6.9367	7.0905
	4	10.7838	10.8134	10.6179	10.6900	10.4318	10.5675	10.2188	10.4475
	5	13.1182	13.1416	12.9163	12.9915	12.6899	12.8427	12.4309	12.6969
Type-3	1	3.5819	3.5528	3.5174	3.4582	3.4473	3.3574	3.3705	3.2490
	2	7.3000	7.2405	7.1685	7.0477	7.0258	6.8422	6.8691	6.6213
	3	7.3000	7.2405	7.1685	7.0477	7.0258	6.8422	6.8691	6.6213
	4	10.7541	10.6686	10.5604	10.3845	10.3501	10.0817	10.1193	9.7562
	5	13.0821	12.9656	12.8464	12.6203	12.5906	12.2523	12.3099	11.8567

It can be observed from the results that for all the boundary conditions, magnitude of temperatures, and porosity distribution types considered, the non-dimensional frequency of the system reduces considerably with an increase in temperature and porosity coefficient. It is also evident that the influence of temperature is more prominent for higher values of porosity coefficient for all the porosity distribution types considered. The spherical sandwich shells with type-2 and type-1 porosity were found to be more vulnerable to the temperature and porosity coefficient changes, respectively. Additionally, it is observed that the spherical shells with type-3 and type-2 porosity are more resistant to the change in temperature and porosity coefficient changes, respectively. It was also noticed that the clamped spherical sandwich shells pose higher resistance to the porosity coefficient and thermal variations than the simply supported case.

The investigation is also extended to understand the influence of temperature and porosity on the doubly curved laminated composite ellipsoidal, hyperbolic, cylindrical sandwich shells, and sandwich plates. The results obtained are plotted in Figures 5.5-5.8. It is apparent from the results that for all the porosity distribution types, the magnitude of temperatures, types of shell geometry, and boundary conditions, the natural frequency of the sandwich shells reduces considerably with an increase in temperature and porosity coefficient values. It can also be noted that the doubly-curved sandwich shell with type-2 porosity is more resistant for all the shell types considered. However, the shell type-1 porosity is most vulnerable to change in porosity coefficient values. Similarly, the sandwich shells with type-3 porosity are observed to be more resistant to temperature changes. Further, it is also observed that the doubly-curved sandwich spherical shell exhibits more resistance to the temperature changes and the flat sandwich plate was more resistant to the change in porosity coefficient values.

With the increase in temperature, the materials tend to deform proportionate to the coefficient of thermal expansion of the material and the temperature change. In two-phase materials such as composites, the deformation of the constituent materials are always different for given temperature change. It is mainly due to the variation in the thermal properties of the constituent materials. Due to the variation in thermal expansion of the constituent materials, the bond between the fiber and matrix phase of

121

the composite materials becomes weak on exposure to elevated thermal environments. The weakening of fiber and matrix bond subsequently causes the reduction in stiffness of the structure, which in turn considerably affects the natural frequency of the structure (Rath and Sahu, 2012). Furthermore, in the case of isotropic materials, the strength and modulus reduce substantially with an increase in temperature, causing the reduction in stiffness of the structure.

The pores are nothing but the voids or the gaps formed in the material during fabrication. The pores cause a loss in the effective mass of the structure, in turn reducing its strength and stiffness. On exposure to the elevated thermal environments, the materials might incoherently flow into these pores, causing changes in material properties. The inconsistent change in material properties of the porous materials on exposure to the thermal environments is one of the critical challenges to explore. In a broad scope, it is well established that the structure's stiffness reduces with an increase in porosity coefficient value, in turn significantly affecting the structure's natural frequency (Kiran *et al*., 2018, 2018a: Xue *et al*., 2019).

(a)

(b)

(c)

(d)
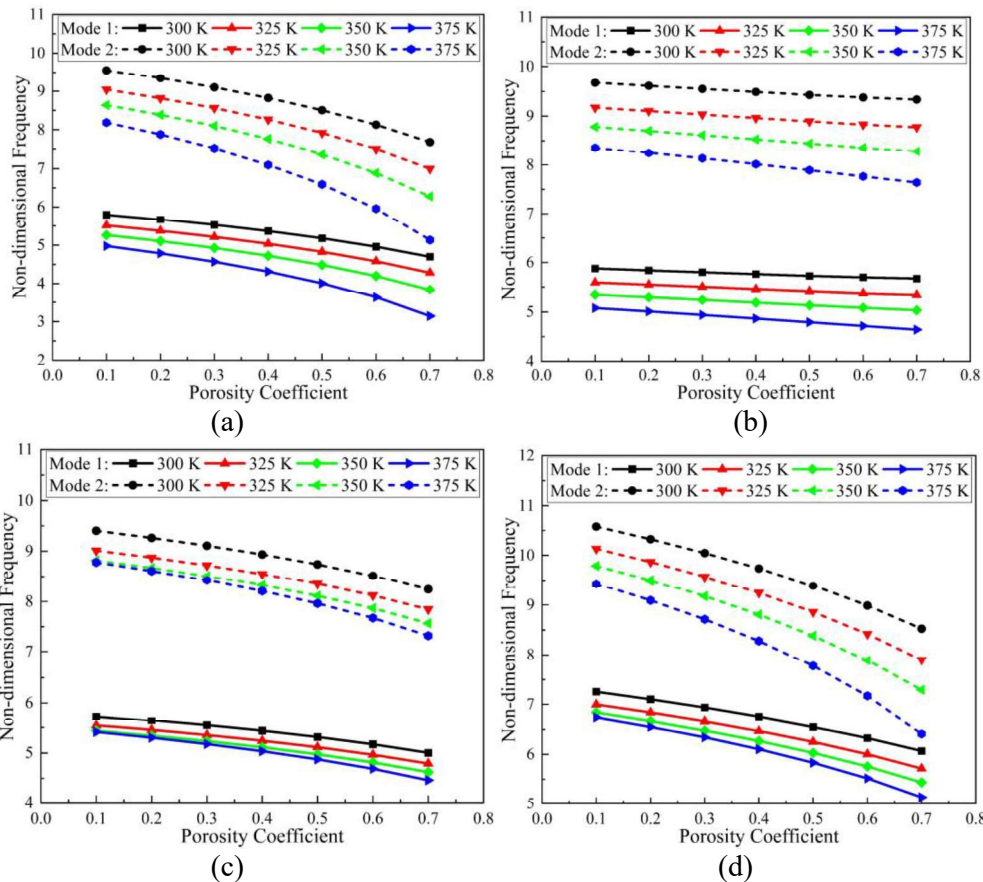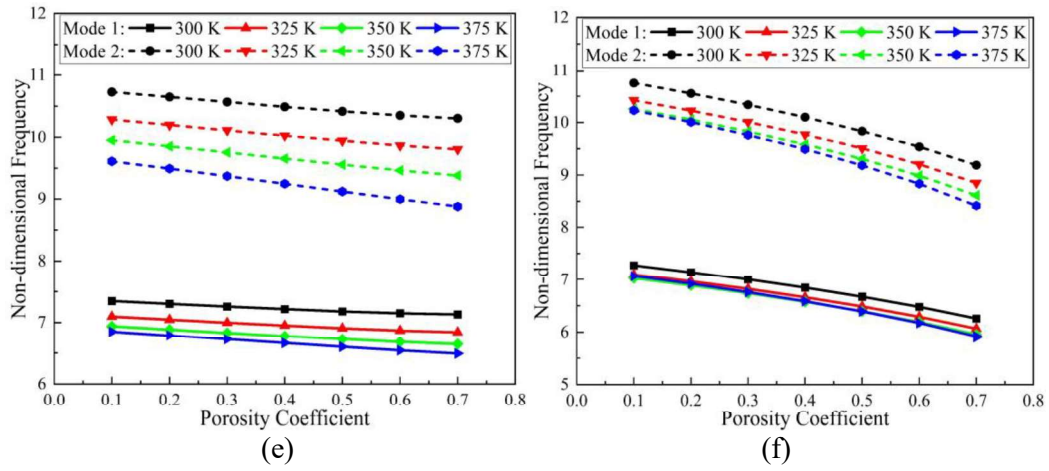
Figure 5.4: Influence of temperature and porosity on the ω_n of the laminated composite spherical shell under SS boundary condition with (a) type-1, (b) type-2, (c) type-3 porosity, and CC boundary condition with (d) type-1, (e) type-2, (f) type-3 porosity.
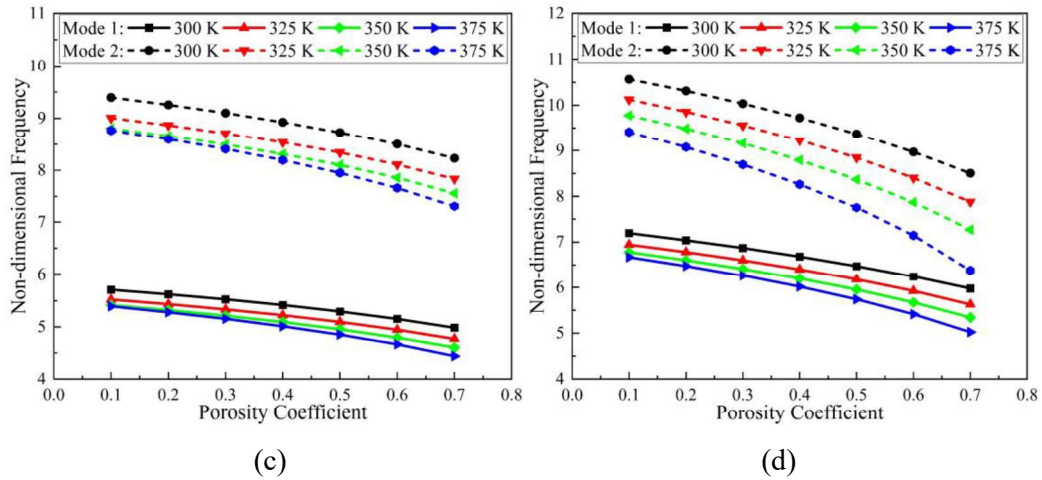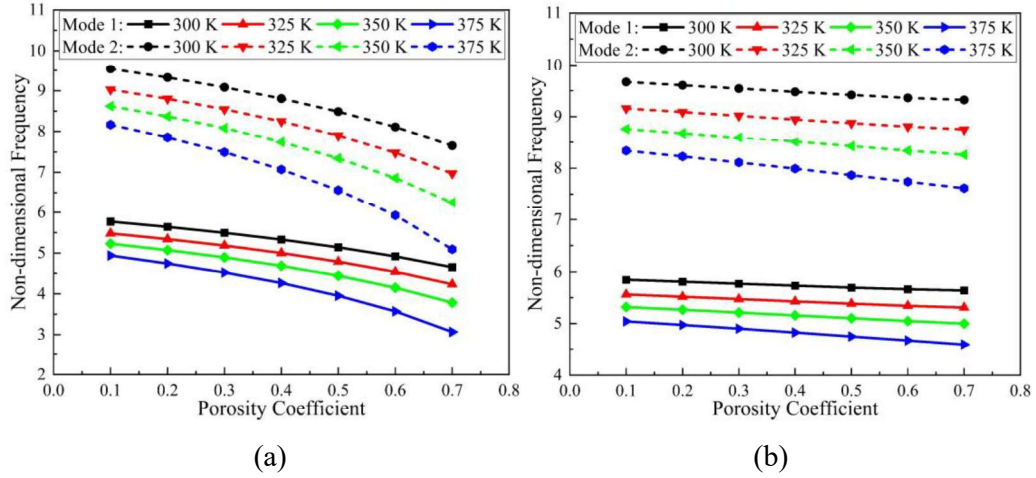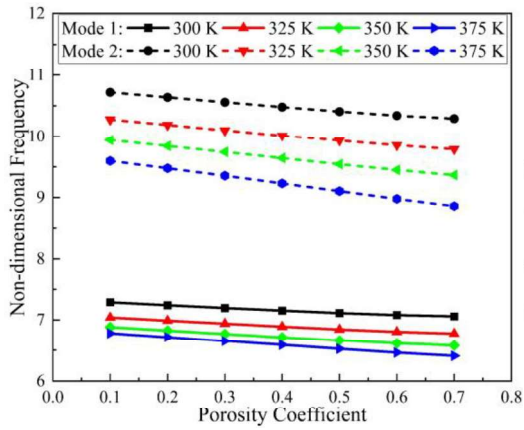
(e)
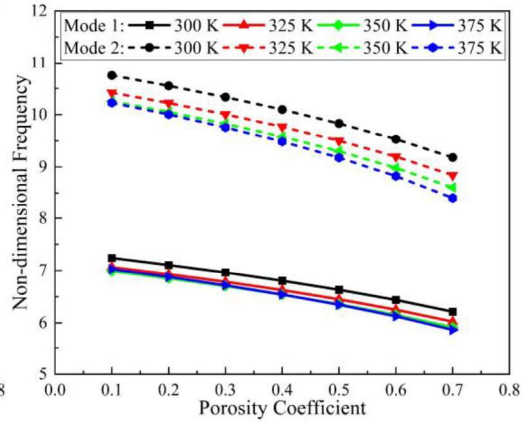
(f)

Figure 5.5: Influence of temperature and porosity on the ω_n of the laminated composite ellipsoidal shell under SS boundary condition with (a) type-1, (b) type-2, (c) type-3 porosity, and CC boundary condition with (d) type-1, (e) type-2, (f) type-3 porosity.

(a)

(b)

(c)

(d)

124
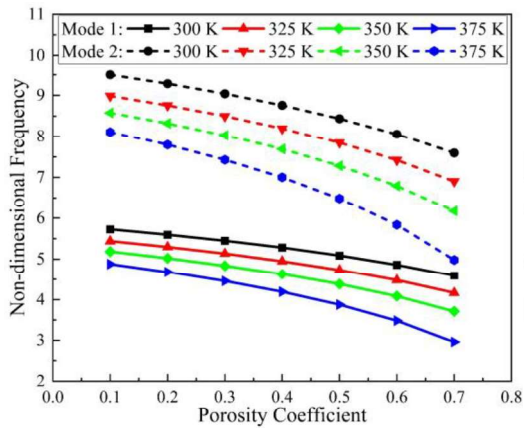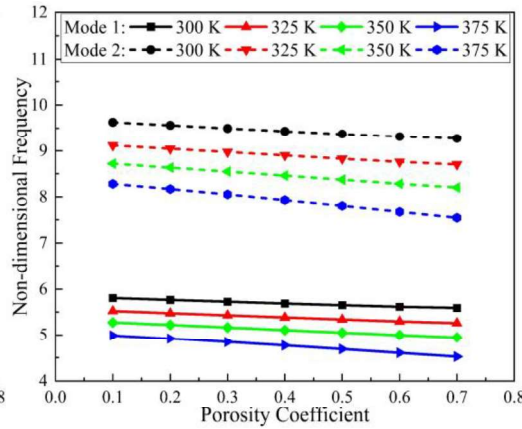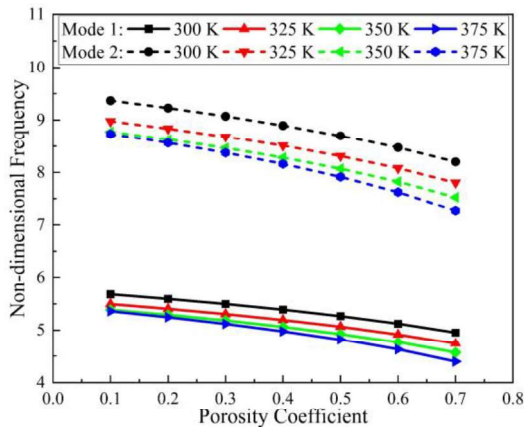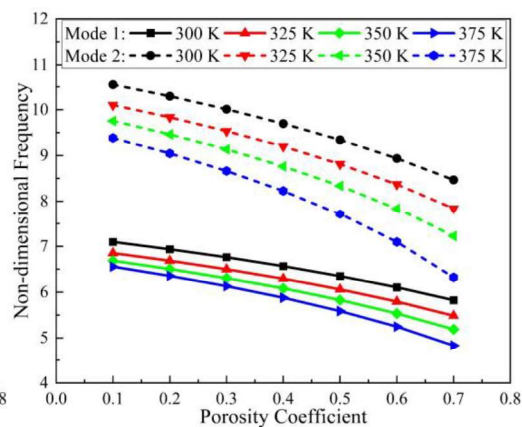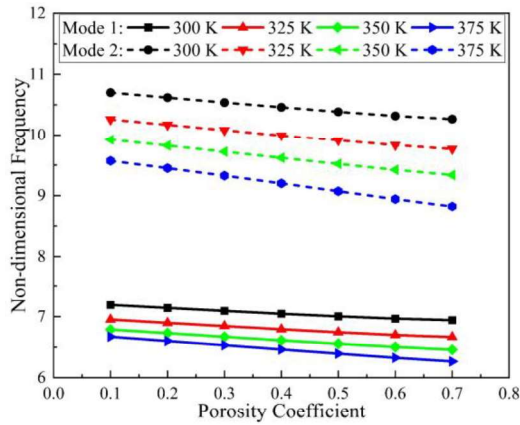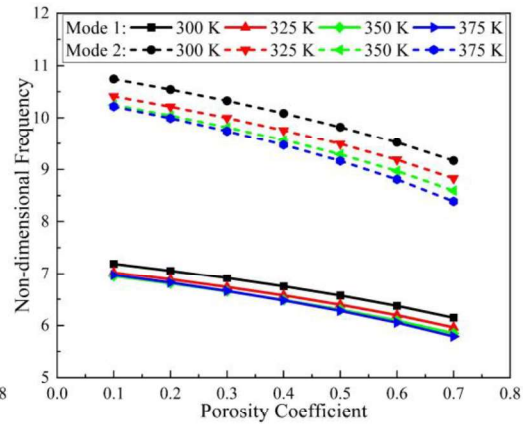
Figure 5.6: Influence of temperature and porosity on ω_n of the laminated composite hyperbolic shell under SS boundary condition with (a) type-1, (b) type-2, (c) type-3 porosity, and CC boundary condition with (d) type-1, (e) type-2, (f) type-3 porosity.
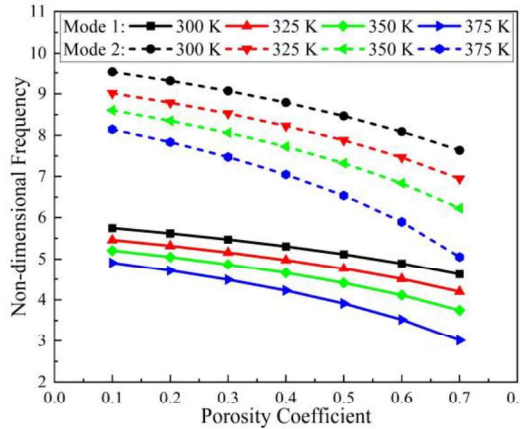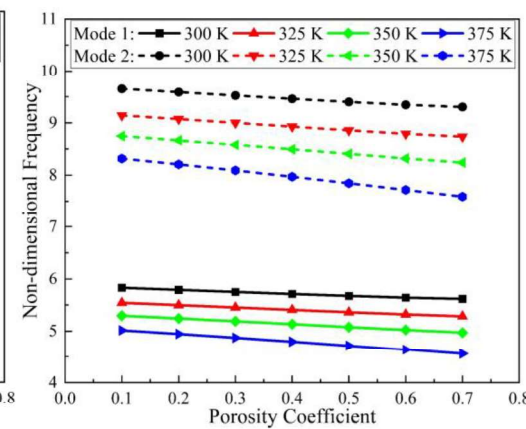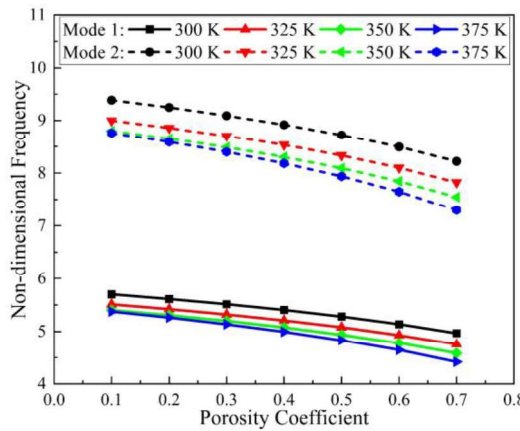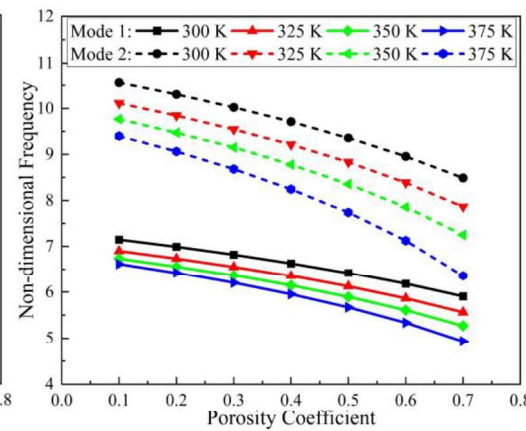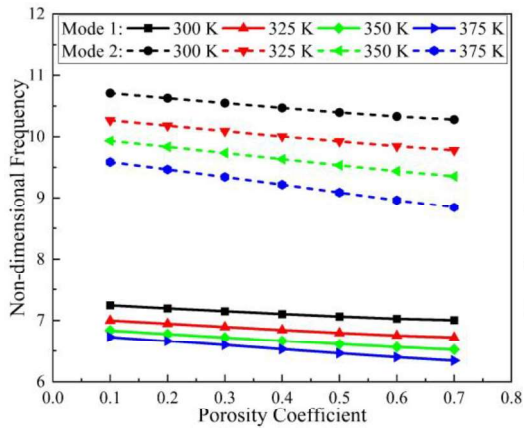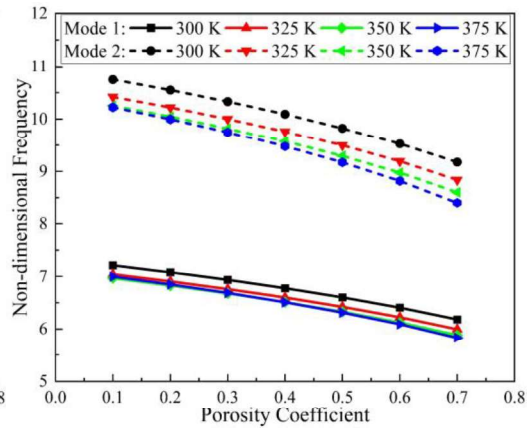
(e)   (f)

Figure 5.7: Influence of temperature and porosity on ω_n of the laminated composite cylindrical shell under SS boundary condition with (a) type-1, (b) type-2, (c) type-3 porosity, and CC boundary condition with (d) type-1, (e) type-2, (f) type-3 porosity.
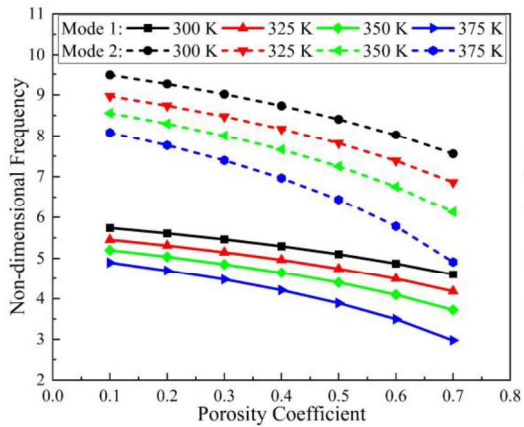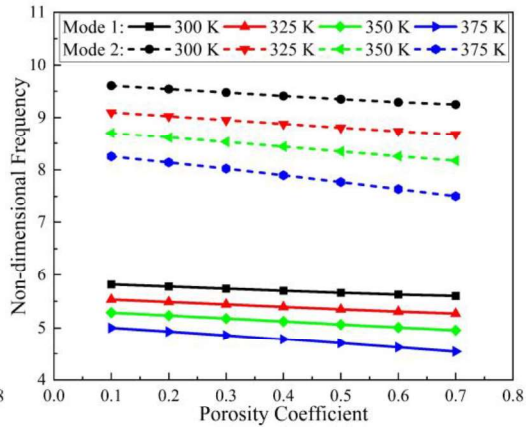
(a)   (b)
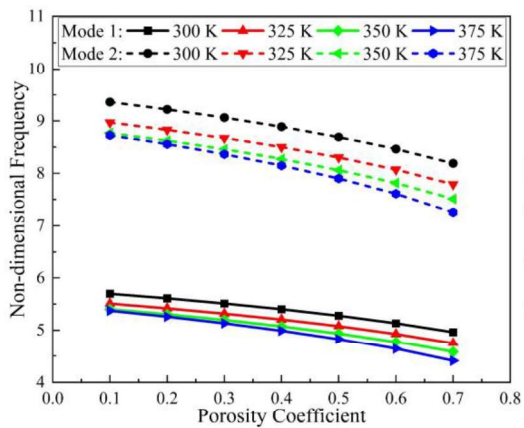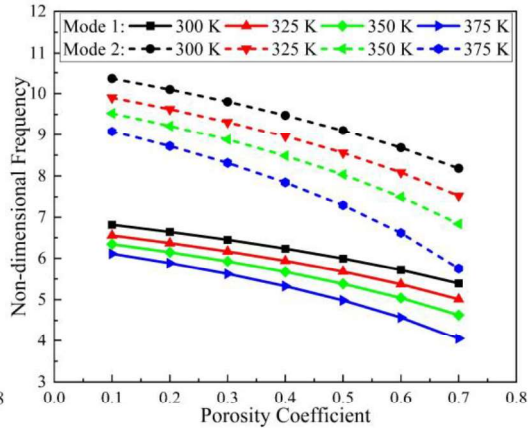
(c)   (d)
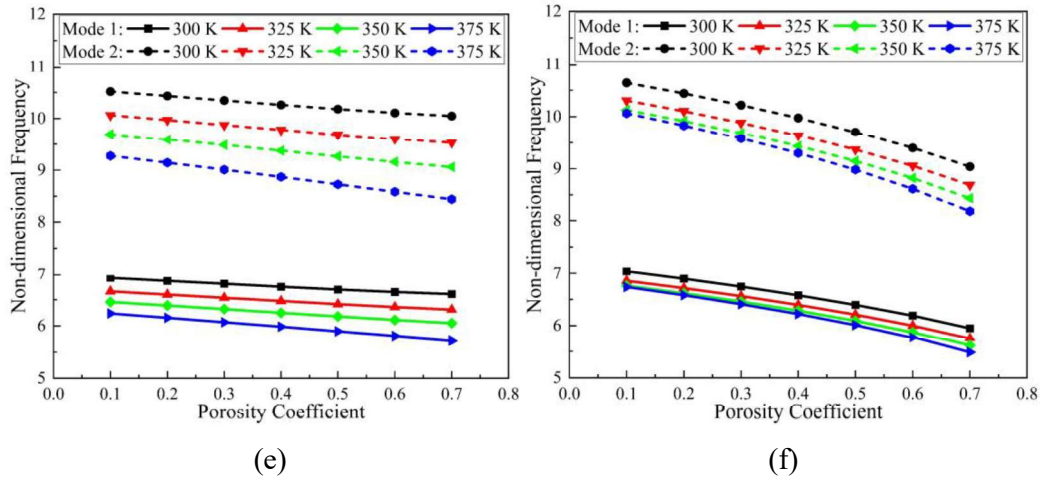
Figure 5.8: Influence of temperature and porosity on the ω_n of the LCS plate under SS boundary condition with (a) type-1, (b) type-2, (c) type-3 porosity, and CC boundary condition with (d) type-1, (e) type-2, (f) type-3 porosity.

The effect of skew angle and the porosity on the natural frequency of the doubly-curved LCS shells operating at 350 K under SS boundary condition is investigated considering $a/b = 2$, $a/H = 40$, $t_c/t_f = 1$, and 0°/C/0° orientation. The results obtained for sandwich shells are presented in Figures 5.9-5.13. The results manifest that for all the shell types considered, the natural frequency increases with an increase in skew angle and reduces with an increase in porosity coefficient value. As the skew angle increases, the stiffness of the system increases. In turn, the natural frequency of the system rises considerably (Kiran *et al*., 2018: Katariya *et al*., 2020). The results also demonstrate that the sandwich shells with type-3 porosity are more resistant to the variations in skew angle and the porosity coefficient values. Additionally, it can be noted that of all the shell types considered, the doubly-curved sandwich spherical shell is most resistant to changes in porosity coefficient values and skew angles.

The study is extended to understand the influence of porosity and a/b ratio on the free vibration characteristics of clamped doubly-curved sandwich shells (with 0°/90°/C/90°/0° orientation, $a/H = 5$, $t_c/t_f = 5$, and skew angle= 15°) operating in 325 K thermal environment. The first two natural frequencies obtained from the investigation of doubly-curved skew laminated composite spherical, ellipsoidal, hyperbolic, cylindrical shells, and flat sandwich plates are presented in Figures 5.14-5.18, respectively. The results show that the structure's natural frequency increases

considerably with an increase in *a/b* ratio values. The variation is mainly due to an increase in stiffness of the structure with an increase in the *a/b* ratio (Panda *et al*., 2013: Mishra and Sahu, 2015). The results also reveal that the doubly-curved sandwich shell with type-3 porosity is more resistant to the variations in the magnitude of the *a/b* ratio. Further, it can be noted that of all the shell types considered, the doubly-curved sandwich spherical shell is the most resistant to changes in the *a/b* ratios and porosity coefficient values.

(a)　　　　　　　　　　　　　(b)

(c)
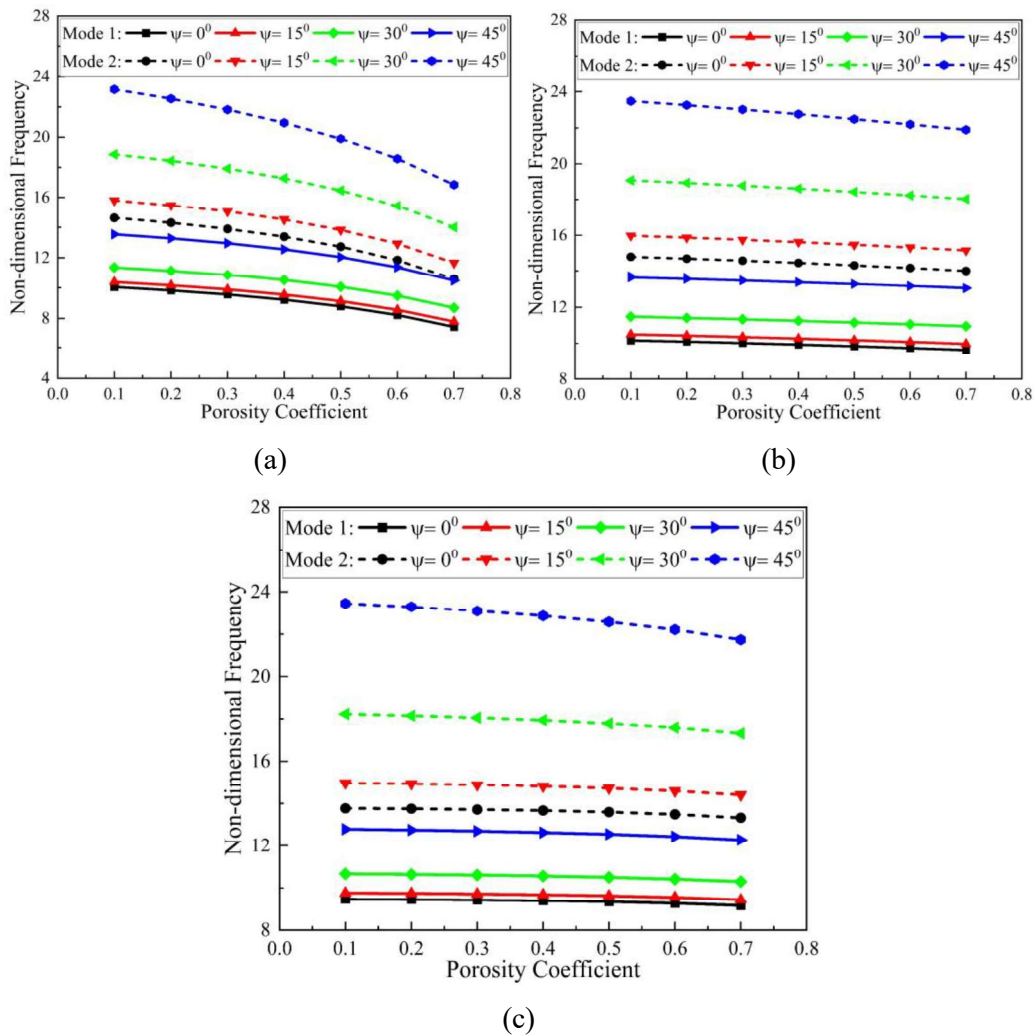
Figure 5.9: Influence of skew angle and porosity on the ω_n of the laminated composite spherical shell under SS boundary conditions with (a) type-1, (b) type-2, and (c) type-3 porosity.
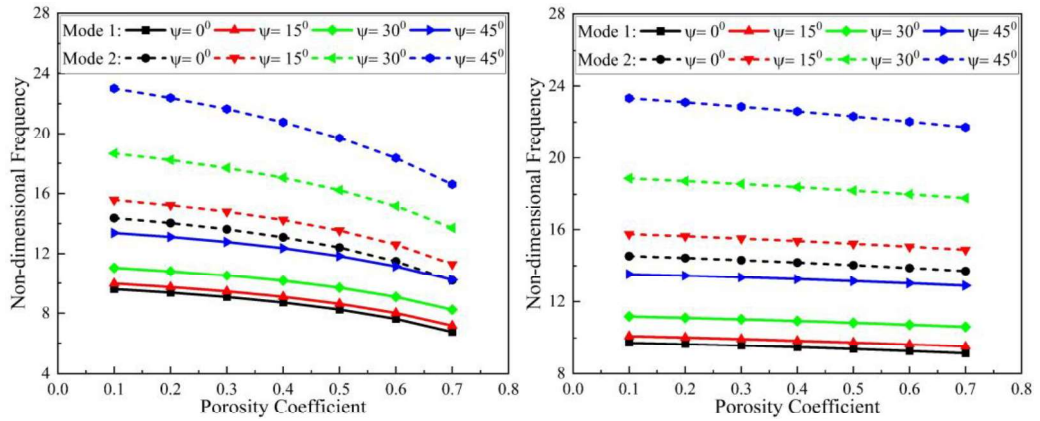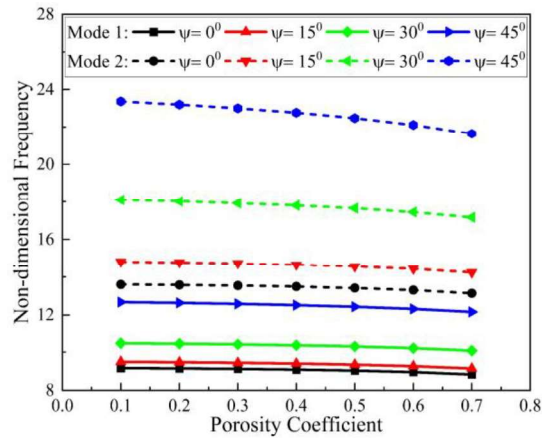
Figure 5.10: Influence of skew angle and porosity on the ω_n of the laminated composite ellipsoidal shell under SS boundary conditions with (a) type-1, (b) type-2, and (c) type-3 porosity.
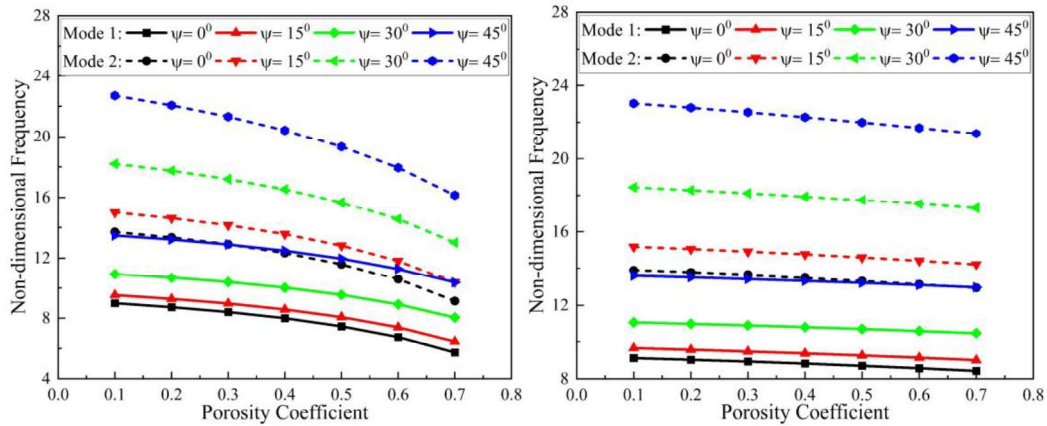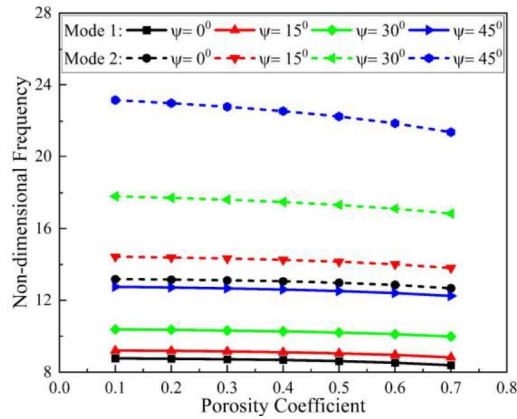
(c)

Figure 5.11: Influence of skew angle and porosity on the ω_n of the laminated composite hyperbolic shell under SS boundary conditions with (a) type-1, (b) type-2, and (c) type-3 porosity.
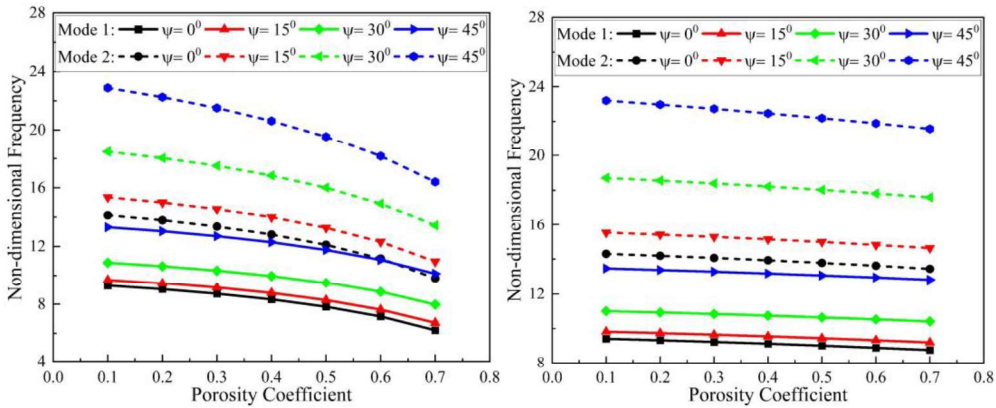
(a)

(b)
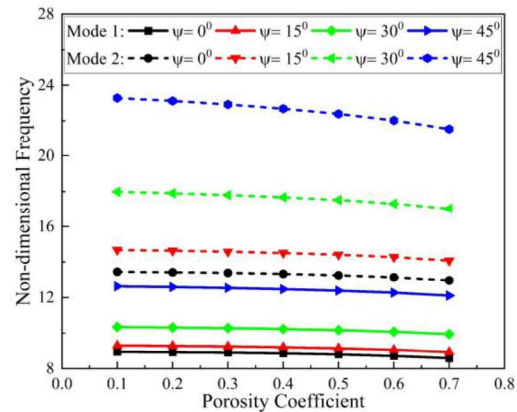
(c)

Figure 5.12: Influence of skew angle and porosity on ω_n of the laminated composite cylindrical shell under SS boundary conditions with (a) type-1, (b) type-2, and (c) type-3 porosity.
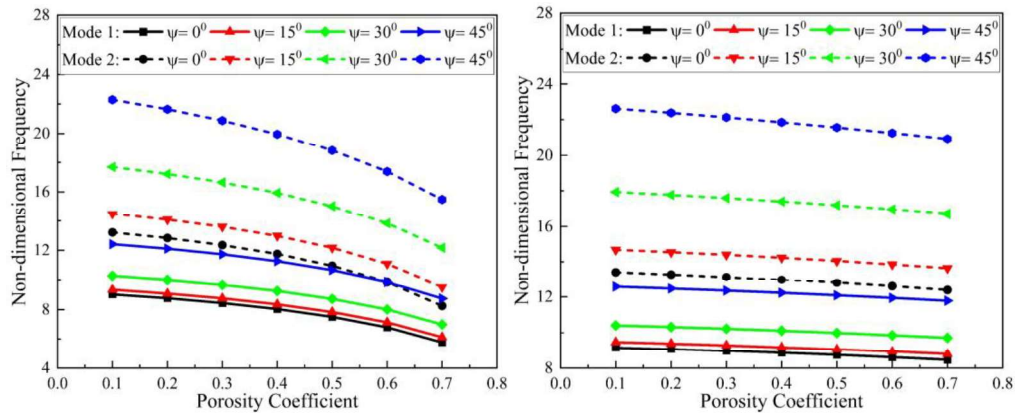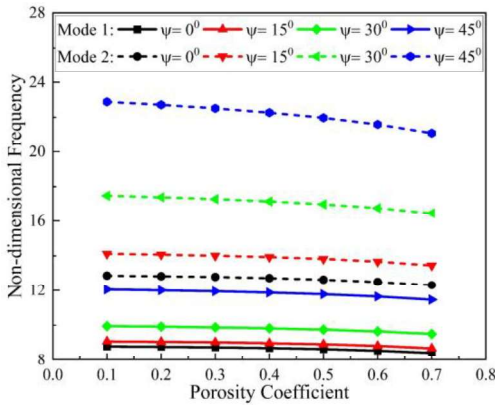
Figure 5.13: Influence of skew angle and porosity on ω_n of the LCS plate under SS boundary conditions with (a) type-1, (b) type-2, and (c) type-3 porosity.
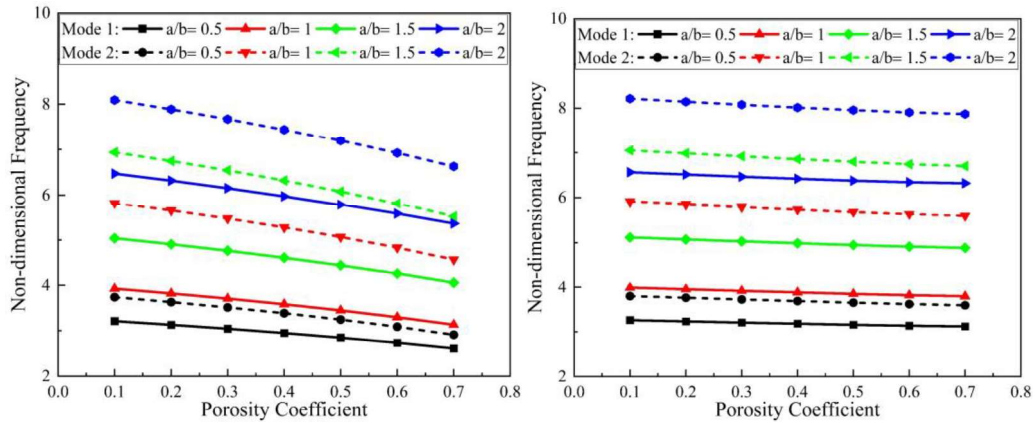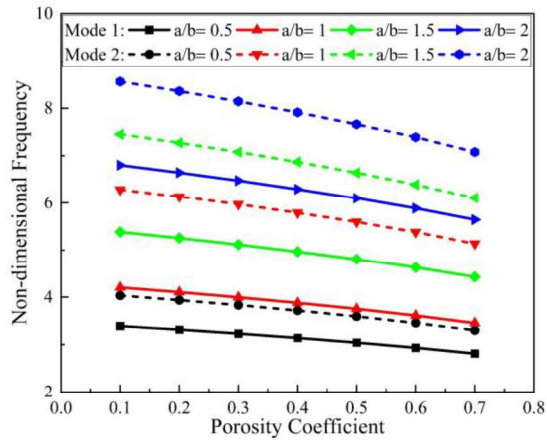
(c)

Figure 5.14: Influence of *a/b* ratio and porosity on the ω_n of the laminated composite spherical shell under CC boundary conditions with (a) type-1, (b) type-2, and (c) type-3 porosity.
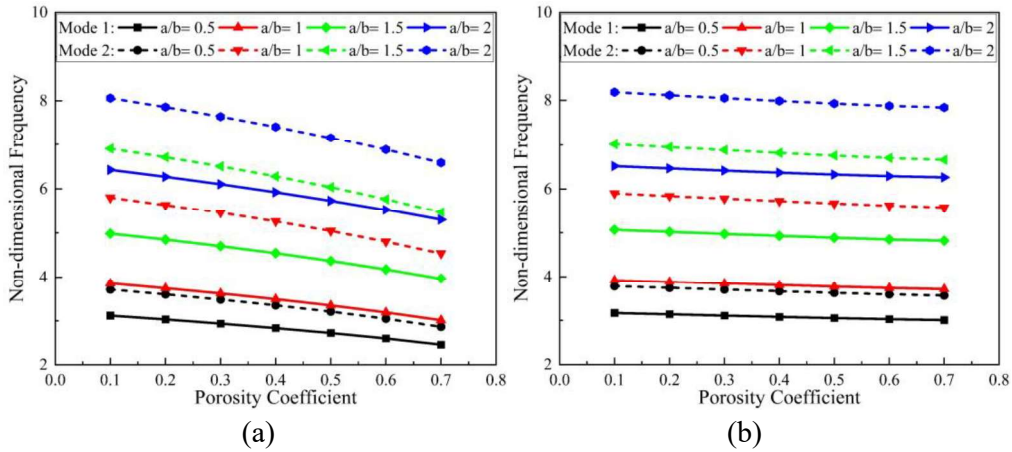
(a)

(b)
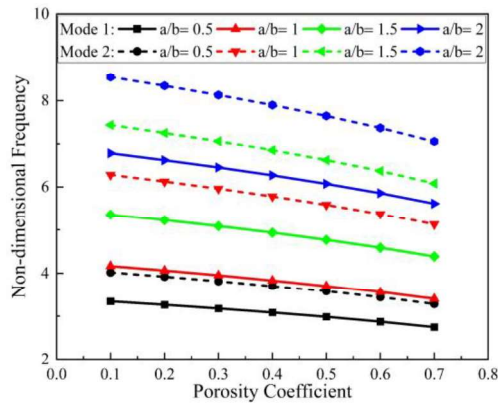
(c)

Figure 5.15: Influence of *a/b* ratio and porosity on the ω_n of the laminated composite ellipsoidal shell under CC boundary conditions with (a) type-1, (b) type-2, and (c) type-3 porosity.
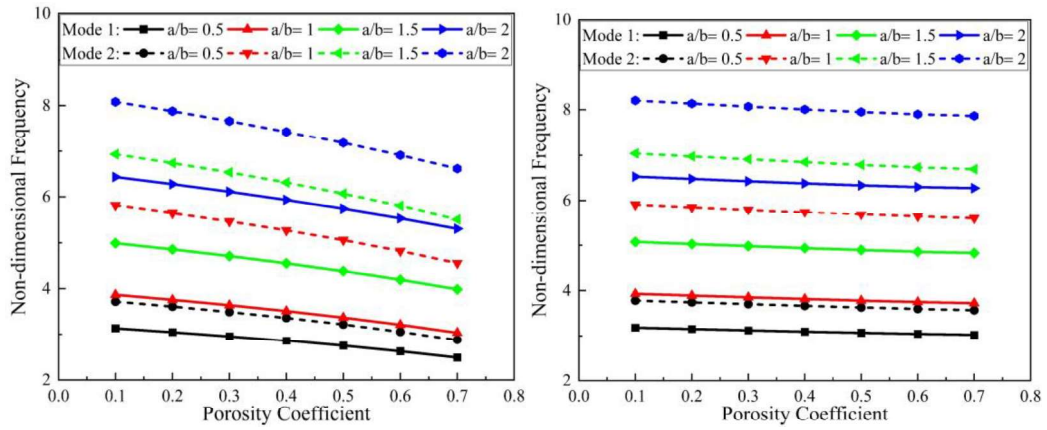
(a)

(b)
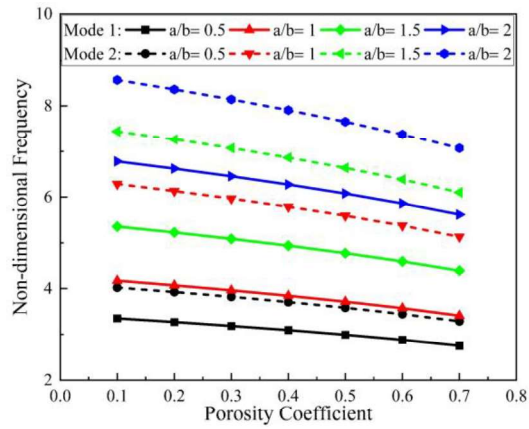
(c)

Figure 5.16: Influence of *a*/*b* ratio and porosity on the ω_n of the laminated composite hyperbolic shell under CC boundary conditions with (a) type-1, (b) type-2, and (c) type-3 porosity.

(a)

(b)
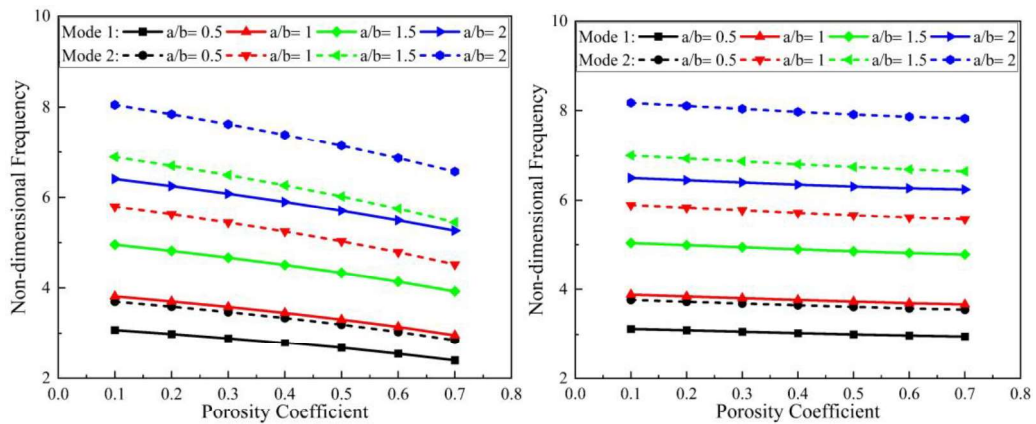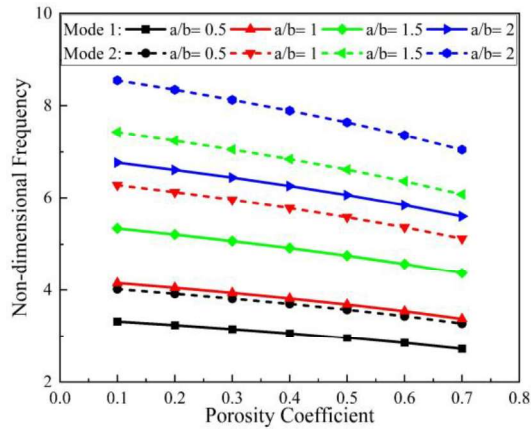
Figure 5.17: Influence of *a/b* ratio and porosity on the ω_n of the laminated composite cylindrical shell under CC boundary conditions with (a) type-1, (b) type-2, and (c) type-3 porosity.
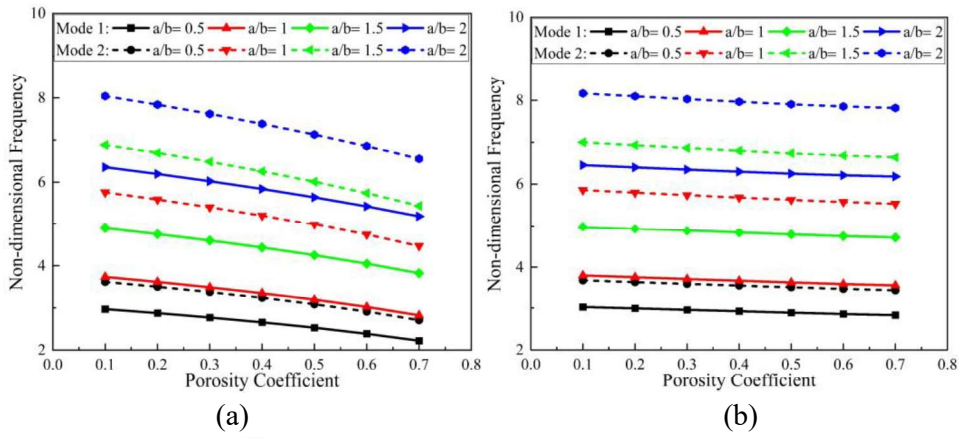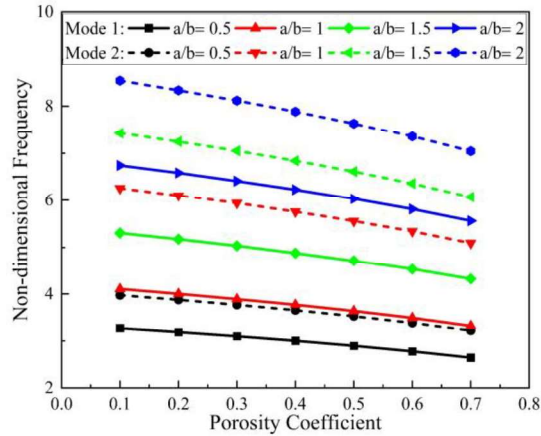
Figure 5.18: Influence of *a/b* ratio and porosity on the ω_n of the LCS plate under CC boundary conditions with (a) type-1, (b) type-2, and (c) type-3 porosity.

Further investigation is performed to understand the influence of the a/H ratio on the natural frequency of doubly-curved SLCS shells. The first five natural frequencies of the clamped sandwich shell with $a/b = 2$, $t_c/t_f = 2$, $e_0 = 0.5$, skew angle= 30° and 90°/0°/90°/C/0°/90°/0° orientation operating at 375 K are presented in Figure 5.19. It is observed from Figure 5.19 that the structure's natural frequency increases with an increase in the a/H ratio due to enhancement in the structure's stiffness (Rath and Sahu, 2012: Biswal and Sahu, 2015: Padhi and Pandit, 2017). The influence of the a/H ratio is more significant for higher modes of vibrations. It is also observed that for varying a/H ratios, the shell with type-1 porosity shows the least variation in the natural frequency of the system. Additionally, of all the types of shells considered, the flat sandwich plate is found to be more resistant to frequency changes for varying a/H ratios. Similar trends in results were observed for the simply supported sandwich shells, as presented in Figure 5.20.

Table 5.6 elaborates the influence of t_c/t_f ratio on the first two natural frequencies of the simply supported doubly-curved sandwich shell operating at 300 K temperature. The sandwich shell with type-3 porosity having $a/b = 1$, $a/H = 10$, skew angle= 15°, and 0°/C/0° orientation was considered for the investigation. It is apparent from the results that the natural frequency of the structure reduces with an increase in t_c/t_f ratio. The variation in natural frequencies may be due to the reduction in the stiffness of the doubly-curved sandwich shell structure. The influence of t_c/t_f ratio was found to be more prominent for higher modes of vibrations. Further, with increasing t_c/t_f ratio from 2 to 10, the percentage reduction in natural frequency of the sandwich spherical shells exhibits the highest (15.61 %), while the lowest value (15.17 %) was noted for the flat sandwich plate.

(a)   (b)
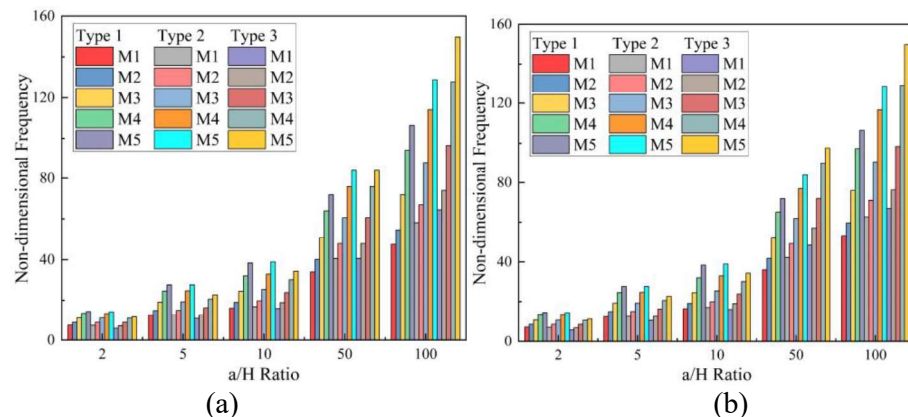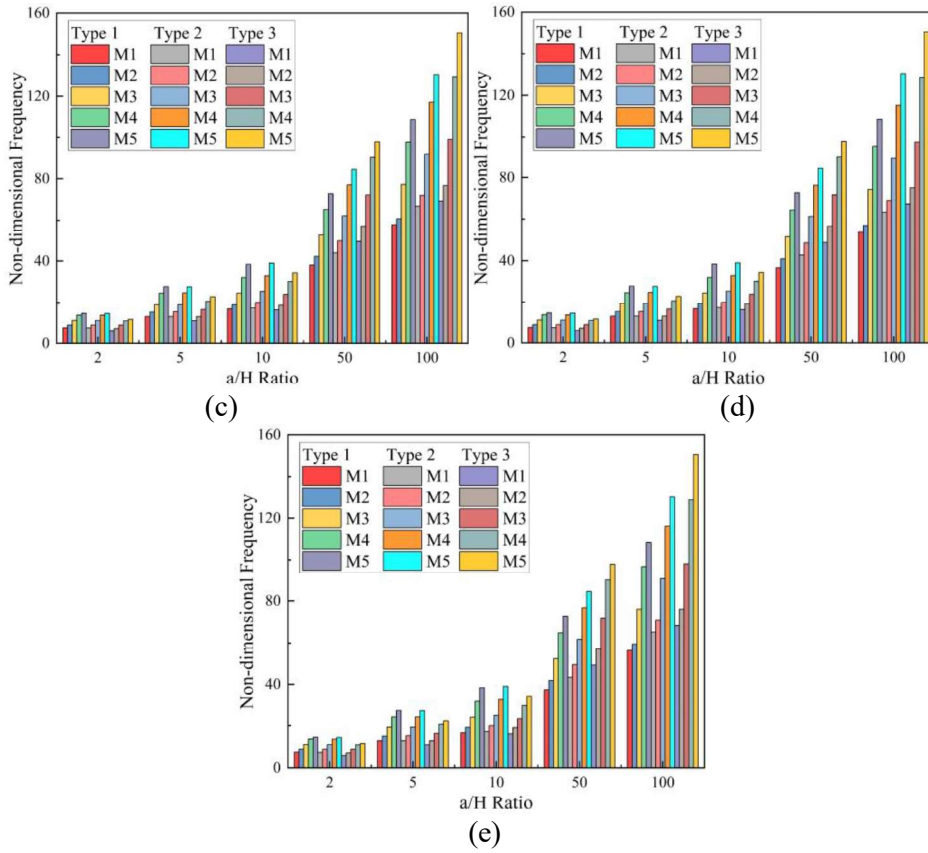
Figure 5.19: Influence of a/H ratio on the ω_n of the LCS panel under CC boundary conditions with (a) spherical, (b) ellipsoidal, (c) hyperbolic, (d) cylindrical shell, and (e) flat plate.
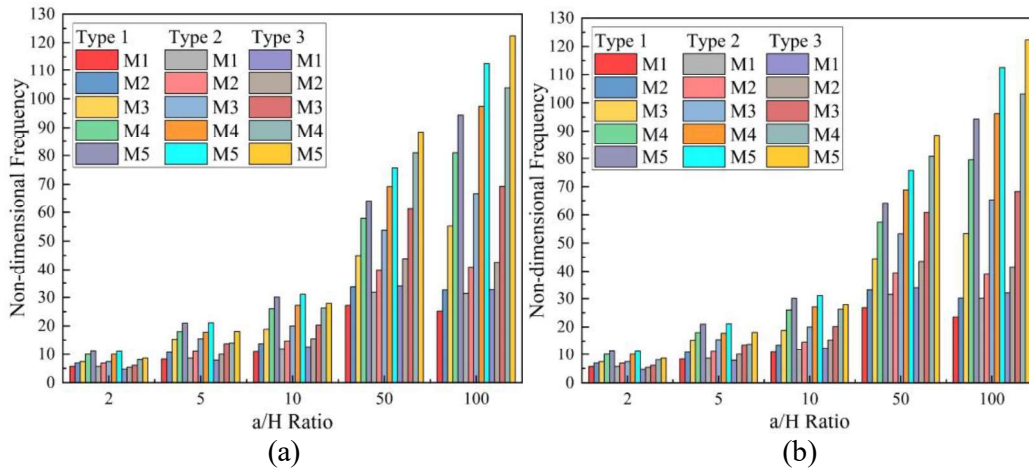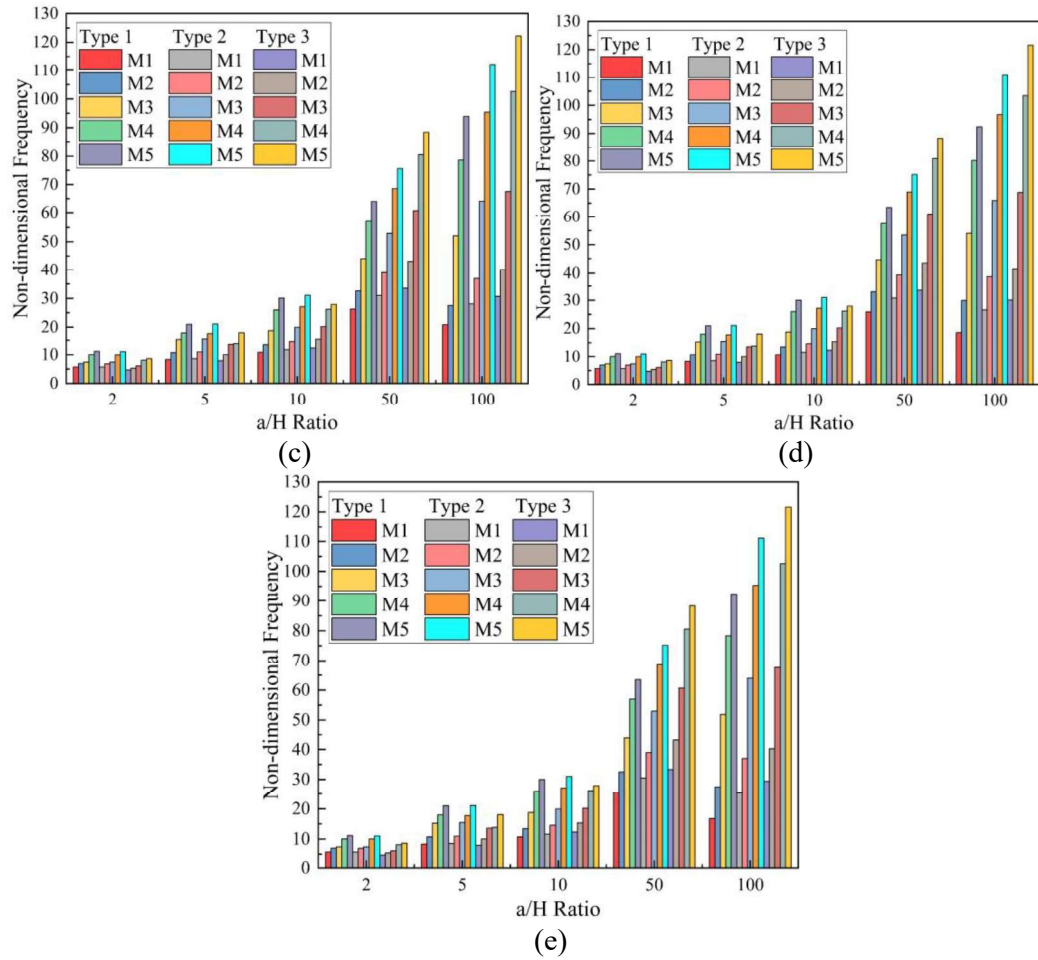
Figure 5.20: Influence of a/H ratio on ω_n of the LCS panel under SS boundary condition with (a) spherical, (b) ellipsoidal, (c) hyperbolic, (d) cylindrical shell, and (e) flat plate.

Investigations were also performed to appreciate the influence of the R/a ratio on the vibration characteristics of sandwich shells (with $a/b = 1$, $a/H = 10$, $t_c/t_f = 2$, skew angle= 30°, 0°/C/0° orientation, and SS boundary condition) with type-1 porosity, operating at 325 K temperature. The results presented in Table 5.7 show that the structure's natural frequency reduces with an increase in the R/a ratio. Further, for higher values of R/a ratios, the natural frequency of the doubly-curved sandwich shells coincides with the natural frequency of the flat sandwich plate. The concurrence of results is due to the drastic change in radius values ($R/a = 1$ to 10^{30}) which cause the transformation of shell structures into flat plate structures. Additionally, from all the shell types considered, the natural frequency of the sandwich spherical shell is most affected by the change in R/a ratios.

Table 5.6: Effect of t_c/t_f ratio on the non-dimensional frequency of the doubly curved LCS shell.

Shell Type	t_c/t_f Ratio	Modes	Porosity Coefficient				
			0.1	0.2	0.3	0.4	0.5
Spherical Shell	2	1	6.4102	6.2987	6.1764	6.0411	5.8893
		2	10.4949	10.3104	10.1076	9.8823	9.6288
	5	1	5.8794	5.7900	5.6911	5.5805	5.4552
		2	9.6265	9.4753	9.3083	9.1219	8.9106
	10	1	5.4093	5.3428	5.2685	5.1845	5.0883
		2	8.8944	8.7719	8.6369	8.4865	8.3163
Ellipsoidal Shell	2	1	6.3848	6.2727	6.1498	6.0136	5.8608
		2	10.4819	10.2970	10.0938	9.8681	9.6139
	5	1	5.8635	5.7738	5.6746	5.5637	5.4379
		2	9.6187	9.4673	9.3002	9.1134	8.9018
	10	1	5.3991	5.3326	5.2584	5.1744	5.0782
		2	8.8902	8.7676	8.6326	8.4821	8.3118
Hyperbolic Shell	2	1	6.3536	6.2409	6.1174	5.9805	5.8267
		2	10.4453	10.2599	10.0561	9.8295	9.5744
	5	1	5.8421	5.7522	5.6528	5.5415	5.4153
		2	9.5932	9.4417	9.2743	9.0874	8.8754
	10	1	5.3838	5.3175	5.2434	5.1596	5.0635
		2	8.8695	8.7471	8.6122	8.4618	8.2916
Cylindrical Shell	2	1	6.3669	6.2544	6.1310	5.9943	5.8408
		2	10.4693	10.2841	10.0806	9.8545	9.5999
	5	1	5.8520	5.7622	5.6627	5.5516	5.4255
		2	9.6106	9.4591	9.2918	9.1049	8.8930
	10	1	5.3915	5.3250	5.2508	5.1669	5.0707
		2	8.8846	8.7621	8.6271	8.4765	8.3062
Flat Plate	2	1	6.3531	6.2400	6.1158	5.9782	5.8236
		2	10.4304	10.2441	10.0392	9.8114	9.5547
	5	1	5.8457	5.7555	5.6556	5.5439	5.4172
		2	9.5879	9.4358	9.2677	9.0800	8.8671
	10	1	5.3894	5.3229	5.2486	5.1646	5.0682
		2	8.8706	8.7477	8.6124	8.4615	8.2907

Table 5.7: Effect of R/a ratio on the non-dimensional frequency of the doubly curved LCS shell.

Shell Type	R/a Ratio	Modes	Porosity Coefficient				
			0.1	0.2	0.3	0.4	0.5
Spherical Shell	5	1	6.2555	6.0939	5.9182	5.7260	5.5142
		2	9.7093	9.4521	9.1741	8.8720	8.5411
		3	11.6246	11.3296	11.0164	10.6830	10.3271
	10	1	5.9224	5.7448	5.5505	5.3361	5.0974
		2	9.3769	9.1011	8.8011	8.4724	8.1086
		3	11.4671	11.1665	10.8473	10.5076	10.1451
	10^{30}	1	5.8065	5.6230	5.4216	5.1988	4.9498
		2	9.2600	8.9774	8.6693	8.3306	7.9545
		3	11.4162	11.1139	10.7929	10.4512	10.0865
Ellipsoidal Shell	5	1	6.1233	5.9561	5.7739	5.5741	5.3531
		2	9.6135	9.3523	9.0699	8.7625	8.4254
		3	11.5470	11.2489	10.9321	10.5945	10.2337
	10	1	5.8877	5.7085	5.5123	5.2956	5.0542
		2	9.3524	9.0755	8.7743	8.4441	8.0786
		3	11.4473	11.1459	10.8258	10.4850	10.1211
	10^{30}	1	5.8065	5.6230	5.4216	5.1988	4.9498
		2	9.2600	8.9774	8.6693	8.3306	7.9545
		3	11.4162	11.1139	10.7929	10.4512	10.0865
Hyperbolic Shell	5	1	6.0668	5.8974	5.7126	5.5096	5.2846
		2	9.4202	9.1509	8.8587	8.5392	8.1869
		3	11.4709	11.1725	10.8556	10.5182	10.1578
	10	1	5.8731	5.6933	5.4963	5.2787	5.0362
		2	9.3013	9.0221	8.7181	8.3845	8.0147
		3	11.4297	11.1283	10.8083	10.4677	10.1040
	10^{30}	1	5.8065	5.6230	5.4216	5.1988	4.9498
		2	9.2600	8.9774	8.6693	8.3306	7.9545
		3	11.4162	11.1139	10.7929	10.4512	10.0865
Cylindrical Shell	5	1	6.0467	5.8762	5.6902	5.4857	5.2592
		2	9.5336	9.2691	8.9828	8.6708	8.3280
		3	11.4948	11.1950	10.8764	10.5367	10.1734
	10	1	5.8678	5.6877	5.4904	5.2725	5.0295
		2	9.3316	9.0538	8.7516	8.4201	8.0530
		3	11.4345	11.1326	10.8121	10.4707	10.1063
	10^{30}	1	5.8065	5.6230	5.4216	5.1988	4.9498
		2	9.2600	8.9774	8.6693	8.3306	7.9545
		3	11.4162	11.1139	10.7929	10.4512	10.0865
Flat Plate	--	1	5.8065	5.6230	5.4216	5.1988	4.9498
		2	9.2600	8.9774	8.6693	8.3306	7.9545
		3	11.4162	11.1139	10.7929	10.4512	10.0865

5.3.3. Experimental challenges

This sub-section explores the challenges involved in the experimental study on the free vibration behavior of LCS plates with a 3D printed PLA core. The sandwich plate with a glass-epoxy (280 GSM) face sheet and 3D printed PLA core is considered for the study. The sandwich plates are prepared using the hand layup and compression molding methods. The prepared samples are placed in the thermal chamber capable of maintaining the desired temperatures with an accuracy of ±1 K. The edges of the sandwich plates are clamped to achieve the cantilever (CFFF) and fixed-free (CFCF) boundary conditions. Figure 5.21 shows the thermal profile generated to create the desired thermal environment. For every desired temperature, the sample is allowed to thermally age for at least half an hour (t = 30 minutes) so that the sample material is allowed to attain stability.

As the temperature crossed 325 K (point A in Figure 5.21), the sandwich structure started to undergo permanent deformation. The deformation may be due to the localized thermal buckling as the temperature reaches near the glass transition zone of the PLA material (336.07 K). Figure 5.22 shows the field emission scanning electron microscopy (FESEM) image of the fractured tensile test sample tested at 300 K. The fractography images indicate that the material tends to flow in the gaps caused by scaffolds under mechanical loading. This phenomenon may accelerate in elevated thermal environments. Additionally, the pores and voids may also get filled by the deformed flowing material (Senatov *et al*., 2016a, 2016b). The clamping forces applied to achieve the desired boundary conditions may cause the combined thermo-elastic local buckling in the vibration study, as shown in Figures 5.23 and 5.24. In elevated thermal environments, the localized thermal buckling (due to clamping forces and self-weight) and delamination between the face sheets and core material can be witnessed. The phenomenon of local buckling and delamination may be due to the direct exposure of PLA to higher temperatures at the edges and the variation in thermal properties of the glass-epoxy and PLA materials. It is difficult to include all these phenomena into the mathematical FE models and mimic the exact behavior of the LCS plates operating in elevated thermal environments. Hence, the research works pertaining to the prediction of the exact physical behavior of the structure are of necessity and higher importance.
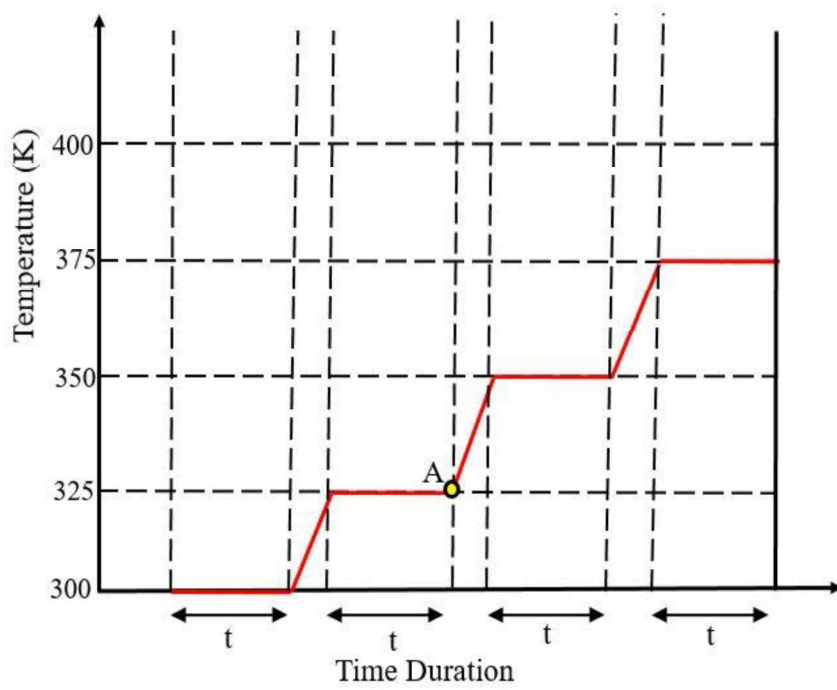
Figure 5.21: Temperature profile generated to achieve the desired temperatures.
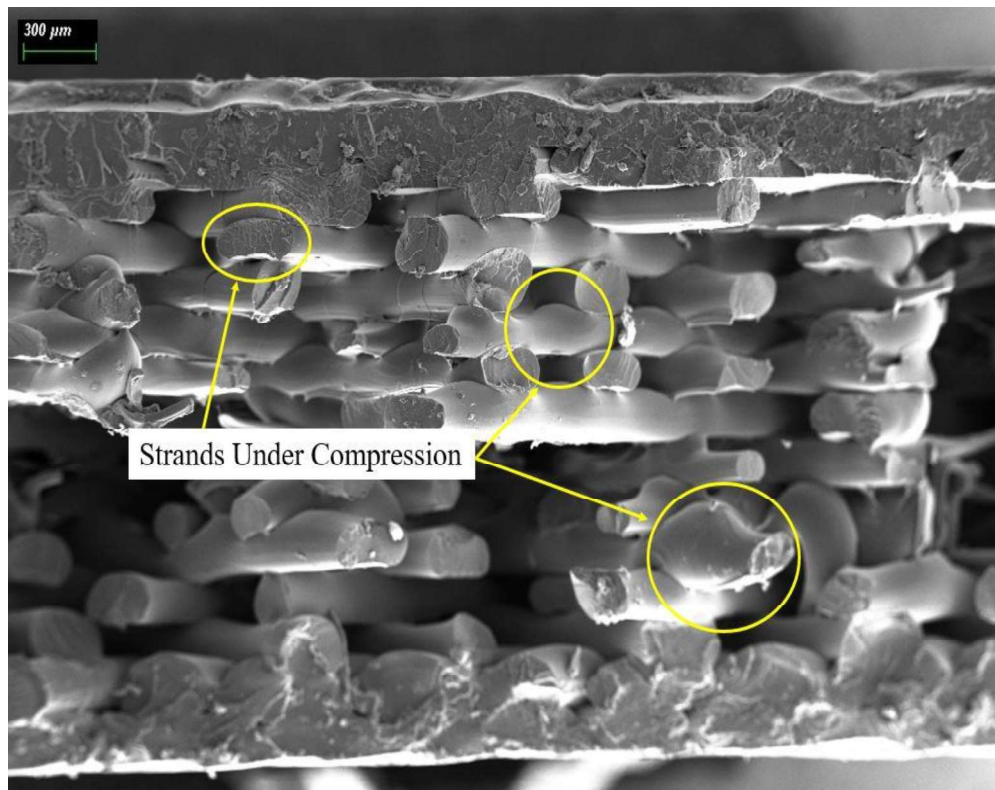
Figure 5.22: Fractography of the 3D printed PLA sample (tensile test sample tested at 300 K).
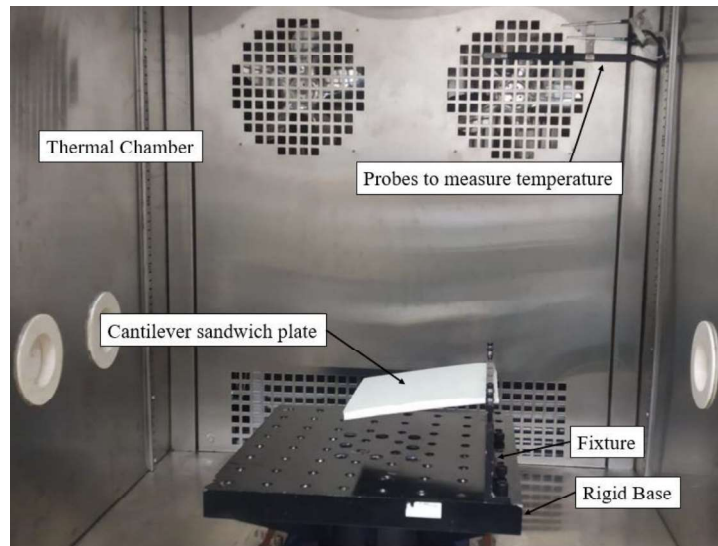
(a)
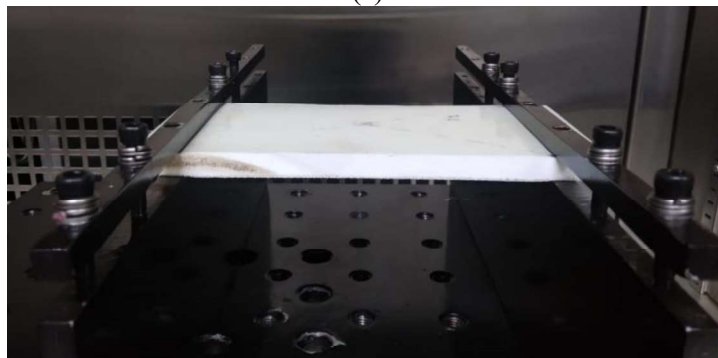
(b)
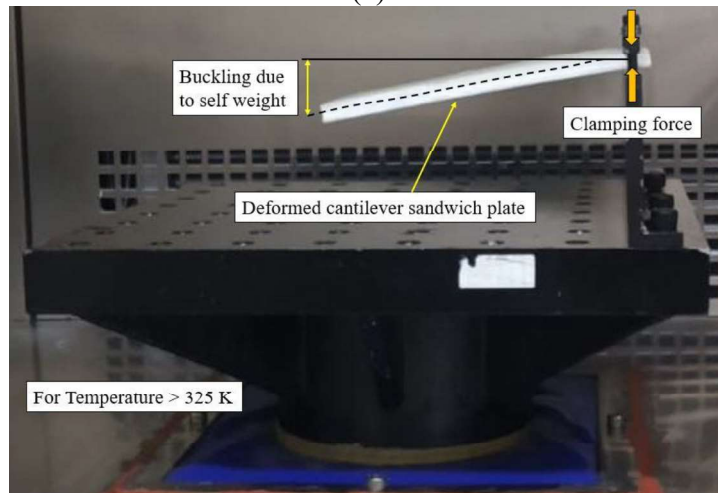
(c)

Figure 5.23: Pictorial representation of the (a) cantilever and (b) fixed-free sandwich plate operating in elevated thermal environments and (c) permanent deformation of cantilever beam operating above 325 K temperature.
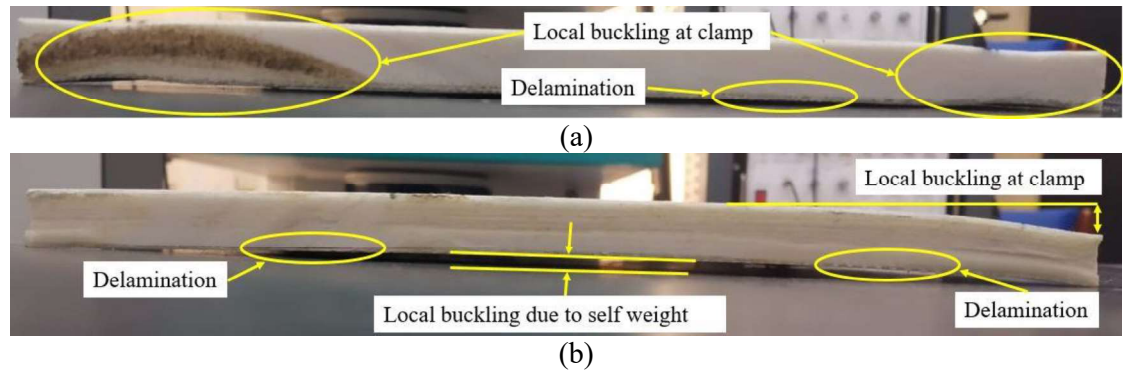
Figure 5.24: Pictorial representation of local thermal buckling and delamination of the (a) fixed-free and (b) cantilever sandwich composite plate.

5.4 CONCLUSION

In this chapter, the influence of temperature and porosity on the free vibration characteristics of a doubly-curved SLCS shell with a 3D printed PLA core is explored. The layerwise FE model was developed using eight noded isoparametric elements having nine degrees of freedom per node. The temperature-dependent material properties of the graphite-epoxy and the 3D printed PLA core materials are considered for the simulations. The degradation of stiffness of the structure on exposure to the elevated thermal environments was incorporated in the formulations using the initial stress stiffness matrix. The doubly-curved structures such as cylindrical, ellipsoidal, hyperbolic, spherical shells, and flat plates were used for the analysis. Three different types of porosity distribution patterns (in the thickness directions) are considered to understand the influence of the porosity coefficient on the natural frequency of the simply supported and clamped sandwich shells. The simulation results suggest that for all the shell types and porosity distribution patterns considered, the natural frequency of the sandwich shell structures decreases with a rise in temperature and porosity coefficient values. It is also observed that the natural frequency of the sandwich shell structure increases with an increase in skew angle, a/b ratio, and a/H ratios. In contrast, the system's natural frequency reduces with an increase in t_c/t_f and R/a ratios. Further, the practical difficulties involved in the vibration study of the sandwich plates in elevated thermal environments are also discussed.

Chapter 6

PERFORMANCE OF ACTIVE CONSTRAINED LAYER DAMPING OF SKEW SANDWICH PLATE WITH CNT REINFORCED COMPOSITE CORE IN THERMAL ENVIRONMENT

This chapter presents a new method to investigate the performance characteristics of the active constrained layer damping (ACLD) system in the thermal environment. For such investigation, a skew laminated composite sandwich (SLCS) plate with graphite-epoxy face sheet and the carbon nanotube-reinforced composite (CNTRC) core are considered. The viscoelastic materials are modeled using the complex modulus approach. The negative velocity feedback control law is used to control the first few modes of the vibrating sandwich plate. A comprehensive investigation is carried out to understand the effect of temperature, skew angle, functional gradation types/methods, the volume fraction of carbon nanotubes (CNT) in the core material, type of viscoelastic material used, and position of the patches on the vibration attenuation characteristics of sandwich plate integrated with the ACLD patches. Further investigation is devoted to studying the effect of temperature and geometric parameters of the sandwich plate on the damping characteristics of the ACLD of an SLCS plate.

6.1 INTRODUCTION

Vibration control of laminated composite and laminated composite sandwich (LCS) structures has been finding importance in recent years. Piezoelectric materials are extensively used as distributed sensors and actuators for vibration control based on the direct and converse piezoelectric effects phenomena. The piezo-sensors and actuators can be directly mounted on the base structures to achieve the self-monitoring and self-controlling capabilities (Bailey and Ubbard, 1985: Crawley and Luis, 1987: Song *et al*., 2001: Li, 2012: Zhao *et al*., 2020). For satisfactory vibration attenuation of base structures, these monolithic piezoelectric materials need high-control voltage. Research about the development of low-control-authority monolithic piezoelectric

materials led to the discoveries of ACLD treatment. In ACLD treatment, the piezoelectric materials are used as the constraining/actuating layer, and the viscoelastic materials are used as a constrained layer.

In this chapter, the first attempt has been made to investigate the influence of temperature on the performance of the ACLD of sandwich plates considering temperature-dependent material properties of all the constituent materials and respective initial stress stiffness matrices. The effect of skew angle, the type of gradation, the volume fraction of CNT, the type of viscoelastic material, the position of ACLD patch, the length to thickness ratio, the length to width ratio, the ratio of core thickness to the thickness of face sheet, the face sheet fiber orientation, and boundary conditions on the vibrational attenuation characteristics are studied under different thermal conditions.

6.2. PROBLEM DESCRIPTION

The schematic illustration of an SLCS plate integrated with the ACLD patches is demonstrated in Figure 6.1. The top and bottom face sheets of the LCS plate contain 'N' number of orthotropic polymer composite layers, and the core is made of CNTRC material. The length, breadth, and thickness of the plate are denoted as a, b, and H, respectively. The thickness of each composite layer is considered as h ($h_t = h_b = h$), half of the core thickness is symbolized as h_c, the thickness of the viscoelastic layer and piezoelectric layers are considered as h_v and h_p, respectively. Figure 6.2 illustrates the kinematics of the deformation of a sandwich plate in XZ- and YZ-planes. The angles θ_x, ϕ_x, α_x, β_x, and γ_x represent the rotation of a portion of the normal lying in the core, the bottom face sheet, the top face sheet, the viscoelastic layer, and the piezoelectric layer respectively, in XZ- plane, whereas the angles θ_y, ϕ_y, α_y, β_y, and γ_y respectively, denote the same in YZ- plane. The displacement fields relating to the kinematics of deformation can be articulated as follows (Suresh Kumar *et al*., 2012, 2013: Kanasogi and Ray, 2013),

146
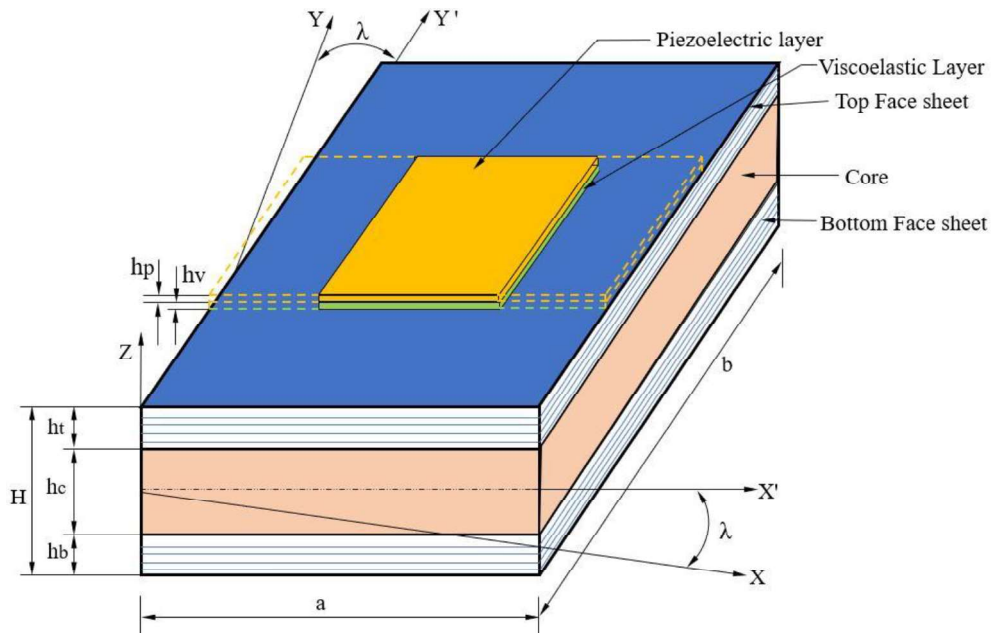
Figure 6.1: Schematic representation of an SLCS plate integrated with the ACLD patches.
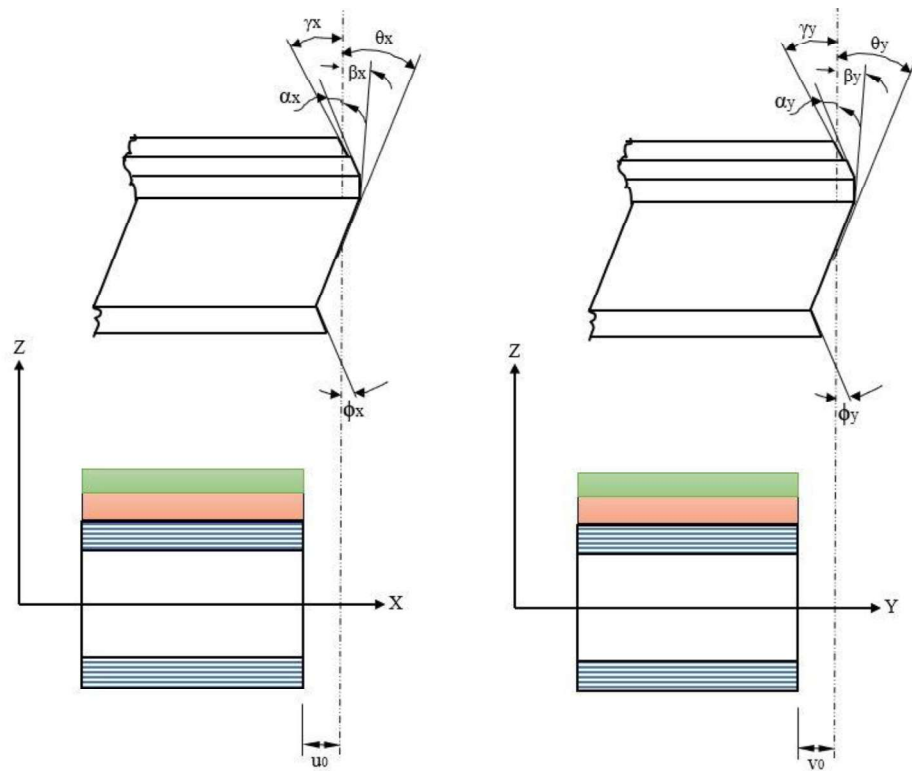
Figure 6.2: Schematic representation of kinematics of deformation of LCS plate integrated with the ACLD patches.

For the bottom face sheet:

$$u_{bot}(\mathrm{x,y,z,t}_i)=u_0(\mathrm{x,y,t}_i)-\mathrm{h}_c\,\theta_x(\mathrm{x,y,t}_i)+(\mathrm{z+h}_c)\phi_x(\mathrm{x,y,t}_i) \qquad (6.1.a)$$

$$v_{bot}(\mathrm{x,y,z,t}_i)=v_0(\mathrm{x,y,t}_i)-\mathrm{h}_c\,\theta_y(\mathrm{x,y,t}_i)+(\mathrm{z+h}_c)\phi_y(\mathrm{x,y,t}_i) \qquad (6.1.b)$$

$$w_{bot}(\mathrm{x,y,z,t}_i)=w_0(\mathrm{x,y,t}_i) \qquad (6.1.c)$$

For the core:

$$u_{core}(\mathrm{x,y,z,t}_i)=u_0(\mathrm{x,y,t}_i)+\mathrm{z}\theta_x(\mathrm{x,y,t}_i) \qquad (6.2.a)$$

$$v_{core}(\mathrm{x,y,z,t}_i)=v_0(\mathrm{x,y,t}_i)+\mathrm{z}\theta_y(\mathrm{x,y,t}_i) \qquad (6.2.b)$$

$$w_{core}(\mathrm{x,y,z,t}_i)=w_0(\mathrm{x,y,t}_i) \qquad (6.2.c)$$

For the top face sheet:

$$u_{top}(\mathrm{x,y,z,t}_i)=u_0(\mathrm{x,y,t}_i)+\mathrm{h}_c\,\theta_x(\mathrm{x,y,t}_i)+(\mathrm{z-h}_c)\alpha_x(\mathrm{x,y,t}_i) \qquad (6.3.a)$$

$$v_{top}(\mathrm{x,y,z,t}_i)=v_0(\mathrm{x,y,t}_i)+\mathrm{h}_c\,\theta_y(\mathrm{x,y,t}_i)+(\mathrm{z-h}_c)\alpha_y(\mathrm{x,y,t}_i) \qquad (6.3.b)$$

$$w_{top}(\mathrm{x,y,z,t}_i)=w_0(\mathrm{x,y,t}_i) \qquad (6.3.c)$$

For the viscoelastic layer:

$$u_{visc}(\mathrm{x,y,z,t}_i)=u_0(\mathrm{x,y,t}_i)+h_c\theta_x(\mathrm{x,y,t}_i)+h\alpha_x(\mathrm{x,y,t}_i)+(\mathrm{z}-\tfrac{H}{2}-h_v)\beta_x \quad (6.4.a)$$

$$v_{visc}(\mathrm{x,y,z,t}_i)=v_0(\mathrm{x,y,t}_i)+h_c\theta_y(\mathrm{x,y,t}_i)+h\alpha_y(\mathrm{x,y,t}_i)+(\mathrm{z}-\tfrac{H}{2}-h_v)\beta_y \quad (6.4.b)$$

$$w_{visc}(\mathrm{x,y,z,t}_i)=w_0(\mathrm{x,y,t}_i) \qquad (6.4.c)$$

For the piezoelectric layer:

$$u_{piezo}(\mathrm{x,y,z,t}_i)=u_0(\mathrm{x,y,t}_i)+h_c\theta_x(\mathrm{x,y,t}_i)+h\alpha_x(\mathrm{x,y,t}_i)+h_v\beta_x(\mathrm{x,y,t}_i)+(\mathrm{z}-\tfrac{H}{2}-h_v-h_p)\gamma_x \,(6.5.a)$$

$$v_{piezo}(\mathrm{x,y,z,t}_i)=v_0(\mathrm{x,y,t}_i)+h_c\theta_y(\mathrm{x,y,t}_i)+h\alpha_y(\mathrm{x,y,t}_i)+h_v\beta_y(\mathrm{x,y,t}_i)+(\mathrm{z}-\tfrac{H}{2}-h_v-h_p)\gamma_y \,(6.5.b)$$

$$w_{piezo}(\mathrm{x,y,z,t}_i)=w_0(\mathrm{x,y,t}_i) \qquad (6.5.c)$$

In Eqs. 6.1-6.5, $u_{bot, core, top, visc, piezo}$, $v_{bot, core, top, visc, piezo}$ and $w_{bot, core, top, visc, piezo}$ are the axial displacements along *X*, *Y*, and *Z*- directions, respectively. The suffixes bot, core, top, visc, and piezo denote the axial displacements concerned with the bottom face sheet, the core, the top face sheet, the viscoelastic layer, and the piezoelectric layer, respectively. u_0, v_0, and w_0 represent the translational displacements at any arbitrary point at the center plane of the core along *X*, *Y*, and *Z* directions, respectively. The term t_i in Eqs. 6.1-6.5 indicates time. For simplification, the translational displacements are disjointed from the other variables as follows:

148

$\{d_t\} = \begin{bmatrix} u_0 & v_0 & w_0 \end{bmatrix}^T$, and $\{d_r\} = \begin{bmatrix} \theta_x & \theta_y & \phi_x & \phi_y & \alpha_x & \alpha_y & \beta_x & \beta_y & \gamma_x & \gamma_y \end{bmatrix}^T$ (6.6)

To implement the selective integration rule, the state of strain at any point in the overall plate is divided into the two strain vectors as:

$$\{\varepsilon_b\} = \begin{Bmatrix} \varepsilon_x & \varepsilon_y & \varepsilon_{xy} \end{Bmatrix}^T, \text{ and } \{\varepsilon_s\} = \begin{Bmatrix} \varepsilon_{xz} & \varepsilon_{yz} \end{Bmatrix}^T \qquad (6.7)$$

where, ε_x and ε_y are the normal strains along X and Y directions, respectively. ε_{xy} is the in-plane shear strain, and ε_{xz}, ε_{yz} are the transverse shear strains. By using the displacement fields and linear strain-displacement relations, the strain vectors $\{\varepsilon_b\}_{bot}$, $\{\varepsilon_b\}_{core}$, $\{\varepsilon_b\}_{top}$, $\{\varepsilon_b\}_{visc}$, and $\{\varepsilon_b\}_{piezo}$ defining the state of in-plane and transverse normal strains at any point in the bottom face sheet, the core, the top face sheet, the viscoelastic layer, and the piezoelectric layer can be expressed as:

$$\begin{aligned}
\{\varepsilon_b\}_{bot} &= \{\varepsilon_{bt}\} + [z_1]\{\varepsilon_{br}\} \\
\{\varepsilon_b\}_{core} &= \{\varepsilon_{bt}\} + [z_2]\{\varepsilon_{br}\} \\
\{\varepsilon_b\}_{top} &= \{\varepsilon_{bt}\} + [z_3]\{\varepsilon_{br}\} \\
\{\varepsilon_b\}_{visc} &= \{\varepsilon_{bt}\} + [z_4]\{\varepsilon_{br}\} \\
\{\varepsilon_b\}_{piezo} &= \{\varepsilon_{bt}\} + [z_5]\{\varepsilon_{br}\}
\end{aligned} \qquad (6.8)$$

Similarly, the strain vectors $\{\varepsilon_s\}_{bot}$, $\{\varepsilon_s\}_{core}$, $\{\varepsilon_s\}_{top}$, $\{\varepsilon_s\}_{visc}$, and $\{\varepsilon_s\}_{piezo}$ define the state of transverse shear strains at any point in the bottom face sheet, the core, the top face sheet, the viscoelastic layer, and the piezoelectric layer, and can be expressed as:

$$\begin{aligned}
\{\varepsilon_s\}_{bot} &= \{\varepsilon_{st}\} + [z_6]\{\varepsilon_{sr}\} \\
\{\varepsilon_s\}_{core} &= \{\varepsilon_{st}\} + [z_7]\{\varepsilon_{sr}\} \\
\{\varepsilon_s\}_{top} &= \{\varepsilon_{st}\} + [z_8]\{\varepsilon_{sr}\} \\
\{\varepsilon_s\}_{visc} &= \{\varepsilon_{st}\} + [z_9]\{\varepsilon_{sr}\} \\
\{\varepsilon_s\}_{piezo} &= \{\varepsilon_{st}\} + [z_{10}]\{\varepsilon_{sr}\}
\end{aligned} \qquad (6.9)$$

The vectors and matrices denoted in the above equation are presented in Appendix D. The state of stress in consistence with the state of strain at any point in the overall plate is described by the two stress vectors as follows:

$$\{\sigma_b\} = \begin{Bmatrix} \sigma_x & \sigma_y & \sigma_{xy} \end{Bmatrix}^T, \text{ and } \{\sigma_s\} = \begin{Bmatrix} \sigma_{xz} & \sigma_{yz} \end{Bmatrix}^T \qquad (6.10)$$

where, σ_x and σ_y are the normal stresses along X and Y directions, respectively. σ_{xy} is the in-plane shear stress, and σ_{xz}, σ_{yz} are the transverse shear stresses. The constitutive relation for the materials of the different layers of the top and the bottom face sheets of the sandwich plate and that of the core are given by,

$$\left\{\sigma_b^K\right\}_{bot} = \left[C_b^K\right]\left\{\varepsilon_b^K\right\}_{bot}, \ \left\{\sigma_b^c\right\}_{core} = \left[C_b^c\right]\left\{\varepsilon_b^K\right\}_{core}, \text{ and } \left\{\sigma_b^K\right\}_{top} = \left[C_b^K\right]\left\{\varepsilon_b^K\right\}_{top} \quad (6.11)$$

$$\left\{\sigma_s^K\right\}_{bot} = \left[C_s^K\right]\left\{\varepsilon_s^K\right\}_{bot}, \ \left\{\sigma_s^c\right\}_{core} = \left[C_s^c\right]\left\{\varepsilon_s^K\right\}_{core}, \text{ and } \left\{\sigma_s^K\right\}_{top} = \left[C_s^K\right]\left\{\varepsilon_s^K\right\}_{top} \quad (6.12)$$

(K= 1, 2, 3,…..N) and

$$\left[C_b^K\right] = \begin{bmatrix} \bar{C}_{11}^K & \bar{C}_{12}^K & \bar{C}_{16}^K \\ \bar{C}_{21}^K & \bar{C}_{22}^K & \bar{C}_{26}^K \\ \bar{C}_{61}^K & \bar{C}_{62}^K & \bar{C}_{66}^K \end{bmatrix}, \ \left[C_s^K\right] = \begin{bmatrix} \bar{C}_{55}^K & \bar{C}_{45}^K \\ \bar{C}_{45}^K & \bar{C}_{44}^K \end{bmatrix},$$

$$\left[C_b^c\right] = \begin{bmatrix} \bar{C}_{11}^c & \bar{C}_{12}^c & \bar{C}_{16}^c \\ \bar{C}_{21}^c & \bar{C}_{22}^c & \bar{C}_{26}^c \\ \bar{C}_{61}^c & \bar{C}_{62}^c & \bar{C}_{66}^c \end{bmatrix}, \text{ and } \left[C_s^c\right] = \begin{bmatrix} \bar{C}_{55}^c & \bar{C}_{45}^c \\ \bar{C}_{45}^c & \bar{C}_{44}^c \end{bmatrix}$$

The complex modulus approach is adopted for modeling the viscoelastic material. Hence, the shear modulus of the material is expressed as:

$$G = G'(1+i\eta) \quad (6.13)$$

in which G' is storage modulus and η is the loss factor at any operating temperature and frequency. The constitutive relations for the constraining piezoelectric layer of the ACLD treatment are given by,

$$\left\{\sigma_b\right\}_{piezo} = \left[C_b\right]_p \left\{\varepsilon_b\right\}_{piezo} + \left[C_{bs}\right]_p \left\{\varepsilon_s\right\}_{piezo} - \left\{e_b\right\} E_z \quad (6.14.a)$$

$$\left\{\sigma_s\right\}_{piezo} = \left[C_{bs}\right]_p^T \left\{\varepsilon_b\right\}_{piezo} + \left[C_s\right]_p \left\{\varepsilon_s\right\}_{piezo} - \left\{e_b\right\} E_z \quad (6.14.b)$$

$$D_z = \left\{e_b\right\}^T \left\{\varepsilon_b\right\}_p + \left\{e_s\right\}^T \left\{\varepsilon_s\right\}_p + \in_{33} E_z \quad (6.14.c)$$

where, E_z and D_z are the electric field and the electric displacement along the Z-direction, respectively. $\in_{33}$ is the dielectric constant of the piezoelectric material. The forms of the transformed elastic coefficient matrices $[C_b]_p$ and $[C_s]_p$ are similar to those of $[C_b]$ and $[C_s]$, respectively. It may be noted from the above form of constitutive relations that the transverse shear strains are coupled with the in-plane stresses, and the corresponding coupling elastic constant matrix $[C_{bs}]_p$ is given by,

150

$$[C_{bs}]_p = \begin{bmatrix} C_{15} & 0 \\ C_{25} & 0 \\ 0 & C_{46} \end{bmatrix} = \begin{bmatrix} 0 & C_{14} \\ 0 & C_{24} \\ C_{56} & 0 \end{bmatrix}$$

Also, the piezoelectric constant matrices $\{e_b\}$ and $\{e_s\}$ are expressed as,

$$\{e_b\} = \{\bar{e}_{31} \quad \bar{e}_{32} \quad \bar{e}_{36}\}^T, \text{ and } \{e_s\} = \{\bar{e}_{35} \quad \bar{e}_{34}\}^T \tag{6.15}$$

The total potential energy T_p and the kinetic energy T_k of the overall plate are given by,

$$
\begin{aligned}
T_p = \frac{1}{2} & \left\{ \left(\sum_{k=1}^{N} \int_{\Omega} \left(\{\varepsilon_b^k\}_b^T \{\sigma_b^k\}_b + \{\varepsilon_s^k\}_b^T \{\sigma_s^k\}_b \right) d\Omega \right) + \left(\int_{\Omega} \left(\{\varepsilon_b\}_c^T \{\sigma_b\}_c + \{\varepsilon_s\}_c^T \{\sigma_s\}_c \right) d\Omega \right) \right. \\
& + \left(\sum_{k=1}^{N} \int_{\Omega} \left(\{\varepsilon_b^k\}_t^T \{\sigma_b^k\}_t + \{\varepsilon_s^k\}_t^T \{\sigma_s^k\}_t \right) d\Omega \right) + \left(\int_{\Omega} \left(\{\varepsilon_b\}_v^T \{\sigma_b\}_v + \{\varepsilon_s\}_v^T \{\sigma_s\}_v \right) d\Omega \right) \\
& \left. + \left(\int_{\Omega} \left(\{\varepsilon_b\}_p^T \{\sigma_b\}_p + \{\varepsilon_s\}_p^T \{\sigma_s\}_p \right) d\Omega \right) - \int_{\Omega} E_z D_z d\Omega \right\} - \int_A \{d\}^T \left(\{f\} + \{f^{therm}\} \right) dA
\end{aligned} \tag{6.16}
$$

$$
\begin{aligned}
T_k = \frac{1}{2} & \left\{ \left(\sum_{k=1}^{N} \int_{\Omega} \rho_b^k \left(\dot{u}_b^2 + \dot{v}_b^2 + \dot{w}_b^2 \right) d\Omega \right) + \left(\rho_c \left(\dot{u}_c + \dot{v}_c + \dot{w}_c \right) d\Omega \right) + \left(\sum_{k=1}^{N} \int_{\Omega} \rho_t^k \left(\dot{u}_t^2 + \dot{v}_t^2 + \dot{w}_t^2 \right) d\Omega \right) \right. \\
& \left. + \left(\rho_v \left(\dot{u}_v + \dot{v}_v + \dot{w}_v \right) d\Omega \right) + \left(\rho_p \left(\dot{u}_p + \dot{v}_p + \dot{w}_p \right) d\Omega \right) \right\}
\end{aligned} \tag{6.17}
$$

In which ρ_c, ρ_v, and ρ_p are the mass densities of the core, the viscoelastic material, and the piezoelectric material, respectively; ρ_b^k and ρ_t^k are the densities of the k-th layer of the top and the bottom face sheets respectively, $\{f\}$ and $\{f^{therm}\}$ are the externally applied surface traction and thermal forces acting over a surface area A. The term Ω represents the volume of the concerned layer. The rotary inertia of the plate is not considered for estimating the kinetic energy of the system as the thickness of the plate is very small compared to the lateral dimensions of the plate.

6.3. FINITE ELEMENT FORMULATION

The overall sandwich plate with ACLD is discretized by the eight noded isoparametric quadrilateral elements. Three translational (u, v, w) and ten rotational (θ_x, θ_y, ϕ_x, ϕ_y, α_x, α_y, β_x, β_y, γ_x, γ_y) degrees of freedom are considered at each node. Generalized displacement vectors associated with the i-th node (i = 1, 2, ..., 8) of the element can be expressed as:

$$\{d_{ti}\} = [u_{0i} \quad v_{0i} \quad w_{0i}]^T, \text{ and } \{d_{ri}\} = [\theta_{xi} \quad \theta_{yi} \quad \phi_{xi} \quad \phi_{yi} \quad \alpha_{xi} \quad \alpha_{yi} \quad \beta_{xi} \quad \beta_{yi} \quad \gamma_{xi} \quad \gamma_{yi}]^T \tag{6.18}$$

Thus, the generalized displacement vector at any point within the element can be represented in terms of the nodal generalized displacement vectors.

$$\{d_t\} = [N_t]\{\mathrm{d}_t^e\}, \text{ and } \{d_r\} = [N_r]\{\mathrm{d}_r^e\} \tag{6.19}$$

in which,

$$[N_t] = [N_{t1} \quad N_{t2} \quad ... \quad N_{t8}]^T, \text{ and } [N_r] = [N_{r1} \quad N_{r2} \quad ... \quad N_{r8}]^T$$

$$N_{ti} = n_i I_t, \quad N_{ri} = n_i I_r \tag{6.20}$$

$$\{\mathrm{d}_t^e\} = [\{\mathrm{d}_{t1}^e\}^T \quad \{\mathrm{d}_{t2}^e\}^T \quad ... \quad \{\mathrm{d}_{t8}^e\}^T]^T, \text{ and } \{\mathrm{d}_r^e\} = [\{\mathrm{d}_{r1}^e\}^T \quad \{\mathrm{d}_{r2}^e\}^T \quad ... \quad \{\mathrm{d}_{r8}^e\}^T]^T$$

where, I_t and I_r are (3×3) and (10×10) identity matrices, respectively, and n_i is the shape function of the natural coordinate associated with the i-th node.

6.3.1. Elemental stiffness matrix

The linear strain matrix $\{\varepsilon\}$ can be expressed as,

$$\{\varepsilon\} = [\mathrm{B}]\{\delta_e\} \tag{6.21}$$

where,

$$\{\delta_e\} = \left\{ \mathrm{u}_1, \mathrm{v}_1, \mathrm{w}, \theta_{x1}, \theta_{y1}, \phi_{x1}, \phi_{y1}, \alpha_{x1}, \alpha_{x2}, \beta_{x1}, \beta_{x2}, \gamma_{x1}, \gamma_{x2}, ..., \right.$$
$$\left. \mathrm{u}_8, \mathrm{v}_8, \mathrm{w}, \theta_{x8}, \theta_{y8}, \phi_{x8}, \phi_{y8}, \alpha_{x8}, \alpha_{y8}, \beta_{x8}, \beta_{x8}, \gamma_{x8}, \gamma_{x8} \right\}^T$$

The strain vectors at any point within the element can be expressed as:

$$\{\varepsilon_b\}_{bot} = [\mathrm{B}_{tb}]\{\mathrm{d}_t^e\} + [z_1][\mathrm{B}_{rb}]_{bot}\{\mathrm{d}_r^e\}, \quad \{\varepsilon_b\}_{core} = [\mathrm{B}_{tb}]\{\mathrm{d}_t^e\} + [z_2][\mathrm{B}_{rb}]_{core}\{\mathrm{d}_r^e\} \tag{6.22.a}$$

$$\{\varepsilon_b\}_{top} = [\mathrm{B}_{tb}]\{\mathrm{d}_t^e\} + [z_3][\mathrm{B}_{rb}]_{top}\{\mathrm{d}_r^e\}, \quad \{\varepsilon_b\}_{visc} = [\mathrm{B}_{tb}]\{\mathrm{d}_t^e\} + [z_4][\mathrm{B}_{rb}]_{visc}\{\mathrm{d}_r^e\} \tag{6.22.b}$$

$$\{\varepsilon_b\}_{piezo} = [\mathrm{B}_{tb}]\{\mathrm{d}_t^e\} + [z_5][\mathrm{B}_{rb}]_{piezo}\{\mathrm{d}_r^e\} \tag{6.22.c}$$

$$\{\varepsilon_s\}_{bot} = [\mathrm{B}_{ts}]\{\mathrm{d}_t^e\} + [z_6][\mathrm{B}_{rs}]_{bot}\{\mathrm{d}_r^e\}, \quad \{\varepsilon_s\}_{core} = [\mathrm{B}_{ts}]\{\mathrm{d}_t^e\} + [z_7][\mathrm{B}_{rs}]_{core}\{\mathrm{d}_r^e\} \tag{6.23.a}$$

$$\{\varepsilon_s\}_{top} = [\mathrm{B}_{ts}]\{\mathrm{d}_t^e\} + [z_8][\mathrm{B}_{rs}]_{top}\{\mathrm{d}_r^e\}, \quad \{\varepsilon_s\}_{visc} = [\mathrm{B}_{ts}]\{\mathrm{d}_t^e\} + [z_9][\mathrm{B}_{rs}]_{visc}\{\mathrm{d}_r^e\} \tag{6.23.b}$$

$$\{\varepsilon_s\}_{piezo} = [\mathrm{B}_{ts}]\{\mathrm{d}_t^e\} + [z_{10}][\mathrm{B}_{rs}]_{piezo}\{\mathrm{d}_r^e\} \tag{6.23.c}$$

where,

$$[B_{tb}] = \begin{bmatrix} B_{tb1} & B_{tb2} & .... & B_{tb8} \end{bmatrix}^T, \quad [B_{rb}] = \begin{bmatrix} B_{rb1} & B_{rb2} & .... & B_{rb8} \end{bmatrix}^T \tag{6.24.a}$$

$$[B_{ts}] = \begin{bmatrix} B_{ts1} & B_{ts2} & .... & B_{ts8} \end{bmatrix}^T, \quad [B_{rs}] = \begin{bmatrix} B_{rs1} & B_{rs2} & .... & B_{rs8} \end{bmatrix}^T \tag{6.24.b}$$

In which $[B_{tb}]$, $[B_{rb}]$, $[B_{ts}]$ and $[B_{rs}]$ are the nodal displacement matrices and are presented in appendix E. The element stiffness matrix is given by:

$$[K_e] = \int_{-1}^{+1}\int_{-1}^{+1} [B]^T [D][\text{B}]|J|d\xi d\eta \qquad (6.25)$$

6.3.2. Elemental initial stress stiffness matrix

The non-linear strains can be expressed as,

$$\{\varepsilon_{nl}\} = \{\varepsilon_{xnl}, \varepsilon_{ynl}, \varepsilon_{xynl}\} = [\text{R}]\{\text{d}\}/2 \qquad (6.26)$$

where,

$$\{d\} = \Big\{ \text{u}_{,x}, \text{u}_{,y}, \text{v}_{,x}, \text{v}_{,y}, \text{w}_{,x}, \text{w}_{,y}, \theta_{x,x}, \theta_{x,y}, \theta_{y,x}, \theta_{y,y}, \phi_{x,x}, \phi_{x,y}, \phi_{y,x}, \phi_{y,y}, \alpha_{x,x}, \alpha_{x,y}, \alpha_{y,x}, \alpha_{y,y}, $$
$$\beta_{x,x}, \beta_{x,y}, \beta_{y,x}, \beta_{y,y}, \gamma_{x,x}, \gamma_{x,y}, \gamma_{y,x}, \gamma_{y,y}, \theta_x, \theta_y, \phi_x, \phi_y, \alpha_x, \alpha_y, \beta_x, \beta_y, \gamma_x, \gamma_y \Big\}^T$$

and, $\{d\}$ can be expressed as:

$$\{d\} = [G]\{\partial_e\} \qquad (6.27)$$

where,

$$[G] = \sum_{i=1}^{8} \begin{bmatrix} \hat{N} & \bar{O} & \bar{O} & \bar{O} & \breve{O} \\ \bar{O} & \hat{N} & \bar{O} & \bar{O} & \breve{O} \\ \bar{O} & \bar{O} & \hat{N} & \bar{O} & \breve{O} \\ \bar{O} & \bar{O} & \bar{O} & \hat{N} & \breve{O} \\ \widehat{O} & \widehat{O} & \widehat{O} & \widehat{O} & \tilde{N} \\ \tilde{O} & \hat{I} & \tilde{O} & \tilde{O} & \ddot{O} \\ \tilde{O} & \tilde{O} & \hat{I} & \tilde{O} & \ddot{O} \\ \tilde{O} & \tilde{O} & \tilde{O} & \hat{I} & \ddot{O} \\ \dot{O} & \dot{O} & \dot{O} & \dot{O} & \tilde{I} \end{bmatrix}, \text{ in which } \hat{N} = \begin{bmatrix} N_{i,x} & 0 & 0 \\ N_{i,y} & 0 & 0 \\ 0 & N_{i,x} & 0 \\ 0 & N_{i,y} & 0 \\ 0 & 0 & N_{i,x} \\ 0 & 0 & N_{i,y} \end{bmatrix}, \tilde{N} = \begin{bmatrix} N_{i,x} \\ N_{i,y} \end{bmatrix}$$

$\bar{O}$, $\breve{O}$, $\widehat{O}$, $\tilde{O}$, $\dot{O}$, and $\ddot{O}$ are (6×3), (6×1), (2×3), (3×3), (1×3), and (3×1) null matrices, respectively. Similarly, the identity matrix $\hat{I}$ is of size (3×3) and $\tilde{I}$ is of size (1×1). The initial stress stiffness matrix due to thermal loads is given by:

$$[K_\sigma^e] = \int_{-1}^{+1}\int_{-1}^{+1} [G]^T [S][G]|J|d\xi d\eta \qquad (6.28)$$

6.4. EQUATION OF MOTION

The three-point and two-point Gaussian integration rules are used to obtain the element matrices corresponding to the bending and the transverse shear deformation, respectively. The elemental matrices such as the initial stress stiffness matrix $[K_\sigma^e]$,

the stiffness matrix $[K^e]$, and the mass matrix $[M^e]$ are computed separately. The computed element matrices are then assembled to obtain the global stiffness matrices $[K]$, $[K_\sigma]$, and $[M]$. The global matrices can then be used to calculate the natural frequency of the system as:

$$\left| [[K] + [\mathrm{K}_\sigma]] - \omega^2 [M] \right| = 0 \tag{6.29}$$

where, ω is the natural frequency of the system. While dealing with skew plates, the skew coordinates (x', y', z') are considered in place of rectangular coordinates. The generalized displacement vectors of an arbitrary point lying on the skew edge are transformed as follows:

$$\{d_t\} = [\mathrm{L}_t]\{d_t'\}, \qquad \{d_r\} = [\mathrm{L}_r]\{d_r'\} \tag{6.30}$$

where, $\{d_t'\}$ and $\{d_r'\}$ are generalized displacement vectors of the point concerning the new (x', y', z') coordinate system.

$$\{d_t'\} = \begin{bmatrix} u_0' & v_0' & w_0' \end{bmatrix}^T, \text{ and } \{d_r'\} = \begin{bmatrix} \theta_x' & \theta_y' & \phi_x' & \phi_y' & \alpha_x' & \alpha_y' & \beta_x' & \beta_y' & \gamma_x' & \gamma_y' \end{bmatrix}^T \tag{6.31}$$

The transformation matrices are given as:

$$[L_t] = \begin{bmatrix} \cos\lambda & \sin\lambda & 0 \\ -\sin\lambda & \cos\lambda & 0 \\ 0 & 0 & 1 \end{bmatrix}, [L_r] = \begin{bmatrix} \hat{L}_r & \hat{0} & \hat{0} & \hat{0} & \hat{0} \\ \hat{0} & \hat{L}_r & \hat{0} & \hat{0} & \hat{0} \\ \hat{0} & \hat{0} & \hat{L}_r & \hat{0} & \hat{0} \\ \hat{0} & \hat{0} & \hat{0} & \hat{L}_r & \hat{0} \\ \hat{0} & \hat{0} & \hat{0} & \hat{0} & \hat{L}_r \end{bmatrix}, \text{ and } \hat{L}_r = \begin{bmatrix} \cos\lambda & \sin\lambda \\ -\sin\lambda & \cos\lambda \end{bmatrix}$$

In which, $\hat{0}$ is the null vector of size (2×2). The total potential energy and the kinetic energy of a typical element integrated with the ACLD treatment can be expressed as,

$$T_p = \frac{1}{2}\left[\left(\{d_t^e\}^T \left[K_{tt}^e\right]\{d_t^e\}\right) + \left(\{d_t^e\}^T \left[K_{tr}^e\right]\{d_r^e\}\right) + \left(\{d_r^e\}^T \left[K_{tr}^e\right]^T\{d_t^e\}\right) + \left(\{d_r^e\}^T \left[K_{rr}^e\right]^T\{d_r^e\}\right) \right.$$
$$\left. -2\{d_t^e\}^T\{F^e\} - 2\{d_t^e\}^T\{F_t^{therm}\} - 2\{d_r^e\}^T\{F_r^{therm}\} - 2\{d_t^e\}^T\{F_{tp}^e\}V - 2\{d_r^e\}^T\{F_{rp}^e\}V \right] - \in_{33} \frac{V^2}{h_p} \tag{6.32}$$

$$T_k = \frac{1}{2}\int_0^{a_e}\int_0^{b_e} \bar{m}\{\dot{d}_t^e\}^T [N]^T [N]\{\dot{d}_t^e\} \, dxdy \tag{6.33}$$

The terms used in the Eqs. 6.32 and 6.33 are presented in Appendix F. Applying the dynamic version of the virtual work principle, the following open-loop equations of motion are obtained:

$$[M^e]\{\ddot{d}_t^e\} + [K_{tt}^e]\{d_t^e\} + [K_{tr}^e]\{d_r^e\} = \{F^e\} + \{F_{tp}^e\}V + \{F_t^{therm}\} \qquad (6.34)$$

$$[K_{tr}^e]^T\{d_t^e\} + [K_{rr}^e]\{d_r^e\} = \{F_{rp}^e\}V + \{F_r^{therm}\} \qquad (6.35)$$

Finally, the global equation of motion of the overall plate is obtained by assembling the elemental equation of motion as follows:

$$[M]\{\ddot{X}\} + [K_{tt}]\{X\} + [K_{tr}]\{X_r\} = \{F\} + \{F_t^{therm}\} + \sum_{j=1}^{q}\{F_{tp}^j\}V^j \qquad (6.36)$$

$$[K_{rt}]\{X\} + [K_{rr}]\{X_r\} = \{F_r^{therm}\} + \sum_{j=1}^{q}\{F_{rp}^j\}V \qquad (6.37)$$

where, $[M]$ is the global mass matrix, $[K_{tt}]$, $[K_{tr}]$ and $[K_{rr}]$ are the global stiffness matrices, $\{F_{tp}\}$, $\{F_{rp}\}$ are the global electro-elastic coupling vectors, $\{F_t^{therm}\}$, $\{F_r^{therm}\}$ are the global thermal force vectors, $\{X\}$ and $\{X_r\}$ are the global nodal generalized displacement vectors, $\{F\}$ is the global nodal force vector, V^j is the applied voltage to the j-th patch, and q is the number of patches.

6.4.1. Closed-loop model

The main function of the ACLD treatment is to incorporate supplementary damping characteristics into the vibrating host structure. This is achieved by activating the constraining layer of each patch of the treatment with a control voltage proportional to the transverse velocity of a point. Thus, the control voltage for each patch can be expressed as follows (Suresh Kumar and Ray, 2012),

$$V^j = -K_d^j\dot{w} = -K_d^j[U_t^j]\{\dot{X}\} - K_d^j\frac{H}{2}[U_r^j]\{\dot{X}_r\} \qquad (6.38)$$

where, K_d^j is the control gain of the j-th patch, $[U_t^j]$ and $[U_r^j]$ are the unit vectors for expressing the transverse velocity of a point concerned in terms of the derivative of the global nodal generalized translational displacements. Substituting Eq. 6.38 into Eqs. 6.36 and 6.37, the final equations of motion governing the closed-loop dynamics of the overall plate can be obtained as follows:

$$[M]\{\ddot{X}\} + [K_{tt}]\{X\} + [K_{tr}]\{X_r\} + \sum_{j=1}^{m}\{F_{tp}^j\}K_d^j[U_t^j]\{\dot{X}\} + \sum_{j=1}^{m}\{F_{tp}^j\}K_d^j = \{F\} + \{F_t^{therm}\} \quad (6.39)$$

$$[K_{rt}]\{X\} + [K_{rr}]\{X_r\} + \sum_{j=1}^{m}\{F_{rp}^j\}K_d^j[U_t^j]\{\dot{X}\} + \sum_{j=1}^{m}\{F_{rp}^j\}K_d^j\frac{H}{2}[U_r^j]\{\dot{X}_r\} = \{F_r^{therm}\} \quad (6.40)$$

155

6.5. RESULTS AND DISCUSSIONS

In this section, an investigation of the influence of temperature on the vibration attenuation characteristics of SLCS plates integrated with ACLD patches is presented. The temperature-dependent material properties of the graphite-epoxy face sheets and the CNTRC cores material are utilized as presented in chapter 4. The CNT efficiency parameters (η_i) and corresponding values of CNT volume fraction are noted in Table 6.1.

Table 6.1: Values of the CNT efficiency parameters corresponding to CNT volume fraction values (Alibeigloo and Emtehani, 2015).

$V_{CNT}{}^{*}$	η_1	η_2	η_3
0.11	0.149	0.934	0.654
0.14	0.150	0.941	0.659
0.17	0.141	1.381	0.967

In the case of viscoelastic materials, the values of storage modulus and loss factor are considered to change with respect to temperature as presented in Figure 2.3, and the mechanism of variation of material behavior is expressed as,

$$G(T) = G'(T)[1 + i\eta(T)] \tag{6.41}$$

The PZT-5H crystal is considered as the actuating layer. The electro-elastic material properties such as piezoelectric constant and dielectric constants are assumed to vary with an increase in the magnitude of temperature, as presented in Table 6.2.

Table 6.2: Piezoelectric and Dielectric properties of PZT-5H material at different temperatures (Wang et al., 1998: Sharma et al., 2015).

Temperature (°C)	Piezoelectric constant, $(d_{31})\ 10^{-12}$ (C/N)	Dielectric constant, 10^{-9} (F/m)
-70	1.60	1.67
-50	1.84	1.92
-25	2.13	2.22
0	2.43	2.49
25	2.72	2.84
50	3.00	3.11
70	3.24	3.34
100	3.59	3.74
120	3.82	4.21

6.5.1. Validation study

The validation study is performed to verify the present model with the well-established models available in the literature. The non-dimensional deflection of simply supported (SS) composite plates subjected to uniformly distributed temperature fields are presented in Table 6.3. The material properties are considered for the simulation are: $E_1 = 25E_2$, $G_{12} = G_{13} = 0.5E_2$, $\upsilon_{12} = 0.25$, and $\alpha_1 = 3\alpha_3$. The obtained results are found to be in good agreement with the published results (Reddy, 2003: Gupta and Ghosh, 2019).

Table 6.3: Non-dimensional transverse deflections of a laminated composite plate with SS boundary condition subjected to uniformly distributed temperature ($\Delta T = 100$ K).

a/b	a/H	Orthotropic plate			$0^o/90^o$ composite plate		
		Reddy (2003)	Gupta and Ghosh (2019)	Present	Reddy (2003)	Gupta and Ghosh (2019)	Present
	10	1.4603	1.4606	1.4605	1.7213	1.7215	1.7214
1	20	1.4409	1.4412	1.4411	1.7269	1.7271	1.7270
	100	1.4334	1.4338	1.4337	1.7293	1.7295	1.7295
	10	3.1321	3.1325	3.1325	2.1446	2.1449	2.1449
1.5	20	3.1339	3.1343	3.1342	2.1394	2.1398	2.1397
	100	3.1343	3.1348	3.1347	2.1377	2.1381	2.1380
	10	4.5966	4.5972	4.5971	2.1100	2.1106	2.1105
2	20	4.6243	4.6249	4.6248	2.0965	2.0970	2.0969
	100	4.6342	4.6348	4.6347	2.0918	2.0924	2.0923
	10	5.4269	5.4277	5.4276	1.9862	1.9870	1.9869
2.5	20	5.4609	5.4617	5.4616	1.9703	1.9711	1.9710
	100	5.4729	5.4737	5.4735	1.9649	1.9658	1.9656
	10	5.6987	5.6997	5.6995	1.8796	1.8808	1.8806
3	20	5.7239	5.7249	5.7248	1.8649	1.8661	1.8659
	100	5.7327	5.7340	5.7335	1.8600	1.8611	1.8609

Further, the open and closed-loop behavior of the sandwich plate is also compared with the published results. Figure 6.3 represents the frequency response function of the transverse displacements of the sandwich plate with $(0^o/90^o/0^o/\text{Core}/0^o/90^o/0^o)$ combination for SS boundary condition. The obtained results show that the developed model is in decent agreement with Suresh and Ray (2012).
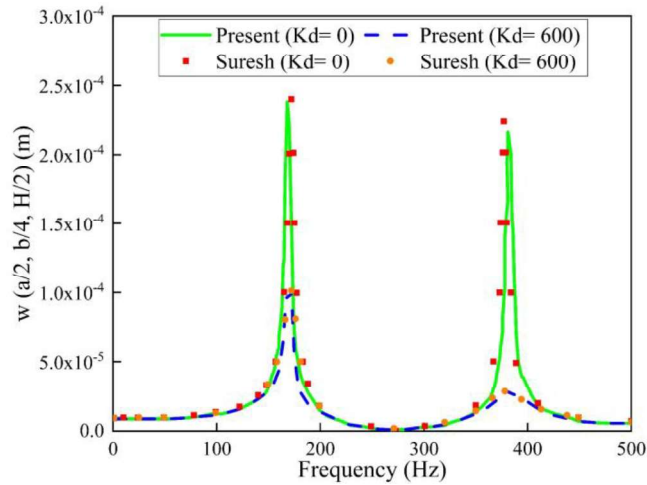
Figure 6.3: Validation study of the frequency response function plots for the transverse displacement of an LCS plate (0º/90º/0º/Core/0º/90º/0º) with HEREX core and graphite-epoxy face sheet.

6.5.2. Numerical results

The influence of the thermal environment on the vibration attenuation characteristics of the cross-ply LCS plate (0º/90º/0º/Core/0º/90º/0º) is presented in Figure 6.4. A square sandwich plate of length to thickness ratio $a/H = 10$, and the ratio of core thickness to face sheet thickness $t_c/t_f = 100$, operating at an elevated temperature of 400 K, is considered for the analysis. The CNTRC core with FG-V type gradation with 0.11 volume fraction of CNT is considered. The behavior of the plate is studied by the frequency response functions for the transverse displacement evaluated at a point ($a/2$, $b/4$, $H/2$) on the top surface of the substrate plate. A time-harmonic point force of magnitude 1 kN is considered to act at the same point to excite the first few modes of the plate. The thicknesses of the viscoelastic layer and PZT-5H layer are considered to be 250 μm each. The control gains are arbitrarily selected such that the first few modes are satisfactorily controlled while the value of the control voltage is nominal. Unless otherwise mentioned, the constraining/actuating layer is considered to be positioned at the center of the plate, and the viscoelastic material is considered as EC 2216.

The active vibration control of the LCS plate is achieved at elevated temperature (400 K) under two cases. In the first case, the thermal effect is considered only to the substrate sandwich plate, i.e., by ignoring the temperature dependence of material

properties of viscoelastic and piezoelectric layers (Non-robust), while in the second case, the temperature dependence of material properties of viscoelastic and piezoelectric layers (Robust) are considered, i.e., the whole system is exposed to the thermal environment (thermal effect on substrate plate, viscoelastic and piezoelectric layer together). It is evident from Figure 6.4 that the non-robust control strategy underpredicts the damping performance of the sandwich plate for both simply supported and clamped (CC) boundary conditions. The vibration attenuation characteristics obtained from the non-robust control strategy exhibit more deviations from the experimental results in comparison with the robust control strategy (Gupta *et al*., 2011: Sharma *et al*., 2015).

(a)   (b)
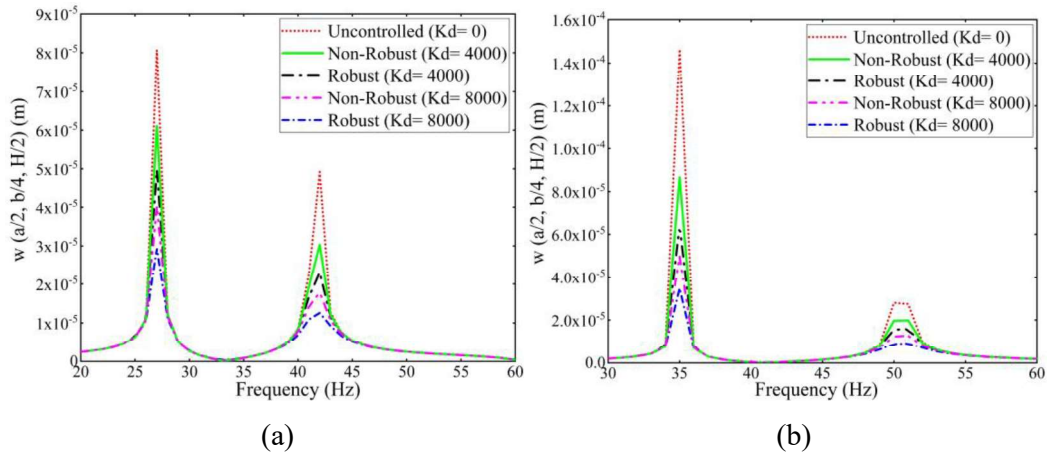
Figure 6.4: Frequency response function for the transverse displacement of an LCS plate (0º/90º/0º/Core/0º/90º/0º) operating at 400 K under (a) SS and (b) CC boundary conditions.

Analogously, the investigation is performed to understand the control voltage requirement for both robust and non-robust control strategies. From the results presented in Figure 6.5, it is evident that the non-robust control strategy demands more control voltage in comparison with the robust control strategy. In reality, the material properties of the constraining/actuating layer change in the presence of an elevated thermal environment, which in turn affects the vibration attenuation characteristics of the structure. From the results, it can be noted that in elevated thermal environments, the actual demand for control voltage is much lesser than the voltage demand predicted by the non-robust control strategy. Consequently, the non-robust control strategy sends in more control voltage into the system. Thus, it may cause instability

159

problems in the structure. Similar observations were made by Sharma *et al*. (2015). Hence, from the present results, it can be deduced that the non-robust control strategy is ineffective in the presence of an elevated thermal environment (Gupta *et al*., 2011: Sharma *et al*., 2015, 2016).

(a)   (b)
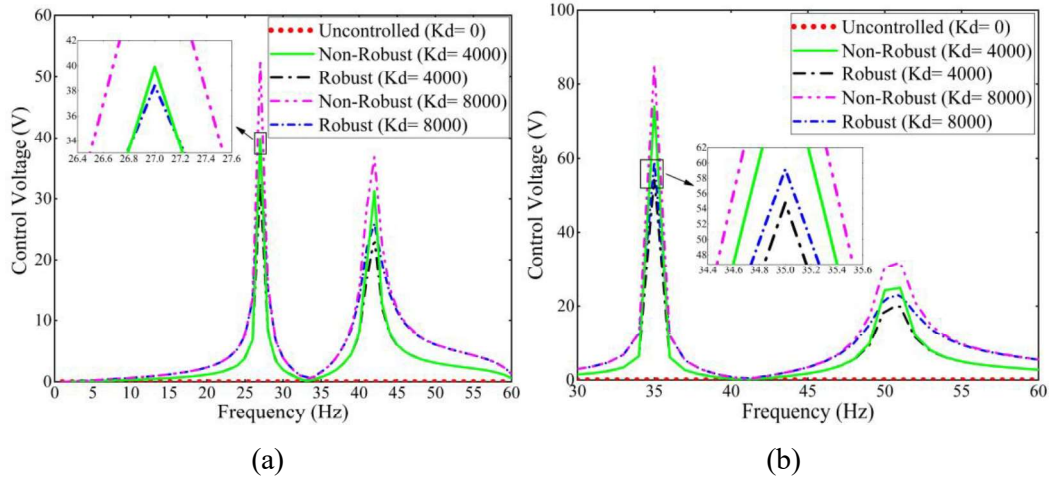
Figure 6.5: Frequency response function for the control voltages of active damping of an LCS plate (0º/90º/0º/Core/0º/90º/0º) operating at 400 K under (a) SS and (b) CC boundary conditions.

Further analysis is carried out to study the effect of temperature on the ACLD of sandwich plate considering elevated temperatures ranging from 300 K to 425 K. The clamped cross-ply LCS plate (0º/90º/0º/Core/0º/90º/0º) with $a/H = 10$, $a/b = 2$, and $t_c/t_f = 100$ is considered for the analysis. The CNTRC core with FG-V type material gradation with 0.11 volume fraction of CNT is considered, and the results are presented in Figure 6.6. It is evident from Figure 6.6 that the robust control strategy is more effective in the elevated thermal environment. The phenomenon is mainly due to a reduction in the stiffness of the substrate materials. The stiffness of the system considerably reduces with an increase in temperature, which in turn causes a reduction in the strength of the material (Biswal *et al*., 2015). Moreover, the control force of the actuator is completely dependent on the piezoelectric constant (d_{31}), and hence the vibration attenuation increases with an increase in temperature (Sharma *et al*., 2015).

160
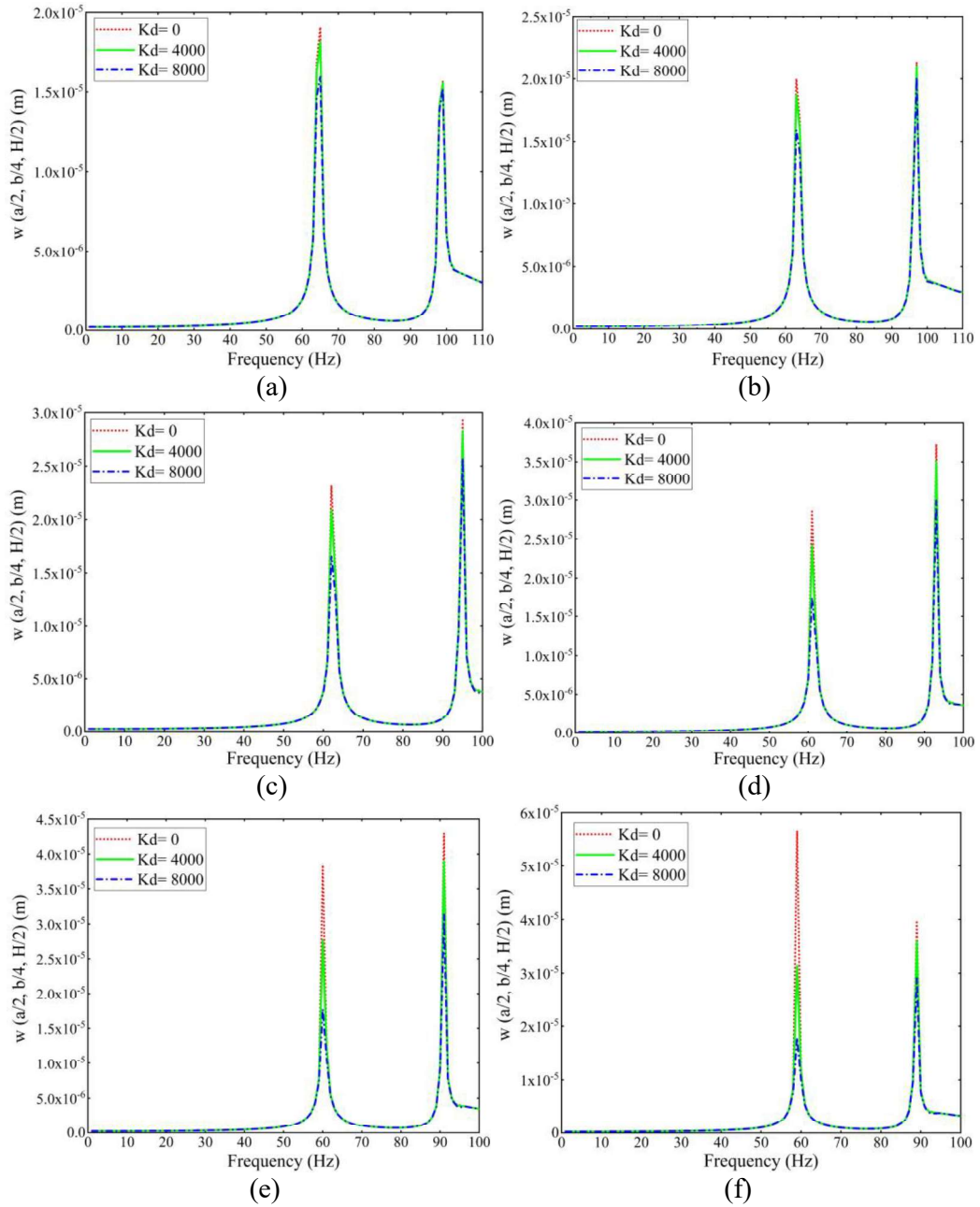
Figure 6.6: Effect of temperature on frequency response function of the LCS plate with CC boundary condition ($a/b = 2$) operating at (a) 300 K, (b) 325 K, (c) 350 K, (d) 375 K, (e) 400 K, and (f) 425 K.

Considering the control gain as Kd = 8000, the vibration attenuation of 16.08 % is observed at 300 K, whereas for 425 K, the vibration attenuation of 68.48 % is recorded for the first mode. For the second mode, the vibration attenuation of 2.72 % and 26.21 % is noted for 300 K and 425 K, respectively. Superior vibration attenuation

characteristics can be obtained with higher values of control gain magnitude at both room temperature and elevated thermal environments. The estimated control voltage requirements for the above-mentioned vibration attenuations are plotted in Figure 6.7. A similar trend in variation of the frequency response and control voltage requirements is observed for the LCS plate with SS boundary condition for increasing temperature values.

To demonstrate the influence of temperature on the vibration attenuation characteristics of a robust controller, the frequency response plot and the control voltage requirements for different temperature values are plotted in Figure 6.8. It can be observed that with an increase in temperature, the transverse deflection of the system increases, and the natural frequency of the system reduces. Both the face sheet material (Graphite and epoxy) and core material (CNT and epoxy) are two-phase structures. At elevated temperatures, both the phases behave differently; due to this, the bond between the reinforcing and matrix phase weakens (Rezaei *et al*., 2021). At the same time, with an increase in temperature, the mechanical properties of constituent materials, such as strength, stiffness, etc., reduce considerably. Reduction in stiffness and strength causes a reduction in natural frequency and an increase in transverse deflection (Kundalwal *et al*., 2013, 2015: Sharma *et al*., 2015).

The study is extended to understand the effect of skew angle on vibration characteristics of LCS plates operating in elevated thermal environments. Square sandwich plate (0°/Core/0°) with $a/H = 10$, $t_c/t_f = 100$, operating at an elevated temperature of 400 K, is considered for the analysis. The uniformly distributed (FG-UD) CNTRC core with a 0.17 volume fraction of CNT is considered. The responses of both SS and CC boundary conditions considering control gain Kd = 8000 are presented in Figure 6.9. It is evident from the results that with the increase in skew angle, the natural frequency of the system increases, and the transverse deflection of the system reduces for both the boundary conditions. This is mainly due to the increase in stiffness of the structure with an increase in skew angle (Biswal *et al*., 2015).

The investigation is further extended to understand the effect of the material gradation on vibration characteristics of SLCS plates operating in elevated thermal environments. Gradation type FG-X, FG-O, FG-V, and FG-UD with a volume

162

fraction of 0.14 are considered for the study. A square sandwich plate (0^{0}/Core/0^{0}) with an a/H ratio of 10, t_c/t_f ratio of 100, operating at an elevated temperature of 400 K, is considered for the simulation.
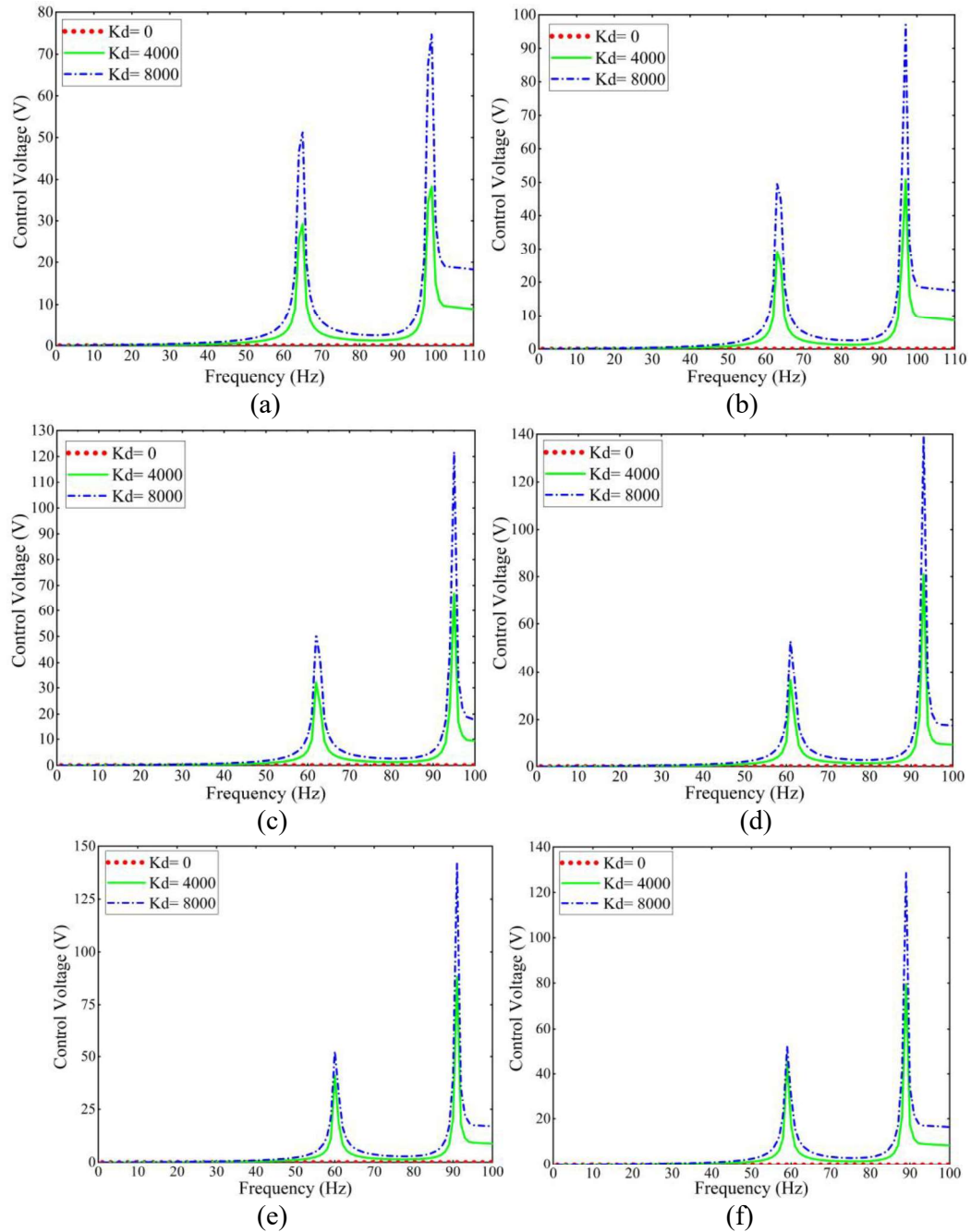
Figure 6.7: Control voltage distribution of ACLD of LCS plate with CC boundary condition ($a/b = 2$) operating at (a) 300 K, (b) 325 K, (c) 350 K, (d) 375 K, (e) 400 K, and (f) 425 K.

(a)   (b)
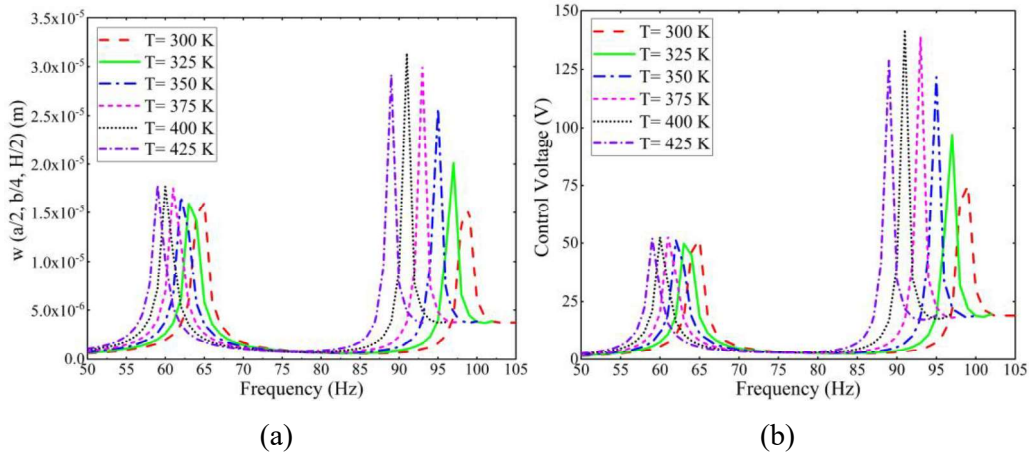
Figure 6.8: Effect of temperature on the LCS plate with CC boundary condition (Kd = 8000) on (a) frequency response function and (b) control voltage distribution.

(a)   (b)
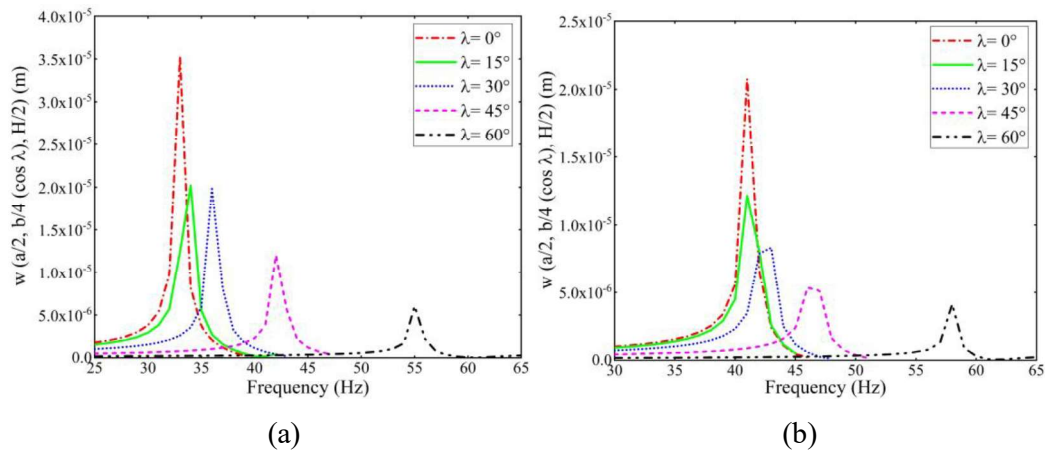
Figure 6.9: Effect of skew angle on frequency response function of an LCS plate (0°/Core/0°, Kd = 8000) operating at 400 K under (a) SS and (b) CC boundary conditions.

The plate with a skew angle of 15° and a control gain of 8000 is considered for the analysis for both SS and CC boundary conditions. The results plotted in Figure 6.10 show that the plate with FG-O gradation has a lower natural frequency than other gradation types. The frequency response plots of gradation types FG-X and FG-V coincide with each other. The transverse deflection of FG-UD gradation is almost the same as that of FG-X and FG-V gradation types for the second mode. Whereas, for the first mode, the plate with FG-UD gradation has a higher transverse deflection in comparison with the FG-X and FG-V gradation types. Further, the influence of the volume fraction of CNT on the frequency response and control voltage requirements

164

of a SLCS plate is investigated at an elevated temperature environment (425 K) for SS boundary condition. In addition, a square sandwich plate ($0^\circ/90^\circ/0^\circ$/Core/$0^\circ/90^\circ/0^\circ$) with $a/H = 10$, $t_c/t_f = 100$ is also considered for the analysis. Further, the skew angle of 30°, the CNTRC core with FG-UD type functional gradation, and control gain of 8000 are considered for the simulation. The results obtained are presented in Figure 6.11. It is evident from the results that with the increase in the volume fraction, the natural frequency of the system increases, whereas the transverse deflection of the system reduces. This variation is due to an increase in stiffness of structure with an increase in the volume fraction of CNT (Dat *et al*., 2020).
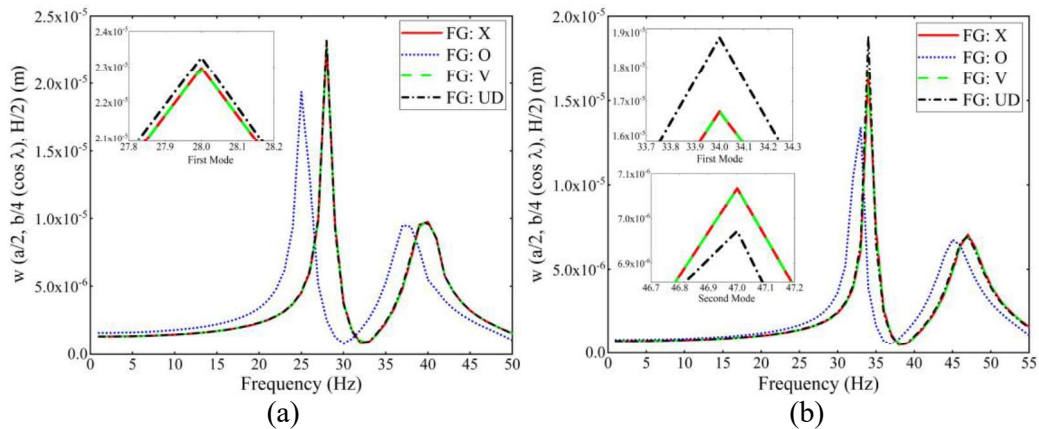
Figure 6.10: Effect of gradation method on frequency response function of an LCS plate (Kd = 8000) operating at 400 K under (a) SS and (b) CC boundary conditions.
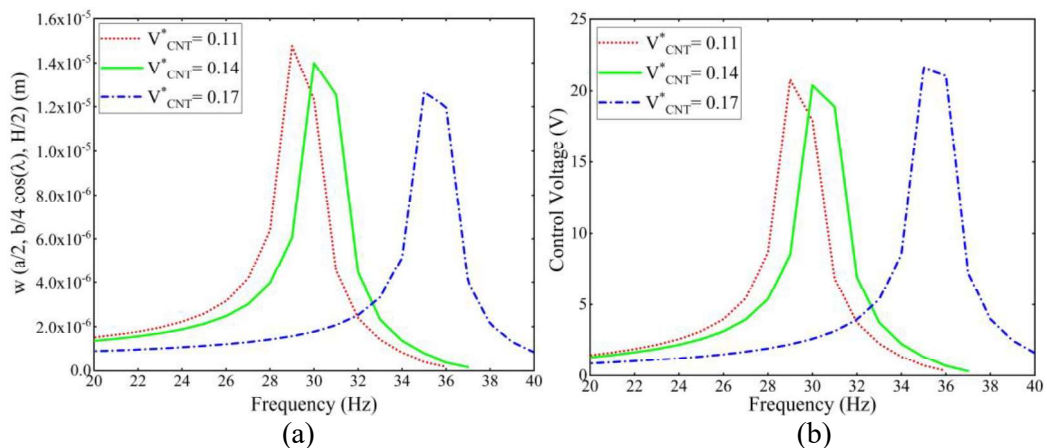
Figure 6.11: Effect of volume fraction of CNTRC on LCS plate with SS boundary conidtion (Kd = 8000) operating at 425 K (a) frequency response function and (b) control voltage distribution.

In order to study the influence of viscoelastic materials used in the ACLD of the SLCS plate, two types of viscoelastic materials are chosen for the analysis, namely, DYAD 606 and EC 2216. A square sandwich plate ($0^o/90^o/0^o/Core/0^o/90^o/0^o$) with $a/H = 10$, $t_c/t_f = 100$, operating at an elevated temperature of 425 K is considered. Also, to appreciate the difference in the vibration attenuation capabilities of both the materials, the viscoelastic layer thickness is considered as 25 mm. The uniformly distributed CNTRC core with a volume fraction of 0.17 is adopted. Both SS and CC boundary conditions are explored, considering control gain as 8000 and the skew angle of 60°. The results obtained from the simulations are presented in Figure 6.12. From the results, it can be noted that there is no considerable difference between vibration attenuation characteristics of ACLD of an SLCS plate with DYAD 606 and EC 2216 viscoelastic layers.

The analysis is further extended to understand the effect of the position of constraining/actuating layers on vibration attenuation capabilities of ACLD of an SLCS plate. The constraining layers are positioned at the edge ($a/4$, $b/2$, h_v+h_p) and at the center ($a/2$, $b/2$, h_v+h_p) are chosen for the analysis without altering the volumes for both the cases. In Figure 6.1, the dotted lines represent the position of the edge patch. A square sandwich plate ($0^o/90^o/0^o/Core/0^o/90^o/0^o$) with $a/H = 10$, $t_c/t_f = 100$, operating at an elevated temperature of 375 K, is considered for the analysis. The CNTRC core with FG-UD type functional gradation and 0.11 volume fraction of CNT is considered. A skew angle of 30° is selected for the simulation. The results obtained for both SS and CC boundary conditions are plotted in Figure 6.13. It is evident from the results that the center patch has a better vibration attenuation capability in comparison with the plate with the edge patches.

The influence of t_c/t_f ratio on vibration characteristics of an LCS plate is investigated at 425 K. The plate with fiber orientation $0^o/Core/0^o$, and a/H ratio of 10 are analyzed for different t_c/t_f ratios (i.e., 10, 50, 100). The CNT volume fraction of 0.17 is considered with FG-V type functional gradation. Both SS and CC boundary conditions are used for the analysis considering control gain as 8000, and the results obtained are presented in Figure 6.14. The results show that the transverse deflection and the natural frequency of the system reduce with an increase in t_c/t_f ratio. The clamped cross-ply LCS plate ($0^o/Core/0^o$) with varying a/b ratios is analyzed

considering a/H ratio as 10, and t_c/t_f ratio as 100, operating at 400 K. Uniformly distributed functional gradation with 0.11 volume fraction is considered for the FG-CNTRC core. The results obtained for control gain of 8000 and varying a/b ratio are plotted in Figure 6.15. It is seen from the figure that with an increase in the a/b ratio, the transverse deflection of the system reduces, whereas the natural frequency of the system increases.

(a)   (b)
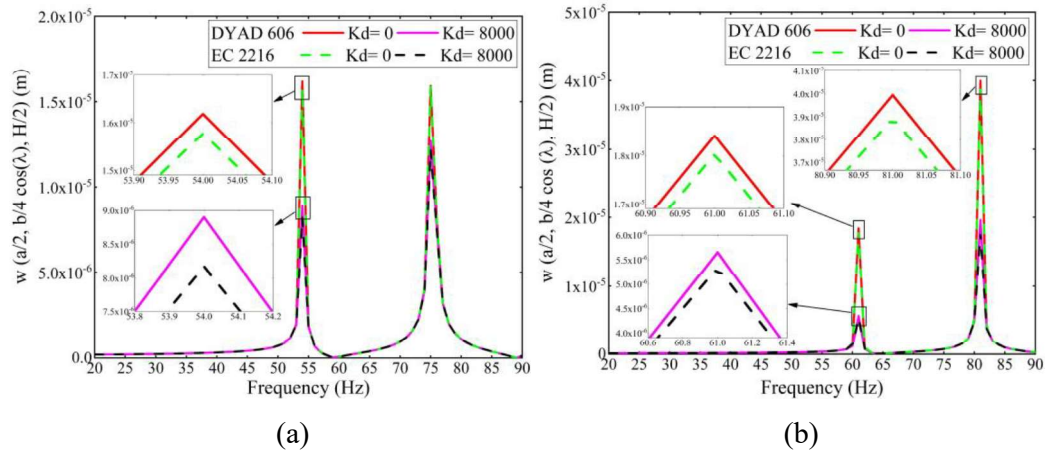
Figure 6.12: Effect of type of viscoelastic material on LCS plate operating at 425 K under (a) SS and (b) CC boundary conditions.

(a)   (b)
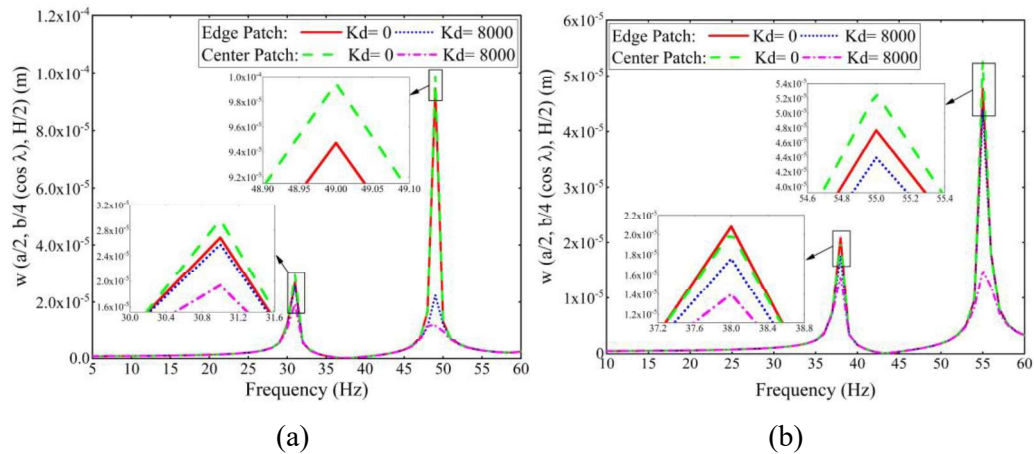
Figure 6.13: Effect of position of the patch on LCS plate operating at 425 K under (a) SS and (b) CC boundary conditions.

The clamped cross-ply LCS plate (0º/Core/0º) with varying a/H ratios is analyzed considering a/b ratio as 2, and t_c/t_f ratio as 100, operating at 425 K. The CNTRC core with FG-UD type functional gradation and 0.11 volume fraction of CNT is

considered. The results obtained for the control gain of 8000 and varying a/H ratio are plotted in Figure 6.16. It can be seen from the results that with an increase in the a/H ratio, the transverse deflection of the system reduces, whereas the natural frequency of the system increases.

(a)

(b)
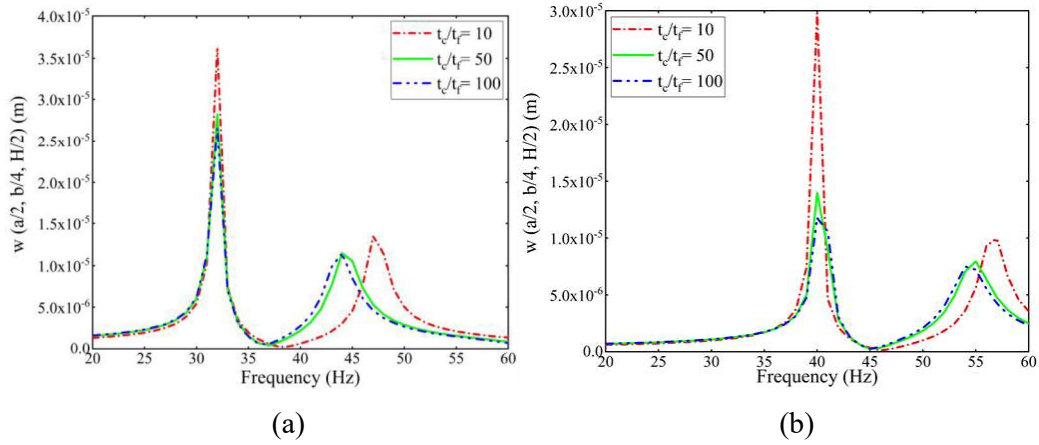
Figure 6.14: Effect of ratio of the thickness of core to the thickness of face sheet on an LCS plate (Kd = 8000) operating at 425 K under (a) SS and (b) CC boundary conditions.
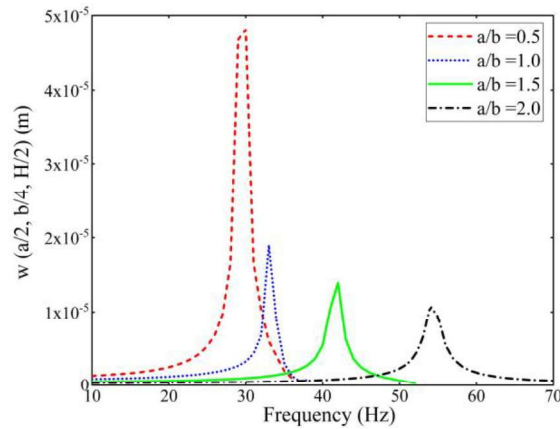
Figure 6.15: Effect of length to width ratio on a clamped LCS plate (Kd = 8000) operating at 400 K under CC boundary conditions.

Influence of the number of layers and fiber orientation of face sheet of the square LCS plate are investigated considering t_c/t_f = 100, a/H = 10, operating at 375 K. The volume fraction of CNT of 0.17 and FG-UD type functional gradation are considered for the simulation of cross-ply sandwich plate [N...90º/0º/Core/90º/0º...N] with SS boundary condition. From the results plotted in Figure 6.17, it can be

observed that the 0º/core/0º (i.e., N = 1) sandwich plate has the lowest natural frequency, and the plates with an even number of layers (N = 2,4..) tend to have the same natural frequencies.
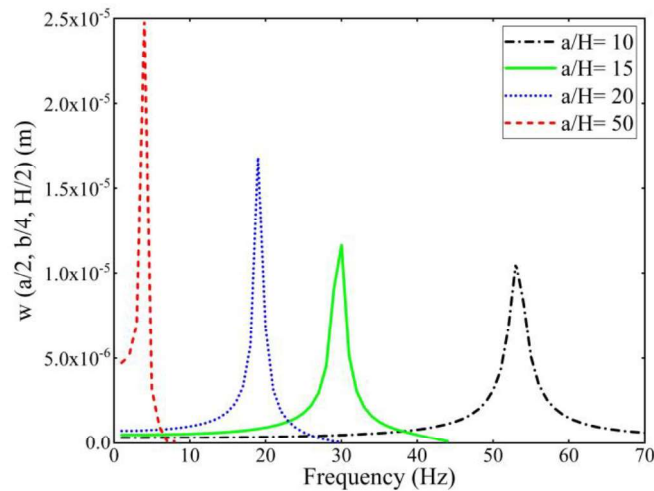
Figure 6.16: Effect of a/H ratio on a LCS plate with CC boundary condition (Kd = 8000, a/b = 2) operating at 425 K under CC boundary conditions.
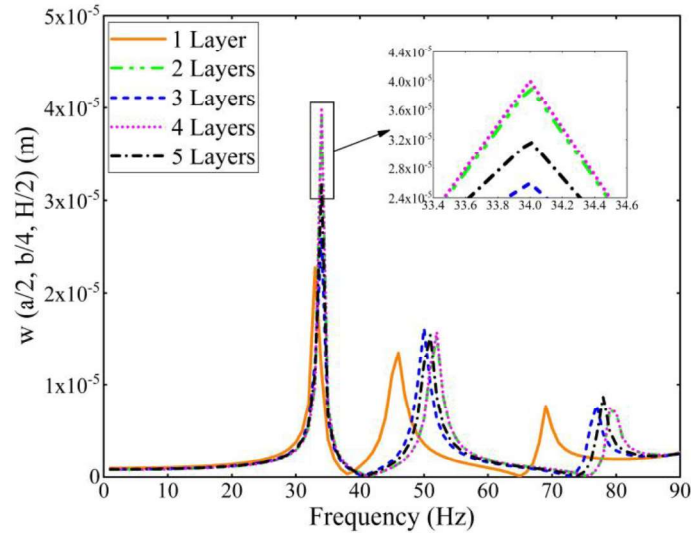
Figure 6.17: Effect of fiber orientation and the number of layers on an LCS plate (Kd = 8000, a/b = 1) operating at 375 K under SS boundary conditions.

Similarly, the highest magnitude of the transverse deflection of the system is observed for the plates with an even number of layers. It can also be noted that as the number of layers of the face sheets increases (N > 3), the change in the frequency response of the system becomes insignificant (Suresh Kumar et al., 2013).

6.6 CONCLUSION

In this chapter, the effect of pre-stresses induced due to temperature change on the vibration attenuation characteristics of the ACLD of the SLCS plate with CNTRC core is investigated. A unique robust control strategy used in this study provides an accurate prediction of vibration characteristics of ACLD of sandwich plates, involving the study of the effect of temperature on the complete system (i.e., substrate plate, viscoelastic, and piezoelectric layers). The damping characteristics are examined for both robust and non-robust control strategies. The results suggested that the non-robust control strategy under-predicts the damping characteristics of the system. Hence, the change in material properties due to temperature variations should be considered for the whole system to obtain accurate responses. It is also observed that the natural frequency of the LCS plate increases with an increase in skew angle and aspect (a/b and a/H) ratios, while the transverse deflection of the system reduces with an increase in aspect ratios. The effect of variation of CNT volume fraction and type of CNT distribution has also been investigated. The results reveal that the addition of CNT increases the natural frequency and decreases the transverse deflection of the system. The sandwich plate with FG-O type distribution has the lowest natural frequency and deflection in all four cases. The simulation results indicate that the ratio of core thickness to the thickness of the face sheet significantly dictates the vibrational behavior of the system. With the increase in t_c/t_f ratio, both the natural frequency and the transverse deflection of the structure reduce. The numerical evaluations also indicated that the centrally located ACLD patches are more efficient in vibration attenuation than the patches located at the edge of the plate.

Chapter 7

EXPERIMENTAL INVESTIGATION OF VIBRATION CHARACTERISTICS OF LAMINATED COMPOSITE SANDWICH PLATES IN THERMAL ENVIRONMENT

This chapter presents the experimental investigation on the free vibration response of laminated composite and sandwich plates operating in thermal environments. The influence of temperature on the vibration response of the glass-epoxy composite plate is investigated at an elevated thermal atmosphere (25 °C to 100 °C). Further, the free vibration tests are performed on the laminated composite sandwich (LCS) plate with a 3D printed PLA core operating in the sub-ambient thermal setup. For such investigation, two thermal profiles are considered to sweep through the required temperatures (-20 °C to +30 °C). The natural frequency values obtained from the experimental method are compared with the numerical results. Additionally, the influence of plate dimensions and boundary conditions on the natural frequency of sandwich plates are investigated.

7.1. INTRODUCTION

The generalized assumptions adopted to solve the complex engineering problems cause the deviation between numerical and experimental results. The inherent experimental errors such as material non-homogeneity, fixture clamping forces, repeatability of the testing equipment, etc., also cause the nonconformity in experimental and numerical results. Hence, it is important to explore the influence of test parameters on the outcomes of the experimentation and compare the same with the existing numerical models.

This chapter discusses the experimental investigation of vibration response of laminated composite and composite sandwich plates operating in elevated thermal environments. The glass-epoxy composites and 3D printed PLA material are considered for the study. The laminated composite and sandwich vibration samples are fabricated using the hand layup technique. The influence of temperature profiles, boundary conditions, and geometric dimensions on the natural frequency of LCS

plates are also investigated. Further, the experimental results are compared with the outcomes obtained from the developed numerical model.

7.2. MATERIALS AND METHODS

7.2.1. Specimen preparation

The glass-epoxy laminated composite samples are fabricated by hand layup and compression molding methods keeping the weight fraction as 50:50. The epoxy resin is prepared by blending the araldite LY-556 resin and HY-951 hardener (S. M. Composites, Chennai) in the ratio of 10:1. Firstly, the plastic sheet (OHP sheet) with a mold releasing agent (petroleum jelly) is roofed on the metal base plate having a smooth surface. The blended resin mixture is then applied to the surface of the sheet as a gel coat. The gel coat helps keep the surface smooth and protects the fibers from exposure to the environment. Then the 280 GSM bidirectional glass fiber mats (Marktech Composites, Bangalore) are laid one above the other to achieve the desired thickness. A sufficient amount of resin mixture is applied before placing the next layer of the glass fiber mat. Care is taken to make sure that the glass fiber mats are completely wet. Metal rollers are used to remove any entrapped air bubbles in the layup. The fabricated laminates are then cured at room temperature (28 °C) under the pressure of 50 bars for 24 hours in a pressure-controlled hydraulic press. After proper curing, the laminates are freed from the plastic sheets (release films). The laminate fabrication process is pictorially represented in Figure 7.1. The cured samples are then cut into the required dimensions. For the tensile test, laminates were cut to 2.5 cm × 25 cm dimensions (as per ASTM 3039). The vibration test samples are cut based on the aspect ratio requirements. The average thickness of the prepared laminates is measured to be 0.25 cm.

The LCS plates are also fabricated using a combination of hand layup and compression molding methods. Initially, the composite bottom face sheet is prepared as discussed above. The 3D-printed PLA core is then placed at the center of the wet bottom face sheet layup. Then the hand layup procedure is followed to produce the top face sheet on top of the centrally placed PLA core. The layup procedure adopted is briefly demonstrated in Figure 7.2. In order to achieve excellent bonding between the core and the face sheet, a sufficient amount of epoxy mixture was applied on to the

PLA core before the layup. The wet sandwich laminate was then cured for 24 hours at room temperature and 50 bar pressure.

7.3. TENSILE TEST

The tensile tests are conducted to understand the influence of temperature on the constituent materials of the LCS structures. The determination of temperature-dependent material properties of the 3D printed PLA material is discussed in chapter 5. The thermal chamber used for the thermal aging is pictorially presented in Figure 7.3. Similar to PLA material, the glass-epoxy samples are also thermally aged for 12 hours in the thermal chamber as shown in Figure 7.4. The temperatures 25 ⁰C, 50 ⁰C, 75 ⁰C, and 100 ⁰C were selected for the investigation. Then the tensile tests are performed on the thermally aged samples. In order to achieve the repeatability and for accurate assessment of modulus values of the glass-epoxy composite material, the tests are performed on five samples for every desired temperature. The average elastic modulus and standard deviation results calculated from the stress-strain curves are presented in Table 7.1. It is apparent from the results that Young's modulus of the composite samples reduces considerably with an increase in temperature.

Table 7.1: Effect of temperature on the elastic modulus of the glass-epoxy composite.

Temperature (⁰C)	Young's Modulus (GPa)
25	4.6718 ± 0.340
50	4.5440 ± 0.299
75	4.4360 ± 0.710
100	4.1894 ± 0.153

7.4. FREE VIBRATION TEST

The vibration samples prepared are firmly fitted to the fixture to obtain the desired boundary condition. The vibration specimen is then excited using an impact hammer (PCB model: 086C03), and the resulting vibration signals are picked up by the high-temperature triaxial-accelerometer (PCB model: 339A31/NC). The accelerometer is attached to the vibration specimen using flex bond instant adhesive, which can operate in high-temperature environments. The impact hammer and accelerometer are connected to an analog input module (NI-DAQ 9234) which is mounted in the USB chassis (NI-USB-9162), as shown in Figure 7.5.
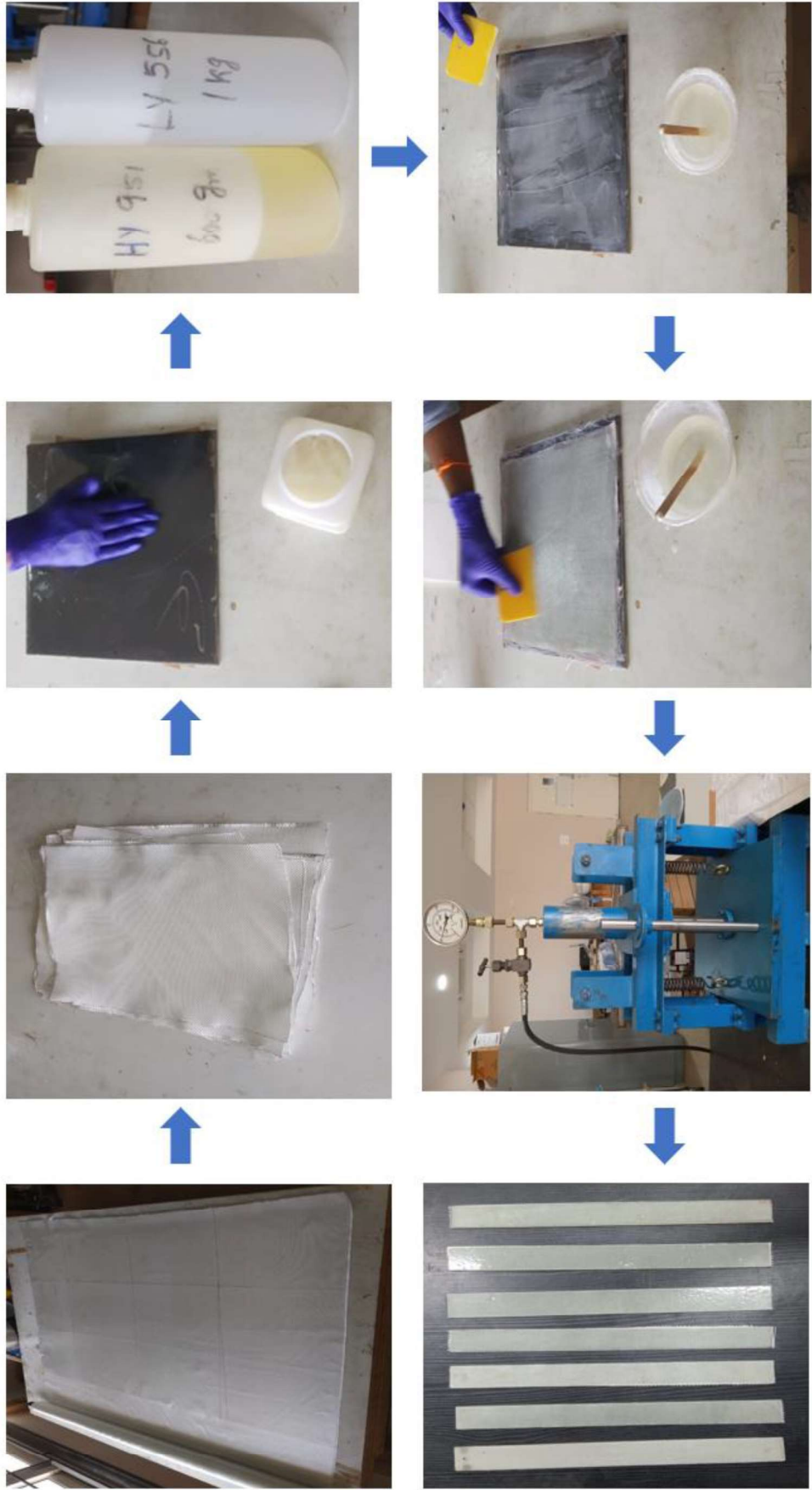
Figure 7.1: Pictorial representation of glass-epoxy composite laminate fabrication.

174

Figure 7.2: Graphical representation of fabrication of LCS plates with 3D printed PLA core.

(a)

(b)

Figure 7.3: Images representing (a) front view (b) side view of the thermal chamber (Ultra-thermo Scientific, Chennai).

(a)
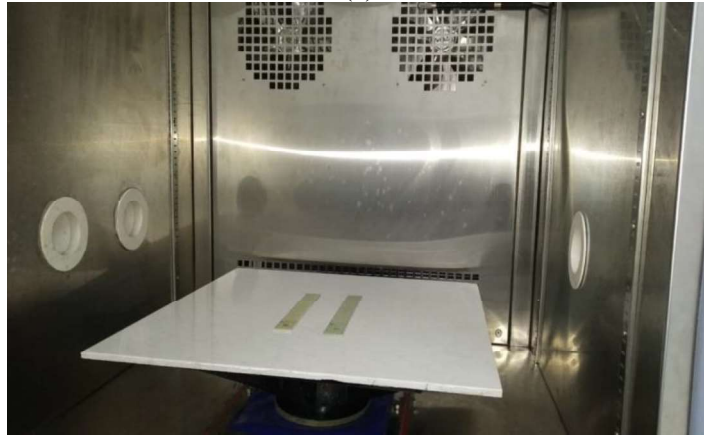
(b)

Figure 7.4: Images representing the (a) glass-epoxy composite tensile test specimen (b) thermal aging of the tensile test samples.
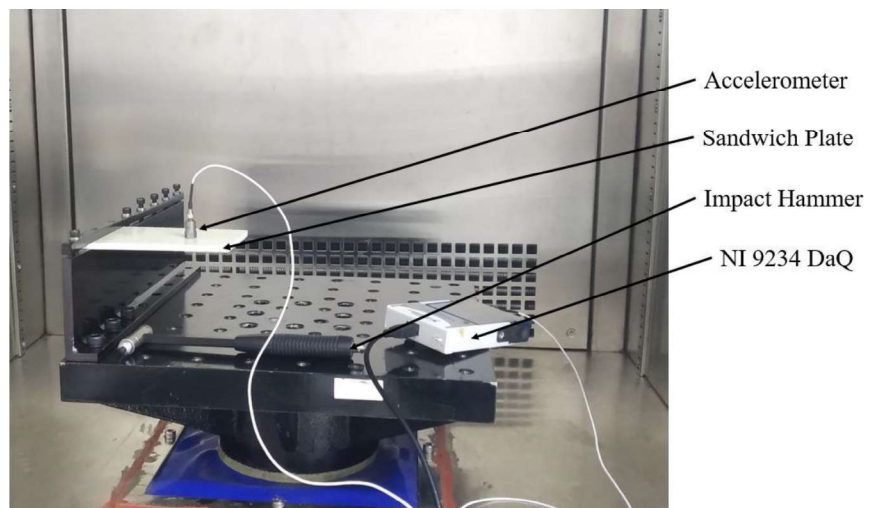
Figure 7.5: Free vibration test setup.

The input force and output acceleration (Z-direction) time-domain signals were captured with a sampling frequency of 25.6 kHz.

7.4.1. Preliminary validation study

The initial set of experiments are conducted on the laminated composite beams to validate the experimental results with the FE results. The unidirectional glass-epoxy composite beam of length 20 cm, width 3 cm, and thickness 0.2 cm is considered for the investigation. A 900 GSM glass-epoxy composite beam with 0° and 90° fiber orientation is then fixed in a cantilever condition to perform the free vibration study. The free vibration results presented in Table 7.2 indicate that the experimental results are in good agreement with the results obtained from the FE commercial package (ANSYS).

Table 7.2: Validation study of 900 GSM unidirectional cantilever composite beam

0° fiber orientation		90° fiber orientation	
Experiment (Hz)	ANSYS (Hz)	Experiment (Hz)	ANSYS (Hz)
40	38.44	23	22.35

7.4.2. Thermal environment: laminated composite beams and plates

The influence of temperature on the free vibration characteristics of laminated composite beam and plates are investigated by thermally aging the samples for 12 hours. The laminated composite beam and plate samples are clamped in the desired boundary conditions and are thermally aged in the thermal chamber before performing the vibration test. The experiments are conducted for temperatures ranging from 25 °C to 100 °C.

The bidirectional 280 GSM glass-epoxy laminated composite beam (of length 21.9 cm, width 2.72 cm, and thickness 0.25 cm) and plate (of length 21 cm, width 21 cm, and thickness 0.19 cm) were thermally aged for 12 hours at 25 °C, 50 °C, 75 °C, and 100 °C, respectively. The cantilever boundary condition was adopted for the investigation. The results obtained are tabulated in Table 7.3. The results show that the natural frequency of the system reduces considerably with an increase in temperature.

Table 7.3: Natural frequency (Hz) of the thermally aged cantilever composite beam and plate

Specimen	25 °C	50 °C	75 °C	100 °C
Composite Beam	15.0050	14.0060	13.9960	13.006
Composite Plate	11.9986	11.0034	11.0006	10.9993

Further, the experimental outcomes are compared with the results obtained from the in-house developed mathematical model (discussed in previous chapters). The numerical and experimental results are found to be in decent agreement with each other, as shown in Figure 7.6.
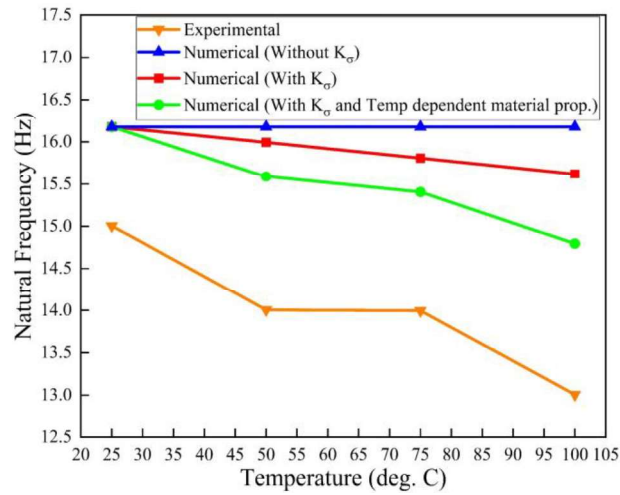
(a)
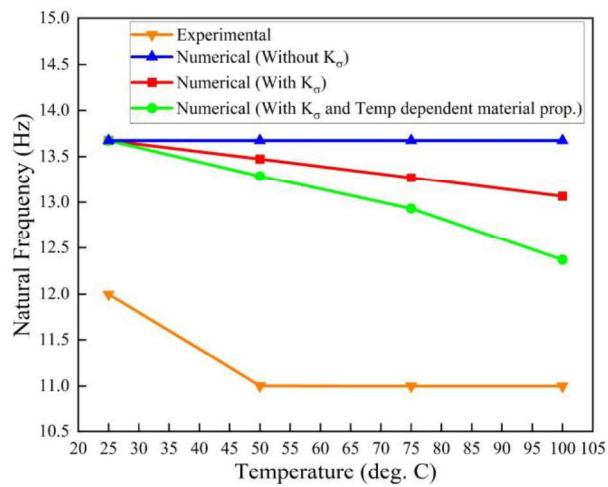
(b)

Figure 7.6: Comparison of experimental vibrational results of (a) composite beam (b) composite plate with the numerical results

From the results presented in Figure 7.6 following conclusions can be drawn:

- Without considering the initial stress stiffness matrix $[K_\sigma]$, the numerical model neglects the reduction in the stiffness of the structure when exposed to a thermal environment. Hence, it depicts constant natural frequency for all the temperature values.

- The FE model considering the initial stress stiffness matrix $[K_\sigma]$ yields more accurate results as it considers the reduction in stiffness of the system caused by temperature change.

- The mathematical model considering the initial stress stiffness matrix $[K_\sigma]$ and temperature-dependent material properties more accurately predict the natural frequency of the structure. The model incorporates a reduction in stiffness of the system due to thermal exposure by considering $[K_\sigma]$ matrix. And it also considers the degradation in material properties of the composite structure upon exposure to elevated thermal environments. Hence, the FE model considering both the initial stress stiffness matrix $[K_\sigma]$ and temperature-dependent material properties more accurately mimics the practical conditions.

7.4.3. Thermal environment: LCS plates

The vibration studies are also performed on the LCS plates operating in sub-ambient temperatures. The sandwich plate with glass-epoxy composite face sheets and 3D printed PLA core is considered for the study. The plate dimensions of 15.5 × 10 × 1.2 cm (D1) and 15.5 × 20 × 1.2 cm (D2) are considered for the investigation with cantilever (CFFF) and clamped-free (CFCF) boundary conditions. Two temperature profiles are generated to sweep through the considered temperature range of -20 ⁰C to +30 ⁰C, as shown in Figure 7.7.

Profile 1: Initially, the temperature of the chamber was reduced to 25 °C from ambient temperature (27 °C to 30 °C). The LCS plate was allowed to stay at 25 °C for 30 minutes. Then the temperature of the chamber was reduced to -20 °C, and the sample was allowed to cure for 30 minutes before taking the reading. The temperature of the chamber was again bought back to 25 °C and allowed to stay for 30 minutes. Subsequently, the temperature was reduced to -10 °C and then maintained for 30

minutes. The procedure is repeated to obtain the readings at other sub-ambient temperatures, as represented in Figure 7.7a.
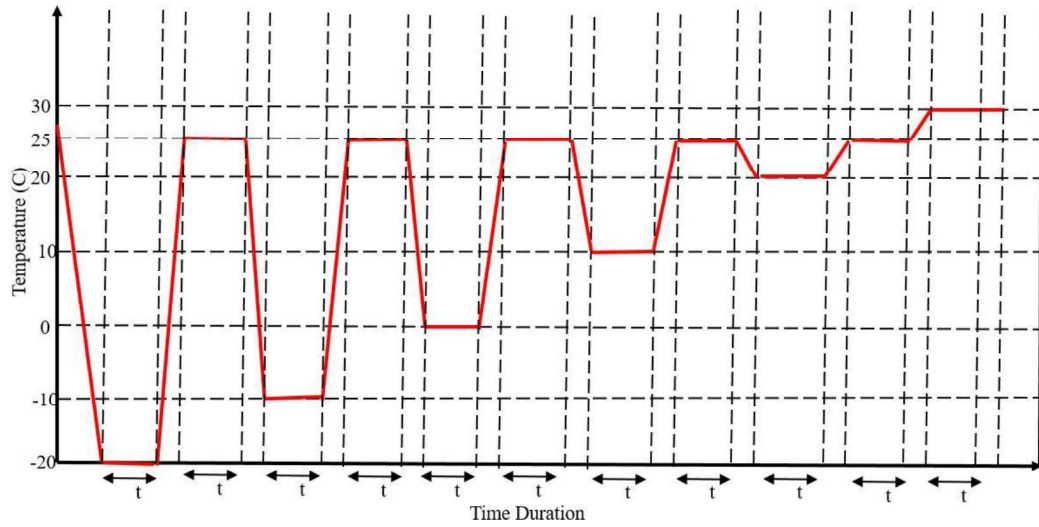
(a)
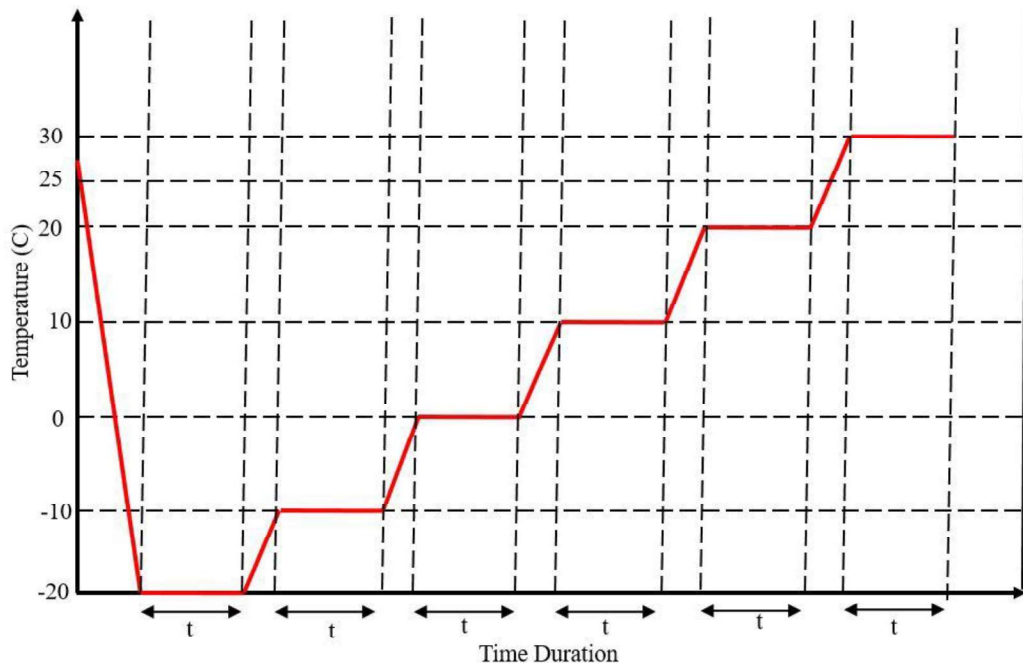
(b)

Figure 7.7: Schematic representation of the thermal profiles (a) profile 1 (b) profile 2 incorporated to investigate the free vibration response of LCS plates operating in sub-ambient thermal environments (t = 30 min).
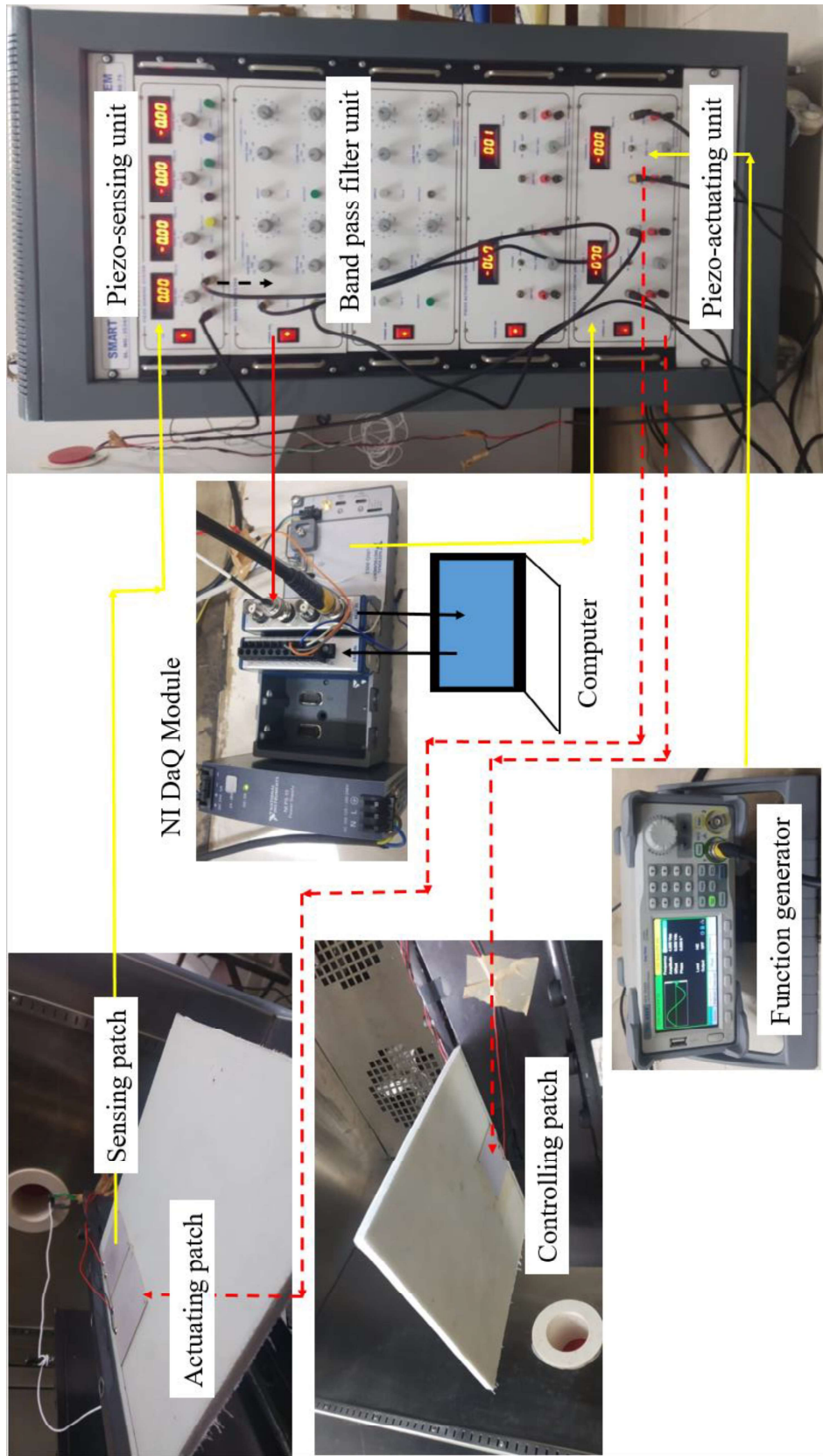
Figure 7.8: Vibration control setup.

182

Profile 2: The temperature of the chamber was reduced to 25 °C from room temperature. The samples were allowed to thermally age for 30 minutes. Then the temperature was reduced to -20 °C, and the sample was allowed to cure for 30 minutes before taking the reading. Further, the temperature was raised to -10 °C and was thermally aged for 30 minutes before taking the vibration readings. The procedure is repeated to obtain the readings at other sub-ambient temperatures, as shown in Figure 7.7b.

The non-dimensional natural frequencies of the first two modes are presented in Table 7.4 and 7.5 for CFCF and CFFF boundary conditions, respectively. From the tables it can be observed that the natural frequency of the sandwich plate reduces with an increase in temperature. Additionally, the numerical results are compared with the experimental outcomes. It is observed that the results are in decent agreement with each other.

7.4.4. Vibration control of LCS plate

The vibration attenuation characteristics of LCS plates integrated with PZT-5H patches operating in sub-ambient temperature are investigated. A cantilever LCS plate is considered for the investigation. Three PZT-5H patches were glued to the sandwich plate surface for actuation, sensing, and controlling, respectively. The actuating and the sensing patches were positioned on the top surface of the plate near the fixed end. However, the controlling patch was positioned on the bottom surface of the sandwich plate. The PZT patches were attached to the sandwich structure using the flex bond adhesives. As the vibration control of the sandwich structures is planned at sub-ambient temperatures, the non-conductive PCB coating spray was applied on the top of the patches to protect them from moisture.

The signal generator was used to excite the actuating PZT5H patch with the sine signal. The function generator signal was amplified through the piezo-actuating unit. The sensing patch reads the displacement magnitude of the sandwich plate, and the sensed signal was amplified using the piezo-sensing unit. The physical bandpass filter was used to irradicate the noise present in the sensed signal. The filtered signals are then fed to the computer through the analog input (AI) module (NI 9234 DAQ). The sensor signals were processed to determine the controlling signal. Then the controlling signal was sent to the controlling patch through the analog output (AO)

module (NI 9236 DAQ) and the piezo-amplification unit. The AI and AO cards were loaded into the NI CRIO 9053 data acquisition module for data acquisition and processing of the signals. All the signal data were collected with a sampling rate of 25.6 kHz. The connectivity diagram illustrating the signal flow is presented in Figure 7.8. The vibration attenuation capabilities of the LCS plate integrated with the PZT-5H piezo patches operating at 10 °C, 20 °C, and 30 °C are investigated. The sandwich plate with dimensions 18.2 cm × 19.5 cm, having 0.6 cm thickness, was used for the study. The PLA core of 0.5 cm thickness and face sheets of 0.05 cm thickness were considered for the examination. The PZT-5H patches (Sparkler Ceramics, Pune) of dimensions 5 cm × 5 cm and 0.05 cm thickness were attached to the sandwich plate.

The constant excitation voltage of 80 V was provided to the actuating patch through the function generator and the piezo-actuating amplification module (Smart structure instrumentation system, Bangalore). The proportional control algorithm was adopted to attenuate the vibrating cantilever LCS plate operating in sub-ambient thermal environments. Through the trial and error method, the proportional control gain of 2 was considered for the experimental study. The control voltage of 40 V was supplied into the controlling patch through the controlling PZT5H patch for vibration control. The controlling cancellation signal was sent through the NI AO card, the piezo-actuation amplification module, and the physical bandpass filter. The vibration reduction of the sandwich plate achieved through the proportional controller is plotted in 7.9.

The results suggest that the developed proportional control algorithm is efficient enough to attenuate the vibrating LCS plate. However, the inherent errors of proportional controllers, such as settling time, were reflected in the sensor signals in terms of a transition phase. The transition phase is the time taken by the sandwich structure to attain stability for the given control excitation signal. The results also show that the transition zone increases with an increase in the temperature. This phenomenon will exist in most of the control algorithms; however, the transition zone can be reduced by utilizing advanced controllers such as fuzzy logic controller, fuzzy PID controller, LQR controller, etc.

Table 7.4: Non-dimensional natural frequency of thermally aged sandwich plates under CFCF boundary condition

Temperature (°C)	D1						D2					
	Mode 1			Mode 2			Mode 1			Mode 2		
	Experimental		Numerical	Experimental		Numerical	Experimental		Numerical	Experimental		Numerical
	Profile 1	Profile 2		Profile 1	Profile 2		Profile 1	Profile 2		Profile 1	Profile 2	
-20	2.27263	1.95282	3.28859	4.19964	3.99836	3.89457	1.19333	2.12227	2.15889	2.80538	2.61545	2.45225
-10	2.22707	1.98935	3.27824	4.18696	3.97138	3.87910	1.19002	2.00962	2.14910	2.78542	2.31977	2.43918
0	2.19919	1.95836	3.26786	4.14322	3.92770	3.86355	1.19015	1.45371	2.13926	2.73019	2.11898	2.42603
10	2.16117	1.90729	3.25743	4.12838	3.84003	3.84794	1.17715	1.25927	2.12936	2.69741	2.10796	2.41279
20	2.12268	1.85973	3.24696	4.11369	3.79257	3.83226	1.16806	1.13929	2.11940	2.69935	2.10241	2.39947
30	2.11885	1.82135	3.23646	4.13001	3.71765	3.81651	1.14805	1.11141	2.10939	2.67370	2.10246	2.38607

*Numerical results are obtained by considering uniform temperature and moisture rise.

Table 7.5: Non-dimensional natural frequency of thermally aged sandwich plates under CFFF boundary condition

Temperature (°C)	D1						D2					
	Mode 1			Mode 2			Mode 1			Mode 2		
	Experimental		Numerical	Experimental		Numerical	Experimental		Numerical	Experimental		Numerical
	Profile 1	Profile 2		Profile 1	Profile 2		Profile 1	Profile 2		Profile 1	Profile 2	
-20	0.43781	0.39235	0.64985	3.13731	3.01133	1.75319	0.31743	0.24637	0.40953	1.61703	2.10246	1.02133
-10	0.43263	0.38878	0.64313	3.12122	3.02057	1.70108	0.30492	0.22998	0.40306	1.63724	2.05320	0.98352
0	0.43257	0.38873	0.63630	3.08808	3.01710	1.64724	0.30301	0.22996	0.39645	1.49105	1.98743	0.94412
10	0.43809	0.38874	0.62938	3.02782	2.98947	1.59151	0.29762	0.23000	0.38968	1.52578	1.96019	0.90290
20	0.43257	0.38879	0.62235	2.98954	2.97490	1.53367	0.28927	0.22453	0.38274	1.38148	1.95463	0.85962
30	0.43255	0.38878	0.61520	2.95679	2.93478	1.47348	0.28467	0.22453	0.37562	1.37978	1.93270	0.81394

*Numerical results are obtained by considering uniform temperature and moisture rise.
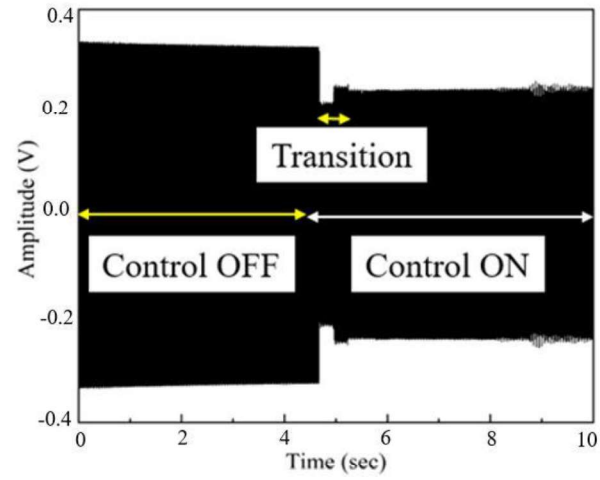
(a)
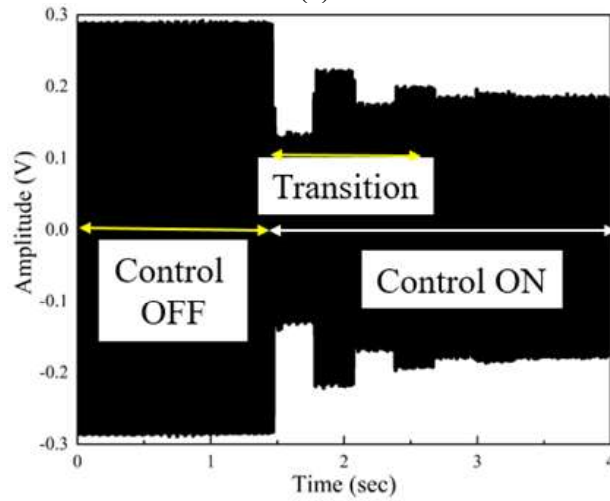
(b)
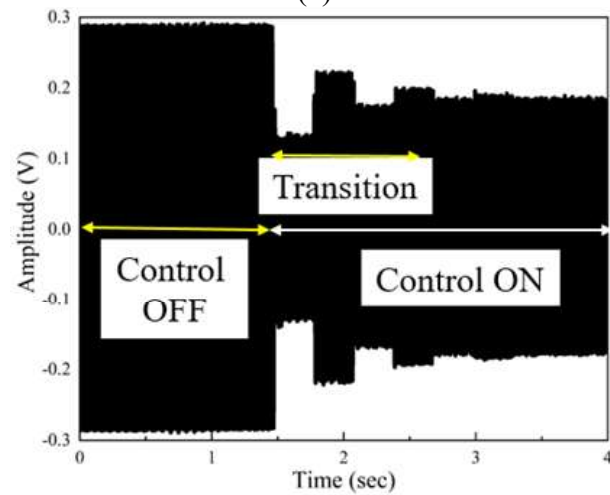
(c)

Figure 7.9: Vibration control of LCS plate at (a) 10 ⁰C (b) 20 ⁰C and (c) 30 ⁰C.

The sensor voltages (Vpp) measured during control off and on positions are tabulated in Table 7.6. The results show that the sensor voltage measured at the control-off condition considerably reduces with an increase in temperature. The fall in voltage is mainly due to the reduction in stiffness of the structure on exposure to the thermal environment.

Table 7.6: Measure of performance of the proportional controller

Temperature (°C)	Voltage at control OFF (Vpp)	Voltage at control ON (Vpp)	Percentage Reduction (%)
10	0.32	0.24	25.61
20	0.28	0.19	32.14
30	0.22	0.14	36.36

The sensor voltages (Vpp) measured during the control on position and percentage reduction in sensor voltage also reduces considerably with an increase in temperature. This phenomenon may be due to two reasons. Firstly, as the temperature increases, the stiffness of the structure reduces. In turn, the voltage required for the control action is considerably smaller. In this study, as the control voltages and gains are kept constant hence, the vibration attenuation characteristics of the controller improve with an increase in temperature. Secondly, the performance of PZT-5H patches enhances with an increase in temperature and thus the improvement in percentage reduction in vibrations.

7.5 CONCLUSION

In this chapter, the influence of temperature on the natural frequency of the laminated composite and sandwich plate is experimentally investigated. Series of tensile tests are performed to obtain the temperature-dependent material properties of the glass-epoxy and 3D printed PLA core materials at elevated thermal environments. The obtained modulus values are fed to the in-house developed mathematical model to predict the natural frequency of the sandwich structures operating in elevated thermal environments. The natural frequency values obtained from both the experimental and numerical methods are compared to validate the obtained outcomes. It was observed that the natural frequency of the LCS plate reduces considerably with an increase in temperature. The reduction in natural frequency is more significant for the higher

mode of vibrations. The influence of boundary conditions and length to width ratio on the natural frequency of the LCS plate was also investigated for various thermal profiles. Additionally, it was observed that the developed proportional controller algorithm efficiently controls the vibrating cantilever LCS plate operating in sub-ambient thermal environments. Most importantly, the vibration attenuation characteristics improved with an increase in temperature.

Chapter 8

CONCLUSIONS AND FUTURE SCOPE

This chapter summarizes the major findings of the present research work and the possible future works on the analysis of laminated composite sandwich (LCS) panels operating in elevated thermal and moisture environments.

8.1 MAJOR FINDINGS

This dissertation encompasses the investigation of the influence of temperature and moisture on the free vibration characteristics of skew laminated composite sandwich (SLCS) plates and shells. A layer-wise first-order shear deformation theory has been used to develop a finite element model to evaluate the vibration response of the skew sandwich panels. Uniform temperature and moisture concentration rise are considered to develop the coupled thermo-elastic and hygro-elastic relations. The numerical investigation suggests that the thermal and moisture fields considerably affect the natural frequency of SLCS plates. Special emphasis is devoted to evaluate the influence of process parameters on the vibration characteristics of the sandwich panels.

The temperature-dependent and moisture-dependent material properties of the constituent materials are considered for the accurate evaluation of the natural frequency of composite, hybrid composite, and sandwich panels. For the analysis of the sandwich panels, the glass-epoxy and graphite-epoxy composite materials are considered as face sheets, and the DYAD 606, EC 2216 viscoelastic materials, CNTRC materials, 3D printed PLA are considered as the core materials. The results suggest that the natural frequency of the composite and sandwich structures reduces with an increase in temperature and moisture values. Additionally, the results obtained from the ANN-based predictive model developed to predict the free vibration characteristics of SLCS plates are found to be efficient and reliable.

Further analysis revealed that the thermal environment considerably affects the vibration attenuation characteristics of the ACLD treated sandwich structures. The

results indicate that the newly proposed control strategy is more effective and efficient in controlling the vibrating sandwich plates in elevated thermal environments.

Furthermore, a series of experiments are conducted to understand the influence of temperature on the free vibration characteristics of LCS plates. The temperature-dependent material properties of glass-epoxy and 3D printed PLA material are obtained by conducting the tensile test for the specimens. Then the temperature-dependent modulus values are fed into the developed mathematical model to evaluate the natural frequency of the system. Later the experimental and numerical results are compared with each other.

The major outcomes drawn from the present research work are outlined as follows:

1. The fundamental frequency of the laminated composite plate, hybrid composite plate, and sandwich plate reduces with an increase in temperature and moisture values. The variation is more significant for the thicker plates.

2. The non-dimensional frequency of the laminated composite plate, hybrid composite plate, and sandwich plate increases with an increase in skew angle and aspect (a/b and a/H) ratios.

3. The reduction in natural frequency in the presence of temperature and moisture is significant for the smaller values of skew angles. Hence, the plates with higher skew angles are more resistant to temperature and moisture environments.

4. The ratio of core thickness to the thickness of the face sheet significantly dictates the vibrational behavior of the system in sandwich plates. The fundamental frequencies considerably reduce with an increase in t_c/t_f ratio.

5. The results predicted by the ANN model trained through the Levenberg–Marquardt algorithm are reliable and of good accuracy. The effective utilization of the developed model may significantly improve SHM techniques for engineering structures.

6. From the analysis of sandwich shells and plates, it is observed that the thermal and moisture environment predominantly influences the natural frequency of flat sandwich plate structure. In contrast, the spherical sandwich

shell emerges as the highly resistant structure for the changing environmental conditions.

7. The sandwich plates with FG-X gradation were observed to be more vulnerable to thermal and moisture changes. For all the thermal and moisture conditions considered, the magnitude of natural frequency increases with an increase in a V^*_{CNT} value.

8. The natural frequency of the doubly-curved SLCS panels reduces with an increase in R/a and t_c/t_f ratio.

9. The modulus of the 3D printed PLA reduces considerably with an increase in temperature, which in turn reduces the stiffness and natural frequency of the system.

10. The natural frequency of the LCS panel considerably reduces with increasing porosity value.

11. A unique methodology is proposed (robust control strategy) for the accurate prediction of vibration attenuation characteristics of ACLD of sandwich plates operating in the thermal environment.

12. The investigation reveals that the non-robust control strategy under-predicts the damping characteristics of the system.

13. The natural frequencies obtained from experimental techniques were in good agreement with the numerical results.

8.2. SCOPE FOR THE FUTURE RESEARCH

The fundamental purpose of this Thesis has been fulfilled by the contributions presented in the prior chapters of this dissertation. However, there is scope for further improvement in the research, which enables the improvement in the performance of LCS structures. Among them, a few possible future research themes have been charted as follows:

1. Experimental investigation to understand the vibration behavior of the LCS panels in elevated thermal and moisture environments can be explored.

2. Effective and reliable predictive models can be developed using state-of-the-art computational tools in ANN and machine learning modules.

3. Experimental and numerical investigation of free and forced vibration analysis of the bio-degradable composite sandwich structures operating in elevated thermal and moisture setup may be carried out.

4. Mathematical models can be developed using modern computational techniques such as iso-geometric analysis, higher-order zig-zag theories, continuum-based theories, mesh-less techniques, etc.

REFERENCE

Abdelmalek, A., Bouazza, M., Zidour, M., and Benseddiq, N. (2019). "Hygrothermal Effects on the Free Vibration Behavior of Composite Plate Using nth-Order Shear Deformation Theory: a Micromechanical Approach." *Iran. J. Sci. Technol. - Trans. Mech. Eng.*, 43, 61–73.

Alibeigloo, A., and Emtehani, A. (2015). "Static and free vibration analyses of carbon nanotube-reinforced composite plate using differential quadrature method." *Meccanica*, 50(1), 61–76.

Altenbach, H., Johannes Altenbach, and Kissing, W. (2018). *Mechanics of Composite Structural Elements*. Springer Nature Singapore Pte Ltd.

Amoushahi, H., and Goodarzian, F. (2018). "Dynamic and buckling analysis of composite laminated plates with and without strip delamination under hygrothermal effects using finite strip method." *Thin-Walled Struct.*, 131, 88–101.

Arafa, M., and Baz, A. (2000). "Dynamics of active piezoelectric damping composites." *Compos. Part B Eng.*, 31, 255–264.

Atilla, D., Sencan, C., Goren Kiral, B., and Kiral, Z. (2020). "Free vibration and buckling analyses of laminated composite plates with cutout." *Arch. Appl. Mech.*, 90(11), 2433–2448.

Badia, J. D., Santonja-Blasco, L., Martínez-Felipe, A., and Ribes-Greus, A. (2012). "Hygrothermal ageing of reprocessed polylactide." *Polym. Degrad. Stab.*, 97, 1881–1890.

Bailey, T., and Ubbard, J. E. (1985). "Distributed piezoelectric-polymer active vibration control of a cantilever beam." *J. Guid. Control. Dyn.*, 8(5), 605–611.

Baz, A., and Ro, J. (1996). "Vibration control of plates with active constrained layer damping." *Smart Mater. Struct.*, 5, 272–280.

Becker, H., and Locascio, L. E. (2002). "Polymer microfluidic devices." *Talanta*, 56, 267–287.

Behera, R. R., Ghadai, R. K., Kalita, K., and Banerjee, S. (2016). "Simultaneous prediction of delamination and surface roughness in drilling GFRP composite using ANN." *Int. J. Plast. Technol.*, 20(2), 424–450.

Belarbi, M.-O., Tati, A., Ounis, H., and Khechai, A. (2017). "On the Free Vibration Analysis of Laminated Composite and Sandwich Plates : A Layerwise Finite Element Formulation." *Lat. Am. J. Solids Struct.*, 14, 2265–2290.

Bendine, K., Boukhoulda, F. B., Haddag, B., and Nouari, M. (2019). "Active

vibration control of composite plate with optimal placement of piezoelectric patches." *Mech. Adv. Mater. Struct.*, 26(4), 341–349.

Biswal, M., Sahu, S. K., and Asha, A. V. (2015). "Experimental and numerical studies on free vibration of laminated composite shallow shells in hygrothermal environment." *Compos. Struct.*, 127, 165–174.

Biswal, M., Sahu, S. K., and Asha, A. V. (2016a). "Vibration of composite cylindrical shallow shells subjected to hygrothermal loading-experimental and numerical results." *Compos. Part B Eng.*, 98, 108–119.

Biswal, M., Sahu, S. K., and Asha, A. V. (2017). "Dynamic Stability of Woven Fiber Laminated Composite Shallow Shells in Hygrothermal Environment." *Int. J. Struct. Stab. Dyn.*, 17(8), 1–26.

Biswal, M., Sahu, S. K., Asha, A. V., and Nanda, N. (2016b). "Hygrothermal effects on buckling of composite shell-experimental and FEM results." *Steel Compos. Struct.*, 22(6), 1445–1463.

Biswas, D., and Ray, C. (2017). "Comparative perspective of various shear deformation theories with experimental verification for modal analysis of hybrid laminates." *J. Vib. Control*, 23(8), 1321–1333.

Bouazza, M., and Zenkour, A. M. (2020). "Hygro-thermo-mechanical buckling of laminated beam using hyperbolic refined shear deformation theory." *Compos. Struct.*, 252(June), 112689.

Burlayenko, V. N., and Sadowski, T. (2009). "Analysis of structural performance of sandwich plates with foam-filled aluminum hexagonal honeycomb core." *Comput. Mater. Sci.*, 45(3), 658–662.

Cascardi, A., Micelli, F., and Aiello, M. A. (2017). "An Artificial Neural Networks model for the prediction of the compressive strength of FRP-confined concrete circular columns." *Eng. Struct.*, 140, 199–208.

Castanie, B., Bouvet, C., and Ginot, M. (2020). "Review of composite sandwich structure in aeronautic applications." *Compos. Part C Open Access*, 1(July).

Chakrabarti, A., and Sheikh, A. H. (2004). "Vibration of Laminate-Faced Sandwich Plate by a New Refined Element." *J. Aerosp. Eng.*, 17(3), 123–134.

Chalak, H. D., Chakrabarti, A., Hamid, A., and Ashraf, M. (2014). "C0 FE model based on HOZT for the analysis of laminated soft core skew sandwich plates : Bending and vibration." *Appl. Math. Model.*, 38(4), 1211–1223.

Chandra, S., Sepahvand, K., Matsagar, V. A., and Marburg, S. (2019). "Stochastic

dynamic analysis of composite plate with random temperature increment." *Compos. Struct.*, 226(June).

Chantalakhana, C., and Stanway, R. (2001). "Active constrained layer damping of clamped-clamped plate vibrations." *J. Sound Vib.*, 241(5), 755–777.

Crawley, E. F., and Luis, J. De. (1987). "Use of piezoelectric actuators as elements of intelligent structures." *AIAA J.*, 25(10), 1373–1385.

Daikh, A. A. (2020). "Temperature dependent thermomechanical bending response of functionally graded sandwich plates Temperature dependent thermomechanical bending response of functionally graded sandwich plates." *Eng. Res. Express*, 2(1).

Dat, N. D., Quan, T. Q., Mahesh, V., and Duc, N. D. (2020). "Analytical solutions for nonlinear magneto-electro-elastic vibration of smart sandwich plate with carbon nanotube reinforced nanocomposite core in hygrothermal environment." *Int. J. Mech. Sci.*, 186(June), 105906.

Datta, P., and Ray, M. C. (2016). "Three-dimensional fractional derivative model of smart constrained layer damping treatment for composite plates." *Compos. Struct.*, 156, 291–306.

Dewangan, H. C., Panda, S. K., and Sharma, N. (2020). "Experimental Validation of Role of Cut-Out Parameters on Modal Responses of Laminated Composite - A Coupled FE Approach." *Int. J. Appl. Mech.*, 12(6).

Ding, A., Wang, J., Ni, A., and Li, S. (2018). "Hygroscopic ageing of nonstandard size sandwich composites with vinylester-based composite faces and PVC foam core." *Compos. Struct.*, 206(August), 194–201.

Ding, A., Wang, J., Ni, A., and Li, S. (2019). "Assessment on the ageing of sandwich composites with vinylester-based composite faces and PVC foam core in various harsh environments." *Compos. Struct.*, 213(January), 71–81.

Ebrahimi, F., and Dabbagh, A. (2019). "Vibration analysis of multi-scale hybrid nanocomposite plates based on a Halpin-Tsai homogenization model." *Compos. Part B*, 173(May), 106955.

Elshafey, A. A., Dawood, N., Marzouk, H., and Haddara, M. (2013). "Crack width in concrete using artificial neural networks." *Eng. Struct.*, 52, 676–686.

Erik, T., Zhipheng, R., Chou, T., "Advances in the science and technology of carbon nanotubes and their composites: a review." *Composite Sciences and Technology*, 61(2001), 1899-1912.

Farrar, C. R., and Worden, K. (2007). "An introduction to structural health

monitoring." *Philos. Trans. R. Soc. A Math. Phys. Eng. Sci.*, 365(1851), 303–315.

Gagani, A. I., Monsås, A. B., Krauklis, A. E., and Echtermeyer, A. T. (2019). "The effect of temperature and water immersion on the interlaminar shear fatigue of glass fiber epoxy composites using the I-beam method." *Compos. Sci. Technol.*, 181(June), 107703.

Galatas, A., Hassanin, H., Zweiri, Y., and Seneviratne, L. (2018). "Additive Manufactured Sandwich Composite / ABS Parts for Unmanned Aerial Vehicle Applications." *Polymers (Basel).*, 10.

Garg, A., and Chalak, H. D. (2019). "A review on analysis of laminated composite and sandwich structures under hygrothermal conditions." *Thin-Walled Struct.*, 142(March), 205–226.

Garg, A. K., Khare, R. K., and Kant, T. (2006). "Free vibration of skew fiber-reinforced composite and sandwich laminates using a shear deformable finite element model." *J. Sandw. Struct. Mater.*, 8(1), 33–53.

Garg, N., Karkhanis, R. S., Sahoo, R., Maiti, P. R., and Singh, B. N. (2019). "Trigonometric zigzag theory for static analysis of laminated composite and sandwich plates under hygro-thermo-mechanical loading." *Compos. Struct.*, 209(May 2018), 460–471.

Gomes, G. F., Almeida, F. A. de, Junqueira, D. M., Cunha, S. S. da, and Ancelotti, A. C. (2019). "Optimized damage identification in CFRP plates by reduced mode shapes and GA-ANN methods." *Eng. Struct.*, 181(November 2018), 111–123.

Guermazi, N., Tarjem, A. Ben, Ksouri, I., and Ayedi, H. F. (2016). "On the durability of FRP composites for aircraft structures in hygrothermal conditioning." *Compos. Part B*, 85, 294–304.

Gupta, A., and Ghosh, A. (2019). "NURBS-based thermo-elastic analyses of laminated and sandwich composite plates." *Sadhana*, 44(84), 1–19.

Gupta, V., Sharma, M., Thakur, N., and Singh, S. P. (2011). "Active vibration control of a smart plate using a piezoelectric sensor-actuator pair at elevated temperatures." *Smart Mater. Struct.*, 20(10).

Haji Agha Mohammad Zarbaf, S. E., Norouzi, M., Allemang, R., Hunt, V., Helmicki, A., and Venkatesh, C. (2018). "Vibration-based cable condition assessment: A novel application of neural networks." *Eng. Struct.*, 177(December 2017), 291–305.

Heshmati, M., and Daneshmand, F. (2018). "A study on the vibrational properties of weight-efficient plates made of material with functionally graded porosity." *Compos. Struct.*

Islam, M. S., Pickering, K. L., and Foreman, N. J. (2010). "Influence of Hygrothermal Ageing on the Physico-Mechanical Properties of Alkali Treated Industrial Hemp Fibre Reinforced Polylactic Acid Composites." *J. Polym. Environ.*, 18, 696–704.

Jalal, M., Grasley, Z., Gurganus, C., and Bullard, J. W. (2020). "A new nonlinear formulation-based prediction approach using artificial neural network (ANN) model for rubberized cement composite." *Eng. Comput.*, (0123456789).

Jodaei, A., Jalal, M., and Yas, M. H. (2012). "Free vibration analysis of functionally graded annular plates by state-space based differential quadrature method and comparative modeling by ANN." *Compos. Part B Eng.*, 43(2), 340–353.

Joseph, S. V., and Mohanty, S. C. (2017). "Temperature effects on buckling and vibration characteristics of sandwich plate with viscoelastic core and functionally graded material constraining layer." *J. Sandw. Struct. Mater.*, 21(4), 1557–1577.

Kanasogi, R. M., and Ray, M. C. (2013). "Active Constrained Layer Damping of Smart Skew Laminated Composite Plates Using 1–3 Piezoelectric Composites." *J. Compos.*, 1–17.

Karimiasl, M., and Ebrahimi, F. (2019). "Large amplitude vibration of viscoelastically damped multiscale composite doubly curved sandwich shell with flexible core and MR layers." *Thin-Walled Struct.*, 144(April), 106128.

Karnik, S. R., Gaitonde, V. N., Rubio, J. C., Correia, A. E., Abrão, A. M., and Davim, J. P. (2008). "Delamination analysis in high speed drilling of carbon fiber reinforced plastics (CFRP) using artificial neural network model." *Mater. Des.*, 29(9), 1768–1776.

Katariya, P. V., Panda, S. K., and Mahapatra, T. R. (2018). "Bending and vibration analysis of skew sandwich plate." *Aircr. Eng. Aerosp. Technol.*, 90(6), 885–895.

Katariya, P. V., Panda, S. K., and Mehar, K. (2021). "Theoretical modelling and experimental verification of modal responses of skewed laminated sandwich structure with epoxy-filled softcore." *Eng. Struct.*, 228(September 2020), 111509.

Katariya, P. V, Mehar, K., and Kumar, S. (2020). "Nonlinear dynamic responses of layered skew sandwich composite structure and experimental validation." *Int. J. Non. Linear. Mech.*, 125(December 2019), 103527.

Kattimani, S. C. (2017a). "Geometrically nonlinear vibration analysis of multiferroic composite plates and shells." *Compos. Struct.*, 163(December), 185–194.

Kattimani, S. C. (2017b). "Active damping of multiferroic composite plates using 1-3

piezoelectric composites." *Smart Mater. Struct.*, 26(12), 0–36.

Kattimani, S. C., and Ray, M. C. (2014). "Active control of large amplitude vibrations of smart magneto–electro–elastic doubly curved shells." *Int. J. Mech. Mater. Des.*, 10(4), 351–378.

Kattimani, S. C., and Ray, M. C. (2015). "Control of geometrically nonlinear vibrations of functionally graded magneto-electro-elastic plates." *Int. J. Mech. Sci.*, 99, 154–167.

Kattimani, S. C., and Ray, M. C. (2018). "Vibration control of multiferroic fibrous composite plates using active constrained layer damping." *Mech. Syst. Signal Process.*, 106, 334–354.

Kaya, Z., Balcıoglu, H. E., and Gün, H. (2020). "The effects of temperature and deformation rate on fracture behavior of S-2 glass / epoxy laminated composites." *Polym. Compos.*, (July), 1–12.

Khare, R. K., Garg, A. K., and Kant, T. (2005). "Free vibration of sandwich laminates with two higher-order shear deformable facet shell element models." *J. Sandw. Struct. Mater.*, 7(3), 221–244.

Khatir, S., Boutchicha, D., Thanh, C. Le, Tran-Ngoc, H., Nguyen, T. N., and Abdel-Wahab, M. (2020). "Improved ANN technique combined with Jaya algorithm for crack identification in plates using XIGA and experimental analysis." *Theor. Appl. Fract. Mech.*, 107(January), 102554.

Kheirikhah, M. M., and Khosravi, P. (2018). "Buckling and free vibration analyses of composite sandwich plates reinforced by shape - memory alloy wires." *J. Brazilian Soc. Mech. Sci. Eng.*, 40(11), 1–12.

Kiran, M. C., and Kattimani, S. C. (2018). "Assessment of porosity infl uence on vibration and static behaviour of functionally graded magneto-electro-elastic plate : A finite element study." *Eur. J. Mech. / A Solids*, 71(January), 258–277.

Kiran, M. C., Kattimani, S. C., and Vinyas, M. (2018). "Porosity influence on structural behaviour of skew functionally graded magneto-electro-elastic plate." *Compos. Struct.*

Kulkarni, S. D., and Kapuria, S. (2008). "Free vibration analysis of composite and sandwich plates using an improved discrete Kirchhoff quadrilateral element based on third-order zigzag theory." *Comput. Mech.*, 42, 803–824.

Kumar, R. S., Kundalwal, S. I., and Ray, M. C. (2013). "Active damping of smart functionally graded sandwich plates under thermal environment using 1-3 piezoelectric composites." *ISHMT-ASME Heat Mass Transf. Conf.*, (December 2013).

Kumar, R. S., and Ray, M. C. (2012). "Active constrained layer damping of smart laminated composite sandwich plates using 1-3 piezoelectric composites." *Int. J. Mech. Mater. Des.*, 8(3), 197–218.

Kumar, R. S., and Ray, M. C. (2013). "Active constrained layer damping of geometrically nonlinear vibrations of smart laminated composite sandwich plates using 1-3 piezoelectric composites." *J. Compos.*

Kumar, R. S., and Ray, M. C. (2016). "Smart damping of geometrically nonlinear vibrations of functionally graded sandwich plates using 1-3 piezoelectric composites." *Mech. Adv. Mater. Struct.*, 23(6), 652–669.

Kundalwal, S. I. (2013). "Active damping of smart functionally graded sandwich plates under thermal environment using 1-3 piezoelectric composites." *Proc. 22th Natl. 11th Int. ISHMT-ASME Heat Mass Transf. Conf.*

Kundalwal, S. I., and Meguid, S. A. (2015). "Effect of carbon nanotube waviness on active damping of laminated hybrid composite shells." *Acta Mech.*, 226(6), 2035–2052.

Kundu, C. K., and Han, J. H. (2009). "Vibration characteristics and snapping behavior of hygro-thermo-elastic composite doubly curved shells." *Compos. Struct.*, 91(3), 306–317.

Lai, D., Zhuang, K., Wu, Q., and Dindarloo, M. H. (2021). "A novel nonlocal higher-order strain gradient shell theory for static analysis of CNTRC doubly-curved nanoshells subjected to thermo-mechanical loading." *Mech. Based Des. Struct. Mach.*, 1–17.

Li, J., Li, F., and Narita, Y. (2019). "Active control of thermal buckling and vibration for a sandwich composite laminated plate with piezoelectric fiber-reinforced composite actuator facesheets." *J. Sandw. Struct. Mater.*, 21(7), 2563–2581.

Lim, Y.-H., Varadan, V. V, and Varadan, V. K. (2002). "Closed loop finite-element modeling of active constrained layer damping in the time domain analysis." *Smart Mater. Struct.*, 11, 89–97.

Liu, Z., Lei, Q., and Xing, S. (2019). "Mechanical characteristics of wood , ceramic , metal and carbon fiber-based PLA composites fabricated by FDM." *J. Mater. Reseach Technol.*, 8(5), 3741–3751.

Luo, L., Zhang, B., Zhang, G., and Xu, Y. (2020). "Rapid prediction of cured shape types of composite laminates using a FEM-ANN method." *Compos. Struct.*, 238(37), 111980.

Ma, X., Tian, K., Li, H., Zhou, Y., Hao, P., and Wang, B. (2019). "Concurrent Multi-

Scale Optimization of Hybrid Composite." *Compos. Struct.*, 111635.

Mahapatra, T. R., Panda, S. K., and Kar, V. R. (2016). "Nonlinear hygro-thermo-elastic vibration analysis of doubly curved composite shell panel using finite element micromechanical model." *Mech. Adv. Mater. Struct.*, 23(11), 1343–1359.

Mahi, A., Abbas, El Bedia, A., and Tounsi, A. (2015). "A new hyperbolic shear deformation theory for bending and free vibration analysis of isotropic , functionally graded , sandwich and laminated composite plates." *Appl. Math. Model.*, 39(9), 2489–2508.

Marques, F. D., and Anderson, J. (2001). "Identification and prediction of unsteady transonic aerodynamic loads by multi-layer functionals." *J. Fluids Struct.*, 15, 83–106.

Marques, F. D., Souza, L. D. F. R. De, Rebolho, D. C., Caporali, A. S., Belo, E. M., and Ortolan, R. L. (2005). "Application of time-delay neural and recurrent neural networks for the identification of a hingeless helicopter blade flapping and torsion motions." *J. Brazilian Soc. Mech. Sci. Eng.*, 27(2), 97–103.

Marques, F. D., Natarajan, S., and Ferreira, A. J. M. (2017). "Evolutionary-based aeroelastic tailoring of stiffened laminate composite panels in supersonic flow regime." *Compos. Struct.*, 167, 30–37.

Mehar, K., and Kumar Panda, S. (2018). "Thermoelastic flexural analysis of FG-CNT doubly curved shell panel." *Aircr. Eng. Aerosp. Technol.*, 90(1), 11–23.

Mehar, K., and Panda, S. K. (2015). "Vibration analysis of functionally graded carbon nanotube reinforced composite plate in thermal environment." *J. Sandw. Struct. Mater.*, 1–23.

Mehar, K., and Panda, S. K. (2017). "Numerical investigation of nonlinear thermomechanical deflection of functionally graded CNT reinforced doubly curved composite shell panel under different mechanical loads." *Compos. Struct.*, 161, 287–298.

Mehar, K., Panda, S. K., and Sharma, N. (2020). "Numerical investigation and experimental verification of thermal frequency of carbon nanotube-reinforced sandwich structure." *Eng. Struct.*, 211(February), 110444.

Mishra, I., and Sahu, S. K. (2015). "Modal Analysis of Woven Fiber Composite Plates with Different Boundary Conditions." *Int. J. Struct. Stab. Dyn.*, 15(1).

Mouloodi, S., Rahmanpanah, H., Burvill, C., Gohari, S., and Davies, H. M. S. (2020). "Experimental, regression learner, numerical, and artificial neural network analyses on a complex composite structure subjected to compression loading." *Mech. Adv.*

Mater. Struct., 1–17.

Nashif, A., Jones, D. I. G., and Hildebrand, M. (1985). *Vibration damping*. John Wiley & Sons.

Nguyen, N. D., Nguyen, T. K., Nguyen, T. N., and Thai, H. T. (2018). "New Ritz-solution shape functions for analysis of thermo-mechanical buckling and vibration of laminated composite beams." *Compos. Struct.*, 184(October 2017), 452–460.

Nguyen, S. N., Lee, J., Han, J. W., and Cho, M. (2020). "A coupled hygrothermo-mechanical viscoelastic analysis of multilayered composite plates for long-term creep behaviors." *Compos. Struct.*, 242(August 2019), 112030.

Nguyen, S. N., Truong, T. T., Cho, M., and Trung, N. T. (2021). "A cell-based smoothed finite element formulation for viscoelastic laminated composite plates considering hygrothermal effects." *J. Compos. Mater.*, 55(14), 1967–1978.

Nguyen-Thoi, T., Liu, G. R., Vu-Do, H. C., and Nguyen-Xuan, H. (2009). "A face-based smoothed finite element method (FS-FEM) for visco-elastoplastic analyses of 3D solids using tetrahedral mesh." *Comput. Methods Appl. Mech. Eng.*, 198(41–44), 3479–3498.

Nguyen-Thoi, T., Vu-Do, H. C., Rabczuk, T., and Nguyen-Xuan, H. (2010). "A node-based smoothed finite element method (NS-FEM) for upper bound solution to visco-elastoplastic analyses of solids using triangular and tetrahedral meshes." *Comput. Methods Appl. Mech. Eng.*, 199(45–48), 3005–3027.

Nguyen, N. D., Nguyen, T. K., Nguyen, T. N., and Thai, H. T. (2018). "New Ritz-solution shape functions for analysis of thermo-mechanical buckling and vibration of laminated composite beams." *Compos. Struct.*, 184(October 2017), 452–460.

Oliver, G. A., Ancelotti, A. C., and Gomes, G. F. (2020). "Neural network-based damage identification in composite laminated plates using frequency shifts." *Neural Comput. Appl.*, 3, 1–12.

Padhi, A., and Pandit, M. K. (2017). "Bending and free vibration response of sandwich laminate under hygrothermal load using improved zigzag theory." *J. Strain Anal. Eng. Des.*, 52(5), 288–297.

Palomba, G., Epasto, G., and Crupi, V. (2021). "Lightweight sandwich structures for marine applications: a review." *Mech. Adv. Mater. Struct.*, 0(0), 1–26.

Pan, E., and P. R. Heyliger. (2002). "Free vibrations of simply supported and multilayered magneto-electro-elastic plates." *J. Sound Vib.*, 252.

Pan, E., and Han, F. (2005). "Exact solution for functionally graded and layered

magneto-electro-elastic plates." *Int. J. Eng. Sci.*, 43, 321–339.

Pan, E. (2013). "Exact Solution for Simply Supported and Multilayered Magneto-Electro-Elastic Plates." *Trans. ASME*, 68(July 2001), 608–618.

Panda, H. S., Sahu, S. K., and Parhi, P. K. (2013). "Hygrothermal effects on free vibration of delaminated woven fiber composite plates - Numerical and experimental results." *Compos. Struct.*, 96, 502–513.

Panda, H. S., Sahu, S. K., Parhi, P. K., and Asha, A. V. (2015). "Vibration of woven fiber composite doubly curved panels with strip delamination in thermal field." *J. Vib. Control*, 21(November 2013), 3072–3089.

Parhi, P. K., Bhattacharyya, S. K., and Sinha, P. K. (2001). "Hygrothermal effects on the dynamic behavior of multiple delaminated composite plates and shells." *J. Sound Vib.*, 248(2), 195–214.

Park, T., Lee, S., Seo, J. W., and Voyiadjis, G. Z. (2008). "Structural dynamic behavior of skew sandwich plates with laminated composite faces." *Compos. Part B Eng.*, 39, 316–326.

Paula, N. C. G. de, and Marques, F. D. (2019). "Multi-variable Volterra kernels identification using time-delay neural networks: application to unsteady aerodynamic loading." *Nonlinear Dyn.*, 97(1), 767–780.

Paula, N. C. G. De, Marques, F. D., and Silva, W. A. (2019). "Volterra kernels assessment via time-delay neural networks for nonlinear unsteady aerodynamic loading identification." *AIAA J.*, 57(4), 1725–1735.

Pouresmaeeli, S., and Fazelzadeh, S. A. (2016). "Frequency analysis of doubly curved functionally graded carbon nanotube-reinforced composite panels." *Acta Mech.*, 227(10), 2765–2794.

Pradeep, V., and Ganesan, N. (2006). "Vibration behavior of ACLD treated beams under thermal environment." *J. Sound Vib.*, 292(3–5), 1036–1045.

Prasad, E. V., and Sahu, S. K. (2018). "Vibration Analysis of Woven Fiber Metal Laminated Plates — Experimental and Numerical Studies." *Int. J. Struct. Stab. Dyn.*, 18(11), 1–23.

Putic, S., Stamenovic, M., BRANISLAV BAJČETA, STAJČIĆ, P., and BOŠNJAK, S. (2007). "The influence of high and low temperatures on the impact properties of glass – epoxy composites." *J. Serbian Chem. Soc.*, 72(7), 713–722.

Qian, C., Ran, Y., He, J., Ren, Y., Sun, B., Zhang, W., and Wang, R. (2020). "Application of artificial neural networks for quantitative damage detection in

unidirectional composite structures based on Lamb waves." *Adv. Mech. Eng.*, 12(3), 1–9.

Qin, B., Zhong, R., Wang, T., Wang, Q., Xu, Y., and Hu, Z. (2020a). "A unified Fourier series solution for vibration analysis of FG-CNTRC cylindrical, conical shells and annular plates with arbitrary boundary conditions." *Compos. Struct.*, 232, 111549.

Qin, B., Zhong, R., Wang, T., Wang, Q., Xu, Y., and Hu, Z. (2020b). "A unified Fourier series solution for vibration analysis of FG-CNTRC cylindrical, conical shells and annular plates with arbitrary boundary conditions." *Compos. Struct.*, 232.

Ram, K. S. S., and Sinha, P. K. (1991). "Hygrothermal effects on the bending characteristics of laminated composite plates." *Comput. Struct.*, 40(4), 1009–1015.

Ram, K. S. S., and Sinha, P. K. (1992). "Hygrothermal effects on the free vibration of laminated composite plates." *J. Sound Vib.*, 158(1), 133–148.

Rath, M. K., and Sahu, S. K. (2012). "Vibration of woven fiber laminated composite plates in hygrothermal environment." *J. Vib. Control*, 18(13), 1957–1970.

Raville, M. E., and Ueng, C. E. S. (1967). "Determination of natural frequencies of vibration of a sandwich plate - Experimental procedures and results for the determination of natural frequencies of vibration of a rectangular sandwich plate, simply supported on all edges, are presented." *Exp. Mech.*, 7(11), 490–493.

Ray, B. C. (2006). "Temperature effect during humid ageing on interfaces of glass and carbon fibers reinforced epoxy composites." *J. Colloid Interface Sci.*, 298(1), 111–117.

Ray, M. C., and Pradhan, A. K. (2006). "The performance of vertically reinforced 1-3 piezoelectric composites in active damping of smart structures." *Smart Mater. Struct.*, 15(2), 631–641.

Ray, M. C., and Pradhan, A. K. (2007). "On the use of vertically reinforced 1-3 piezoelectric composites for hybrid damping of laminated composite plates." *Mech. Adv. Mater. Struct.*, 14(4), 245–261.

Ray, M. C., and Pradhan, A. K. (2008). "Performance of vertically and obliquely reinforced 1-3 piezoelectric composites for active damping of laminated composite shells." *J. Sound Vib.*, 315(4–5), 816–835.

Reddy, J. N. (2003). *Mechanics of Laminated Composite Plates and Shells Theory and Analysis*. CRC Press.

Rezaei, M., Karatzas, V., Berggreen, C., and Carlsson, L. A. (2018). "The effect of elevated temperature on the mechanical properties and failure modes of GFRP face

sheets and PET foam cored sandwich beams." *J. Sandw. Struct. Mater.*, 22(4), 1235–1255.

Rjou, Y. S. Al, and Alshatnawi, J. A. (2020). "Free vibration of functionally-graded porous cracked plates." *Structures*, 28(September), 2392–2403.

Rocha, I. B. C. M., Raijmaekers, S., Nijssen, R. P. L., Meer, F. P. Van Der, and Sluys, L. J. (2017). "Hygrothermal ageing behaviour of a glass / epoxy composite used in wind turbine blades." *Compos. Struct.*, 174, 110–122.

Sadowski, T., and Be, J. (2011). "Effective properties for sandwich plates with aluminium foil honeycomb core and polymer foam filling – Static and dynamic response." *Comput. Mater. Sci.*, 50, 1269–1275.

Sahoo, S. R., and Ray, M. C. (2019). "Active control of laminated composite plates using elliptical smart constrained layer damping treatment." *Compos. Struct.*, 211(November 2018), 376–389.

Salehi, H., and Burgueño, R. (2018). "Emerging artificial intelligence methods in structural engineering." *Eng. Struct.*, 171(November 2017), 170–189.

Schubert, M., and Dafnis, A. (2019). "Multifunctional load-bearing aerostructures with integrated space debris protection." *MATEC Web Conf.*, 1–8.

Senatov, F. S., Niaza, K. V, Stepashkin, A. A., and Kaloshkin, S. D. (2016a). "Low-cycle fatigue behavior of 3d-printed PLA-based porous scaffolds." *Compos. Part B*, 97, 193–200.

Senatov, F. S., Niaza, K. V, Zadorozhnyy, M. Y., Maksimkin, A. V, Kaloshkin, S. D., and Estrin, Y. Z. (2016b). "Mechanical properties and shape memory effect of 3D-printed PLA-based porous scaffolds." *J. Mech. Behav. Biomed. Mater.*, 57, 139–148.

Sfarra, S., Regi, M., Santulli, C., Sarasini, F., Tirillò, J., and Perilli, S. (2016). "An innovative nondestructive perspective for the prediction of the effect of environmental aging on impacted composite materials." *Int. J. Eng. Sci.*, 102, 55–76.

Shah, A. U., Sultan, M. T., and Jawaid, M. (2019). "Sandwich-structured bamboo powder / glass fibre-reinforced epoxy hybrid composites – Mechanical performance in static and dynamic evaluations." *Sandw. Struct. Mater.*, 23(1), 47–64.

Shankar, G., Keshava Kumar, S., and Mahato, P. K. (2017). "Vibration analysis and control of smart composite plates with delamination and under hygrothermal environment." *Thin-Walled Struct.*, 116(March), 53–68.

Sharma, A., Kumar, A., Susheel, C. K., and Kumar, R. (2016a). "Smart damping of functionally graded nanotube reinforced composite rectangular plates." *Compos.*

Struct., 155, 29–44.

Sharma, A., Kumar, R., Vaish, R., and Chauhan, V. S. (2015). "Active vibration control of space antenna reflector over wide temperature range." *Compos. Struct.*, 128, 291–304.

Sharma, A., Kumar, R., Vaish, R., and Chauhan, V. S. (2016b). "Experimental and numerical investigation of active vibration control over wide range of operating temperature." *J. Intell. Mater. Syst. Struct.*, 27(13), 1846–1860.

Sharma, N., Mahapatra, T. R., and Panda, S. K. (2019). "Hygrothermal effect on vibroacoustic behaviour of higher-order sandwich panel structure with laminated composite face sheets." *Eng. Struct.*, 197(May 2018), 109355.

Sharma, N., Swain, P. K., Maiti, D. K., and Singh, B. N. (2020). "Stochastic frequency analysis of laminated composite plate with curvilinear fiber." *Mech. Adv. Mater. Struct.*, 1–16.

Sharnappa, Ganesan, N., and Sethuraman, R. (2007). "Dynamic modeling of active constrained layer damping of composite beam under thermal environment." *J. Sound Vib.*, 305(4–5), 728–749.

Shokry, K. M. (2014). "Effect of Temperature on Mechanical Properties of Glass Reinforced Plastic GRP." *World Appl. Sci. J.*, 31(7), 1341–1344.

Singh, S. D., and Sahoo, R. (2020). "Static and free vibration analysis of functionally graded CNT reinforced composite plates using trigonometric shear deformation theory." *Structures*, 28, 685–696.

Sit, M., and Ray, C. (2019). "Free vibration characteristics of glass and bamboo epoxy laminates under hygrothermal effect: A comparative approach." *Compos. Part B Eng.*, 176(January), 107333.

Song, O., Kim, J.-B., and Librescu, L. (2001). "Synergistic implications of tailoring and adaptive materials technology on vibration control of anisotropic thin-walled beams." *Int. J. Eng. Sci.*, 39, 71–94.

Suresh Kumar, R., and Ray, M. C. (2012). "Active constrained layer damping of smart laminated composite sandwich plates using 1-3 piezoelectric composites." *Int. J. Mech. Mater. Des.*, 8(3), 197–218.

Swamy Naidu, N. V., and Sinha, P. K. (2006). "Nonlinear transient analysis of laminated composite shells in hygrothermal environments." *Compos. Struct.*, 72(3), 280–288.

Vinyas, M., Athul, S. J., Harursampath, D., and Thoi, T. N. (2019). "Experimental

evaluation of the mechanical and thermal properties of 3D printed PLA and its composites." *Mater. Res. Express*, 6(11).

Vinyas, M., and Kattimani, S. C. (2017). "Hygrothermal analysis of magneto-electro-elastic plate using 3D finite element analysis." *Compos. Struct.*, 180, 617–637.

Wang, D., Fotinich, Y., and Carman, G. P. (1998). "Influence of temperature on the electromechanical and fatigue behavior of piezoelectric ceramics." *J. Appl. Phys.*, 83(10), 5342–5350.

Wang, K, A. K., and Yang, L. (2000). "Free Vibration of Skew Sandwich Plates With Laminated Facings." *J. Sound Vib.*, 235, 317–340.

Wang, S. (1997). "Free vibration analysis of skew fibre-reinforced composite laminates based on first-order shear deformation plate theory." *Comput. Struct.*, 63(3), 525–538.

Whitney, J. M., and Ashton, J. E. (1971). "Effect of environment on the elastic response of layered composite plates." *AIAA J.*, 9(9), 1708–1713.

Xue, Y., Jin, G., Ma, X., Chen, H., Ye, T., and Chen, M. (2019). "Free vibration analysis of porous plates with porosity distributions in the thickness and in-plane directions using isogeometric approach." *Int. J. Mech. Sci.*, 152(October 2018), 346–362.

Yuan, W. X., and Dawe, D. J. (2002). "Free vibration of sandwich plates with laminated faces." *Int. J. Numer. Methods Eng.*, 54(2), 195–217.

Zenkour, A. M., and Alghanmi, R. A. (2019). "Hygro-thermo-electro-mechanical bending analysis of sandwich plates with FG core and piezoelectric faces." *Mech. Adv. Mater. Struct.*, 1–13.

Zenzen, R., Khatir, S., Belaidi, I., Thanh, C. Le, and Abdel Wahab, M. (2020). "A modified transmissibility indicator and Artificial Neural Network for damage identification and quantification in laminated composite structures." *Compos. Struct.*, 248(June).

Zhao, Y., Chen, Y., and Zhou, Y. (2019). "Novel mechanical models of tensile strength and elastic property of FDM AM PLA materials : Experimental and theoretical analyses." *Mater. Des.*, 181, 108089.

Zhao, Z., Wang, B., Qian, Z., and Yong, Y. K. (2020). "A novel approach to quantitative predictions of high-frequency coupled vibrations in layered piezoelectric plates." *Int. J. Eng. Sci.*, 157.

Zhu, P., Lei, Z. X., and Liew, K. M. (2012). "Static and free vibration analyses of

carbon nanotube-reinforced composite plates using finite element method with first order shear deformation plate theory." *Compos. Struct.*, 94(4), 1450–1460.

Zippo, A., Ferrari, G., Amabili, M., Barbieri, M., and Pellicano, F. (2015a). "Active vibration control of a composite sandwich plate." *Compos. Struct.*, 128, 100–114.

APPENDIX A:

$$\{\varepsilon_{bt}\} = \left[\begin{array}{ccc} \dfrac{\partial u_0}{\partial x} & \dfrac{\partial v_0}{\partial y} & \dfrac{\partial u_0}{\partial y} + \dfrac{\partial v_0}{\partial x} \end{array}\right]^T ; \{\varepsilon_{st}\} = \left[\begin{array}{cc} \dfrac{\partial w_0}{\partial x} & \dfrac{\partial w_0}{\partial y} \end{array}\right]^T$$

$$\{\varepsilon_{br}\} = \left[\begin{array}{ccccccccc} \dfrac{\partial \theta_x}{\partial x} & \dfrac{\partial \theta_y}{\partial y} & \dfrac{\partial \theta_y}{\partial x} + \dfrac{\partial \theta_x}{\partial y} & \dfrac{\partial \phi_x}{\partial x} & \dfrac{\partial \phi_y}{\partial y} & \dfrac{\partial \phi_y}{\partial x} + \dfrac{\partial \phi_x}{\partial y} & \dfrac{\partial \alpha_x}{\partial x} & \dfrac{\partial \alpha_y}{\partial y} & \dfrac{\partial \alpha_y}{\partial x} + \dfrac{\partial \alpha_x}{\partial y} \end{array}\right]^T$$

$$\{\varepsilon_{sr}\} = \left[\begin{array}{cccccc} \theta_x & \theta_y & \phi_x & \phi_y & \alpha_x & \alpha_y \end{array}\right]^T$$

$$[z_1] = \begin{bmatrix} -h_c & 0 & 0 & z+h_c & 0 & 0 & 0 & 0 & 0 \\ 0 & -h_c & 0 & 0 & z+h_c & 0 & 0 & 0 & 0 \\ 0 & 0 & -h_c & 0 & 0 & z+h_c & 0 & 0 & 0 \end{bmatrix}$$

$$[z_2] = \begin{bmatrix} z & 0 & 0 & 0 & 0 & 0 & 0 & 0 & 0 \\ 0 & z & 0 & 0 & 0 & 0 & 0 & 0 & 0 \\ 0 & 0 & z & 0 & 0 & 0 & 0 & 0 & 0 \end{bmatrix}$$

$$[z_3] = \begin{bmatrix} h_c & 0 & 0 & 0 & 0 & 0 & z-h_c & 0 & 0 \\ 0 & h_c & 0 & 0 & 0 & 0 & 0 & z-h_c & 0 \\ 0 & 0 & h_c & 0 & 0 & 0 & 0 & 0 & z-h_c \end{bmatrix}$$

$$[z_4] = \begin{bmatrix} 0 & 0 & 1 & 0 & 0 & 0 \\ 0 & 0 & 0 & 1 & 0 & 0 \end{bmatrix}; [z_5] = \begin{bmatrix} 1 & 0 & 0 & 0 & 0 & 0 \\ 0 & 1 & 0 & 0 & 0 & 0 \end{bmatrix};$$

$$[z_6] = \begin{bmatrix} 0 & 0 & 0 & 0 & 1 & 0 \\ 0 & 0 & 0 & 0 & 0 & 1 \end{bmatrix}$$

APPENDIX B:

$$[B_{tbi}] = \begin{bmatrix} \dfrac{\partial n_i}{\partial x} & 0 & 0 \\ 0 & \dfrac{\partial n_i}{\partial y} & 0 \\ \dfrac{\partial n_i}{\partial y} & \dfrac{\partial n_i}{\partial x} & 0 \end{bmatrix}; [B_{tsi}] = \begin{bmatrix} 0 & 0 & \dfrac{\partial n_i}{\partial x} \\ 0 & 0 & \dfrac{\partial n_i}{\partial y} \end{bmatrix}; [B_{rsi}] = \begin{bmatrix} 1 & 0 & 0 & 0 & 0 & 0 \\ 0 & 1 & 0 & 0 & 0 & 0 \\ 0 & 0 & 1 & 0 & 0 & 0 \\ 0 & 0 & 0 & 1 & 0 & 0 \\ 0 & 0 & 0 & 0 & 1 & 0 \\ 0 & 0 & 0 & 0 & 0 & 1 \end{bmatrix}$$

$$[B_{rbi}] = \begin{bmatrix} \dfrac{\partial n_i}{\partial x} & 0 & \dfrac{\partial n_i}{\partial y} & 0 & 0 & 0 & 0 & 0 & 0 \\ 0 & \dfrac{\partial n_i}{\partial y} & \dfrac{\partial n_i}{\partial x} & 0 & 0 & 0 & 0 & 0 & 0 \\ 0 & 0 & 0 & \dfrac{\partial n_i}{\partial x} & 0 & \dfrac{\partial n_i}{\partial y} & 0 & 0 & 0 \\ 0 & 0 & 0 & 0 & \dfrac{\partial n_i}{\partial y} & \dfrac{\partial n_i}{\partial x} & 0 & 0 & 0 \\ 0 & 0 & 0 & 0 & 0 & 0 & \dfrac{\partial n_i}{\partial x} & 0 & \dfrac{\partial n_i}{\partial y} \\ 0 & 0 & 0 & 0 & 0 & 0 & 0 & \dfrac{\partial n_i}{\partial y} & \dfrac{\partial n_i}{\partial x} \end{bmatrix}^T$$

APPENDIX C:

$$[S] = \sum_{i=1}^{8} \begin{bmatrix} S_{11} \\ S_{21} & S_{22} \\ 0 & 0 & S_{33} \\ 0 & 0 & S_{43} & S_{44} \\ 0 & 0 & 0 & 0 & S_{55} \\ 0 & 0 & 0 & 0 & S_{56} & S_{66} \\ 0 & 0 & S_{73} & S_{74} & 0 & 0 & S_{77} \\ 0 & 0 & S_{83} & S_{84} & 0 & 0 & S_{78} & S_{88} \\ S_{91} & S_{92} & 0 & 0 & 0 & 0 & 0 & 0 & S_{99} \\ S_{101} & S_{102} & 0 & 0 & 0 & 0 & 0 & 0 & S_{910} & S_{1010} \\ 0 & 0 & S_{113} & S_{114} & 0 & 0 & 0 & 0 & 0 & 0 & S_{1111} \\ 0 & 0 & S_{123} & S_{124} & 0 & 0 & 0 & 0 & 0 & 0 & S_{1112} & S_{1212} \\ S_{131} & S_{132} & 0 & 0 & 0 & 0 & 0 & 0 & 0 & 0 & 0 & 0 & S_{1313} \\ S_{141} & S_{142} & 0 & 0 & 0 & 0 & 0 & 0 & 0 & 0 & 0 & 0 & S_{1314} & S_{1414} \\ 0 & 0 & S_{153} & S_{154} & 0 & 0 & 0 & 0 & 0 & 0 & 0 & 0 & 0 & 0 & S_{1515} \\ 0 & 0 & S_{163} & S_{164} & 0 & 0 & 0 & 0 & 0 & 0 & 0 & 0 & 0 & 0 & S_{1516} & S_{1616} \\ S_{171} & S_{172} & 0 & 0 & 0 & 0 & 0 & 0 & 0 & 0 & 0 & 0 & 0 & 0 & 0 & 0 & S_{1717} \\ S_{181} & S_{182} & 0 & 0 & 0 & 0 & 0 & 0 & 0 & 0 & 0 & 0 & 0 & 0 & 0 & 0 & S_{1718} & S_{1818} \\ 0 & 0 & S_{193} & S_{194} & 0 & 0 & 0 & 0 & 0 & 0 & 0 & 0 & 0 & 0 & 0 & 0 & 0 & 0 & 0 \\ S_{201} & S_{202} & 0 & 0 & 0 & 0 & 0 & 0 & 0 & 0 & 0 & 0 & 0 & 0 & 0 & 0 & 0 & 0 & 0 & 0 \\ 0 & 0 & S_{213} & S_{214} & 0 & 0 & 0 & 0 & 0 & 0 & 0 & 0 & 0 & 0 & 0 & 0 & 0 & 0 & 0 & 0 & 0 \\ S_{221} & S_{222} & 0 & 0 & 0 & 0 & 0 & 0 & 0 & 0 & 0 & 0 & 0 & 0 & 0 & 0 & 0 & 0 & 0 & 0 & 0 & 0 \\ 0 & 0 & S_{233} & S_{234} & 0 & 0 & 0 & 0 & 0 & 0 & 0 & 0 & 0 & 0 & 0 & 0 & 0 & 0 & 0 & 0 & 0 & 0 & 0 & 0 \\ S_{241} & S_{242} & 0 & 0 & 0 & 0 & 0 & 0 & 0 & 0 & 0 & 0 & 0 & 0 & 0 & 0 & 0 & 0 & 0 & 0 & 0 & 0 & 0 & 0 \end{bmatrix}$$

in which,

$S_{11}=S_{33}=S_{55}= N_x$; $S_{22}=S_{44}=S_{66}= N_y$; $S_{21}=S_{43}=S_{56}= N_{xy}$;

$S_{77}=S_{99}=S_{1111}=S_{1313}=S_{1515}=S_{1717}= (N_x h^2)/12$;

 $S_{88}=S_{1010}=S_{1212}=S_{1414}=S_{1616}=S_{1818}= (N_y h^2/12)$

$S_{75}=S_{910}=S_{1112}=S_{1314}=S_{1516}=S_{1718}= (N_{xy}h^2/12)$; $S_{73}=S_{91}=S_{113}=S_{131}=S_{153}=S_{171}= M_x$;

$S_{84}=S_{102}=S_{124}=S_{142}=S_{164}=S_{182}=$ M$_y$;

$S_{74}=S_{83}=S_{92}=S_{102}=S_{114}=S_{1213}=S_{132}=S_{141}=S_{154}=S_{163}=S_{172}=S_{181}=$ M$_{xy}$;

$S_{193}=S_{201}=S_{213}=S_{221}=S_{233}=S_{241}=$ Q$_x$; $S_{194}=S_{202}=S_{214}=S_{222}=S_{234}=S_{242}=$ Q$_y$

Where, N$_x$, N$_y$, N$_{xy}$ are the in-plane initial internal force resultants per unit length, M$_x$, M$_y$, M$_{xy}$ are the initial internal moment resultants per unit length, and Q$_x$, Q$_y$ are the initial transverse shear resultants.

APPENDIX D:

$$\{\varepsilon_{bt}\} = \left[\frac{\partial u_0}{\partial x} \quad \frac{\partial v_0}{\partial y} \quad \frac{\partial u_0}{\partial y} + \frac{\partial v_0}{\partial x} \right]^T ;$$

$$\{\varepsilon_{st}\} = \left[\frac{\partial w_0}{\partial x} \quad \frac{\partial w_0}{\partial y} \right]^T ;$$

$$\{\varepsilon_{sr}\} = [\theta_x \quad \theta_y \quad \phi_x \quad \phi_y \quad \alpha_x \quad \alpha_y \quad \beta_x \quad \beta_y \quad \gamma_x \quad \gamma_y]^T$$

$$\{\varepsilon_{br}\} = \left[\frac{\partial \theta_x}{\partial x} \quad \frac{\partial \theta_y}{\partial y} \quad \frac{\partial \theta_y}{\partial x} + \frac{\partial \theta_x}{\partial y} \quad \frac{\partial \phi_x}{\partial x} \quad \frac{\partial \phi_y}{\partial y} \quad \frac{\partial \phi_y}{\partial x} + \frac{\partial \phi_x}{\partial y} \quad \frac{\partial \alpha_x}{\partial x} \quad \frac{\partial \alpha_y}{\partial y} \quad \frac{\partial \alpha_y}{\partial x} + \frac{\partial \alpha_x}{\partial y} \quad \frac{\partial \beta_x}{\partial x} \quad \frac{\partial \beta_y}{\partial y} \quad \frac{\partial \beta_y}{\partial x} + \frac{\partial \beta_x}{\partial y} \quad \frac{\partial \gamma_x}{\partial x} \quad \frac{\partial \gamma_y}{\partial y} \quad \frac{\partial \gamma_y}{\partial x} + \frac{\partial \gamma_x}{\partial y} \right]^T$$

$$[z_1] = \left[(-h_c)I \quad \left[\overline{z_1} \right] \quad \overline{0} \quad \overline{0} \quad \overline{0} \right]; \quad [z_2] = \left[\left[\overline{z_2} \right] \quad \overline{0} \quad \overline{0} \quad \overline{0} \quad \overline{0} \right];$$

$$[z_3] = \left[(h_c)I \quad \overline{0} \quad \left[\overline{z_3} \right] \quad \overline{0} \quad \overline{0} \right]$$

$$[z_4] = \left[(h_c)I \quad \overline{0} \quad (h)I \quad \left[\overline{z_4} \right] \quad \overline{0} \right]; \quad [z_5] = \left[(h_c)I \quad \overline{0} \quad (h)I \quad (h_v)I \quad \left[\overline{z_5} \right] \right];$$

$$[z_6] = \left[\tilde{0} \quad \tilde{I} \quad \tilde{0} \quad \tilde{0} \quad \tilde{0} \right]$$

$$[z_7] = \left[\tilde{I} \quad \tilde{0} \quad \tilde{0} \quad \tilde{0} \quad \tilde{0} \right]; \quad [z_8] = \left[\tilde{0} \quad \tilde{0} \quad \tilde{I} \quad \tilde{0} \quad \tilde{0} \right];$$

$$[z_9] = \left[\tilde{0} \quad \tilde{0} \quad \tilde{0} \quad \tilde{I} \quad \tilde{0} \right]; \quad [z_{10}] = \left[\tilde{0} \quad \tilde{0} \quad \tilde{0} \quad \tilde{0} \quad \tilde{I} \right]$$ Where,

$$\left[\overline{z_1} \right] = \begin{bmatrix} (z+h_c) & 0 & 0 \\ 0 & (z+h_c) & 0 \\ 0 & 0 & (z+h_c) \end{bmatrix}; \quad \left[\overline{z_2} \right] = \begin{bmatrix} z & 0 & 0 \\ 0 & z & 0 \\ 0 & 0 & z \end{bmatrix};$$

$$\left[\overline{z_3} \right] = \begin{bmatrix} (z-h_c) & 0 & 0 \\ 0 & (z-h_c) & 0 \\ 0 & 0 & (z-h_c) \end{bmatrix}$$

$$\left[\overline{z_4}\right]=\begin{bmatrix}(z-h_4)&0&0\\0&(z-h_4)&0\\0&0&(z-h_4)\end{bmatrix};\ \left[\overline{z_5}\right]=\begin{bmatrix}(z-h_5)&0&0\\0&(z-h_5)&0\\0&0&(z-h_5)\end{bmatrix}$$

$$\overline{0}=\begin{bmatrix}0&0&0\\0&0&0\\0&0&0\end{bmatrix};\ I=\begin{bmatrix}1&0&0\\0&1&0\\0&0&1\end{bmatrix};\ \tilde{0}=\begin{bmatrix}0&0\\0&0\end{bmatrix};\ \tilde{I}=\begin{bmatrix}1&0\\0&1\end{bmatrix}$$

APPENDIX E:

$$[B_{tbi}]=\begin{bmatrix}\dfrac{\partial n_i}{\partial x}&0&0\\0&\dfrac{\partial n_i}{\partial y}&0\\\dfrac{\partial n_i}{\partial y}&\dfrac{\partial n_i}{\partial x}&0\end{bmatrix};\ [B_{tsi}]=\begin{bmatrix}0&0&\dfrac{\partial n_i}{\partial x}\\0&0&\dfrac{\partial n_i}{\partial y}\end{bmatrix};$$

$$[B_{rbi}]=\begin{bmatrix}\widehat{B}_{rbi}&\widehat{0}&\widehat{0}&\widehat{0}&\widehat{0}\\\widehat{0}&\widehat{B}_{rbi}&\widehat{0}&\widehat{0}&\widehat{0}\\\widehat{0}&\widehat{0}&\widehat{B}_{rbi}&\widehat{0}&\widehat{0}\\\widehat{0}&\widehat{0}&\widehat{0}&\widehat{B}_{rbi}&\widehat{0}\\\widehat{0}&\widehat{0}&\widehat{0}&\widehat{0}&\widehat{B}_{rbi}\end{bmatrix};\ [\widehat{B}_{rbi}]=\begin{bmatrix}\dfrac{\partial n_i}{\partial x}&0\\0&\dfrac{\partial n_i}{\partial y}\\\dfrac{\partial n_i}{\partial y}&\dfrac{\partial n_i}{\partial x}\end{bmatrix};$$

$$[B_{rsi}]=\begin{bmatrix}\tilde{I}&\tilde{0}&\tilde{0}&\tilde{0}&\tilde{0}\\\tilde{0}&\tilde{I}&\tilde{0}&\tilde{0}&\tilde{0}\\\tilde{0}&\tilde{0}&\tilde{I}&\tilde{0}&\tilde{0}\\\tilde{0}&\tilde{0}&\tilde{0}&\tilde{I}&\tilde{0}\\\tilde{0}&\tilde{0}&\tilde{0}&\tilde{0}&\tilde{I}\end{bmatrix}$$

APPENDIX F:

$$\left[M^e\right]=\int\limits_{0}^{a_e}\int\limits_{0}^{b_e}\overline{m}\left[N_t\right]^T\left[N_t\right]dxdy;$$

$$\overline{m}=\left(\sum_{k=1}^{N}\rho_b\left(h_{k+1}-h_k\right)\right)+2\rho_c h_c+\left(\sum_{k=1}^{N}\rho_t\left(h_{k+1}-h_k\right)\right)+\rho_v h_v+\rho_p h_p$$

$$\left[K_{tt}^e\right]=\left[K_{tb}^e\right]+\left[K_{ts}^e\right]+\left[K_{tbs}^{pe}\right]_b+\left[K_{tbs}^{pe}\right]_s;\ \left[K_{rr}^e\right]=\left[K_{rrb}^e\right]+\left[K_{rrs}^e\right]+\left[K_{rrbs}^{pe}\right]_b+\left[K_{rrbs}^{pe}\right]_s$$

$$\left[K_{tr}^e\right]=\left[K_{trb}^e\right]+\left[K_{trs}^e\right]+\frac{1}{2}\left(\left[K_{trbs}^{pe}\right]_b+\left[K_{trbs}^{pe}\right]_s+\left[K_{rtbs}^{pe}\right]_b^T+\left[K_{rtbs}^{pe}\right]_s^T\right)$$

$$\left[K_{tr}^{e}\right]^{T}=\left[K_{trb}^{e}\right]^{T}+\left[K_{trs}^{e}\right]^{T}+\frac{1}{2}\left(\left[K_{trbs}^{pe}\right]_{b}^{T}+\left[K_{trbs}^{pe}\right]_{s}^{T}+\left[K_{rtbs}^{pe}\right]_{b}+\left[K_{rtbs}^{pe}\right]_{s}\right)$$

$$\left\{F^{e}\right\}=\int\limits_{0}^{a_{e}}\int\limits_{0}^{b_{e}}\left[N_{t}\right]^{T}\left(\{f\}+\left\{F_{t}^{therm}\right\}+\left\{F_{t}^{therm}\right\}\right)dxdy$$

$$\left\{F_{tp}^{e}\right\}=\left\{F_{tb}^{e}\right\}_{p}+\left\{F_{ts}^{e}\right\}_{p};\quad\left\{F_{rp}^{e}\right\}=\left\{F_{rb}^{e}\right\}_{p}+\left\{F_{rs}^{e}\right\}_{p}$$

Where, $\left[K_{tb}^{e}\right]=\int\limits_{A_{e}}\left[B_{tb}\right]^{T}\left(\left[D_{tb}^{b}\right]+\left[D_{tb}^{c}\right]+\left[D_{tb}^{t}\right]+\left[D_{tb}^{v}\right]+\left[D_{tb}^{p}\right]\right)\left[B_{tb}\right]dA^{e}$

$$\left[K_{trb}^{e}\right]=\int\limits_{A_{e}}\left[B_{tb}\right]^{T}\left(\left[D_{trb}^{b}\right]\left[B_{rb}^{b}\right]+\left[D_{trb}^{c}\right]\left[B_{rb}^{c}\right]+\left[D_{trb}^{t}\right]\left[B_{rb}^{t}\right]+\left[D_{trb}^{v}\right]\left[B_{rb}^{v}\right]+\left[D_{trb}^{p}\right]\left[B_{rb}^{p}\right]\right)dA^{e}$$

$$\left[K_{rrb}^{e}\right]=\int\limits_{A_{e}}\left(\left[B_{rb}^{b}\right]^{T}\left[D_{trb}^{b}\right]\left[B_{rb}^{b}\right]+\left[B_{rb}^{c}\right]^{T}\left[D_{trb}^{c}\right]\left[B_{rb}^{c}\right]+\left[B_{rb}^{t}\right]^{T}\left[D_{trb}^{t}\right]\left[B_{rb}^{t}\right]+\left[B_{rb}^{v}\right]^{T}\left[D_{trb}^{v}\right]\left[B_{rb}^{v}\right]+\left[B_{rb}^{p}\right]^{T}\left[D_{trb}^{p}\right]\left[B_{rb}^{p}\right]\right)dA^{e}$$

$$\left[K_{tbs}^{pe}\right]_{b}=\int\limits_{A_{e}}\left[B_{tb}\right]^{T}\left[D_{tbs}^{b}\right]\left[B_{ts}\right]dA^{e};\left[K_{tbs}^{pe}\right]_{s}=\int\limits_{A_{e}}\left[B_{ts}\right]^{T}\left[D_{tbs}^{b}\right]^{T}\left[B_{tb}\right]dA^{e};$$

$$\left[K_{trbs}^{pe}\right]_{b}=\int\limits_{A_{e}}\left[B_{tb}\right]^{T}\left[D_{trbs}^{p}\right]\left[B_{rs}^{p}\right]dA^{e}$$

$$\left[K_{rtbs}^{pe}\right]_{b}=\int\limits_{A_{e}}\left[B_{rb}^{p}\right]^{T}\left[D_{rtbs}^{p}\right]\left[B_{ts}\right]dA^{e};\left[K_{rrbs}^{pe}\right]_{b}=\int\limits_{A_{e}}\left[B_{tb}\right]^{T}\left[D_{rrbs}^{p}\right]\left[B_{rs}^{p}\right]dA^{e};$$

$$\left\{F_{tb}^{e}\right\}_{p}=\int\limits_{A_{e}}\left[B_{rb}^{p}\right]^{T}\left\{D_{tb}^{p}\right\}dA^{e};\left\{F_{rb}^{e}\right\}_{p}=\int\limits_{A_{e}}\left[B_{tb}^{p}\right]^{T}\left\{D_{rb}^{p}\right\}dA^{e};$$

$$\left[K_{ts}^{e}\right]=\int\limits_{A_{e}}\left[B_{ts}\right]^{T}\left(\left[D_{ts}^{b}\right]+\left[D_{ts}^{c}\right]+\left[D_{ts}^{t}\right]+\left[D_{ts}^{v}\right]+\left[D_{ts}^{p}\right]\right)\left[B_{ts}\right]dA^{e}$$

$$\left[K_{rrb}^{e}\right]=\int\limits_{A_{e}}\left(\left[B_{rs}^{b}\right]^{T}\left[D_{rrs}^{b}\right]\left[B_{rs}^{b}\right]+\left[B_{rs}^{c}\right]^{T}\left[D_{rrs}^{c}\right]\left[B_{rs}^{c}\right]+\left[B_{rs}^{t}\right]^{T}\left[D_{rrs}^{t}\right]\left[B_{rs}^{t}\right]+\left[B_{rs}^{v}\right]^{T}\left[D_{rrs}^{v}\right]\left[B_{rs}^{v}\right]+\left[B_{rs}^{p}\right]^{T}\left[D_{rrs}^{p}\right]\left[B_{rs}^{p}\right]\right)dA^{e}$$

$$\left[K_{trbs}^{pe}\right]_{s}=\int\limits_{A_{e}}\left[B_{ts}\right]^{T}\left[D_{rtbs}^{p}\right]\left[B_{rb}^{p}\right]dA^{e};\left[K_{rtbs}^{pe}\right]_{s}=\int\limits_{A_{e}}\left[B_{rs}^{p}\right]^{T}\left[D_{rtbs}^{p}\right]\left[B_{tb}\right]dA^{e};$$

$$\left[K_{rrbs}^{pe}\right]_{s}=\int\limits_{A_{e}}\left[B_{rs}^{p}\right]^{T}\left[D_{rrbs}^{p}\right]\left[B_{rb}^{p}\right]dA^{e}$$

$$\left\{F_{t}^{therm}\right\}=\int\limits_{A_{e}}\left[B_{tb}\right]^{T}\left\{D_{tb}^{therm}\right\}dA^{e};\left\{F_{r}^{therm}\right\}=\int\limits_{A_{e}}\left[B_{rb}\right]^{T}\left\{D_{rb}^{therm}\right\}dA^{e}$$

$$\left\{F_{ts}^{e}\right\}_{p}=\int\limits_{A_{e}}\left[B_{ts}^{p}\right]^{T}\left\{D_{ts}^{p}\right\}dA^{e};\left\{F_{rs}^{e}\right\}_{p}=\int\limits_{A_{e}}\left[B_{rs}^{p}\right]^{T}\left\{D_{rs}^{p}\right\}dA^{e}$$ In which,

$$\left[D_{tb}^{b}\right]=\left[C_{b}^{b}\right]h_{b},\quad\left[D_{tb}^{c}\right]=2\left[C_{b}^{c}\right]h_{c},\quad\left[D_{tb}^{t}\right]=\left[C_{b}^{t}\right]h_{t},$$

$$\left[D_{tb}^{v}\right]=\left[C_{b}^{v}\right]h_{v},\quad\left[D_{tb}^{p}\right]=\left[C_{b}^{p}\right]h_{p},\quad\left[D_{ts}^{b}\right]=\left[C_{s}^{b}\right]h_{b}$$

$$\left[D_{ts}^c\right]=2\left[C_s^c\right]h_c,\quad \left[D_{ts}^t\right]=\left[C_s^t\right]h_t,\quad \left[D_{ts}^v\right]=\left[C_s^v\right]h_v,\quad \left[D_{ts}^p\right]=\left[C_s^p\right]h_p,\quad \left[D_{tbs}^p\right]=\left[C_{bs}^p\right]h_p$$

$$\left[D_{trbs}^p\right]=\int_{h_5}^{h_6}\left[C_{bs}^p\right][Z_{10}]dz,\quad \left[D_{rtbs}^p\right]=\int_{h_5}^{h_6}[Z_5]^T\left[C_{bs}^p\right]dz,\quad \left[D_{rrbs}^p\right]=\int_{h_5}^{h_6}[Z_5]^T\left[C_{bs}^p\right][Z_{10}]dz$$

$$\left[D_{trb}^b\right]=\int_{h_1}^{h_2}\left[C_b^b\right][Z_1]dz;\quad \left[D_{trb}^c\right]=\int_{h_2}^{h_3}\left[C_b^c\right][Z_2]dz;$$

$$\left[D_{trb}^t\right]=\int_{h_3}^{h_4}\left[C_b^t\right][Z_3]dz;\quad \left[D_{trb}^v\right]=\int_{h_4}^{h_5}\left[C_b^v\right][Z_4]dz;\quad \left[D_{trb}^p\right]=\int_{h_5}^{h_6}\left[C_b^p\right][Z_5]dz$$

$$\left[D_{rrb}^b\right]=\int_{h_1}^{h_2}[Z_1]^T\left[C_b^b\right][Z_1]dz;\quad \left[D_{rrb}^c\right]=\int_{h_2}^{h_3}[Z_2]^T\left[C_b^c\right][Z_2]dz;\quad \left[D_{rrb}^t\right]=\int_{h_3}^{h_4}[Z_3]^T\left[C_b^t\right][Z_3]dz,$$

$$\left[D_{rrb}^v\right]=\int_{h_4}^{h_5}[Z_4]^T\left[C_b^v\right][Z_4]dz,\quad \left[D_{rrb}^p\right]=\int_{h_5}^{h_6}[Z_5]^T\left[C_b^p\right][Z_5]dz$$

$$\left[D_{trs}^b\right]=\int_{h_1}^{h_2}\left[C_s^b\right][Z_6]dz,\quad \left[D_{trs}^c\right]=\int_{h_2}^{h_3}\left[C_s^c\right][Z_7]dz,\quad \left[D_{trs}^t\right]=\int_{h_3}^{h_4}\left[C_s^t\right][Z_8]dz,$$

$$\left[D_{trs}^v\right]=\int_{h_4}^{h_5}\left[C_s^v\right][Z_9]dz,\quad \left[D_{trs}^p\right]=\int_{h_5}^{h_6}\left[C_s^p\right][Z_{10}]dz,\quad \left[D_{rrs}^b\right]=\int_{h_1}^{h_2}[Z_6]^T\left[C_s^b\right][Z_6]dz,$$

$$\left[D_{rrs}^c\right]=\int_{h_2}^{h_3}[Z_7]^T\left[C_s^c\right][Z_7]dz;\quad \left[D_{rrs}^t\right]=\int_{h_3}^{h_4}[Z_8]^T\left[C_s^t\right][Z_8]dz\;;$$

$$\left[D_{rrs}^v\right]=\int_{h_4}^{h_5}[Z_9]^T\left[C_s^v\right][Z_9]dz;\quad \left[D_{rrs}^p\right]=\int_{h_5}^{h_6}[Z_{10}]^T\left[C_s^p\right][Z_{10}]dz$$

$$\{D_{tb}^{therm}\}=\left\{\left(\int_{h_1}^{h_2}\left(\left[C_b^b\right]\{\alpha_b\}T\right)dz\right)+\left(\int_{h_2}^{h_3}\left(\left[C_b^c\right]\{\alpha_c\}T\right)dz\right)+\left(\int_{h3}^{h_4}\left(\left[C_b^t\right]\{\alpha_t\}T\right)dz\right)+\left(\int_{h4}^{h_5}\left(\left[C_b^v\right]\{\alpha_v\}T\right)dz\right)+\left(\int_{h_5}^{h_6}\left(\left[C_b^p\right]\{\alpha_p\}T\right)dz\right)\right\}$$

$$\{D_{rb}^{therm}\}=\left\{\left(\int_{h_1}^{h_2}z\left(\left[C_b^b\right]\{\alpha_b\}T\right)dz\right)+\left(\int_{h_2}^{h_3}z\left(\left[C_b^c\right]\{\alpha_c\}T\right)dz\right)+\left(\int_{h3}^{h_4}z\left(\left[C_b^t\right]\{\alpha_t\}T\right)dz\right)+\left(\int_{h4}^{h_5}z\left(\left[C_b^v\right]\{\alpha_v\}T\right)dz\right)+\left(\int_{h_5}^{h_6}z\left(\left[C_b^p\right]\{\alpha_p\}T\right)dz\right)\right\}$$

$$\{D_{tb}^p\}=-\int_{h_5}^{h_6}\frac{\{e_b\}}{h_p}dz;\quad \{D_{ts}^p\}=-\int_{h_5}^{h_6}\frac{\{e_s\}}{h_p}dz;\quad \{D_{rb}^p\}=-\int_{h_5}^{h_6}[Z_5]^T\frac{\{e_b\}}{h_p}dz;\quad \{D_{rs}^p\}=-\int_{h_5}^{h_6}[Z_{10}]^T\frac{\{e_s\}}{h_p}dz$$

214

LIST OF PUBLICATIONS based on Ph.D Research Work

Sl. No.	Title of the Paper	Authors	Name of the Journal/ Conference Year, Volume & Page Number,	Publication Status / Date	Category *
1	Effect of temperature and moisture on free vibration characteristics of skew laminated hybrid composite and sandwich plates. https://doi.org/10.1016/j.tws.2020.107113	**Vinayak Kallannavar,** Balaji Kumaran, S. C. Kattimani	Thin-Walled Structures, 2020, Vol. 157, 107113. **Q1, IF – 4.442**	Published / September 2020	1
2	Neural Network-Based Prediction Model to Investigate the Influence of Temperature and Moisture on Vibration Characteristics of Skew Laminated Composite Sandwich Plates. https://doi.org/10.3390/ma14123170	**Vinayak Kallannavar,** Subhaschandra Kattimani, Manzoore Elahi M Soudagar, MA Mujtaba, Saad Alshahrani, Muhammad Imran	Materials, 2021, Vol, 14(12), 3170. **Q1, IF – 3.623**	Published / June 2021	1
3	Effect of temperature on the performance of active constrained layer damping of skew sandwich plate with CNT reinforced composite core. https://doi.org/10.1080/15376494.2021.1955315	**Vinayak Kallannavar,** Subhaschandra Kattimani	Mechanics of Advanced Materials and Structures, 2021, 1-20. **Q1, IF – 4.030**	Published / August 2021	1
4	Influence of temperature and moisture on free vibration behavior of skew laminated composite sandwich panels with CNTRC core.	**Vinayak Kallannavar,** Subhaschandra Kattimani, Ramesh H.	International Journal of Structural Stability and Dynamics **Q1, IF – 2.558**	Accepted/ September 2021	1
5	Effect of temperature and porosity on free vibration characteristics of a doubly-curved skew laminated sandwich composite shell with 3D printed PLA core.	**Vinayak Kallannavar,** Subhaschandra Kattimani	Thin-Walled Structures, **Q1,** **IF – 4.442**	Under Review/ November 2021	1

215

6	Dynamic performance of laminated composite plates with a circular hole.	**Vinayak Kallannavar,** Sagar Umatar, S Kattimani	International Conference on Emerging Research in Civil, Aeronautical and Mechanical Engineering	July 2019	3
7	Modal analysis of laminated composite and sandwich plates using finite element method.	**Vinayak Kallannavar,** Subhaschandra Kattimani	International Conference on Design, Materials & Manufacture	December 2019	3
8	Influence of Temperature on the Vibration Control of the Laminated Composite Sandwich Plate with A 3D Printed PLA Core	**Vinayak Kallannavar,** Subhaschandra Kattimani	International Conference on Applied Mechanics, Machine Learning and Advanced Computation. NITK Raipur. 2022. Accepted.	March, 2022	3

Category * 1: Journal paper, full paper reviewed   2 : Journal paper, Abstract reviewed
3 : Conference/Symposium paper, full paper reviewed   4 : Conference/Symposium paper, abstract reviewed
5 : others (including papers in Workshops, NITK Research Bulletins, Short notes etc.

Bkallam
Vinayak Basavanth Kallannavar
Research Scholar

Acatt 18/07/2022
Dr. Subhaschandra Kattimani
Research Guide

6	Dynamic performance of laminated composite plates with a circular hole.	**Vinayak Kallannavar,** Sagar Umatar, S Kattimani	International Conference on Emerging Research in Civil, Aeronautical and Mechanical Engineering	July 2019	3
7	Modal analysis of laminated composite and sandwich plates using finite element method.	**Vinayak Kallannavar,** Subhaschandra Kattimani	International Conference on Design, Materials & Manufacture	December 2019	3
8	Influence of Temperature on the Vibration Control of the Laminated Composite Sandwich Plate with A 3D Printed PLA Core	**Vinayak Kallannavar,** Subhaschandra Kattimani	International Conference on Applied Mechanics, Machine Learning and Advanced Computation. NITK Raipur. 2022. Accepted.	March, 2022	3

Category *   1: Journal paper, full paper reviewed   2 : Journal paper, Abstract reviewed
                3 : Conference/Symposium paper, full paper reviewed   4 : Conference/Symposium paper, abstract reviewed
                5 : others (including papers in Workshops, NITK Research Bulletins, Short notes etc.

Vinayak Basavanth Kallannavar
Research Scholar

Dr. Subhaschandra Kattimani
Research Guide

216

BIODATA

Name: Vinayak Basavanth Kallannavar

Fathers Name: Basavanth Kallannavar

Mothers name: Smt. Vimala B Kallannavar

Date of Birth April 02, 1991

Nationality: Indian

Marital Status: Single

Address:

Permanent Address	Present Address
Sri Siddhivinayak Nilaya,	Department of Mechanical Engineering
Shahunagar, Belgaum.	National Institute of Technology Karnataka
Pin-590010 India	Surathkal Mangalore-575025 India

Mobile Number: 8971050860

E-mail: kallannavarvinayak@gmail.com

Educational Qualification:

Qualification	Institute	University	Year of Passing	Performance
Ph.D. (Smart Sandwich Materials and Structures)	NITK	NITK	2022	8.5 (CGPA)
M.Tech (Design Engineering)	Visvesvariah Technological University	Dr. MSS KLE CET, Belgaum	2015	83.33% (University Gold Medalist)
B.E (Mechanical Engg.)	School of Engineering	MMEC Belgaum	2012	74.03%

I declare that the above information is true and correct to the best of my knowledge.

Bkallanoo

(VINAYAK BASAVANTH KALLANAVAR)

217